Haloperoxidase Mimics

Heterogeneous and Functional Catalysis of Oxidative Halogenation Reactions

Dissertation

zur Erlangung des akademischen Grades

"Doktor der Naturwissenschaften"

am Fachbereich Chemie,

Pharmazie und Geowissenschaften der

Johannes Gutenberg-Universität Mainz

JG|U

JOHANNES GUTENBERG
UNIVERSITÄT MAINZ

Karoline Herget

geboren in ▮▮▮▮▮▮

Chieming 2017

1. Berichterstatter: ██████████████████

2. Berichterstatter: ████████████████

Tag der mündlichen Prüfung: ████████████

To the peope I love most

I hereby declare that I wrote the submitted dissertation without any unauthorized external assistance and I used only sources acknowledged and referenced in the work. All textual passages, which are appropriated verbatim or paraphrased from published and unpublished texts, as well as all information obtained from oral sources are duly indicated and listed in accordance with bibliographical rules.

In carrying out this research, I complied with the rules of standard scientific practice as formulated in the statutes of the Johannes Gutenberg-Universität Mainz to insure standard scientific practice.

Chieming, September 23ʳᵈ, 2017.

Karoline Herget

Publications

[1]   **Herget K**., Pfitzner F., Frerichs H., Tahir M. N., Tremel W., "*Functional Enzyme Mimics for Oxidative Halogenation Reactions to Combat Biofilm Formation*", *Adv. Mater,* under revision.

[2]   Ragg R., Korschelt K., **Herget K**., Natalio F., Tahir M. N., Tremel W., "*Inorganic Nanoparticles as Enzyme Mimics*" in *Biocatalysis & Nanotechnology*, Pan Stanford Publishing Pte. Ltd. Singapore, **2017**.

[3]   **Herget K**., Frerichs H., Pfitzner F., Tremel W., "*Cerdioxid schützt vor marinem Fouling*", *Chem. Unserer Zeit* **2017**.
doi:10.1002/ciuz.201700799.

[4]   **Herget K**., Hubach P., Link T., Pusch S., Deglmann P., Götz H., Gorelik T.E., Gural'skiy I.A., Pfitzner F., Link T., Schenk S., Panthöfer M., Ksenofontov V., Kolb U., Opatz T., André R., Tremel W*., "Haloperoxidase Mimicry by CeO$_{2-x}$ Nanorods Combats Biofouling*", *Adv. Mater.* **2017**, 29 (4), 1603823.
doi: 10.1002/adma.201603823.

[5]   Tremel W., **Herget K.**, *"Use of Cerium dioxide particles as biocides",* Patent application, **2016**.

[6]   **Herget K.**, D. Schollmeyer, H. Detert, *"3,7,11-Tris{4-[(1R,3S,4S)-ne-omenth-yl--oxy]phen-yl}tri[1,2,4]triazolo[4,3-a:4',3'-c:4'',3''-e][1,3,5]triazine–chloro-form–ethanol (1/1/1)"*, *Acta Cryst. E,* **2013**, 69 (3), 0365-0366.
doi:10.1107/S1600536813003498.

Acknowledgments

During the years of study at the University of Mainz I met so many interesting people, had so many acquaintances, colleagues, fellow students, trainees, bachelor, master and Ph.D. students and many genuine friends – here I would like to thank all of you who greatly enriched my life.

But first of all, I would like to thank my family for their overall love and support from my beginning on. We have gone through ups and downs, managed all difficulties together and I only can try to express how much I love my mum, dad, and my two little sisters!

For my Ph.D. thesis, in particular, I would like to extend my sincere thanks to my thesis mentor and professor ███████ so much for that great, interesting and interdisciplinary research topic. Because of him I got therein the opportunity to take a look beyond my own horizon and behind the scenes.

Contents

List of Figures

List of Tables

List of Symbols, Notations and Abbreviations

a	reaction order
A	absorbance
(A)HL	(acyl) homoserine lactone
3-oxo-AHL	N-(3-oxo-acyl)homoserine lactone
5′-FDA	5′-fluoro-5′-deoxyadenosine
ABTS	2,2′-azino-bis(3-ethylbenzothiazoline-6-sulfonic acid) diammonium salt
AI-1/-2	autoinducer -1/-2
AIP	autoinducing peptide
APF	aminophenyl fluorescein
BE	binding energy
BET	Brunauer/Emmett/Teller (mathematical method)
BPO	bromoperoxidase
Br_2TB	3,3'-dibromothymolsulfonphthalein, "bromothymol blue"
Br_4PR	3′,3″,5′,5″-tetrabromophenolsulfonphthalein, "bromophenol blue"
C	catalyst
C. officinalis	Corallina officinalis
C. violaceum	Chromobacterium violaceum
CB	celestine blue
CPO	chloroperoxidase
CSP	competence-stimulating peptide
d	diameter
DAHL	N-(α,α-dibromoacetyl) homoserine lactone
DAPI	4′,6-diamidino-2-phenylindole dihydrochloride
DBHL	dibromine homoserine lactones
DFT	density functional theory
d-H_2O	deuterated water
DHP	2,3-dihydro-4H-pyran
DMB	dimethoxybenzene
DMP	3,5-dimethylphenol
DMPO	5,5-dimethyl-pyrroline N-oxide (spin trap)
DMT	2,3-dimethoxytoluene
DPD	4,5-dihydroxy-2,3-pentanedione
ε	extinction coefficient
E. coli	Escherichia coli
E_A	activation energy
EDTA	ethylenediaminetetraacetic acid
EPR	electron paramagnetic resonance (spectroscopy)
FAAH	fatty acid amide hydrolase

FAD	flavin adenine dinucleotide
F-HG	flavin-dependent halogenases
FT-IR	fourier transform infrared spectroscopy
GBAP	gelatinase biosynthesis-activating pheromone
GFP	green fluorescent protein
GGA-DFT	generalized gradient approximation– density functional theory
HF	hard paint formulation, often silicone alkyd based
HFP	hydroxyphenyl fluorescein
HG	halogenase
HI-HPO	heme iron(II)-dependent haloperoxidases
HO$^\bullet$	hydroxyl radical
HOX	hypohalous acid
HPA	heteropolyacid
HPLC	high performance liquid chromatography
HPLC/ESI-MS	high performance liquid chromatography/ electrospray ionization mass spectrometry
HPO	haloperoxidase
HRTEM	high-resolution transmission electron microscopy
HSAB	Pearson´s HSAB model
HX	halide acid
IC$_x$	inhibitory concentration, specific substance concentration resulting in a x % decrease of e.g. viability
ICP-MS	Inductively electrochemical potential
ICT	intramolecular charge transfer
k_{cat}	rate constant (per time unit) in enzyme kinetics
k_{gen}	general reaction constant (per time unit)
K_m	Michaelis (-Menten) constant
LB	Linewaver-Burk
LB-Medium	Luria/Miller growth medium
LDH	layered double hydroxide
LuxI	example of an acyl-homoserine-lactone synthase
LuxP; LsrB	example of an autoinducer-2 binding (P = periplasmic) protein (receptor)
LuxQ	example of an autoinducer-2 sensor kinase/phosphatase
LuxR; LsrR	examples of transcriptional activator proteins
LuxS	*S*-ribosylhomocysteine lyase
MBHL	monobromine homoserine lactone
MCD	monochlorodimedone
MCM	mesoporous silica
MMO	methane monooxygenases
MPO	myeloperoxidase
MQW	Milli-Q water, "ultrapure water" *via* filtration and deionization process, characteristics: 18.2 MΩ·cm at 25°C

NAD(P)H	nicotinamide adenine dinucleotide (phosphate), reduced form of the enzymatic cofactor
NBS	*N*-bromosuccinimide
NI-HPO	non-heme iron(II)-dependent haloperoxidases
NMR	nuclear magnetic resonance
Nu	nucleophile
nw	nanowire
OHHL	*N*-3-oxohexanoyl homoserine lactone
OVN	Overnight liquid culture (here: of *E. coli*)
OX⁻	hypohalogenite
P	product
PAN	polyacrylonitrile
PEG	polyethylene glycol
PET	positron emission tomography
Ph	phenol
POM	polyoxometallate
PR	phenolsulfonphthalein, "phenol red"
PS	polystyrene
PVC	polyvinyl chloride
q.e.d.	*quod erat demonstrandum*, "what was to be demonstrated"
QS	quorum sensing
R_2NX	halo-amines
REACH	Registration, Evaluation, Authorization and Restriction of Chemicals
R-H	(non-saturated) organic substrate, nucleophilic acceptor
RNS	reactive nitrogen species
ROS	reactive oxygen species
rpm	revolutions per minute
R-X	(non-saturated) halogenated, organic compound
S	substrate
SA	specific activity
SaA	salicylaldehyde
SAH	*S*-adenosylhomocysteine
SAM-HG	*S*-adenosyl-L-methionine-dependent halogenases
SBA	sulphated zirconia on mesoporous silica
SEM	scanning electron microscopy
SF	soft /self-polishing resin paint formulation
SOD	superoxide dismutase
SQUID	superconducting quantum interference device (for magnetic susceptibility measurements)
TB	thymolsulfonephthalein
TBAB	tetrabutylammonium bromide

TEM	transmission electron microscopy
TL	Toplac, a commercial hard paint formulation from Akzo Nobel
TLC	thin-layer chromatography
TMB	1,3,5-trimethoxybenzene
TNB	2-nitro-5-thiobenzoate
TOF	turn over frequency or rate (= k_{cat} = TON/per time unit)
TON	turn over numbers (also often referred to k_{cat} in enzyme kinetics), dimensionless
TRIS (-SO$_4$)	tris(hydroxymethyl)aminomethane sulfate buffer
UV-Vis	Ultraviolet–visible spectroscopy or spectrophotometry (in the ultraviolet-visible spectral region)
V-BPO	vanadium-dependent bromoperoxidase
V-CPO	vanadium-dependent chloroperoxidase
V-HPO	vanadium-dependent haloperoxidases
vmax	maximum reaction rate in enzyme kinetics
X$^-$	halide anion
X$_2$	halogen
XPS	X-ray photoemission/photoelectron spectroscopy
XRD	X-ray diffraction
ZSM; NaX; NaY; KL	examples of different kinds of zeolites

Abstract

Within minutes, all structures in natural waters suffer from biofouling, the colonization of aquatic organisms. This natural phenomenon conserving and expanding habitats as well as species turned out fatal for the marine industry wreaking havoc on shipping and offshore plants each year. Chemical antifouling coatings that are commercially available, currently release toxins like copper and other co-biocides to retard the growth of algae and encrusting organisms. In contrast, Nature's sophisticated and highly efficient defense strategy against epibiont growth mainly relies on halogenating enzymes, a highly specialized subclass of oxidoreductases. In particular, the enzyme vanadium-haloperoxidase (V-HPO) is considered to play an important role in marine organisms by producing brominated organic components within their metabolism as well as in the release of low-molecular hypobromous species. These highly reactive compounds as hypobromous acid and hypobromites (HOBr/BrO$^-$) are essential in their defense system against bacterial attack and biofouling by interfering with the colonization process at its lowest level, the bacterial cell-cell communication ("quorum sensing").

This thesis focusses the catalytic activity of these fascinating halogenating enzymes in general as well as possible applications. The first Chapter presents a detailed introduction into the topic including the variety of transition metal V-HPO mimics that had been explored. Additionally, the underlying BASF cooperation project is described with regards to the development of new antifouling paint formulations based on V-HPO enzyme mimetic activity. Of particular significance and inspired by the Belousov-Zhabotinsky reaction, the scope of interest has been extended to cerium dioxide nanoparticles (nanoceria) emulating natural iron containing halogenating enzymes. In dependency to their morphology and Ce^{3+}/Ce^{4+} ratio, they radically catalyzed the conversion of bromide ions to reactive intermediates that target bacterial signaling compounds controlling bacterial quorum sensing. Laboratory and field tests with paint formulations containing 2 wt% of nanoceria showed a reduction in biofouling comparable to copper(I) oxide, the most typical biocidal pigment. Nanoceria has the potential to be the pioneer for highly stable, non-soluble, non-toxic, low-cost and sustainable substitute for conventional inorganic/organic biocides with high damage in bacterial biofilms but minimal collateral effects to the environment.

Zusammenfassung

Alle Strukturen in natürlichen Gewässern werden innerhalb weniger Minuten von den in Wasser lebenden Mikroorganismen besiedelt. Dieser natürliche Besiedlungs- und Kolonisationsvorgang wird als „Biofouling" bezeichnet und verursacht vor allem in der Schifffahrtsindustrie und dem Offshore-Bereich jährlich verheerende Schäden. Um diesen Schaden zu begrenzen und das „Biofouling" zu verhindern, werden kommerziell verfügbare "Antifouling"-Farben eingesetzt, die über die Zeit meist Kupferverbindungen und andere, toxische Biozide an die Umgebung abgeben. Im Vergleich dazu existiert in der Natur ein wesentlich effizienterer Mechanismus, um dem „Biofouling" entgegen zu wirken. Dieses ausgeklügelte, biologisch-chemisches Abwehrsystem beruht auf der Wirkweise von halogenierenden Enzymen wie der Vanadium-Haloperoxidase (V-HPO), die von vielen marinen Organismen exprimiert werden. Haloperoxidasen stehen unter anderem im engen Zusammenhang mit der Bildung von hochreaktiven niedermolekularen, bromierten Verbindungen wie hypobromige Säure und Hypobromite (HOBr/BrO$^-$). Diese bilden nach Freisetzung die wesentlichen Verteidigungselemente gegen mikrobielle und bakterielle Angriffe, indem sie die unterste Stufe der Kolonisation unterbinden: die bakteriellen Zell-Zell-Kommunikation ("Quorum Sensing").

Der Schwerpunkt dieser Arbeit liegt auf der katalytischen Aktivität dieser faszinierenden Enzymklasse und deren Anwendungsmöglichkeiten. Das erste Kapitel enthält detaillierte Hintergrundinformationen zu halogenierenden Enzymen und den bereits entwickelten, heterogenen Haloperoxidease-Mimetika, gefolgt von der Beschreibung des zugrundeliegenden BASF Kooperationsprojektes zur Entwicklung von modernen Antifouling-Farbformulierungen auf Basis der natürlichen Abwehrstrategie der Haloperoxidasen. Durch die oxidative Bromierung innerhalb der Belousov-Zhabotinsky Reaktion rückte die katalytische Wirkung des Elements Cer in unser Interesse. Aufgrund dessen beschäftigen sich die letzten Kapitel mit Cerdioxid-Nanopartikeln als neuartige Haloperoxidase-Mimetika, deren zugrunde liegender, radikalischer Reaktionsmechanismus mit dem von Eisen-abhängigen, halogenierenden Enzymen vergleichbar ist. In Abhängigkeit zu ihrer Struktur und dem Ce^{3+}/Ce^{4+} Verhältnis konnte gezeigt werden, dass Cerdioxid-Nanopartikel die Bildung von reaktiven Hypobromit-Spezies katalysieren, die in einer Folgereaktion bakterielle Signalmoleküle modifizieren und somit das bakterielle „Quorum Sensing" stören können. Farbformulierungen, die zwei Gewichts-% Cerdioxid-Nanopartikel

enthielten, zeigten im Labor als auch in Feldversuchen einen verminderten, bakteriellen Bewuchs mit einer vergleichbaren Aktivität zu dem Biozid Kupfer(I) oxid. Daher bieten Cerdioxid-Nanopartikel die Möglichkeit, eine Vorreiterrolle in der Entwicklung von hoch stabilen, unlöslichen, ungiftigen, preisgünstigen und nachhaltigen Ersatzstoffen von konventionellen Bioziden mit erhöhter „Antifouling"-Wirkung, aber mit minimalen Umweltauswirkungen, einzunehmen.

1
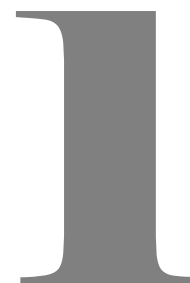
Functional Enzyme Mimics

Functional Enzyme Mimics for Oxidative Halogenation
Reactions to Combat Biofilm Formation

Chemical halogenation is an important transformation in organic synthesis. Halogenations involve the use of reactive, toxic and corrosive halogens (X_2) or hydrogen halides (HX). Chemical halogenations are fast and exothermic, but with little regio- or stereoselectivity. By doing halogenation reactions with halide anions, O_2 or hydrogen peroxide (H_2O_2) as oxidants and vanadium- or iron-dependent haloperoxidases or FAD-dependent halogenases as catalysts biosynthesis provides this specificity and selectivity. In nature, halogenation is a strategy to increase the biological activity of secondary metabolites with antibacterial, antiviral, antiprotozoal, and antifungal properties. State of the art

performance-based regulation of industrial biocides is an opportunity for innovative improvement. Since halogenated secondary metabolites prevent the formation of bacterial biofilms and combat biofouling, halogenating enzymes have been proposed as alternatives to traditional antifouling compounds. Feedback inhibition of haloperoxidase synthesis in bacteria is caused by the halogenated metabolites, thereby limiting the concentration of halogenating agent that can be produced. Thus, regulation of the remedy protects plants and animals from excessive concentrations of biocides. This review classifies these enzymes according to their catalytic functions and in view the current knowledge about the chemistry of settlement and adhesion of fouling organisms. It highlights molecular enzyme analogues and transition metal-based nanoparticles as functional enzyme mimics for the catalytic production of repellents *in situ*. The validity of the various modes of action is evaluated and the enzyme mimics with the highest potential are highlighted. The lesson from nature to innovation in microbial antifouling technology is: Observe nature and try to understand it. Try to imitate it, and explain the copy. There is still much to be learnt for emulating natural defense mechanisms.

1.1 Introduction

Catalysis is at the heart of chemistry as it provides tools for efficiently and selectively making and breaking chemical bonds. This is crucial for enhancing the development of natural resources by preventing waste and air pollution while conserving energy and making our industry safer. It is the basis of large-scale processes in bulk chemistry and petrochemistry. Future environmental requirements will necessitate new catalytic solutions. Enzymes are among the most effective catalysts known in terms of their efficiency and selectivity. They can achieve rate accelerations by several orders of magnitude, and sometimes react exclusively with only one single stereoisomer of a substrate if required. The number of industrial applications has exploded in recent years, mainly because of advances in protein engineering technology and environmental and economic necessities. After introducing enzymatic catalysis[1–4] a number of enzyme-based processes have been commercialized for producing valuable products, but their industrial applications are still restricted because of stability, catalytic efficiency, and specificity. Enzyme engineering allowed to overcome such shortcomings and to extend their substrate range.[5,6]

Chemists have tried to mimic enzymes early on by developing artificial enzyme models. Breslow and coworkers originally coined the terms "biomimetic chemistry" and "artificial enzyme" to describe this field.[7] Many features of an enzyme must be considered when active mimics are sought. Enzymes bind their substrates and catalysis is achieved with the aid of two or more functional groups. This allows for substrate selectivity, reaction selectivity, and stereoselectivity. Binding occurs by metal coordination, ion pairing, metal or Lewis acid-base coordination as well as hydrophobic interactions with roughly half the known enzymes using metal ions while the other half solely relies on organic functional groups. Stability is still a key problem.

To engineer the stability of a protein, modifications at the active site are a good point to start. This may appear paradox, as substitutions at the active site typically reduce the activity of a mutant protein. Still, a multitude of functional artificial enzyme models for very different types and classes of enzymes have been developed, some closely mimicking the mode of action of their natural counterparts while others just adopt some general features encountered in enzymes. Attempts to develop genuine enzyme-mimetic systems have been successful in achieving substrate binding, but less successful in accomplishing high turnover rates. Large and ingeniously-designed molecular binding structures have been synthesized for the purpose of catalysis.[8–10]

Based on reports that nanomaterials can exhibit enzyme-like activities and show *in vitro* biocompatibility, new nanomaterial-based artificial enzymes have been investigated that might have the potential to be functional even inside cells or living organisms.[11–14] An important question is, whether inorganic nanomaterials can mimic the high catalytic efficiency of their natural analogues which speed up a wide variety of different reactions by binding the substrates with exceptional specificity.[15–25]

The activity and reaction specificity of natural enzymes is highly dependent on the specific reaction conditions like temperature, pH and the chemical structure of the substrate, but enzymes generally suffer from low stability, short shelf life and high production costs which limits their versatility compared to nanoparticle mimics. In contrast, nanoparticles can be surface functionalized for specific targeting and tolerate changes in reaction conditions more easily.[26,27] Furthermore, nanoparticle mimics can operate in non-aqueous systems, and they can be manufactured cost-efficiently up to industrial-scale.

One of the key features related to nanoparticles is their enhanced chemical activity due to their large surface area which leads to high catalytic activities. Great efforts have been made in recent years to identify new materials with enzyme-like activities that are equally or even more efficient than their natural counterparts. An exceeding number of reports on peroxidase nanoparticle mimics have been published,[15,28] whereas very few other enzymatic systems have been explored so far. Several enzymes have been particularly intriguing because they catalyze oxidation and/or halogenation reactions that hold great promise for synthetic applications.

As an example, nature oxidizes methane to methanol enzymatically in a single step under aerobic conditions with methane monooxygenases (MMO), a group of enzymes with active sites containing iron- or copper-oxygen centers,[29–31] whereas current industrial processes that convert alkanes, in particular methane, to more valuable products operate at high temperature and pressure and lead to a variety of products. Still, the activity of MMOs has been mimicked at oxygen-activated iron sites,[32] and oxygen-activated copper sites in zeolite Cu-ZSM-5 have been shown to convert methane to methanol at low temperatures (100°C) with almost full selectivity.[33,34]

Another striking example are cytochrome P450 enzymes which catalyze the insertion of one atom of an oxygen molecule into the aliphatic position of an organic substrate (RH) while the other one is reduced to water. Cytochromes P-450 are a superfamily of heme-type mixed-function oxidases of animal or microbial origin. The natural use of P450 requires cofactors such as NAD(P)H and electron-transfer proteins such as P450-reductase, which is one of the main obstacles to commercial implementation. Regeneration systems are available to solve the cofactor problem,[35,36] but these electron transport chains are more difficult to optimize and do not have the robustness required for a chemical transformation at large scale. This is a reason why cofactor-dependent oxidoreductases are lagging behind "simple" cofactor-independent enzymes (e.g. hydrolases, oxidases, peroxidases) considering their implementation in synthetic organic chemistry. The catalytic activities of P450 for the substrate conversion are maintained when a cofactor is replaced by an electrode or metal nanoparticles as an electron donor to P450 dissolved in solution thereby shortcutting the complex natural electron transport chain.[37–39] A redox mediator between the electrode and P450 may or may not be required depending on systems.[40–47]

Cytochrome P450 enzymes have potential uses in the synthesis and discovery of drugs, as well as in drug development. The enzymes have been used already in the 1950s to introduce functional groups into drugs that would be difficult to introduce chemically.[48] The success of P450 enzymes as selective biocatalysts for a wide range of oxygenation reactions of complex substrates has stimulated the study of metalloporphyrin model compounds that mimic P450 reactivity. Key intermediates of the metal porphyrin-catalyzed oxygenation reactions include oxo- and dioxometal(V) species that transfer an oxygen atom to the substrate through a hydrogen abstraction/oxygen recombination pathway known as the oxygen rebound mechanism.[49]

Important in the context of this review is that carbon−halogen bond formation including fluorination reactions are also catalyzed by manganese porphyrins and related salen complexes. Groves and coworkers[50,51] reported that biphasic sodium hypochlorite/manganese porphyrin systems convert even inactivated aliphatic C−H to C− Cl bonds efficiently and selectively. The oxygen rebound rate in Mn-mediated hydroxylation is correlated with the nature of the transaxial ligands L bound to the manganese center (L− Mn^V−O). In particular, Mn-catalyzed aliphatic C−H fluorination reactions could be carried out with simple fluorides because fluoride ions slow down the oxygen rebound step to such an extent that long-lived substrate radicals can be trapped with a Mn−F fluorine source, which in turn promotes carbon−fluorine bond formation.[52,53]

Although C-H fluorination has been achieved with a haloperoxidase-rated Mn complex, the redox potential of fluorine precludes the haloperoxidase-type mechanism used in the metabolic incorporation of chloride and bromide ions with V – or Fe – dependent enzymes. Still, very few enzymes have been described that can convert fluoride to organic fluorine.[54,55] *Streptomyces cattleya* have evolved a fluorinase that overcomes the chemical challenges of using aqueous fluoride to form carbon–fluorine bonds.[56] It catalyzes a S_N2-type nucleophilic substitution at the C-5' position of *S*-adenosyl-*L*-methionine (SAM) and fluoride ions to form 5′-fluoro-5′-deoxyadenosine (5′-FDA) and *L*-methionine as neutral leaving group.[57] The fluorinase-catalyzed reaction show a significant rate enhancement (acceleration by a factor of 10^6 to 10^{15}).[57]

Halogenation reactions belong to the standard toolbox of synthetic organic chemistry because the polarity makes C-X bonds reactive enough to replace the halogen (X) by other substituents (Y). Halogenations are, however, free-radical reactions and therefore very unselective. In industry, halogenation reactions are typically performed with

hazardous, toxic and corrosive halogenating reagents, often in chlorinated solvents.[58–60] Vinyl chloride for example is synthesized by oxidative halogenation in a gas phase reaction from hydrochloric acid, oxygen, ethylene and a heterogeneous copper catalyst.[61] *N*-bromo- and *N*-chlorosuccinimide are more convenient sources of chlorine and bromine radicals for radical substitution and electrophilic addition reactions in organic synthesis. Late-stage fluorination is a popular and growing technology in medicinal chemistry with applications such as blocking site-specific metabolism and development of potential positron emission tomography (PET) ligands.[62,63]

Nature relies on the oxidative halogenation approach by making the halogenating agent *in situ* from halide anions under acidic conditions. This leads to highly efficient halogenations with a 100 % halogen atom economy. Suitable oxidants are either hydrogen peroxide or oxygen. Therefore, biochemical halogenation reactions catalyzed by haloperoxidases (HPOs) and halogenases (HGs) have attracted growing interest in academic and industrial research.[58,59,64–71] These enzymes are considered "green" catalysts for the synthesis of antiviral and anticancer drugs, but also with respect to their antimicrobial activity. Detailed information about fluorinated compounds[62,63] and halogenated[72–75] natural products is available in journals on marine pharmacology.[76–78]

In recent years HPO-like mimics and the corresponding halogenated products have been investigated because of better cost economy, easier large-scale synthesis and higher stability under operating conditions (pH, salt concentrations, organic solvents)[79] compared to native enzymes. The intention of this review is twofold: (i) to review halogenating enzymes and relevant assays to monitor oxidative halogenation reactions and (ii) to highlight new catalysts as functional HPO mimics for the halogenation of organic compounds under ambient conditions and their potential to combat biofouling.

1.2 Halogenating Enzymes

Natural halogenating enzymes encountered in eukaryotes and prokaryotes[80] came into the focus of attention because of their versatile applications.[81] Many halogenating enzymes in bacteria, archaea, fungi and algae are vanadium-dependent, and many hosts are marine organisms. The special enzymes catalyze the electrophilic oxidative halogenation of organic compounds *via* reactive oxygen species (ROS).[82,83] (Pseudo-)halides, especially Cl^-, Br^-, I^-, CN^- and SCN^-, are oxidized in two-electron transitions to the corresponding hypohalous acids or hypohalites.[84] Depending on the required co-oxidants, the enzymes are classified into haloperoxidases (HPOs)[85,86] using hydrogen peroxide and halogenases (HGs) using dioxygen as co-substrate.
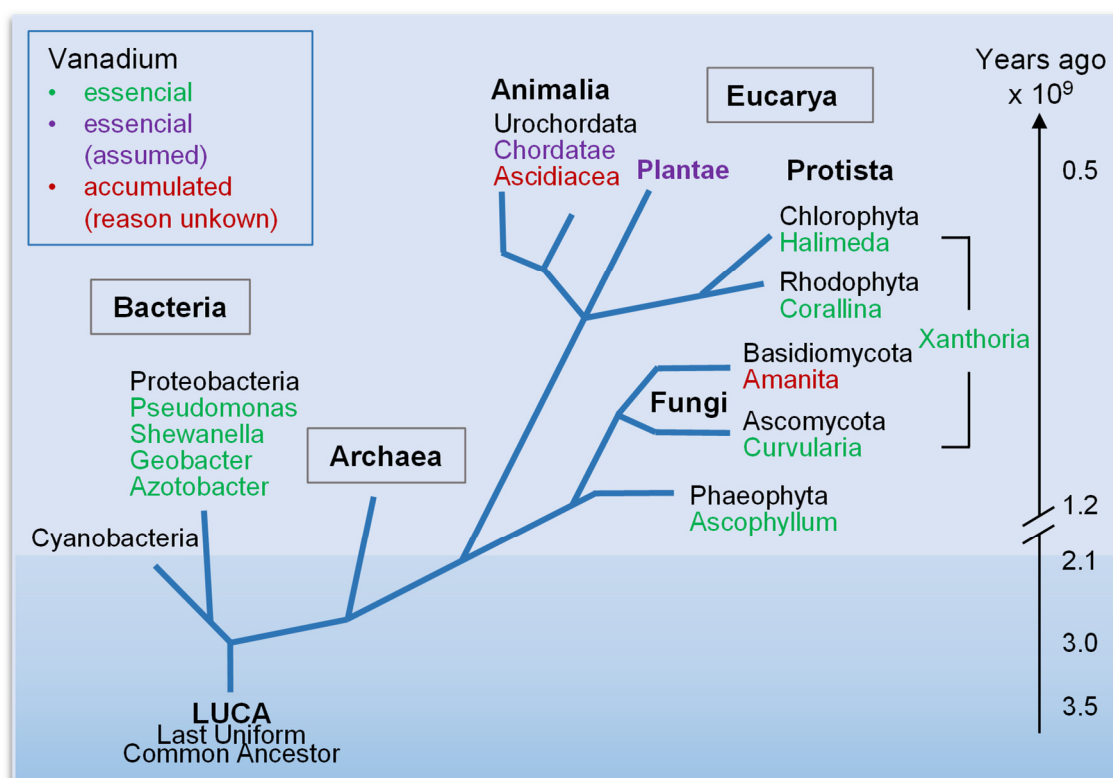
Figure 1. Phylogenetic development of vanadium containing organisms (adapted from ref. [80])

With regard to the nature of their active centers, halogenating enzymes can be subdivided into (i) flavin-, non-heme iron(II)- and *S*-adenosyl-*L*-methionine (SAM) - dependent halogenases (F-, NI-, S-HG) and (ii) cofactor-free-, heme iron(II)- or vanadium-dependent haloperoxidases (HPO, HI-, V-HPO).[87] These six families of halogenating enzymes are suggested to have evolutionary and functional relationships to the α/β - hy-

drolases, phosphatases, peroxidases, oxidoreductases, and the SAM hydroxide adenosyl-transferases, respectively.[87] According to the most electronegative halide that the enzymes can oxidize they are labeled chloroperoxidase (CPO, substrate Cl^-, Br^-, I^-, e.g. myeloperoxidase in neutrophils[88]), bromoperoxidase (BPO, substrate: Br^-, I^-, e.g. eosinophil peroxidase in phagocytes[89] and lactoperoxidase in human exocrine secretions[90]) and iodoperoxidase (IPO, substrate: I^-, e.g. thyroid peroxidase[91]).

The highly reactive intermediates, for example, hypohalous acids (HOX, X = Cl, Br, I, CN, SCN), react subsequently with different nucleophilic acceptors (R-H) to form a variety of halogenated metabolic compounds (R-X, X = (pseudo-) halogen, Equation 1, Equation 2). If the nucleophilic acceptors contain amino groups, halo-amines will be formed (Equation 3).[65] This reaction occurs mainly in the biological inflammatory response involving myeloperoxidase as halogenating enzyme.[92–94] The resulting chloramines are uncharged, reactive halogenating and oxidizing agents,[93,95] and can easily diffuse through the bacterial membranes of bacteria like *Escherichia coli*.[96]

$$R-H+O_2+X^-+H^+ \xrightarrow[\quad"HOX"\quad]{HG/HG\text{-}mimetics} X-R+2H_2O \qquad 1$$

$$R-H+O_2+X^-+H^+ \xrightarrow[\quad"HOX"\quad]{HG/HG\text{-}mimetics} X-R+2H_2O \qquad 2$$

$$\qquad\qquad\qquad\qquad\qquad\qquad\qquad\qquad\qquad 3$$

$$R_2NH+HOX \longrightarrow R_2NX+H_2O$$
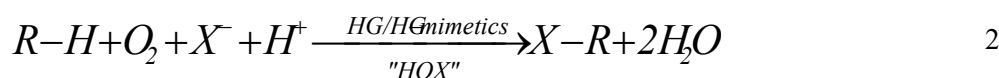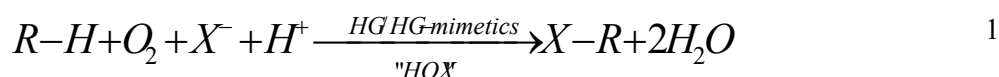
In the absence of an organic acceptor, at more alkaline pH values and, particularly, at high H_2O_2 concentrations, singlet oxygen is formed ($^1O_2$) by HPOs *via* peroxo-halogenide intermediates (Equation 4). Singlet oxygen formation can be detected by its chemiluminescence at 1268 nm ($^1O_2$ ($^1\Delta_g$) → $^3O_2$ ($^3\sum_g^-$) transition).[85,97–104]

$$\qquad\qquad\qquad\qquad\qquad\qquad\qquad\qquad\qquad 4$$

$$HOX + H_2O_2 \xrightarrow{HPO/HPO\,mimetic\,s} {}^1O_2 + H^+ + X^- + H_2O$$
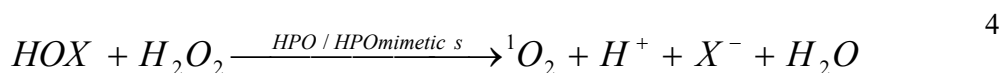
The highly reactive intermediates, particularly, hypohalite and hypohalous compounds (e.g. HOX), halo-amines (R_2NX) and singlet oxygen ($^1O_2$) participate in oxidative halogenation reactions at both electron-rich and non-activated compounds as well as in "simple" oxidation reactions.[105] Halogenating enzymes have been identified as important biocatalysts during the formation of reactive precursors for natural products[106] or metabolic reactions,[107,108] e.g. *via* epoxidation[105,109,110] or cyclization reactions, enantioselective sulfoxidations,[105,107] in the oxidation[111,112] of ascorbate, urate, pyridine

nucleotides, tryptophan, in halohydrin formation as well as in oxidative stress response and signal transduction.[113] The respective enzymes are involved in reactions leading to the formation of (volatile) halogenated compounds in the atmosphere[114–117] (e.g. halomethane[82,118–121]) and in specific host defense and antimicrobial systems.[88] HPOs and HGs participate in the biosynthesis of natural products such as halogenated metabolites[78,83,102,106–108,122–126] like terpenes, indoles, phenols and others derived from amino acids (see examples in Figure 2, 1-12). In mammals, they are responsible for the biosynthesis of the essential tyrosine-based thyroid hormones thyroxine (T4 (11)) and triiodothyronine (T3 (12)).[127,128] Mammalian laccases synthesize iodovanilin with antifungal activity.[129] Halogenating enzymes occurring in marine organisms are more popular because the bioavailability of the reagents and cofactors (e.g. vanadium, sources of bromide and oxidants like hydrogen peroxide and dioxygen) are omnipresent. Although chlorinated[130] and iodinated[114,128] products formed with the aid of enzymes have great application potential, this review is confined to oxidative bromination reactions because the resulting products are easier to synthesize in industrial processes.

As an example, the vanadium-dependent bromoperoxidase (V-BPO), which has been isolated from marine algae, catalyzes the oxidative bromination of the monoterpenes geraniol and nerolidol. In a subsequent step, these compounds react to bromocyclic structures encountered in many marine metabolites[122] (see Figure 2).
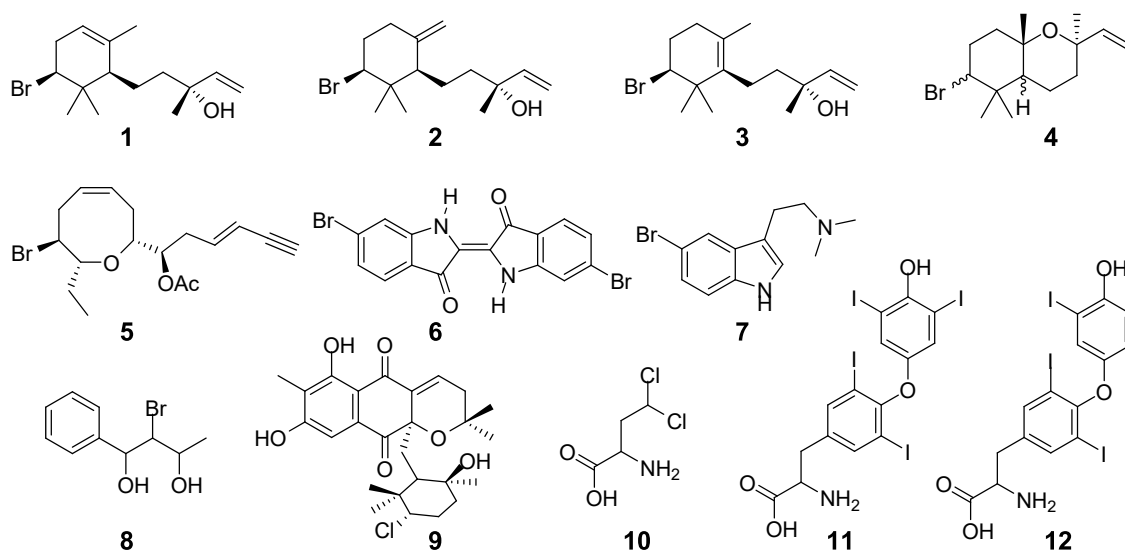
Figure 2. Examples of natural halogenated compounds with biological activity.[83,102,106,108,123,126,131] **1** α-, **2** β-, **3** γ-synderol;[122,124] **4** 3-β-bromo-8- epicarrapioxide;[124] **5** laurencin;[122] **6** tyrion purple;[102] **7** 5-bromo-*N,N*-dimethyltryptamine;[102] **8** bromohydrin;[107] **9** napyradiomycin (derivative);[132] **10** armentomycin;[132,133] **11** thyredoxine (T4);[83,128] **12** triiodothyronine (T3).[83,128]

The enzymes are moderately substrate- and stereo(regio)-selective,[82,134] as indicated by the regio-specific oxidation of 1,3-di-tert-butylindole,[82] the competition kinetics for the oxidative bromination of phenol red in combination with geraniol or nerolidol,[124] asymmetric halogenation reactions yielding α-, β-, or γ-synderol[124] and enantioselective sulfoxidation reactions.[107] This is accomplished with the aid of custom-made substrate pockets and tunnels buffed with hydrophobic amino acids at the catalytic center. In the X-ray structure of V-BPO from *Corallina officinalis* hydrophilic residues are located close to the entrance of the active site.[81,135] This protein scaffold pushes the organic substrate to the active center where it promotes the reaction by providing an electrophilic, reactive bromine species in a non-nucleophilic environment. In addition, it protects the local environment from an uncontrolled release of hypohalous species.[107] A lack of selectivity occurred (i) when the substrates are present only in substoichiometric amounts compared to the hypohalous species,[136] and (ii) when oxidized bromine species (e.g. HOBr, BrO$^-$, Br$_2$, Br$_3$$^-$)[124] were present outside of the active enzyme site.[137,138] Martinez et al.[82] have suggested HPOs to have different selectivities for different substrates, particularly, some compounds bind at the active site and block the release of oxidized intermediates.[82,102,107,139] As a highly reactive and diffusible molecule,[138] unblocked HOX is even more beneficial: hypohalite ions play a critical role in the natural protection and host defense systems of organisms, especially in marine plants such as red and brown seaweed.

This is associated with vanadium-dependent bromo- or chloroperoxidases (V-BPO, V-CPO),[83] prevalent in all classes of marine algae. Their structure contains dodecamers (six homodimers, occurring mainly in red seaweed like *Carex pilulifera, Corallina officinalis*) or single, "homodimeric" forms (fungus *Curvularia inaequalis*, brown seaweed *Ascophyllum nodosum*).[140] Figure 3 and Figure 4 compare the "active states" of the catalytic centers of three selected halogenating metal enzymes, where "active state" refers to the proposed redox state and environment of the metal center just before the halide attack.
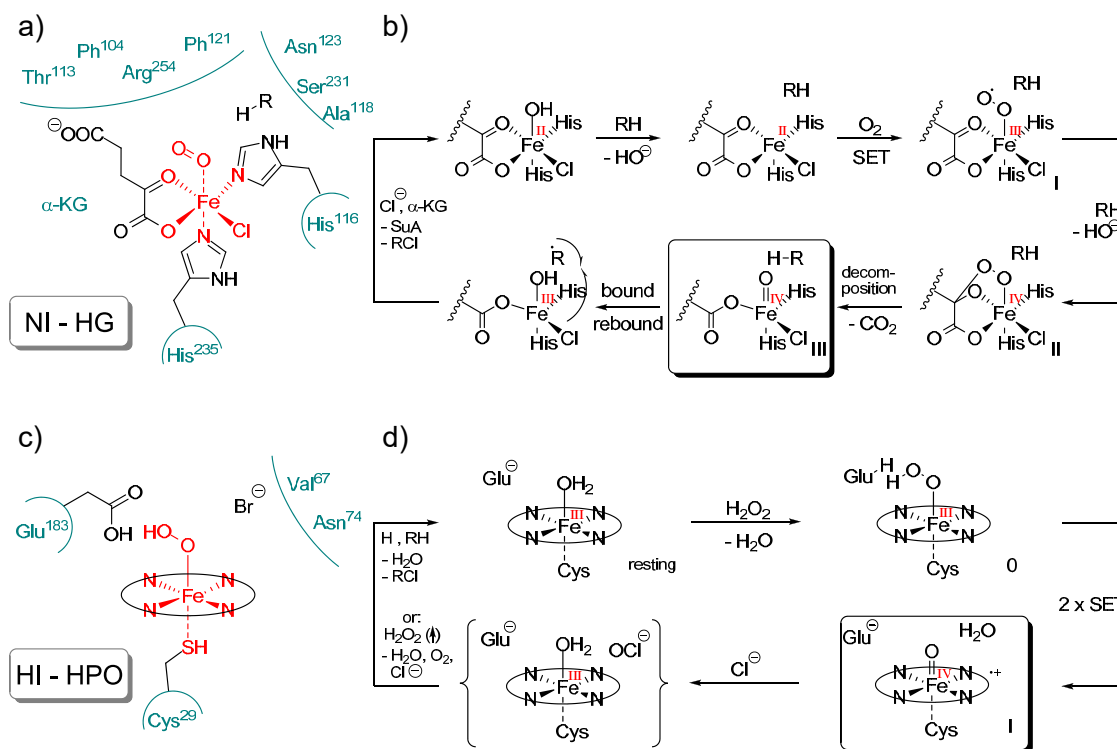
Figure 3. Active centers of halogenating enzymes and proposed mechanisms of HOX formation for (a, b) iron-non heme halogenase (NI-HG) [69,133,141–143] and (c, d) iron-heme haloperoxidase (HI-HPO, here: chloroperoxidase HI-CPO).[69,134,144,145]

The structural differences between non-heme iron halogenase (NI-HG), heme iron or vanadium haloperoxidase (HI-HPO, V-HPO) give rise to an enhanced stability of the heme-independent enzymes and different HOX formation mechanisms. Vanadium-haloperoxidases (V-HPO) are chemically more stable than heme-iron HPO, because de-activation of the active site by oxidation is more difficult.[79,98,146]

The structure of the non-heme iron HG requires a stepwise radical HOX for-mation. Similar as for the iron-dependent peroxidases, a high-valent non-heme iron(IV)-oxo intermediate is formed (Figure 3a, b) and a substrate is halogenated in a bound-re-bound mechanism by another co-substrate (e.g. α-ketoglurate).[143,147] In contrast, heme iron- or vanadium-dependent HPOs catalyze electrophilic halogenations, where the por-phyrin complex is redox active (Figure 3c, d) while the vanadium metal center does not change its oxidation state (Figure 4).[143]
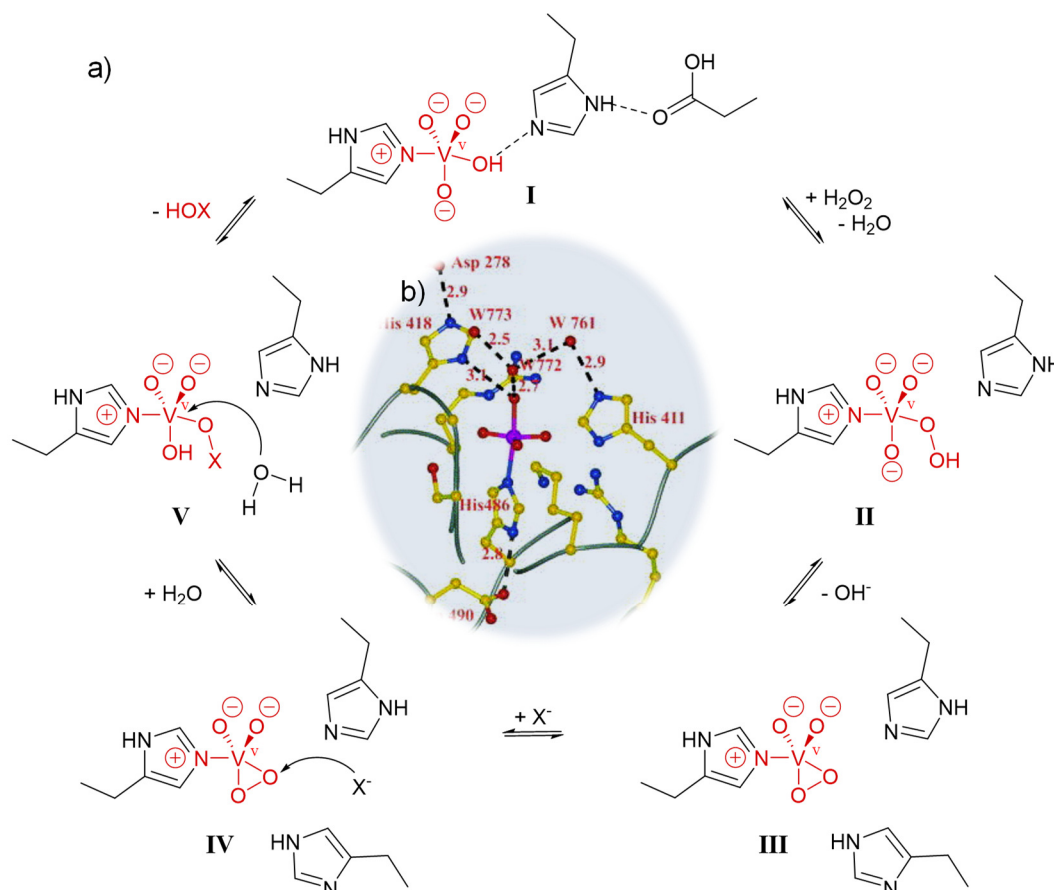
Figure 4. Vanadium-dependent bromoperoxidase. a) Proposed HOX formation mechanism and b) active center of vanadium-dependent bromoperoxidase from *A. nodosum* [79,103,107,137] The active site reproduced with permission from ref. [103] The orthovanadate unit is highlighted in red and the different postulated steps of H_2O_2 binding (I-III), halide ($X^- = Cl^-$, Br^-, I^-) attack (IV) and HOX (V-I) release are shown. In each step, vanadium(V) retains its oxidation state. For the sake of simplicity, the orthovanadate group is shown in its highest deprotonated state and the surrounding protein and hydrogen bonded network is only indicated.

Although heme-iron chloroperoxidase (HI-CPO) is the first halogenating enzyme to be discovered from the terrestrial fungus *Caldariomyces fumago* in 1966,[118]   V-HPOs are the most prominent halogenating enzymes. They occur in a variety of marine organisms and are suggested to be involved in the synthesis of a broad variety of halogenated marine natural products. Most chemical enzyme mimics are based on V-HPOs. The similarity of the haloperoxidase reaction mechanism to that proposed for many homogeneous catalysts prompted the study of structural and functional model compounds, and V-HPOs are described in more detail in the following together with activity assays, enzyme mimics and applications.

The cofactor and catalytic center of V-HPO, particularly the trigonal-bipyramidally coordinated orthovanadate unit, is stabilized through a highly complex hydrogen bonded network from amino acids such as histidine, lysine, arginine and serine (Figure 4,

I).[86] The active sites of different HPOs are almost structurally superimposable, especially the conserved distal histidine appears in every HPO structure.[103,135,140] Interestingly, the conserved active sites are virtually identical to those found in acid phosphatases, which indicates an evolutionary relationship.[140,148] The activity differences between V-BPO and V-CPO are believed to result from slight structural differences of the active centers. As an example, replacing a histidine group in V-BPO by a phenylalanine unit in V-CPO[149,150] leads to a change in hydrogen bonding and thus reactivity.[150,151]

A kinetic study of the V-HPO-catalyzed halide oxidation to the corresponding hypohalous species under steady-state conditions revealed a high degree of similarity between different bromoperoxidases.[79,81,137,152] Figure 4 shows the catalytic center of V-BPO of *A. nodosum* and the proposed reaction mechanism for the HOX formation.[153] Although the biochemical pathways are not fully understood, DFT investigations[154,155] of the vanadium cofactor of V-HPO have suggested protonation to be an important step. The vanadium(V) site binds a peroxo species in a side-on fashion without changing its oxidation state (η^2-peroxo compound, Figure 4, I-III), and thus acts as a Lewis acid by expanding its coordination sphere. The intermediate complex can be attacked by halides (e.g. Br$^-$) (IV), and HOX is released after hydrolysis (V). In summary, an "ionic mechanism" has been postulated involving an electrophilic "Br$^+$" rather than radical "Br$^\bullet$" species described for the Fe-dependent haloperoxidases or halogenases.[79,156,157]

1.3 Antimicrobial Activity of Haloperoxidases

Oxidative bleaching and the antimicrobial activity of singlet oxygen and HOX species generated with the aid of halogenating enzymes have been reported and patented years ago.[65,88,158–160] Haloperoxidases of marine organisms have been studied particularly with regards to their "antifouling activity" to combat bacterial attack, adhesion and colonization that is controlled by quorum sensing (QS), the cell-to-cell communication in bacteria.[133,161] Many bacteria benefit from social interactions. Intercellular signaling provides an opportunity to interfere with their ability to coordinate efforts to invade human, animal, or plant hosts. Communication interference in the microbial world is a ploy to gain an advantage over competitors. QS relies on small, secreted signaling molecules known as autoinducers (AIs) to initiate coordinated responses across a population. In

many cases, the responses elicited by QS contribute to pathogenesis through the synchro-
nized production of virulence determinants, like toxins, proteases, and other immune-
evasive factors. Furthermore, QS can enable bacteria to resist antimicrobial compounds
or drugs, such as in biofilm development. If these efforts to coordinate are blocked, bac-
teria lose their ability to carry out an organized assault on the host's defense or immune
system or would be less able to form organized community structures that promote path-
ogenesis, such as biofilms.[161–165] The most common AIs belong to one of the following
three categories: (i) acyl homoserine lactones (AHLs), used by Gram-negative bacteria
(also referred to as autoinducer-1 (AI-1)), (ii) peptide signals, used by Gram-positive bac-
teria and (iii) autoinducer-2 (AI-2 furanosyl compounds, e.g. furanosylborate)[147,166] used
by both Gram-negative and Gram-positive bacteria. In addition, there are other quorum-
sensing signals that go beyond these classes. Figure 5 illustrates the mode of action of AI
compounds for the AHL regulatory system of the marine symbiotic bacterium *Vibrio
fischeri*.[166–168]
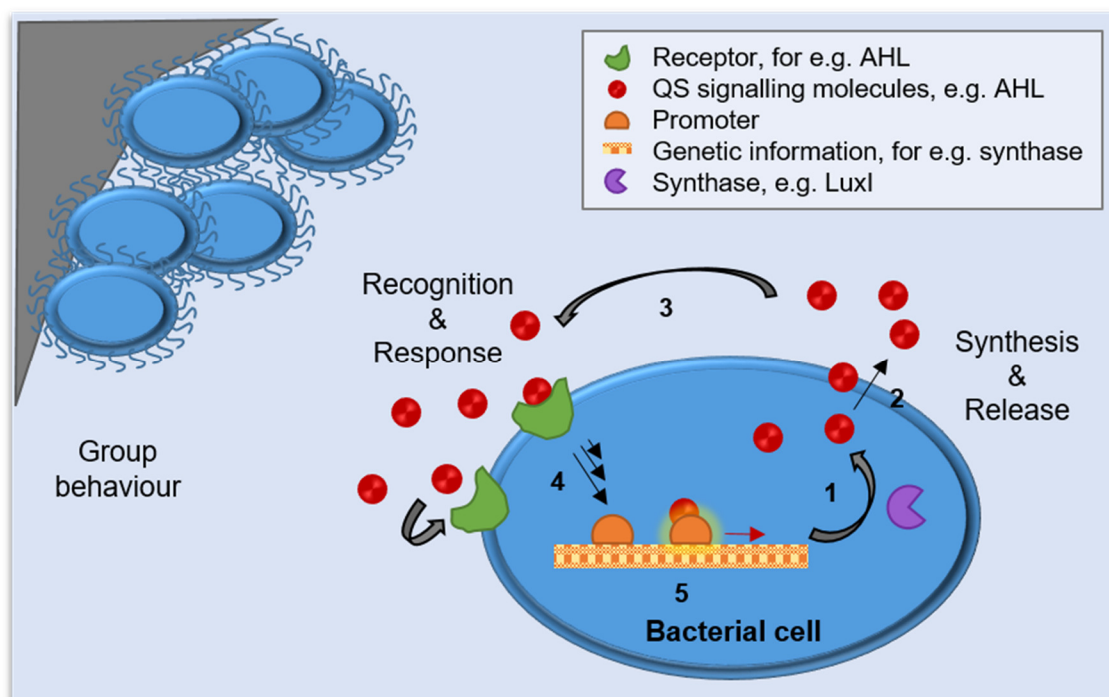
Figure 5. Natural quorum sensing mechanism of marine bacteria *via* QS signaling molecules (e.g.
AHL) that regulate and coordinate group behavior (e.g. biofilm formation, bacterial attachment,
swarming mobility, virulence, antibiotic resistance, synthesis of organic compounds) for the ma-
rine bacterial symbiont *Vibrio fischeri*.[167] The numbers represent different steps in the QS pro-
cess of bacteria. Translated AI molecules (1) pass the membrane (2) *via* diffusion (short chain
AHLs) or active transport (long chain AHLs). (3) Receptor binding of AHLs leads to multiple
responses which can affect gene expression (4), e.g. activation of promoter complexes (5), and
stimulate the synthesis of signaling molecules (1) or bioluminescent phenotypes.[166,167]

AHL-Based Quorum Sensing

AHLs are synthesized and released by bacterial cells *via* different pathways (Figure 5 (1, 2)), and their structures determine their signaling functions and their modes of interaction with environmental factors during cell-to-cell transit.[169] Typically, AHLs contain a five-membered ring with different amide-linked side chains in a range of 4-18 carbons in length, but many structural variants of the basic AHL molecules have been described. The acyl side chain may be saturated or unsaturated and contains a substituted hydroxyl- or oxo- functional group at the C3 position.[170,171] QS depends on signaling molecules which are stable on the timescale of diffusion through the extracellular matrix: Quorum-sensing regulated gene expression depends on factors like the rate of cue degradation as a function of environmental conditions, calling distance, and mobility of the cue.[172]

Extracellular AI compounds have cognate receptors (Figure 5 (3)), thereby regulating specific response mechanisms *via* modification of gene expressions (Figure 5 (4, 5)). The autoinducer synthase gene is a target for special proteins, for example, the Lux-proteins. The Lux-protein family and their homologues include synthases, kinases, phosphatases, receptors, transcriptional activator protens etc. and are common in Gram-negative bacteria.[168] Activation of the quorum-sensing cascade results in increased translation of autoinducer LuxI synthase which triggers the production of more AHLs. This acts as a positive feedback loop and amplifies the quorum-sensing effect.[167,168,173] Particulary, receptor binding and thereby stimulating the AI-dependent transcriptional activator LuxR leads to an enhanced synthesis of signaling molecules *via* LuxI synthase or bioluminescent phenotypes.[174] This model roughly describes the QS mechanism in bacteria (e.g. possible crosstalk). LuxR and LuxI homologues are encountered in different species.[167]

Peptide-Based Quorum Sensing

Gram-positive bacteria do not have LuxI or LuxR homologues. They rely on modified oligopeptides as autoinducer molecules. These are genetically encoded and generated ribosomally within the cell. As these peptides cannot permeate the cell membrane, specialized transporters are needed for an active transport. At points between translation, export, and detection, peptides are subject to various modifications, including processing

and/or cyclization. Detection of these peptide signals can occur either at the cell surface or inside the cells. Many peptide autoinducers are detected by a membrane-bound sensor kinase, which switches its kinase/phosphatase activity in response to the interaction with a peptide. As a result, the phosphorylation state of the cognate response regulator changes yielding in the activation or repression of QS target genes. Systems with extracellular detection include the accessory gene regulator (*agr*) system of *Staphylococcus aureus* and the two-component signal transduction system of *Enterococcus faecalis* (*fsr* system, *E. faecalis regulator)*, both of which control virulence factor production. The *agr* system of *S. aureus* is based on cyclic autoinducing peptides (AIPs) that belong to four distinct groups that interact with cognate AgrC sensor kinases of the same group to regulate exotoxin production and biofilm dispersal.[175] The *fsr* system uses a different cyclic peptide, the gelatinase biosynthesis-activating pheromone (GBAP), which is detected by the FsrC sensor kinase and induces the formation of gelatinase.[176]

Other bacteria rely on linear peptide autoinducers that are detected extracellularly, including the competence-inducing QS system of *Streptococcus pneumoniae,* which is mediated by the competence-stimulating peptide (CSP).[177] Alternatively, some linear-peptide-based QS systems actively transport the autoinducers back into the cell where the peptide signal can interact directly with a cognate regulator to modify target gene expression. A typical example is the pheromone-responsive protein PrgX system of *E. faecalis*.[178]

AI-2-Based Quorum Sensing

AI-2 is formed from the *S*-adenosylhomocysteine (SAH) precursor by the sequential enzymatic activities of 5-methylthioadenosine/*S*-adenosylhomocysteine nucleosidase and the metalloenzyme *S*-ribosylhomocystein-lyase LuxS.[179] 4,5-Dihydroxy-2,3-pentanedione (DPD), the product of these reactions, is unstable in aqueous solution and undergoes spontaneous rearrangement into multiple interconvertible cyclic furanones of the AI-2 group. AI-2 can freely diffuse out of both Gram-negative and Gram-positive bacteria and, as for all other QS signals, accumulates extracellularly. Many species produce and respond to AI-2, and the corresponding AI-2 receptors have been identified in *Vibrio harveyi* and *Salmonella enterica serovar typhimurium. Vibrio harveyi* detects a borate-

complexed form of AI-2 by virtue of the LuxP/LuxQ receptor/sensor kinase complex.[180,181] In contrast, the *S. Typhimurium* transporter LsrB interacts with a non-borated form of AI-2, followed by internalization, phosphorylation, and interaction with the cytoplasmic transcriptional regulator LsrR.[182] Thus, different bacterial species can detect different forms of AI-2, and detection can take place either extra- or intracellularly, depending on the bacterium.

QS depends on signaling molecules which are stable on the timescale of diffusion through the extracellular matrix. Modification like halogenation or displacing of the AI-molecules ("biomimicry") disrupts the quorum sensing through destructive interference with e.g. receptors and/or enzyme inactivation.[166,167,183,184] Some marine algae like *Corallina officinalis* or *Delisea pulchra*, excrete iron- and vanadium-dependent haloperoxidases/halogenases that participate in the disruption of QS, for example, by the synthesis of halogenated organic AI-antagonist.[166,183] Figure 6 illustrates selected examples of autoinducers and natural compounds being active against them.
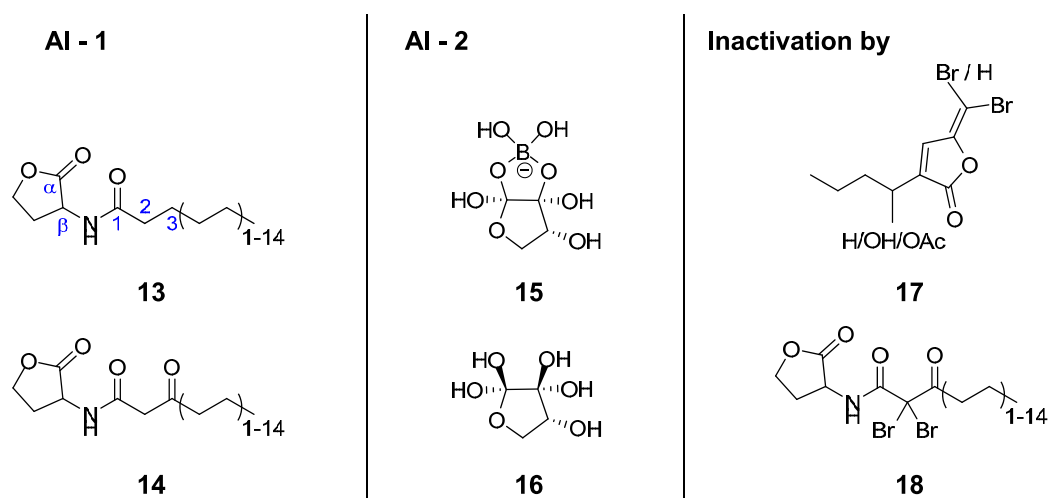
Figure 6. Selected natural QS molecules (autoinducers) AI-1 (**13**, **14**), AI-2 (**15**, **16**) and their inactivation by brominated furanones (**17**) or brominated lactones (**18**) e.g. isolated from *D. pulchra*.[147] The typical numbering and denotation of AHLs is shown for compound **13**.

V-BPOs localized in the exterior region of *Delisea pulchra* disrupt bacterial quorum sensing using oxidative halogenation reactions in different ways: (i) by the bactericidal effect of HOX itself, (ii) by the synthesis of bromofuranone compounds (17) (antagonists both against AI-1 and AI-2 system)[185–187] and (iii) by the oxidative bromination of the bacterial signaling compound 3-oxo-acylhomoserine lactone (3-oxo-AHL, 14) to the corresponding dibromo-acyl-AHL (inactivation, 18).[147,184,188]

Furanones are ubiquitous (e.g. as pheromones and flavoring compounds),[189] and as structural AHL analogues they represent a tool to combat bacterial infection and biofilm formation.[190] Natural halogenated furanones are supposed to disrupt the AI-2 biosynthetic pathway, and brominated furanones target the AI-2 producing recombinant *Bacillus subtilis* enzyme LuxS (*S*-ribosylhomocysteine lyase).[187,191] An addition-elimination mechanism for the covalent modification of LuxS has been proposed to yield an inactive enzyme and to disrupt further quorum signaling.[187] Kjelleberg and coworkers[167,185,192] have described that halogenated furanones occurring in the marine red alga *Delisea pulchra* inhibit QS by down-regulating the LuxR protein of *Vibrio fischeri* overexpressed in *E. coli* (AHL-regulated bioluminescence assay).[185,192] This leads to the conclusion that furanones, at concentrations produced by the alga, control bacterial surface colonization by specifically interfering with AHL-mediated gene expression at the level of the LuxR protein. An evidence for the inhibition of QS by the modulation of gene expression has been provided by Ren et al.[186] who have demonstrated using DNA/RNA microarrays that brominated furanones are able to inactivate the AHL-synthase LuxI while gene expression of the lyase LuxS remains constant.

Several test studies have been carried out with libraries of natural or synthetic furanones and AHLs. Martinelli et al.[190] have tested a variety of furanones regarding their functional role on QS in *Chromobacterium violaceum* mutants. The biosynthesis of the violacein, a bisindole formed by the condensation of two tryptophan molecules, depends on the addition of AHLs for this mutant. As a compound, violacein has several biological activities, including being an anticancer agent and an antibiotic against *Staphylococcus aureus* and other Gram-positive pathogens. In most of violacein-producing bacterial strains isolated from nature, this bisindole is a secondary metabolite that is associated with biofilm production.[193] Its production within *C. violaceum* and other strains is regulated by QS.[194] Because it is easy to visualize, violacein production by *C. violaceum* has become a useful indicator of quorum sensing molecules and their inhibitors ("violacein assay").[195] The concentration dependency for the active compounds[190] showed the interaction of agonists, antagonists and receptors with respect to the signal transduction and bacterial response to be quite complex.

De Keersmaecker and coworkers[196] tested a library of different substituted furanones and (bromo)alkyl-maleic anhydrides for the antagonistic effect against biofilm formation by *Salmonella Typhimurium* and the QS regulated bioluminescence of *Vibrio*

harveyi. The length of the 3-alkyl chain and the bromination pattern of the ring structure are found to have a major effect on the biological activity of the 1'-unsubstituted furanones (AI-2). Remarkably, the introduction of a bromine atom on the 1' position of the 3-alkyl chain has enhanced drastically the activity of the furanones in biologicak test systems. Particulary, the QS regulated bioluminescence and virulence of *Vibrio harveyi* has been decreased. This suggests a negative competition for the activation of LuxR, as the transcriptional activator protein is involved in the regulation of the phenotype expression such as bioluminescence, siderophore production, biofilm formation, and virulence.[196] The introduction of an acetoxy function in this position does not improve the activity in general. Finally, the potential of the (bromo)alkyl-maleic anhydrides as a new and chemically easily accessible class of biofilm and QS inhibitors has been demonstrated.[196]

The inactivation of native bacterial AHLs has been targeted by a variety of marine organisms. AHLs can easily be halogenated through electrophilic halogenation at the α-position, and the receptor recognition is disturbed by the corresponding mono- and dihalogenated AHLs.[133,147] Syrpas et al.[197] have studied the HPO-mediated defense system of the benthic diatom *Nitzschia cf pellucida* system against *Chromobacterium violaceum CV26* by the violacein assay. The halogenation-degradation pathway of QS molecules like *N*-β-keto-acyl homoserine lactones (AHLs) has been analyzed with HPLC-MS in combination with synthetic halogenated AHL reference compounds. The degradation pathway of *N*-β-keto-AHLs triggered by the halogenating enzymes is shown in Figure 7.[188,197] *N*-3-oxohexanoyl homoserine lactone (OHHL 19) is attacked by electrophiles (e.g. hypobromite HOBr) at the α-position. The resulted monobromine and dibromine homoserine lactones (MBHL 20, DBHL 21) are hydrolyzed with hydrolases or by basic hydrolysis. After cleaving off butyric acid (22), *N*-(α,α-dibromoacetyl) homoserine lactone (DAHL 23) and the hydrolyzed product (24) are formed. This shows that the decrease of the QS activity in *E. coli* JB523 microplate assays correlates with halogenation and the cleavage of the halogenated *N*-acyl chain of the lactone.

Similarly, the production of green fluorescent protein (GFP) by *E. coli* JB523 depends on the addition of AI, the effects of AHLs and their halogenated counterparts.
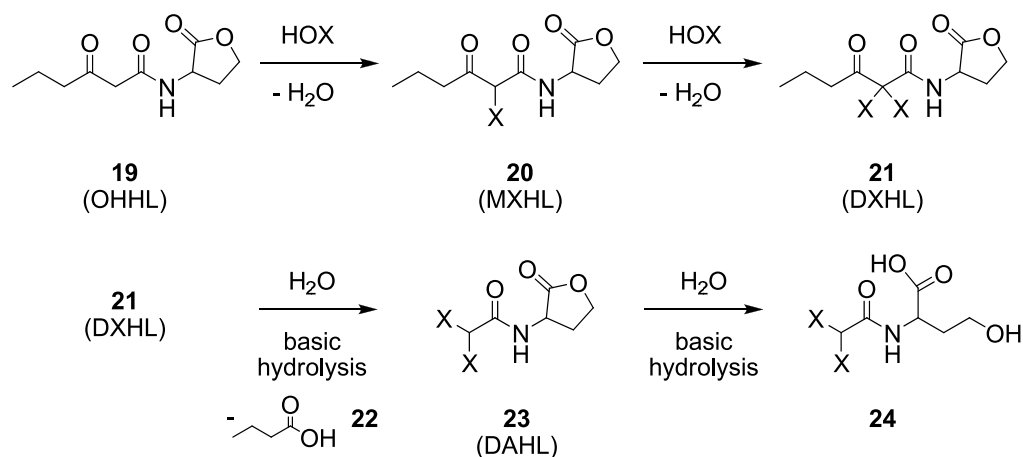
Figure 7. Degradation pathway of *N*-β-keto-AHLs for *N*-3-oxohexanoyl homoserine lactone (OHHL **19**). Scheme adapted from ref. [188,197]. The AHL molecule suffers electrophilic attack at the α-position by HOX (X = Cl, Br, I) formed by enzyme catalysis. The resulting mono- and dihalogenated homoserine lactones (MXHL **20**, DXHL **21**) are hydrolyzed by hydrolases or basic hydrolysis. After cleavage of butyric acid (**22**), *N*-(α,α-dihaloacetyl) homoserine lactone (DAHL **23**) and the follow-on product (**24**) are formed.

Experimental results of Syrpas et al.[197] have illustrated the ability of unmodified OHHL (19) and its brominated homologues MBHL (20) and DBHL (21) to induce fluorescence (Figure 8). As a result, the QS stimulating activity decreases with increasing halogenation of OHHL. The ability to induce GFP formation decreases in the order Br > I > Cl and DAHL (23; no GFP formation). However, comparative assays with natural OHHL (19) and the halogenated compounds as possible antagonists have not led to congruent results.
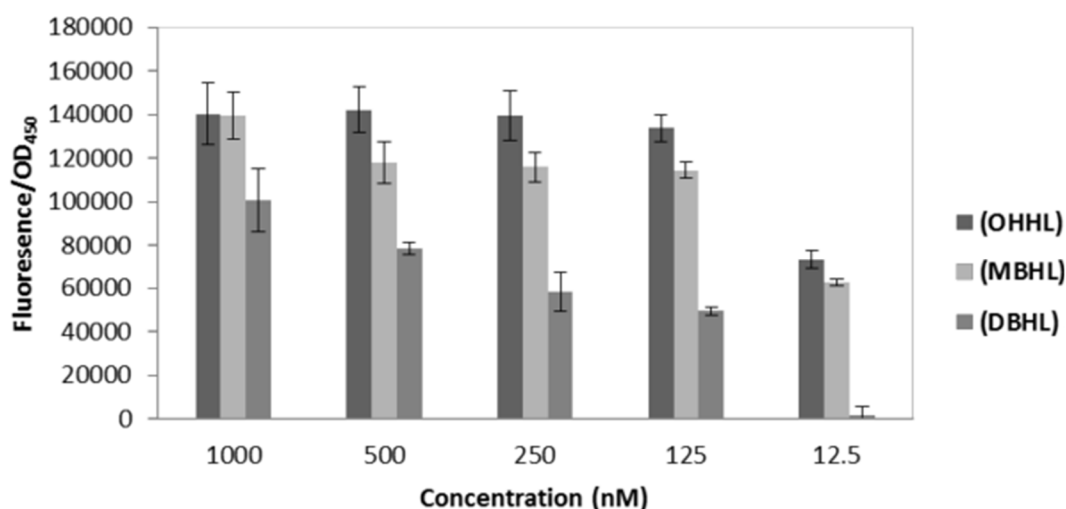
Figure 8. Quorum sensing-regulated green fluorescent protein (GFP) production by *E. coli* JB523 induced by OHHL (**19**) and brominated degradation products (MBHL **20**, DBHL **21**). GFP production has been determined by measuring the specific fluorescence (six repetitions). GFP fluorescence has been corrected for the cell density of the reporter strain (fluorescence/OD450). Phosphate buffer saline has been used as control. Reprinted with permission from ref. [197].

The ubiquitous occurrence and the involvement in communication and regulatory systems demonstrate the importance of halogenating enzymes in Nature and their high potential for a broad range of application in fouling control and drug design. Quorum sensing in marine organisms and potential applications have been reviewed by several authors.[166,169,198–208] Dobretsov et al.[203] have reported that QS inhibitors like furanone derivates do not only effect bacterial biofilm formation in a destructive and concentration-dependent manner (cf. violacein assay) but also prevent the larval settling of the poly-chaeta *Hydroides elegans* and the bryozoan *Bugula neritina*. AI analogues are ubiquitous, and numerous responses by eukaryotes have been established, the inhibition of biofilm formation of *Pseudomonas aeruginosa*[209] by sesquiterpene lactones from the seeds of the tropical tree *Annona cherimolia* being a textbook example.

Native AHLs of a variety of bacteria modulate the response of the model plant hosts *Arabidopsis thaliana* and *Medicago truncatula*. Here, AHL amidolysis is catalyzed by a fatty acid amide hydrolase (FAAH) yielding *L*-homoserine,[210] which enhances transpiration or inhibits plant growth in a concentration dependent manner. As FAAHs exist in animals and also in humans (often in the brain and/or liver), AHL-degradation products might also affect the response in their metabolism[210] *via* inter-kingdom signaling.[211] Another study on root-associated fungi from forest environments highlights their ability in the violacein assay to degrade AHLs by lactonases. Thus, endophytic fungi might function as biocontrol agents against pathogenic bacteria.[212]

In summary, bacteria can communicate with each other in a very complex and versatile manner. They play dual roles in maintaining their host´s health and contributing to host´s illness. Chemical communication between bacteria is based on different types of interactions: pathogenic, symbiotic, and transient. Many systems point to a chemical interplay, yet many molecules involved are not characterized. In instances where the chemistry is known or elucidated, important implications for the host´s fate can be proposed and tested.

1.4   Analytical Assays for Oxidative Halogenation

The design, development and validation of reliable enzyme assays is critical for an understanding of the enzyme biochemistry and kinetics. This section provides a brief overview of assays developed for HPOs and HPO enzyme mimics. Enzymes are important drug, herbicide or insecticide targets, and many marketed agents today function through the inhibition of enzymes. Often, these molecules are competitive reversible inhibitors of substrate binding. In some cases, other mechanisms may be desirable which would require a different assay design. To identify competitive inhibitors for an enzymatic assay it is essential to run the reaction under initial rate conditions with substrate concentrations at or below the K_m value (Michaelis-Menten constant) for a given substrate. The substrate can either be the natural substrate or a surrogate (e.g. a peptide) that mimics the natural substrate. The optimum pH and buffer component concentrations shall be determined before measuring K_m.

I_3^- Assay

Historically, the I_3^- assay has been established to detect the halogenating activity of enzymes. It is based on the oxidation of iodine by hypoiodite or bromine by hypobromite species (e.g. HOI, HOBr). The triiodide anion is detected spectrophotometrically by its specific absorption at 350 nm ($\varepsilon_{350} = 25$ M^{-1} cm^{-1}).[124,213] As high iodine concentrations and acidic conditions (pH<6.5) are needed to overwhelm the chemical instability of I_3^- and possible side reactions (e.g. the oxidation of H_2O_2 by HOI) can occur, this is a more qualitative test system (Table 1, entry 1).[213]

Table 1. Assays to monitor haloperoxidase-like activity. I. Entry 1: I_3^- assay (X = I, Br), entry 2: MCD assay (X = Br, Cl), entry 3: TMB/DMP assay (X = I, Br, Cl).

#	Dyes/substrates
1	
2	
3	

MCD Assay

Based on the natural product caldariomycin, Hager et al.[118] have developed a qualitative test method for the oxidative bromo- and chlorination in 1966. In the standard procedure, monochlorodimedone (MCD, $\varepsilon_{290} \approx 20\,000$ M^{-1}cm^{-1})[118] is oxidatively halogenated to dichlorodimedone or monobromo-monochlorodimedone in aqueous solution containing hydrogen peroxide, a bromide source (KBr or NH$_4$Br, in general) and the catalyst.[118,124] As the halo-MCD has a much lower extinction coefficient ($\varepsilon_{290}= 100$ M^{-1}cm^{-1}), the reaction can be monitored by the absorption changes at 290 nm. The rate of the decrease of the absorbance is related directly to the formation of hypohalite (HOX). As MCD is not reactive towards iodination, only CPO- and BPO-like activity can be determined (Table 1, entry 2).[213] Due to the straight forward detection and the reaction kinetics, the MCD assay has been established as a standard test method to explore halogenating enzymes.[137] The nature of the mechanism and the underlying enzyme kinetics have been studied in detail.[104,137,214,215] Wagner et al.[216] have critically reviewed the MCD assay which may lead to false positive results because it focuses on the consumption of the substrate and not on the formation of the product. A decrease in the MCD concentration does not automatically indicate the formation of halogenated compounds. Hansen and Griffin et al.[217–219] have reported an inactivation of MCD *via* dioxygen depending on the experimental conditions and radical forms of MCD. Unfortunately, monitoring the reaction based on UV-Vis absorption and TLC[118] does not give any clues, which products have been formed. NMR and mass spectrometry provide reasonable information concerning the halogenated species, but they are difficult to monitor under operating concentrations. As nanoparticles and other enzyme mimics are less specific, the possibility of "blind activity" in the MCD assay might be problematic. However, if a HPO/HG-like activity is established, this assay is a valuable and facile tool to study enzyme kinetics and allows a comparison for variety of natural enzymes.

TMB and DMP Assays

Electron-rich aromatic systems are accessible to an electrophile attack by hypohalites. Based on this, 1,3,5 trimethoxybenzene (TMB) or 3,5 dimethylphenol (DMP) have been established as substrates to explore oxidative halogenation activity (Table 1, entry 3). A typical reaction mixture contains halide, hydrogen peroxide and the catalyst under acidic conditions (e.g. citrate buffer, pH 3), and the change in absorbance during the halogenation reaction can be monitored by UV-Vis spectrophotometry. The products (mono-, di-, trihalogenated molecules) can be identified by gas chromatography and mass spectrometry as well. The TMB assay has been used to determine the chlorine isotope effect for a CPO catalyzed oxidative chlorination.[130] Since highly acidic conditions are required and TMB is sensitive to oxidation due to the formation of strongly absorbing or fluorescent products,[220] this assay is not well established.

Sulfonphthalein Dyes

Sulfonphthalein dyes can overcome the problems of side reactions. They combine an optical color change (qualitative "quick screening" assay) with quantitative UV-Vis-, NMR- and mass detection for bromination, chlorination and even iodination. Typically, phenol red (PR, phenolsulfonphthalein) or thymol blue (TB, thymolsulfonphthalein) are used as indicator systems. The reaction scheme is shown in Table 2, entry 1. A subsequent oxidative halogenation reaction at the free ortho positions leads to tetra-halophenol blue (X_4PR, X = Br, Cl, I) or di-halothymol blue (X_2TB, X = Br, Cl, I) under neutral, slightly acidic or basic pH conditions. Oxidative bromination reaction is the most studied reaction. Kinetic studies can be evaluated with respect to the brominated products: Turn over numbers (TON, k_{cat}), reaction constants (k), reaction orders (a) and kinetic parameters of enzymes like the Michaelis-Menten constant (K_m) are easily accessible, although the reaction mechanism is more complicated than that of the MCD assay. The stability of the end products of sulfonphthalein dyes and their distinct spectral properties facilitate the optical analysis. Thymol blue and phenol red are common pH indicators, and their color changes in the neutral regime from yellow to red-violet (PR, between pH 6.8 - 8.2)[221] or from yellow to blue (TB, between pH 8.0 - 9.2).[222] Oxidative halogenation of the chromophore changes the pKa values by affecting the delocalization of the π-system.[213] The fully halogenated products can be assigned spectrophotometrically and even by eye inspection.

Br$_4$PR shows a color change between pH 3.0 (yellow) and 4-6 (blue),[223] Br$_2$TB between pH 6.0 (yellow) and 7.6 (blue).[224] Verhaeghe et al.[213] have demonstrated while performing a kinetic study that the enzymatic bromination of TB can be used as qualitative and quantitative assay of the oxidative halogenation activity.

Phenol red is used to detect HPO- or HG-like activity. It is water-soluble without the use of organic solvents such as ethanol, methanol or dimethyl sulfoxide. Although the turnover of phenol red to the fully halogenated end product is more complex regarding the kinetics, the validation for the fourfold halogenated phenol red is simple because it has a distinct absorption maximum at 590 nm at pH > 4.6 (typical operating conditions), and its absorbance differs from that of the educts in any pH range. However, it have to be noted that at high peroxide concentrations phenol red can be halogenated even in the absence of HPO.[225] Kinetic studies have shown that the observed bleaching to colorless products in basic media might be due to the reaction with hydroxyl radicals (Table 2, entry 2).[226,227] They destroy the quinoid system of phenol red yielding isolated aromatic rings with a large hypsochromic shift. Monitoring the halogenation by NMR and mass spectrometry etc. are alternatives to avoid these intricacies.

Table 2. Assays to monitor haloperoxidase-like activity. II. Entry 1: Sulfonphthalein dyes. Entry 2: Side reaction of sulfonphthalein dyes (X = I, Br, Cl). Phenol red (R_1, R_2 = H) or thymol blue (R_1 = iPr, R_2 = Me) are oxidatively halogenated in a stepwise manner to the tetra- or di-halogenated products (e.g. bromophenol blue (X_4PR, X, R_1 = Br and R_2 = H) or dibromo-thymol blue (X_2TB, X = Br, R_1 = iPr, R_2 = Me)).

#	Dyes/substrates
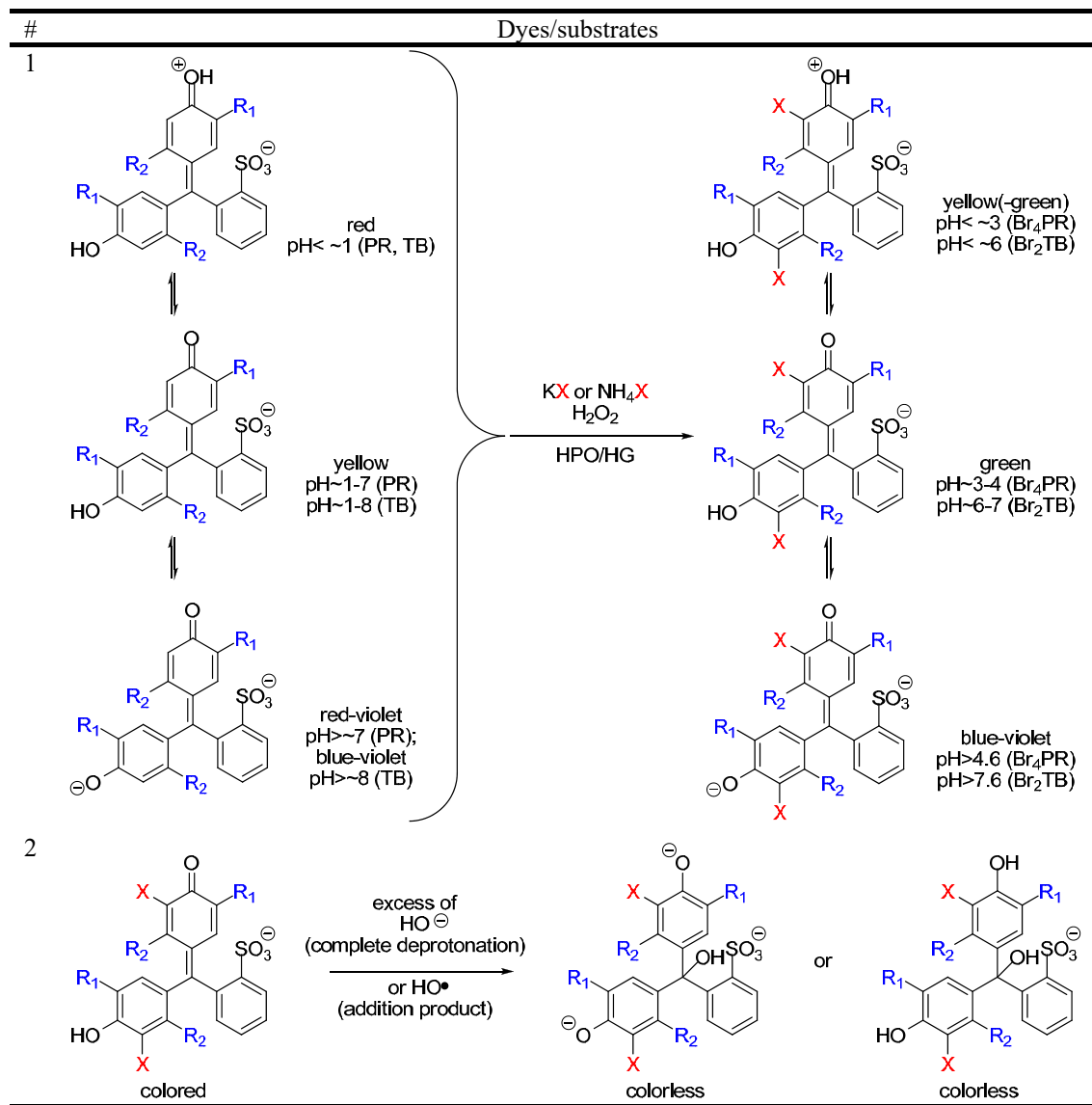
Luminescence Assays

Luminescence (chemiluminescence or fluorescence) assays based on rhodamine, coumarin and fluorescein derivatives [228,229] are popular for detecting reactive oxygen or nitrogen species (ROS, RNS) in biological systems.[230] The detection of haloperoxidase-like reactions is based on the oxidative activity of HOX species (X = Cl or Br). Luminescent dyes are useful for accurate sensing even in multi-component-systems like in living cells.[229] Non-fluorescent aminophenyl fluorescein (APF) or hydroxyphenyl fluorescein (HPF) are converted to fluorescein by oxidative dearylation (Table 3, entry 1) *via* HOX intermediates or by HOX addition.[231,232] The fluorescent product (525 nm) can be monitored and localized in laboratory test systems with immobilized haloperoxidases,[232] and additionally, in native human neutrophils and eosinophils.[231] Hypochlorite promoted ring-opening mechanisms have been proposed for fluorescein[233] (Table 3, entry 2) or rhodamine derivatives[234] (Table 3, entry 3). Rhodamine has been used to demonstrate the existence of phagosomal and mucosal HOCl formation in the intestinal epithelia of *Drosophila melanogaster*.[234,235] These dyes extend the range of applications to detect HOCl in immune response system and in the pathogenesis of human diseases in cells and animal tissues.[234,235] Xanthene derivatives and oximes of phenanthroimidazole derivatives[236] have been used for HOX sensing. Here, deoximination *via* HOCl leads to a red shift relative to the starting compound due to intramolecular charge transfer (ICT, Table 3 entry 4). Chemiluminigenic substrates such as cyclic hydrazides, dioxetane precursors,[237] or ferrocene-modified pyridylthiazole derivatives,[238] which are oxidized by HOCl selectively, have been used as well.

Despite recent advantages in the development of luminescence assays, limitations arise as the luminescent products depend on the oxidizing power of HOX rather than on oxidative halogenation.[239] Thus, a distinction between haloperoxidase- and peroxidase-like activity is difficult. Luminescence methods are useful tools for a spatially-resolved analysis even in multicomponent systems but further alternative dyes have to be used to valid haloperoxidase-like activity.
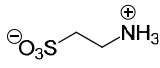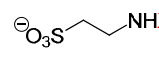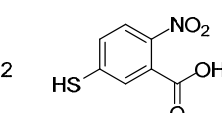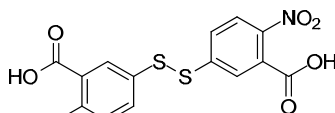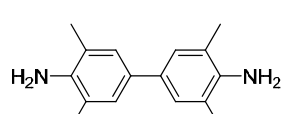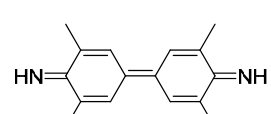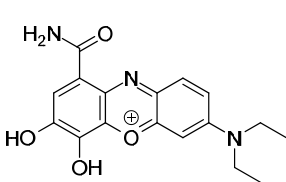
Table 3. Assays to monitor haloperoxidase-like activity. III. Entry 1: Oxidative dearylation of non-fluorescent aminophenyl fluorescein (APF, R = N) or hydroxyphenyl fluorescein (HPF, R = O) to fluorescein. Proposed hypochlorite promoted ring-opening mechanism for non-fluorescent xanthene dyes (entry 2: fluorescein-like, entry 3: rhodamine-like) to their fluorescent counterparts. Entry 4: Deoximination reaction of oxime derivatives of phenanthroimidazole-based compounds (X = Br or Cl (commonly used)).

#	Dyes/substrates
1	
2	
3	
4	
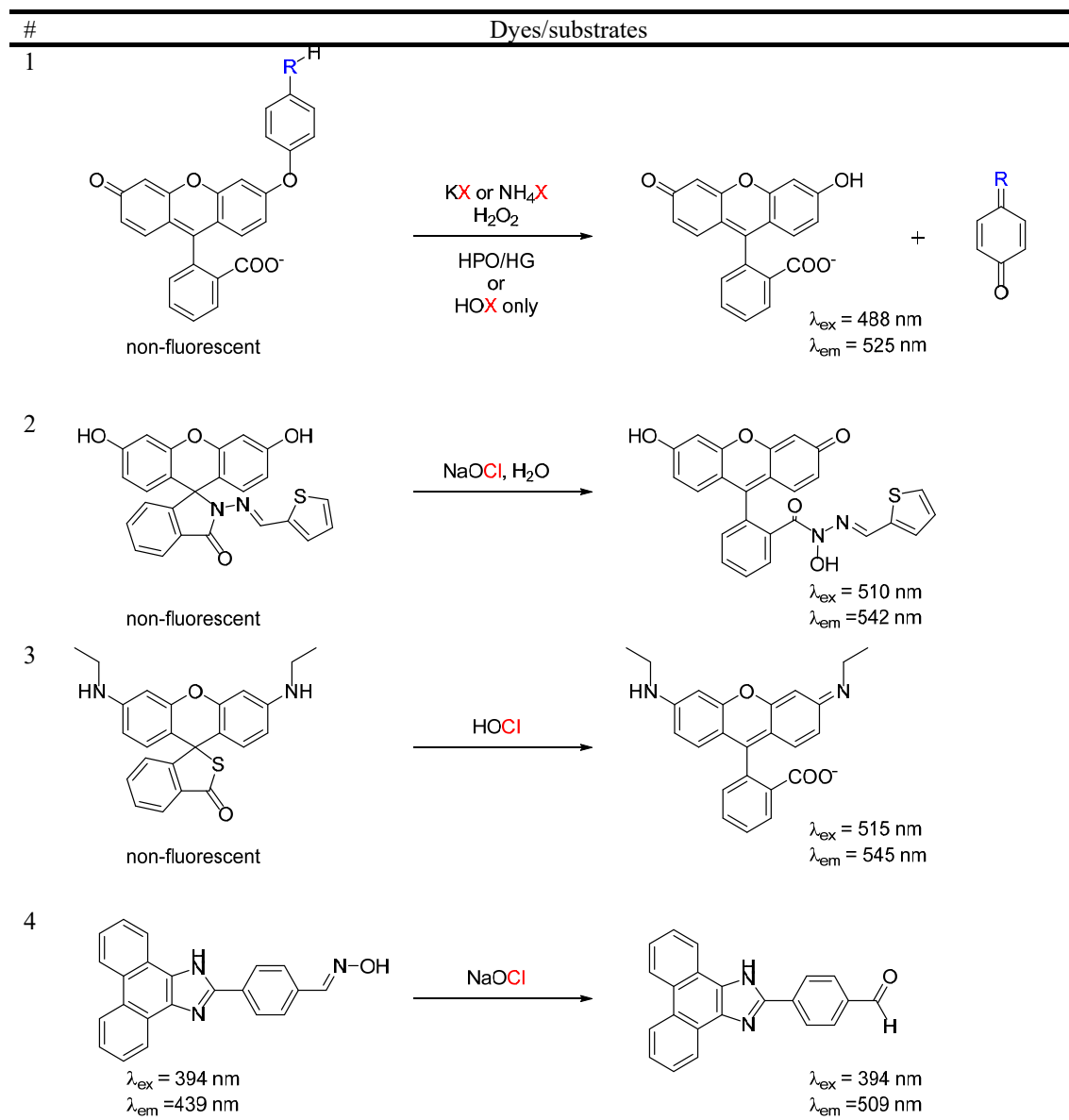
Taurine-Haloamine Assay

Haloamine is formed by the reaction of amines with HOX, and reactive chloramines[240] and bromamines[241] are natural disinfectants in biological systems.[92,112] Thiol oxidation by hypochlorous acid and chloramines is a favorable reaction and may be responsible for alterations in regulatory or signaling pathways in cells exposed to neutrophil oxidants. As a consequence, detection methods for HOX are based on the haloamine reaction (related to the amine taurine reaction, Table 4, entry 1).[92,95,112] The resulting taurine-haloamines react with trapping agents. They can be oxidized or halogenated with haloamine intermediates, for example through disulfide formation with 2-nitro-5-thiobenzoate (TNB, TNB method, Table 4, entry 2)[242,243] or by oxidation of 3,3',5,5'-tetramethylbenzidine (TMB) with additional iodide as co-substrate (TMB method, Table 4, entry 3).[220] Kettle[93] has reviewed methods for the detection of HOCl in biological systems: TNB-taurine/chloramine is suitable for detecting purified peroxidases and isolated neutrophils. Hypochlorous acid chlorinates the tyrosyl residues in small peptides leading to an increase of the 3-chlorotyrosine and 3,5-dichlorotyrosine levels in proteins after exposure. Analysis by gas chromatography and mass spectrometry is currently the most suitable method for probing the oxidation by myeloperoxidase in the pathology of several diseases. Additionally, fluorescent probes or the derivatization of tyrosine or methionine[244] are suitable markers for the halogenation of bacterial proteins in neutrophil phagosomes.[245] Sokolov et al.[246] have established a method to trap HOCl, HOBr and their corresponding taurine haloamines by oxidative degradation of celestine blue (CB method, Table 4, entry 4). This method allows HOX detection with increased selectivity and specificity over a broad pH range to monitor the reaction kinetics colorimetrically.

Table 4. Assays to monitor haloperoxidase-like activity. IV. Entry 1: HOX catalyzed reaction of taurine to taurine haloamine (X = I, Br, Cl), entry 2 – 4 trapping reagents for haloamines. Entry 2: TNB method, entry 3: TMB method, entry 4: CB method.

#	Dyes/substrates
1	
2	
3	
4	

Natural Compounds and Their Analogues as Test Systems

Hypochlorous acid is the major strong oxidant generated by neutrophils. Heme enzyme myeloperoxidase catalyzes the biosynthesis of hypochlorous acid from hydrogen peroxide and chloride. Myeloperoxidase has been implicated in the tissue damage associated with many diseases that involve inflammatory cells. Difficulties to clearly demonstrate its crucial role in pathology can be overcome with the advent of sensitive biomarkers for hypochlorous acid. The use of other biomarkers provides complementary information.[93]

Table 5 compiles test reactions and marker molecules modelled after natural compounds and reactions.[122,124] The mono-terpene nerol (Table 3, entry 1) is formed by ring closure similarly as laurencin. Geraniol and its derivates are converted to synderol and bromo-8-epicaparrapi oxide sesquiterpenes[122,133] (Table 3, entry 2-4), and the bacterial signaling molecule 3-acyl-homoserine lactone (AHL) is transformed to its inactive ana-

logue by oxidative bromination (Table 3, entry 5). The bactericidal antagonist bromo-furanone can be synthesized with V-BPO (Table 3, entry 6) and utilized to disrupt the bacterial QS as shown by Butler et al.[147] Oxidation reactions with HOX, for example sulfoxidations, are conceivable.[107] Since the yields of the halogenated products are lower and the formation of side products may be expected, kinetic studies should not rely on these assays only.

Table 5. Assays to monitor haloperoxidase-like activity. V. Entry 1: Oxidative bromination reaction of nerol to brominated laurencin-analogue. Entry 2 - 4: Oxidative bromination reaction of geraniol (and derivatives) to brominated synderol (and derivatives) and sesquiterpenes (entry 4). Entry 5: Oxidative bromination reaction of AHL to brominated AHL and subsequent degradation by basic or enzymatic hydrolysis. Entry 6: Oxidative bromination cyclization reaction of 4-pentynoic acid to bromofuranone.

1.5   Homogeneous Biomimetic HPO/HG-like Catalysts

Based on the structure of the active centers of halogenating metallo-enzymes and the mechanistic hypothesis outlined in Figure 3 and Figure 4, the requirements for catalysts in any application are as follows: (i) They should have a tunable redox-system with metal atoms in a high oxidation state whose coordination sphere can easily expand, (ii) good binding and release capabilities of oxygen compounds with low energy barriers, (iii) low toxicity, (iv) ecofriendly extraction of the raw materials, (v) large scale applicability to improve the enzyme-like activity, (vi) high operational stability (especially with regard to temperature, pH, solvents), (vii) high enzyme-like selectivity, and (viii) regioselectivity (enantioselective synthesis). Transition metal ions/complexes may fulfil many of these demands. Current research is focused on a fundamental understanding of structural and functional HPO/HG-like mimics.[247]

Organometallic vanadium compounds[97,248] modelling the structure of the active site of V-HPO and peroxo-compounds[97,249,250] have shown good efficiency and selectivity for a variety of oxidation reactions.[97,251,252] Examples are halogenation,[253] decarbonylative halogenation,[254] (enantioselective) sulfoxidation in the absence of halides,[255–257] epoxidation,[258] hydroxylation of alkenes,[259] and oxidation of primary and secondary alcohols[260] analogous to the native enzyme.[105] Homogenous complexes with established kinetics are Schiff-base complexes of vanadium,[253,261] *N*-heterocycle-vanadium pincer compounds,[262] as well as imidazole, scorperate[263,264] and amino acid complexes.[265,266] Additionally, vanadium acetylacetonate[267,268] and ammonium metavanadate[269–271] have found applications as "green" catalysts.[272] In any case, oxoperoxovanadium (V) complexes are the active species.[273,274] Many of the active catalysts require pre-treatment in strong acidic media to reduce a catalase-type degradation of H_2O_2 by halides and halogens.[272] Therefore their application in biological systems operating at neutral or moderate pH conditions is rather limited.

Although vanadium catalysts show promising activity, their industrial application becomes problematic as vanadium compounds are classified as critical according to an European Union regulation and have difficulties to fulfil the criteria of registration, evaluation, authorization and restriction of chemicals (REACH).[275,276] Hetero-polyoxometalates containing Mo(VI),[273,274,277–281] W(VI),[249,272,273,282–290] Re(VII),[217,291] Mn(II-VII),[50,51,292,293] Cu(II),[294–304] Ag(I)/Cu(II),[305,306] Ru(III),[307–309] Ce(IV),[310–318]

Fe(III),[319–322] Pd(II),[323–329] Ti(II,IV),[330,331] and Nb(V)[332] are useful, but often much more expensive and less active alternatives.[287,333–336] The haloperoxidase-like activities of main group compounds of B(III),[337] Ba(II),[338] Bi(III),[339] Sb(V),[340] Se[341–344] and Te[272,341,343,345–348] have been reviewed[309,335,336,349–351] with a focus on the synthesis of (hetero) aryl halides, vinyl halides and alkyl halides by C-H activation under homogeneous conditions.

1.6   Heterogeneous *versus* Enzyme HPO/HG-like Catalysts

New directions are explored to meet the demand for sustainable and environmentally friendly solutions that avoid the formation of hazardous waste while preserving high selectivity, stability, low energy-consumption at an industrial scale.[352] Reactions without (metal) catalysts[272] appear to be a good and cost-saving option, but they require harsh reaction conditions that are incompatible with the thermal stability of most organic compounds. Biocatalysis is a viable alternative, where enzymes or microorganisms catalyze various biochemical reactions. Enzymes have several advantages over conventional catalysts, including high degrees of chemo-, regio-, and stereospecificity and requiring only mild reaction conditions.[353,354] Despite their appealing potential, an industrial-scale application of biocatalysts is still modest compared to that of conventional chemical catalysts. Enzyme-catalyzed reactions greatly depend on temperature, pH, solvent and the chemical structure of the substrates. In addition, enzymes suffer from low stability in non-aqueous solvents, short shelf life and high production costs. However, they can be immobilized on various carriers such as porous glass, SiO_2, and organic polymers.[355–358] Prominent examples of biochemical reactions are the isomerization of glucose to fructose, important in the production of soft drinks, by using enzymes such as glucoamylase immobilized on SiO_2, and the conversion of acrylonitrile to acrylamide by cells of *Corynebacteria* entrapped in a polyacrylamide gel. Enzymes and microorganisms are used in sewage treatment plants, biosensors, organic synthesis, the food and textile industry, and pharmaceutics.[16,359–362]

Halogenases have a high potential for bioengineering and the biosynthesis of new halogenated metabolites in organic synthesis or as potent drugs.[69,363,364] Enzymes are used for oxidation reactions and hydrolysis by companies like BASF, DSM and Lonza.[365] The shortcomings of enzymatic reactions are their complexity, their stability

under operating conditions (solvent, pH, temperature etc.) and their lifetime. Several strategies have been developed to produce enzyme-organic/inorganic hybrid materials in combination with recombinant enzymes to enhance stability, activity and lifetime of the proteins.[366,367] The goal of biomimetic chemistry is to emulate the structural and functional aspects of natural enzymes.[10,368,369] Nature has served as a source of inspiration for "designing" functional (supra)molecular enzyme models, "artificial enzymes".[9] Much effort has been invested in the synthesis of (supra)molecular models that are more stable and cost efficient compared to their natural counterparts.[8] Most supracompounds contain a receptor or cavity and connected to an active site, with the aim to mimic reactions that are carried out by enzymes.[370,371] This approach has led to several elegant examples of catalytically active model compounds that display enhanced selectivity and/ or activity. Still, model catalysts, especially in the presence of other competing reactions inside living cells or even organisms, remain a challenge.[372]

Although biochemical processes are triggered by enzymes, biocatalysis is mechanistically a special case of heterogeneous catalysis.[373,374] In analogy to enzymes, the catalyst may be stabilized by a matrix or support.[375,376] If a surface reaction occurs through the steps $A + S \rightleftharpoons AS \rightarrow$ products, where S is the substrate, A is an adsorption site of the enzyme/surface, AS the substrate complex and k_1, k_{-1} and k_2 are the rate constants for the adsorption, desorption and reaction to the final product, the global reaction rate r is given by $k_2 \cdot \theta \cdot C_A$, (where θ is the surface coverage, C_A is the total number of occupied and unoccupied sites, provided that the rate constant of the enzyme/substrate complex $k_2 >> k_{-1}/k_1$ ($\equiv$ the Michaelis-Menten constant K_m). Although functions of enzymes are governed by the enzyme dynamics,[377] an enzyme is typically much larger than its substrate. The reaction environment exposed by the enzyme differs highly from the surrounding solvent that it may be considered a solid catalyst.[373,378]

The radii of enzymes and nanoparticles are comparable to nanometer-sized cellular features, and the interactions of enzymes and nanoparticles with soluble molecules have comparable strength.[379] In particular, Isupov et al. have determined the size of the V-BPO subunit, extracted from the *C. officinalis*, to 85 Å × 56 Å × 55 Å which is on the same scale as nanoparticles.[135] Nanoparticles are highly reactive, as demonstrated by the use of transition metal or metal oxide nanoparticles in catalysis.[4,15,374] They can be stabilized in solution with ligands, surfactants, or polymers, and their activity and selectivity are determined by characteristics such as size and the atomic-level structure of the planes

they expose. The most active particles in catalysis have diameters of a few nanometers and contain only a few hundred atoms. Their reactivity may even be higher than that of enzymes, because *any* surface site can be catalytically active, whereas enzymes have only a *single* binding site, although with exceptional specificity and complexity. Therefore, enzyme mimetic catalysis with nanoparticles has been successfully implemented in those cases where small species (peroxides,[380,381] superoxides[382] or sulfites[13]) are involved and steric demands play only a minor role for the specificity of the reaction.[15,374,383]
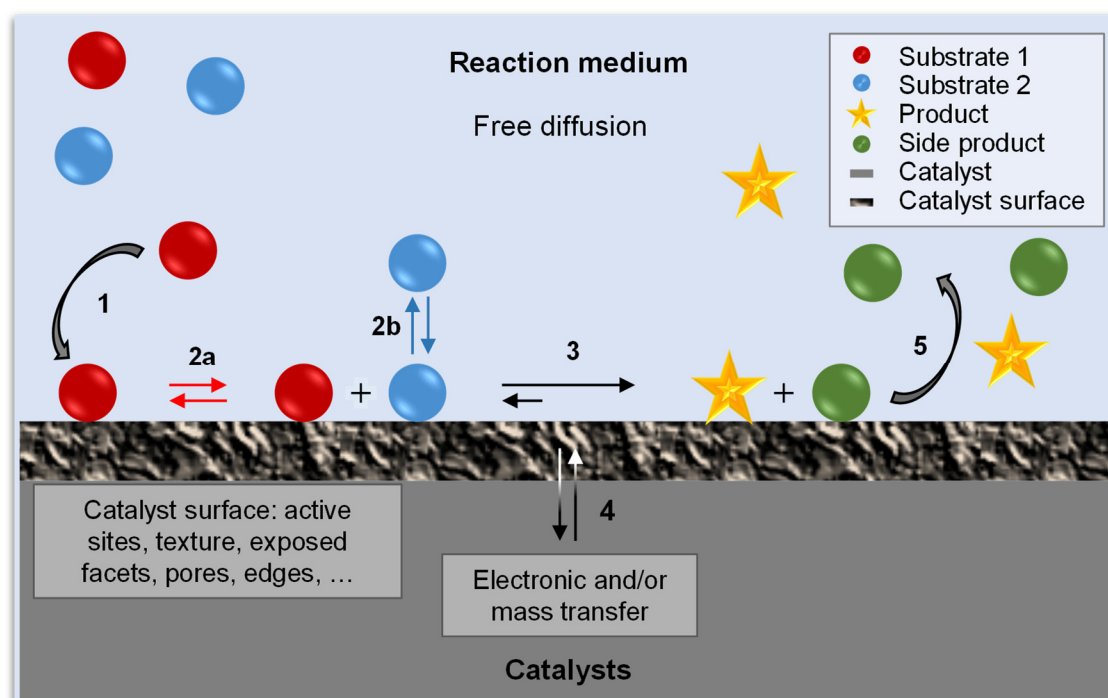
Figure 9. Reaction and diffusion pathways for a surface reaction. (1) Substrate 1 and 2 adsorb at the catalyst surface. Depending on the energy profile of the reaction, lateral diffusion (2a), desorption (2b) or reactions (3) are possible. The reaction involves mass- and, for redox processes, electron transfer at the solid/liquid (or solid/gas) interface (4). In the final step, the products desorb from the surface (5). Enzyme-catalyzed reactions proceed in an analogous fashion, but only at a single active site. The reactivity of the surface is controlled by its real defect structure.

Figure 9 illustrates the reaction at the catalyst surface for a reaction involving three components: substrate 1, 2 and the catalyst. The adsorbed components (1) can diffuse on the catalyst`s surface (2a), desorb (2b) or react to the products that can desorb afterwards as well (3). The probability of each step depends on the activation barriers associated with changes of the coordination sphere and/or the oxidation state of the metal sites, which in turn are related to the surface composition, structure, texture, exposed facets, defects, oxygen content and separation between adjacent active sites.

The reaction at the active site of V-HPOs proceeds without a change in the oxidation state by the formation of a η^2-peroxo group (Figure 4). Many functional HPO mimics have been devised based on that mechanism. Similarly, transition metals like tungsten, molybdenum and titanium that are known to form related peroxo-complexes are active in halogenation reactions. In contrast, non heme-iron HGs generate HOX *via* a radical mechanism HOX (Figure 3)[141,143] and other one-electron-transfer redox catalysts might also exhibit HG-like activity. However, most of them are highly reactive in peroxidase- rather than haloperoxidase-like reactions. The HOX selectivity can be enhanced by reducing their reactivity. Enzymes and biomimetic catalysts increase the reaction rate by providing an alternative reaction pathway for breaking and re-making of bonds. The activation energy (E_A) for the new pathway is less than the activation energy of the conventional route because transition states and intermediates are stabilized by the catalyst (Figure 10a).

Enzymes are classified according to their catalytic performance and rate constants under steady-state conditions, where the concentration of the enzyme-substrate complex remains constant (rate constants $k_1 = k_{-1} > k_2$, Figure 10a). The quantitative connection between the decrease of the substrate concentration ($[S]_0 =$ initial substrate concentration) and the reaction rate (v; $v_{max} =$ maximal reaction rate) is given by the Michaelis-Menten Equation (Equation 5). The formation of the enzyme/catalyst complex is the rate determining step. The Michaelis constant K_m indicates the substrate affinity of the catalyst/enzyme (Equation 6).

$$v = \frac{v_{max} \cdot [S]_0}{K_m + [S]_0} \tag{5}$$

$$K_m = \frac{k_{-1} + k_2}{k_1} = \frac{1}{2} v_{max} \tag{6}$$

$$\frac{1}{v} = \frac{K_m}{v_{max}} \cdot \frac{1}{[S]} + \frac{1}{v_{max}} \tag{7}$$

Additionally, K_m corresponds to the half maximal reaction rate (Equation 6, *via* Equation 5) and it represents the substrate concentration where half of the enzyme exist as an enzyme-substrate ([ES]) complex. The reaction shows a Langmuir-like behavior (Figure 10b). As an accurate determination of the kinetic parameters from the Michaelis-

Menten plot is difficult, several linearization methods have been established, the most popular being the double reciprocal representation (Lineweaver Burk plot, Equation 7).

a)

$$[E] + [S] \underset{k_{-1}}{\overset{k_1}{\rightleftharpoons}} [ES] \underset{(k_{-2})}{\overset{k_2}{\rightleftharpoons}} [E] + [P]$$

b)

$$v_0 = \frac{v_{max} [S]}{K_m} \qquad K_m = \frac{k_{-1} + k_2}{k_1}$$

Michaelis-Menten curve
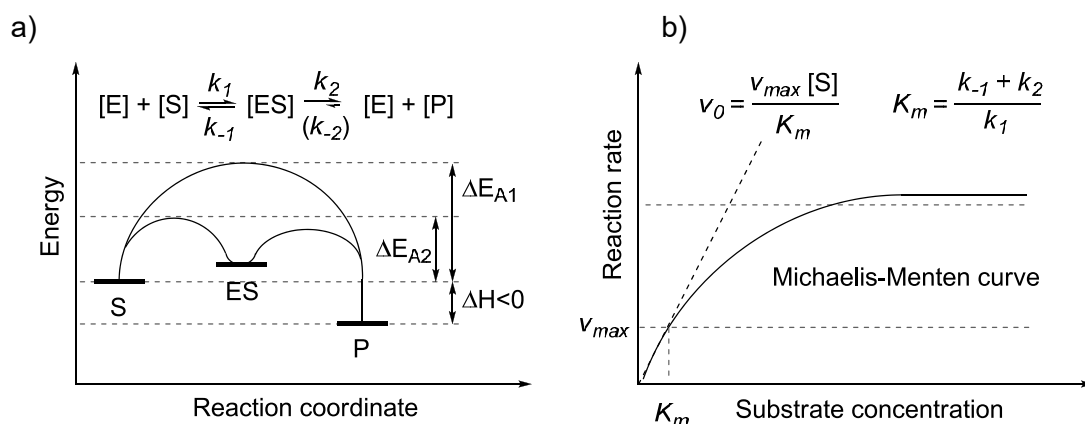
Figure 10. Theoretical aspects of enzyme-catalyzed reactions. a) Energy profile of an enzyme-catalyzed reaction. The substrate (S) and the enzyme (E) reversibly form an enzyme-substrate (ES) complex that dissociates to the final product (P). The enzyme offers an alternate reaction pathway (shown in red) where the rate determining step has a smaller activation barrier (ΔE_{A1}> ΔE_{A2}). b) Michaelis-Menten (MM)-plot, v_0: initial rate, v_{max}: maximum rate, K_m: MM constant.

The activity of haloperoxidases is often evaluated with the model substrates monochlorodimedone (MCD) or phenol red (PR). Jittam et al.[384] have reported the oxidative bromination of sulfonphthalein-dyes with bromoperoxidases (BPO) extracted from native red algae. The K_m values with respect to the co-substrates H_2O_2, bromide and to myeloperoxidase (MPO) in comparison are compiled in Table 6. The K_m values are in the range of ca. 10^{-5} M for both, the organic substrate and H_2O_2, indicating a strong affinity of the substrate to the enzyme. As bromide is always present in sufficient concentration, the affinity of the enzyme towards bromide is less pronounced in order to provide HOBr in the required amounts. The catalytic efficiency as a measure of substrate specificity of an enzyme is given by the turnover rate (k_{cat}) over K_m. For surface reactions, a Michaelis-Menten analysis is less common.

Table 6. K_m values of phenol red (PR) and dibromo/dichlorophenol red (Br2PR/Cl2PR) for extracted bromoperoxidase (BPO) of the marine red alga *Gracilaria tangi* and commercial myeloperoxidase (MPO). Reprinted with permission from ref. [384].

Enzyme	K_m (Dye) / mM	K_m (H_2O_2) / mM	K_m (KBr) / mM
BPO (crude)	PR, $1.5 \cdot 10^{-2}$ (pH 5.8)	$3.7 \cdot 10^{-2}$	$3.7 \cdot 10^{-1}$
BPO (crude)	Br2PR, $3.1 \cdot 10^{-2}$ (pH 6.5)	$1.5 \cdot 10^{-1}$	$2.9 \cdot 10^{-1}$
MPO (commercial)	PR, $8.0 \cdot 10^{-3}$ (pH 5.8)	$3.5 \cdot 10^{-1}$	$4.5 \cdot 10^{-0}$
MPO (commercial)	Cl2PR, $2.3 \cdot 10^{-2}$ (pH 5.8)	$3.5 \cdot 10^{-2}$	$2.7 \cdot 10^{-0}$

Kinetic studies for HPO or HG in wastewater treatment support the formation of hypobromite[84,385] and bromamine[386] as active species. Hypobromite is formed according to Equation 8. Besides HOBr, the oxidants and halogenating agents mono- and dibromamine are formed from the reaction of NH_4^+ with HOBr[386] or through the formation of bromochloramines.[387,388]

$$\left[HOBr \right] \equiv \left[Br_2 + Br^- \right] \equiv \left[Br_3^- \right] \qquad\qquad 8$$

The oxidation of bromine (compared to chlorine and iodine) prevails in most cases, because bromine is more reactive than chlorine (c.f. drinking water treatment) by several orders of magnitude.[103] The specific rate constants for a homolytic cleavage of H_2O_2 suggest that a slow radical transfer from a hydroxyl radical ($HO^\bullet$) to bromide (Br^-) and hypobromite species (HOBr) is dominant.[385] Von Gunten et al.[84,156,385,389–391] have analyzed the kinetics of bromide oxidation for waste water treatment with hydroxyl radicals or ozone experimentally and theoretically.

An overview about possible oxidation reactions and their equilibrium constants *via* hydroxyl radicals/H_2O_2 is given in refs.[156,385] Under laboratory conditions, a constant supply of hydroxyl radicals is ensured by γ-radiolysis of H_2O_2. The initial rate of HOBr formation with respect to oxidation and reduction processes is calculated as $6.5 \cdot 10^{-8}$ M^{-1} s^{-1}.[156] The corresponding rate constants, the reaction conditions and organic "trapping agents" are found - depending on the oxidized bromine species – to be in the range between 10^7 and 10^{10} M^{-1} s^{-1}.[156] Studies on the rate constants for the oxidative bromination of phenolic compounds have resulted in maximum values for the reaction of HOBr with phenolate ions, particularly, in $\approx 2 \cdot 10^8$ M^{-1} s^{-1} when ionic forms of *p*-cresol or phenol have been involved (pH $\approx$ 7-8).[84,386,388]

The reaction rates for the oxidative bromination reaction are $\approx 10^3$ times higher than for the oxidative chlorination.[386] Analogous results were obtained from a kinetic study for HOBr in comparison to HOCl.[388] HOCl preferably reacts with bromide according to HOCl + $Br^- \rightarrow$ HOBr + Cl^-, and thus the bromination reaction prevails as long as bromide ions are present in the reaction mixture. The *ortho* positions of the phenolic compounds are preferred over the *para* position.[388] The kinetic studies have shown that the oxidative halogenation proceeds *via* complex multistage reactions and includes radical, electrophilic or combined mechanisms with respect to the formation of HOBr and the reactive centers of the substrate. In enzymology, the turnover number (TON) is defined

as the maximum number of chemical conversions of substrate molecules that a single catalytic site can execute per second for a given enzyme concentration. It is calculated from the maximum reaction rate and catalyst site concentration. The catalysts can be assessed with respect to their specific catalytic activity through the TON, turn over frequency or rate (TOF, k_{cat}) and the specific activity (SA).[392] TOF and SA are the most significant indicators for catalytic efficiency.

In other chemical fields, for example in organometallic catalysis, the turnover number is defined by the amounts of moles of products (P) that a mole of active catalyst (C) can convert before becoming inactivated (Equation 9). The TOF is defined here as TON/per time unit (per hour or second, dimension: 1/t, Equation 10). It corresponds to the rate constant of the rate-determining step in enzyme kinetics (k_{cat}) and is typically determined by Michaelis-Menten-type analysis *via* the maximum reaction rate (v_{max}) per catalytically active site (Equation 10). The catalytically active sites may be considered as the catalytic centers in enzymes or the metal ions in an organo-metal complex.

$$TON = \frac{n(P)_{total}}{n(C)_0} = \frac{[P]_{total}}{[C]_0} \qquad\qquad 9$$

$$TOF_{[t^{-1}]} = k_{cat} = \frac{d[P]_t / dt}{[C]_0} = \frac{v_{max}}{[C]_0} \qquad\qquad 10$$

$$SA_{[mole \cdot g^{-1} t^{-1}]} = \frac{n(P)_t / dt}{m(C)_0} \qquad\qquad 11$$

Different from enzymes that typically have only a single active site, nanoparticles have many independent catalytic surface sites.[382,393] As turnover numbers (TON) and catalytic rate constants are given *per* active subunit (as in classical enzymology),[352] the activity of nanoparticle enzyme mimics has to be normalized to one active site.

The number of catalytically active sites per nanoparticle may be estimated based on the crystal structure and the particle size (in general determined from transmission electron microscopy). The ratio between the crystal volume and the volume of a single unit cell of the respective compound can be used as a calibration factor to convert the total metal concentration (determined e.g. from atomic absorption spectroscopy) to the number of active surface sites.[382,393] Finally, the total mass of the catalyst required for a specific reaction is needed for large scale applications. The specific activity (SA) is given

by the formation rate of the product (in mole) *versus* time and the supplied amount of catalytic materials (in gram, Equation 11). The SA value allows estimating efficiency, costs and even the design of production units.

1.7   Supported Biomimetic Catalysts for Halogenation Reactions

Current research focuses on bromoperoxidase-like reactions. A variety of catalytically active transition metal complexes in combination with different supporting materials have been described. Table 7 compiles bromoperoxidase-like catalysts sorted by active metal, support and reaction conditions. Environmentally friendly (in terms of solvent, starting compounds, temperature and pressure) catalysts are highlighted, and suitable assays (e.g. phenol red (PR),[394] phenol (Ph),[395,396] salicylaldehyde (SaA),[396] thymol blue (TB),[213] monochlorodimedone (MCD)[118] for validation are given. In addition, oxidative halogenation reactions beyond HOBr catalysis are considered. Major examples are oxidation, hydrohalogenation or epoxidation. Multibromination (Equation 12) and conversion (Equation 13) are considered as well.

$$nBr^{ox}{}_{(mmol)} = x \cdot nBr_x dye_{(mmol)}$$

$$\hspace{10cm} 12$$

$$nBr^{ox}{}_{(mmol)} = \sum conversion_{(\%)} \cdot x \cdot nBr_x dye_{(mmol)}$$

$$\hspace{10cm} 13$$

Sels et al.[397,398] have reported a specific activity of 600 mmol of oxidized bromine per gram of enzyme per hour for vanadium-dependent bromoperoxidase isolated from *C. officinalis* (Table 7, entry 1). The activity decreases by two orders of magnitude after immobilization on surfaces (Table 7, entry 2). TOF and SA values of synthetic catalysts are comparable with those of native enzymes, and significantly higher than the background activity of the corresponding supporting materials (Table 7, entry 3 - 7). It is low for magnesium/aluminum layered double hydroxides (Mg, Al-LDH; Table 7, entry 3), but sizeable for zirconia and zeolites (entry 4 - 7).

Table 7. Heterogeneous catalysts for oxidative halogenation reactions sorted by their active elements and supports (entry 8 - 59). (i) Organic/polymer (PS = polystyrene); (ii) inorganic (LDH = layered double hydroxide, ZrO_2 = zirconia, SiO_2 = silica, MCM = mesoporous silica, zeolite), (iii) without support (entry 60 - 65). Reaction conditions (educts, educt concentrations and assays, solvent, pH, temperature). Bromide sources: (a) NH_4Br, (b) KBr, (c) NaBr; substrate/dye: MCD = monochlorodimedone, PR = phenol red, Ph = phenol, SaA = salicylaldehyde, TB = thymol blue; DHP = 2,3-dihydro-4H-pyran, St = trans-stilbene, CA = cinnamic acid, PA = 4-pentenoic acid, An = anisole, Ch = cyclohexanone. Solvents: (A) water/methanol/tetrahydrofuran (4:3:2), (B) acetonitrile/water (1:4), (C) acetic acid, (D) methanol, (E) hepes buffer, (F) phosphate buffer, (G) diethyl ether, (H) carbon tetrachloride, (I) acetonitrile/ diethyl ether (1:3), (K) dichloromethane/water (1:1), (L) phosphate buffered saline, PBS, M) Tris-SO4 buffer. Comparison of catalytic activities by TOF = turn over frequency, SA = specific activity, listed or determined (*) based on the oxidized Br with the given specifications (TOF [1/h] = mol(Br^{ox})/(mol(cat)·h); SA [mmol/g·h] = mmol(Br^{ox})/(g(cat)·h)). Reference materials (native enzyme, supports) are listed in entries 1-7. Detailed determination of TOF and SA values are presented at the Experimental Section, page 217.

# [Ref.]	Catalyst	Support	Totat cat. amount	Br^- [mM]	H_2O_2 [mM]	Dye [mM]	Reaction conditions	TOF [1/h]	SA [mmol/g·h]
1 [397]	V-HPO	None		100[a]	2.5-5	MCD (0.5)	A) 20 mL, pH 6.5	n.a.	600
2 [397]	V-HPO	immobilized		100[a]	2.5-5	MCD (0.5)	A) 20 mL, pH 6.5	n.a.	$1.5·10^{-1}$ - $6.0·10^0$
3 [398]	MgAl	(MgAl) LDH	2.7 mg	100[a]	2.5	PR (0.05)	A) 10 mL	n.a.	$0.3·10^{-1}$
4 [399]	Zr	mZrO2 (m-700; m-630)	20 mg	100[a]	10.3	PR (0.05)	H_2O, 32 mL	n.a.	$4.2·10^{-1}$; $8.4·10^{-1}$
5 [400]	Zr	ZrO_2	200 mg	550[b]	550	PR (0.5)	C) 4 mL, 5h	$1.2·10^{-1}$*	$9.8·10^{-1}$ *
6 [395]	Al, Si	HZSM-5(30) Zeolite	200 mg	550[b]	550	Ph (500)	C) 4 mL, 5h	n.a.	1.8*
7 [395]	Al, Si	HY Zeolite	200 mg	550[b]	550	Ph (500)	C) 4 mL, 5ht	n.a.	1.5*
8 [401]	V(IV)O complex	salen-like polymeric backbone	20 mg	1000[b]	2500	SaA (500) [13]	4 mL H_2O, 1M $HCClO_4$, 2h	31.5 – 33.8	141.0 – 158.0*
9 [402]	$V(V)O_2$ complexes	PS	30 mg	2000[b]	2000	SaA (1000)	10 mL H_2O, 2M H_2SO_4, 2h	100.0 - 104.3	137.5*
10 [403]	$V(V)O_2$ complexes	PS	5 mg	500[b]	500	SaA (250)	20 mL H_2O, 1M $HCLO_4$, 2h	2254	634*
11 [404]	$V(V)O_2$ complexes (1.3 – 1.4 wt% V)	PS	20 mg, ≈ 1 mM V	12500[b]	3750	SaA (2500) [11]	4 mL H_2O, rt, 2h, 10 M $HClO_4$	775; 800	192.6*; 183.0*
12 [398]	$V(V)O_3^-$	(MgAl) LDH	5.4 mg, 200 μM V	100[a]	2.5	PR (0.05)	A) 10 mL	0.1	$0.4·10^{-1}$
13 [398]	$V_{10}O_{28}^{6-}$	(MgAl) LDH	6 mg, 2 mM V	100[a]	2.5	PR (0.05)	A) 10 mL, ≈2h	$1.3·10^{-2}$	$0.4·10^{-2}$
14 [405]	V(IV)O complex, 0.65 wt%V	MCM-41	25 mg, 640 μM V	1000[b]	6000	SaA (1000) [5]	5 mL H_2O/ACN	448	56.6*

							(4:1), 0.4 M HClO$_4$ 3.5h		
15 [396]	V(V)O$_2$ complexes	Zeolite-Y	20 mg, 0.8; 0.6 wt% V	1000[b]	3750	SaA (500)	4 mL H$_2$O, 0.2 mL 70% HClO$_4$, 4h	52; 67	8.5; 6.7*
16 [406]	WO$_2$(O$_2$)(CN$_2$)	PAN	≈200 mg, 3 mM W	2000[b]	80	PR (1.6)[9]	F) 25 mL, 50 mM, pH 5.5, 30°C, 1.33 h	274.0*	0.6
17 [398]	WO$_4^{2-}$	(MgAl) LDH	2.7 mg, 50 μM W	100[a]	2.5	PR (0.05)[2]	A) 10 mL	21.6	4.0
18 [397]	WO$_4^{2-}$	(MgAl) LDH	50 μM W	100[a]	2.50	PR (0.05)[1]	A) 20 mL, pH 6-8	33	6.2
19 [397]	WO$_4^{2-}$	(MgAl) LDH	50 μM W	100[a]	5.00	MCD (0.5)[1]	A) 20 mL, pH 6-8	71	13.3
20 [397]	WO$_4^{2-}$	(NiAl) LDH	50 μM W	100[a]	5.00	MCD (0.5)[1]	A) 20 mL, pH 6-8	48	9
21 [407]	WO$_4^{2-}$	(NiAl) LDH (Taktovite)	80 mg, 4 mM W	800[a]	440	DHP (360)[3]	B), 10 mL, 25 min	192.8 (r.t)*; 497.2 (35°C)*	96.4 (r.t)*; 248.6 (35°C)*
22 [408]	15 wt% H$_3$PW$_{12}$O$_{40}$	(ZnAl) LDH (hydrotalcite-like)	200 mg, 31 mM W	550[b]	550	Ph (500)	C) 4 mL, 5h, 110°C	2.3*	1.4*
23 [409]	WO$_x$	mZrO$_2$	0.3-1.6 wt% W	100[a]	27.7	Ph (0.05)	H$_2$O	57 - 84	n.a.
24 [410]	15 wt% H$_4$SiW$_{12}$O$_{40}$	ZrO$_2$	200 mg, 31 mM W	550[b]	550	Ph (500)	C) 4 mL, 5h	2.9*	1.8*
25 [410]	15 wt% H$_3$PW$_{12}$O$_{40}$	ZrO$_2$	200 mg, 31 mM W	550[b]	550	PR (500)	C) 4 mL, 5h	3.0*	1.8*
26 [400]	15 wt% H$_3$PW$_{12}$O$_{40}$	ZrO$_2$	200 mg, 31 mM W	550[b]	550	PR (500)	C) 4 mL, 5h	3.0*	1.9*
27 [411]	12 wt% H$_3$PW$_{12}$O$_{40}$	ZrO$_2$	500 mg, 25 mM W	1800[d]		An (1800)[5]	D) 10 mL, 1.5h	46.6*	23.3**
28 [412]	15 wt% H$_4$SiW$_{12}$O$_{40}$	TiP	200 mg, 31 mM W	550[b]	550	Ph (500)	C) 4 mL, 5h	3.1*	1.9*
29 [412]	15 wt% H$_3$PW$_{12}$O$_{40}$	TiP	200 mg, 31 mM W	550[b]	550	Ph (500)	C) 4 mL 5h	3.1*	2.0*
30 [402]	Mo(VI)O$_2$ complex	PS	30 mg	2000[b]	2000	SaA (1000)	10 mL H$_2$O, 2M H$_2$SO$_4$, 2h	213.3	170.8*
31 [413]	Mo(VI)O$_2$ complex	PS	15 mg, 169 μM Mo	500[b]	500	St	K) 40 mL, 0.5 M HClO$_4$, 2h, 40°C	512.0*	230.4*
32 [406]	Mo(VI)O$_2$(O$_2$)(CN)$_2$	PAN	≈100 mg, 3 mM Mo	2000[b]	80	PR (1.6)[9]	F) 25 mL, 50 mM, pH 5.5, 30°C, 1.33h	240.0*	1.2*
33 [414]	Mo(VI)O$_4^{2-}$ 9.9 % Mo	(MgAl) LDH	250 mg, ≈ 26 mM Mo	200[b]	650	CA (100)[4]	10 mL H$_2$O, 20 min	9.3*	9.6*

34 [398]	Mo(VI)O$_4^{2-}$	(MgAl) LDH	2.7 mg, 50 µM Mo	100[a]	2.5	PR (0.05)	A) 10 mL	20.1	3.7
35 [408]	15 wt% H$_3$PMo$_{12}$O$_{40}$	(ZnAl) LDH	200 mg, 49 mM Mo	550[b]	550	Ph (500)	C) 4 mL, 5h, 110°C	1.7*	1.7*
36 [410]	15 wt% H$_4$SiMo$_{12}$O$_{40}$	ZrO$_2$	200 mg, 49 mM Mo	550[b]	550	Ph (500)	C) 4 mL, 5h	1.7*	1.6*
37 [410]	15 wt% H$_3$PMo$_{12}$O$_{40}$	ZrO$_2$	200 mg, 49 mM Mo	550[b]	550	Ph (500)	C) 4 mL, 5h	1.8*	1.7*
38 [395]	5 wt% Mo	ZSM-5(30) Zeolite	200 mg, 26 mM Mo	550[b]	550	Ph (500)	C) 4 mL, 5h	4.3*	2.2*
39 [412]	15 wt% H$_4$SiMo$_{12}$O$_{40}$	TiP	200 mg 49mM Mo	550[b]	550	Ph (500)	C) 4 mL, 5h	1.7*	1.7*
40 [412]	15 wt% H$_3$PMo$_{12}$O$_{40}$	TiP	200 mg, 49 mM Mo	550[b]	550	Ph (500)	C) 4 mL, 5h	2.0*	2.0*
41 [415] [398]	5-18 wt%Ti (IV)	MCM-48	7-30 mg	100[b]	10	PR (0.2)	E) 3 mL, 0.1M pH 6.5 (or organic solvents/mixtures)	1.6·10^{-1} ([398])	1.6·10^{-1} ([398])
42 [398]	Ti 4 wt%	MCM-41	0.5 mM	100[b]	2.5	PR (0.05)	A) 10 mL	5.6·10^{-2}	4.7·10^{-2}
43 [395]	Ti (IV)	TS1 Zeolite	200 mg	550[b]	550	Ph (500)	C) 4 mL, 5h	n.a.	1.8*
44 [398]	Ti (IV)	TS1 Zeolite	0.5 mM Ti	100[a]	2.5	PR (0.05)	A) 10 mL	1.0·10^{-3}	2.5·10^{-4}
45 [331]	Ti(IV)O$_2$ 4 wt%	ZrP	200 mg 41.8 mM Ti	550[b]	550	Ph (500)	C) 4 mL 5h	2.0*	1.6*
46 [331]	Ti(IV)O$_2$ 4 wt%	TiP	200 mg 41.8 mM Ti	550[b]	550	Ph (500)	C) 4 mL 5h	2.7*	2.3*
47 [416]	Zr(IV)/SO$_4^{2-}$	SBA-15-620	50 mg	370[a]	310	Ph (74)[7]	B) (7:3) 6.75 mL, 4h	n.a.	2.3*
48 [395]	Cr 5 wt%	ZSM-5(30) Zeolite	200 mg 48 mM Cr	550[b]	550	Ph (500)	C) 4 mL, 5h	1.7*	1.7*
49 [417]	Fe(III) complex	PS	50 mg 3.66 % Fe	2000[b]	2000	SaA (1000)[10]	H$_2$O, 10 mL, 2 M conc. H$_2$SO$_4$	99.0*	65.3*
50 [397]	Fe(bipyridine)$_2$	NaY Zeolite	50 µM Fe	100[a]	2.50	PR (0.05)	A) 20 mL	1.3·10^{-3}	7.8·10^{-4}
51 [395]	Fe 5 wt%	ZSM-5(30) Zeolite	200 mg 4.5 mM Fe	550[b]	550	Ph (500)	C) 4 mL, 5h	2.2*	2.0*
52 [418]	Cu(II)	PS	15 mg 1.1 mM Cu	440[b]	1000	Ph (400)[11]	C) 5 mL, 2h	174.8*	64.7*
53 [419]	Cu(II) complex	SiO$_2$	50 mg 563 µM Cu	550[b]	550	Ph (500)[5]	C) 4 mL, 60°C, 1.5h	586.7*	26.4*

54 [395]	Cu 5 wt%	ZSM-5(30) Zeolite	200 mg 3.9 mM Cu	$550^{b)}$	550	Ph (500)	C) 4 mL, 5h	2.2*	1.7*
55 [399]	Re 0.04–0.67 wt%	mZrO$_2$-630/700	20 mg	100^{a}	10.3	PR $(0.05)^{5)}$	H$_2$O	n.a.	0.1 - 1.3
56 [420]	Se 2.5 mol%	Xerogel		$1400^{c)}$	350	PA (140)	F), pH 6.2, 5 mL	$9.1 \cdot 10^{-3}$*	n.a.
57 [420]	Te 2.5 mol%	Xerogel		$1400^{c)}$	350	PA (140)	F), pH 6.2, 5 mL	$4.1 \cdot 10^{-2}$*	n.a.
58 [421]	NaHSO$_4$	SiO$_2$	100 mg	$240^{d)}$		Ch (200)	G or H) 5 mL 0.5h, rt	n.a.	18.6*
59 [422]	H$_2$SO$_4$	SiO$_2$	15 mg	$210^{d)}$		Ph $(200)^{5)}$	I) 5 mL, 0.5h	n.a.	110.7*
60 [423]	V	V$_2$O$_5$	91 mg, 40 mM V	$120^{e)}$	636	o-cre-sol (40)	B) (1:1), 25 mL, pH≈2.1, 5°C, 1.5 h	0.6*	6.7*
61 [424]	V	V$_2$O$_5$ nw	0.02 mg 220 µM V	$1^{b)}$	0.01	MCD (0.05)	M) 100mM, 1mL, pH 8.3	$1.4 \cdot 10^{-2}$*	$1.5 \cdot 10^{-1}$*
62 [425]	V	V$_2$O$_5$ nw	1 mg	40 (KI)	1	TB (25) 16)*	L) pH 8.0, 1 mL, 1 min	136.4*	1500*
63 [426]	Ce	CeO$_2$ nr	50 mg, 291 mM	500 (I$_2$)	2 mL 35 %	DMB (1000)	H$_2$O, 1 mL, 100°C, pH 3.0	6.7*	38.8*
64 [427]	Ce	CeO$_2$ np	80 mg, 613 mMl	$250^{b)}$	6bar O$_2$	TMB $(83)^{14)}$	0.75 mL H$_2$O, 100°C, 20h	$6.1 \cdot 10^{-3}$*	$3.5 \cdot 10^{-2}$*
65 [227]	Ce	CeO$_2$ nr	25 µg, 145 µM	$25^{a)}$	0.3	PR (0.01) 15)	1 mL H$_2$O, (v_{max}=0.4µ M$_{HOBr}$/min)	0.2*	1.0*

1) DMT, ^{1}O$_2$, dimedone, methoxystyrene, methylcyclohexene; 2) DMT, ^{1}O$_2$, MCD, 3) oxidative hydrohalogenation, alkoxyhalo-adducts, anhydro-sugars, 4) halodecarboxylation of aromatic derivates, 5) diverse (hetero)aromatics, 6) oxybromination as side reaction, 7) other aromatics, dimethylaniline, methylaniline, aniline, Ph, SaA, 8) (a)cyclic ketone, amide, β-ketoester, 9) aniline, m/p/o-aminophenol, m/p/o-nitroaniline, quinol, pyrogallol, resorcinol, acetamide, salicylaldehyde, o-methoxytoluene, catechol, 10) oxidation of styrenes, benzyl alcohols, various alkenes, sulfides, aromatic alcohols, ethylbenzene, 11) sulfoxidation, aromatic (aliphatic) compounds, 12) hydroxylation of Ph, 13) photocatalytic activity, anisole, olefinic substrates, 14) halogen exchange, 15) halogenation of lactones, 16) L-dopamine, 17) anisole, toluene, ethylbenzene, Ph.

Many structural and functional enzyme mimics have been devised modelling the active site of marine bromoperoxidases. Besides vanadium complexes, molybdenum and tungsten compounds are the most efficient haloperoxidase mimics. Islam et al.[274] have reviewed peroxo complexes of vanadium and molybdenum and their catalytic activity in HPO-like reactions. The transition metals involved are reported to be in their highest oxidation states with ionic radii of V^{5+}: 46 pm, Mo^{6+}: 59 pm and W^{6+}: 60 pm.[428] Oxo- and peroxo-ligands are preferred according to Pearson´s HSAB model.[429] Therefore, all of them follow an oxidative halogenating mechanism with metal-η^2-peroxo-intermediates.

Many compounds suffer from the formation of catalytically less or inactive polyoxometalates (POM), heteropolyacids (HPA) or gel-like structures (e.g. vanadium pentoxide gels[430]) depending on the solution pH. Attempts have been undertaken to overcome this problem by "heterogenization". Several homogenous organo-transition metal complexes have been immobilized on polymer supports,[274] layered double hydroxides (LDHs),[397,398] zirconia (ZrO_2),[410] silica[431] or in zeolites.[395]

A series of oxovanadium(V) and oxomolybdenum(VI) complexes have been attached to a polymer backbone through the anchor groups of a modified salen-like structure (Table 7, entry 8).[401] Likewise, vanadium(V) Schiff-base and related complexes were grafted to a polystyrene (PS) backbone without[402] or with spacer units[403,404,432] (Table 7, entry 9-11). The structure and synthesis of a PS-bound oxovanadium(V)-complex are shown in Figure 11a.[403] The different activities of the polymer-bound catalysts (Table 7, entry 8-11) are related to differences in the degree of loading and the different coordination environment of the vanadium centers. Ligands with electron donor atoms (N- and O- functions) have an impact on the accessibility and the stability of the metal oxidation state, thereby affecting the oxygen storage (η^2-peroxo groups) and release (HOBr formation) behavior.

The PS-grafted compounds have high SA and TOF values and high selectivity with respect to *para*-bromo salicylaldehyde, and they are active oxidation catalysts.[401,402] Their catalytic performance can be enhanced by decreasing the pH (pH $\approx$ 2-4), increasing the temperature to 80°C and the amount of hydrogen peroxide.[401,402] The PS-grafted catalysts can be reused up to three times without activity loss, leaching or decomposition of the catalyst.[403,404]
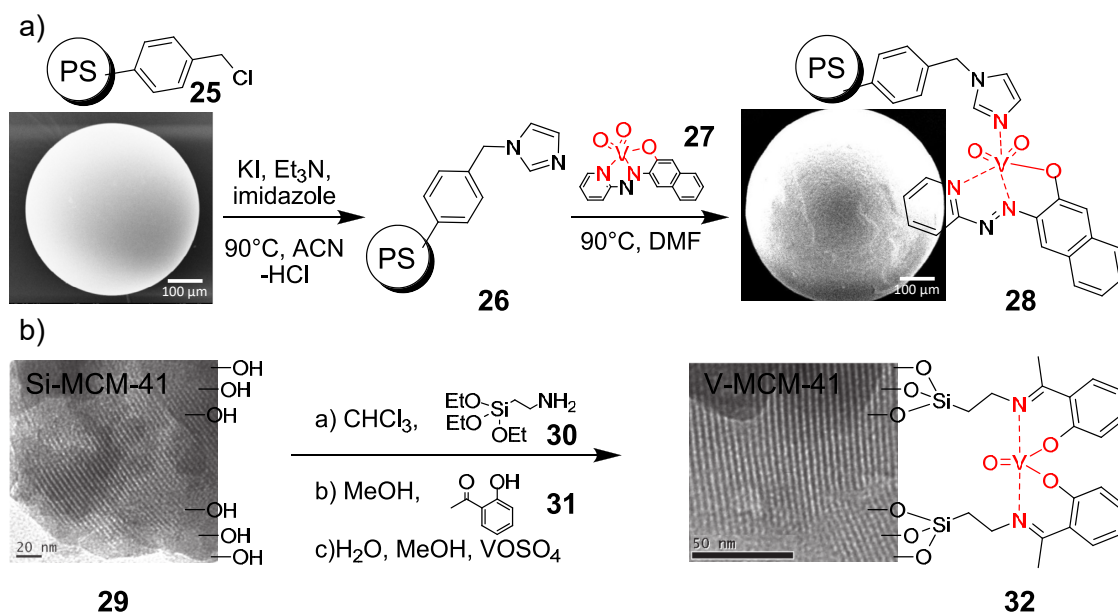
Figure 11. Immobilization of vanadium. Synthesis of a) the polystyrene (PS)-grafted dioxo-vanadium(V) complex **28**[403] and b) a vanadium complex incorporated in mesoporous silica (MCM) **32**.[405] The SEM and the TEM images (left) show the undoped support and (right) the incorporation of the transition metal. The surface of the spherical PS matrix is roughened for V-PS **28**. SEM and TEM images reprinted with permission from ref. [403,405].

LDH supported catalysts[398] are up to four orders of magnitude less reactive (Table 7, entry 12) than their PS-grafted counterparts (Table 7, entry 9-11). Likewise, polyoxometalates showed lower oxidative bromination activities than the corresponding low-molecular compounds, as demonstrated by the decavanadate/vanadate pair (Table 7, entry 13).[398] Vanadium(IV) complexes grafted on mesoporous silica (MCM)[405] or dioxo-vanadium(V)-Schiff-base complexes[396] in zeolite-Y (Figure 11b) have shown enhanced TOF and SA values (Table 7, entry 14, 15). The larger active surface area of MCMs lead to higher activity combined with good selectivity towards monobrominated salicylaldehyde.
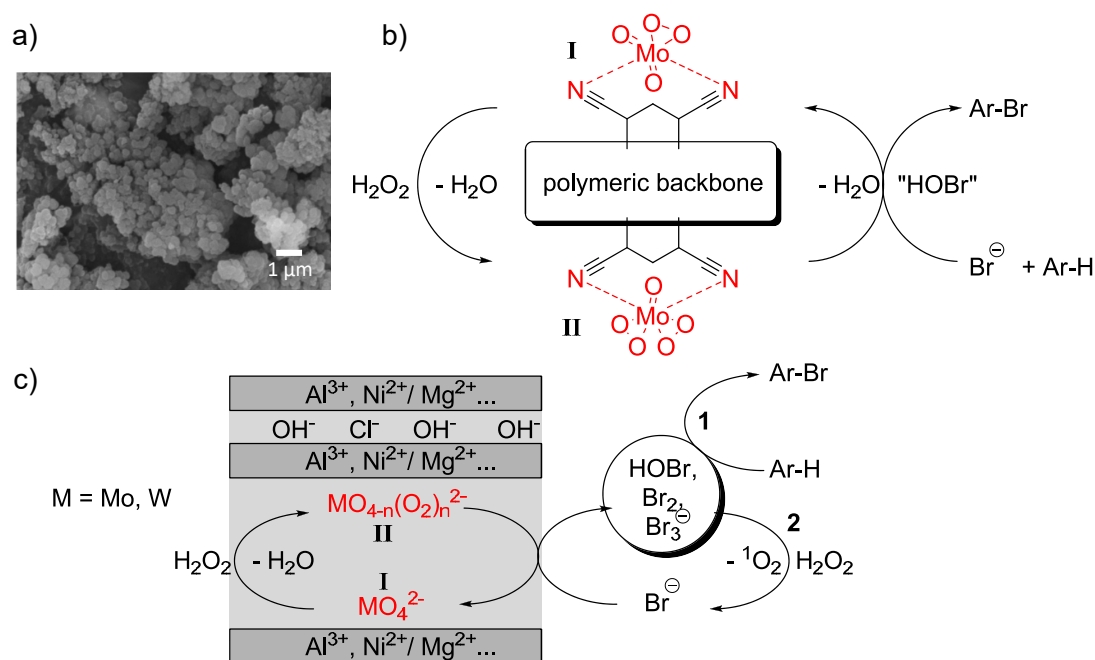
Figure 12. Proposed mechanism for the oxidative bromination with immobilized Mo-PAN complexes. a) SEM image of the Mo-PAN-complex (reprinted with permission from ref. [406]). b) Mo-PAN catalyzed oxidative bromination.[406] c) Oxidative bromination catalyzed by WO_4^{2-} or MoO_4^{2-} exchanged layered double hydroxides (LDHs). Both reactions involve η^2-peroxo species (I to II). A two-electron oxidation of bromide to bromite (HOBr, BrO⁻, Br_2, Br_3^-) is compatible with the electrophilic bromination of an aromatic substrate (1). With excess H_2O_2 (2) $^1O_2$ is generated via a peroxo-bromide species.[397]

Molybdenum and tungsten complexes supported on organic matrices are established as well (Table 7, entry 16, 30-32). The metal coordination is comparable to that of the V-complexes (Figure 11, Figure 12). The overall catalytic activities are similar (TOF for V^{5+}: 100, W^{6+}: 274, Mo^{6+}: 240 h^{-1}; Table 7, entry 9, 16, 32) despite the use of different assays, reaction conditions, and polymer supports (PS or polyacrylonitrile (PAN)). The highest SA (634 mmol Br^{ox} g_{cat}^{-1} h^{-1}) and TOF (2254 h^{-1}) values have been reported for a vanadium-PS complex (Table 7, entry 10). However, vanadium and molybdenum on polymer supports require acidic conditions (H_2SO_4, $HClO_4$), while tungsten catalysts are still active in phosphate buffer (TOF $\approx$ 274 h^{-1}, pH 5.5, Table 7, entry 16).

There are distinct trends for inorganic supports. LDHs exchanged with tungstate and molybdate retain their catalytic activity (SA) in different assays (PR, Ph, MCD; Table 7, entries 17-22, 33-35) at neutral pH (pH $\approx$ 6-8). The increased hydro-bromination rate of 2,3-dihydro-4H-pyran (DHP) with tungstate exchanged takovite (Ni, Al-LDH) shows that the bromination rates can be enhanced by adjusting the reaction conditions and the substrates (Table 7, entry 20, 21). The activity can be further enhanced by increasing the

reaction temperature.[407] DHP and other cyclic enol ethers are susceptible for hydro- or methoxybromination, -iodination and Br-assisted epoxidation reactions.[407] These intermediates are useful for the synthesis of glycoconjugates or oligosaccharides under mild conditions in water.[407] WO_4^{2-}/LDH-based HPO mimics are more effective than their MoO_4^{2-} or VO_4^{3-} analogues.[272,407] The LDH composition affects the reactivity of the catalyst in the order (Mg, Al) ≥ (Ni, Al; takovite-like) > (Zn, Al; hydrotalcite-like)-LDH.[397,398]

Replacement of LDH-intercalated WO_4^{2-} or MoO_4^{2-} by polyoxometalates/ heteropolyacids (HPA) decreases the activity to the level of the support's self-activity. This can be rationalized from the structure of the highly active LDH/WO_4^{2-} (Table 7, entry 19) where isolated WO_4^{2-} anions are mainly located at the edge positions.[397] These peroxotungsten intermediates identified by UV-Vis spectroscopy appear to be the key species for the formation of hypohalous acid (HOBr). The reaction pathway shown in Figure 12 is assumed to be identical for tungstate and molybdate.[397,414,433] The mechanism *via* Br+ species has been demonstrated with 2,3-dimethoxytoluene (DMT), as the methyl group would be attacked in a radical mechanism as well. The formation of ring-substituted Br-DMT is compatible with an electrophilic bromination mechanism.[398] The stability of the exchanged catalyst in LDHs is critical in aqueous media because of deactivation by leaching and polycondensation. Decatungstate ($W_{10}O_{32}^{4-}$) encapsulated in the organic resin Amberlite IRA-900 showed reasonable activity for photocatalytic bromination, bromohydrin formation or epoxidation.[434]

An alternative approach has been pursued by impregnating mesoporous oxide supports (e.g. mZrO_2),[435] silica (MCM)[405,436] or zeolites with transition metal ions. The exposed hydroxyl groups and the large surface area of the support materials allow the attachment of organometallic complexes or W- and Mo-heteropolyacids (HPA) in combination with Si and P (Table 7, entry 22,24-29, 35-37, 39, 40). Mononuclear metal complexes are typically more active than polyoxometalates. The activity increases when halogenating co-agents like *N*-bromosuccinimide (NBS)[411] or Br_2[437] are used instead of bromides. The calcination temperature of the catalyst after doping and the doping degree are crucial for the activity.[400,410] Theoretically, an optimum doping of 15 % may be rationalized by the presence of highly dispersed WO_x species required for efficient oxidation of bromine and enough free surface area for dye adsorption without blocking catalytic sites.[409] However, an optimum tungsten-doping on m-ZrO_2 has been observed for

1.3 wt% of W (1.3W/m-ZrO$_2$).[409] HPA (Mo)-impregnated titanium phosphate (TiP) showed increased SA values compared to molybdenum Keggin clusters.[410,412]

The activity and regioselectivity of the oxidative bromination like an increased yield of *para*-bromophenol[410] depend on the number of exposed Lewis acidic metal sites on the catalyst surface which stabilize peroxo-species and the Wheland intermediates.[416] Brønsted acidic sides are assumed to be involved in the electrophilic bromination process, more precisely, in HOBr formation.[400,438] Figure 13 illustrates the proposed reaction mechanism on oxide supports as zirconia, silica or zeolites. Transition metal catalysts on oxide supports can be recycled. They show reduced activity compared to their polymer-grafted counterparts, although they are stable in acidic media. Regiospecific bromination is possible, and catalysts leaching can be suppressed.
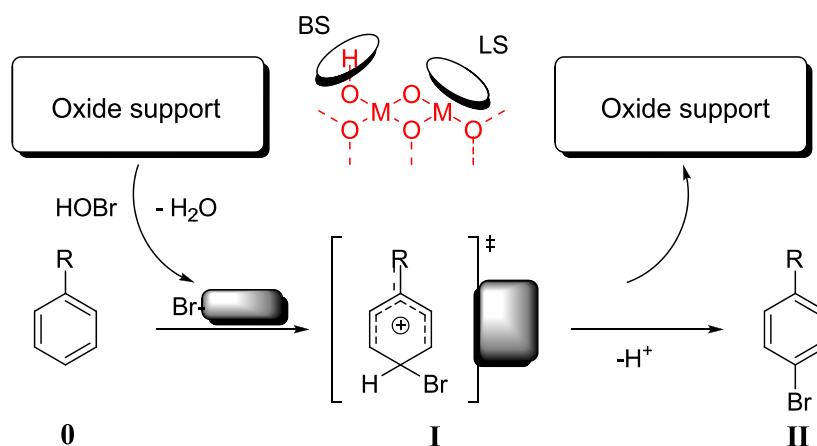
Figure 13. Halogenation reactions catalyzed by metal (M = Zr, Si, Al or Ti, Mo, W etc.) substituted oxide supports (zirconia, zeolites, silica). Brønsted (BS) and Lewis (LS) acidic sites are involved in the oxidative halogenation. BS: HOBr formation, LS: peroxo group binding and stabilization of σ-complexes 0-II (Wheland intermediates).[416]

Ti/MCM materials have been the first heterogeneous oxidative halogenation catalysts in neutral aqueous and organic-aqueous media in the absence of acids.[415] Titanium oxide is a well-known photocatalysts that can carry surface-bound peroxo groups as possible intermediates for electrophilic halogenation reactions. Still, no haloperoxidase- or halogenase-like activity has been reported for the pure TiO$_2$. Grafting titanium(IV) compounds on mesoporous silica or zeolites (Table 7, entry 41-44) results in very low specific activities (Table 7, entry 4-7). The situation is improved for mesoporous silica,[436] cubic (MCM-48) being preferred compared to the hexagonal pore array (MCM-41).[415] Butler, Stucky and coworkers[415] have discussed titania cluster formation as a possible reason for the activity decrease of different catalysts with increasing amounts of Ti. The activity

is slightly increased when zirconium phosphate (ZrP, Table 7, entry 45) has been used as a support instead of titanium phosphate (TiP, Table 7, entry 46). The proposed titanium(IV) peroxo complex on a titanium phosphate surface shows values comparable to those of HPA impregnated TiP supports (Table 7, entry 28, 29, 39, 40). Different amounts of Ti pillared on ZrP or TiP in combination with the calcination temperature control the regioselectivity of oxidative bromination reactions. Materials calcined at 110°C exhibit *ortho*-selectivity in the bromination of phenol, whereas *para*-selectivity has been observed for catalysts calcined at 500°C.[331] Zirconium(IV) oxide showed moderate oxidative bromination activity (Table 7, entry 4, 5), but the reactivity has been increased for sulfated zirconia on mesoporous silica (SBA-15-620, Table 7, entry 47). A good *para*-selectivity has been observed for the bromination of phenol. SBA-15 supported sulfated zirconia has possessed higher catalytic activity than self-supported sulfated zirconia because of its larger surface area and pore size.[416] The good catalytic performance of the sulfated zirconia on SBA-15 obtained by calcination at higher temperature has been attributed to the good dispersion of sulfate groups yielding sulfated silica-zirconia with efficient redox behavior and a high density of acidic sites (Figure 13).[416]

Chromium has been expected to catalyze oxidative halogenation reactions through metal-bound peroxo groups, as shown by Narender et al.[395] for Cr-zeolites (CrZSM-5 or 30, Table 7, entry 48). Although the selectivity for *para*-bromophenol is high, the activities are only moderate compared to catalysts without chromium (Table 7, entry 6, 7). In addition, chromate can be formed in side reactions with subsequent Cr leaching ($\approx$ 3%).[395] No haloperoxidase-like activity has been reported for manganese compounds. Pillared zeolites with Mn-bipyridine complexes showed no bromination activity.[397,398]

Although iron and copper-dependent enzymes are ubiquitous, only a few Fe- and Cu compounds show oxidative halogenation activity. Plausible reasons may be the redox potential for higher oxidation states and the inability to bind peroxo units. Enzymes overcome this problem with specially designed protein scaffolds having active side pockets that allow the stabilization of organic radicals by iron and copper complexes rather than the formation of hypohalites. The peroxidase-, catalase-, and SOD-like activity of iron and copper compounds has been reviewed before.[439,440] Iron and copper compounds have been used as halogenase mimics. When complexed by chloromethylated polystyrene, iron(III) is an active and reusable catalyst for oxidation and oxidative bromination reactions (Table 7, entry 49)[417] with an activity close to that of polymer-bound vanadium

and molybdenum compounds (Table 7, entry 9, 30). Figure 14a illustrates the synthesis of a resin-supported iron(II) salen complex which can be recycled up to five times. An analogous copper complex on polystyrene has TOF values comparable to those of Mo, W and V containing polymers (Figure 14b, Table 7, entry 52). The immobilized compounds also catalyze the oxidation of thioethers to sulfoxides or sulfones in a selective manner.[418] Similarly, copper(II) perfluorophthalocyanine immobilized on silica gel (Figure 14c) showed promising activity and recyclability (up to six times) without loss of activity (Table 7, entry 53).[419]

Raja et al.[436,441] have reported the oxyhalogenation of aromatics with hexadeca-chloro copper phthalocyanine complexes incorporated in zeolites ($CuCl_{16}Pc$-Na-X, 0.27 wt% Cu) with TOF values $\approx$ 160-380 h^{-1}. These values, however, describe the total substrate conversion including simple oxidation reactions. Halogenated products (chlorination and bromination) contribute only to 10-30 wt% in assays with benzene, toluene, phenol, aniline, anisole or resorcinol.[441] With cobalt or iron instead of copper, the TOF value decreases (TOF(Co) = 107 h^{-1}, TOF(Fe) = 210 h^{-1}), but the relative amount of brominated products increased (up to 50 % for Co and 40 % for Fe).[441]
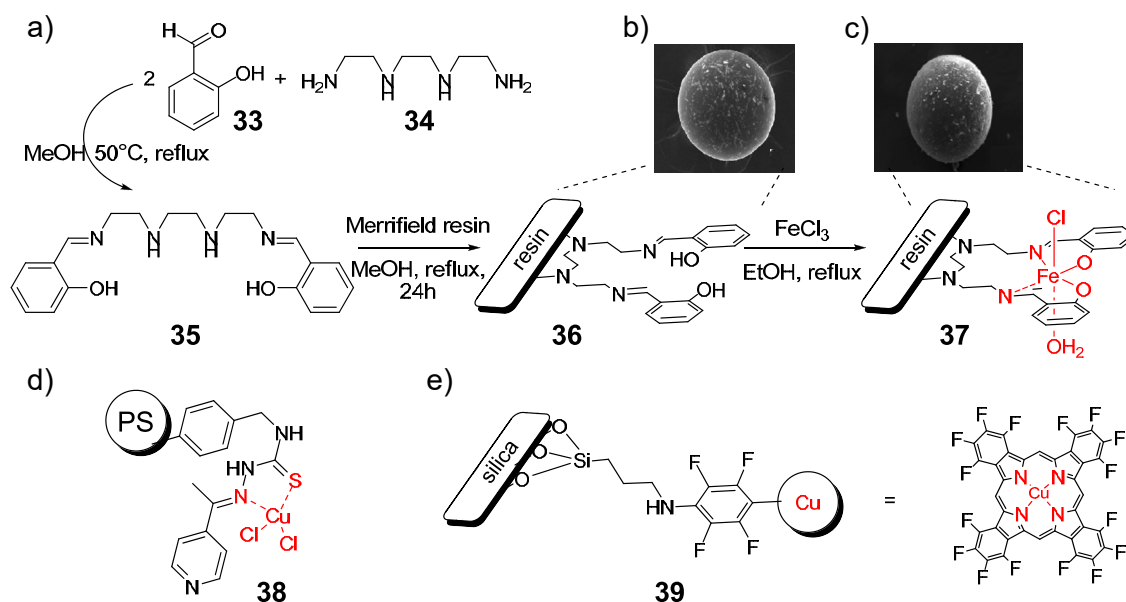
Figure 14. Iron and copper immobilization. a) Synthesis of the polystyrene (PS) anchored Fe(III) complex **37** and b, c) of the corresponding SEM images (left: PS-anchored ligand; right: PS anchored Fe(III) complex (reprinted with permission from ref. [417]). d) PS anchored Cu(II) complex **38**,[418] e) silica supported Cu(II) complex **39**.[419]

The activity of the zeolites (e.g. NaX, NaY, KL etc.) strongly depends on their composition. The catalysts showed activity with H_2O_2 and O_2 as oxidizing agents suggesting a combination of electrophilic haloperoxidase- and radical halogenase-like mechanisms.[441] However, the impregnation of zeolites with iron bipyridine complexes suppressed this activity (Table 7, entry 50), but the deposition of iron or copper salts (instead of coordination compounds) on inorganic supports yielded activities close to those for surface grafted transition metal oxides (Table 7, entry 51, 54).
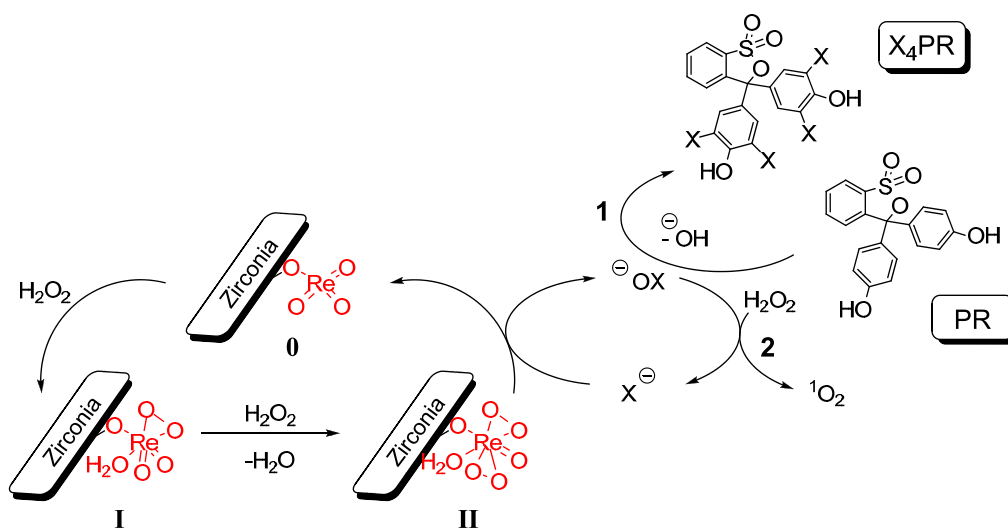
Figure 15. Hypothetic mechanism of the oxidative halogenation (X = Br) reaction of PR to X_4PR (1) catalyzed by Re/m-ZrO$_2$ (0-II) and side reaction (2) yielding O$_2$ (scheme in analogy to [399]).

Although rhenium and rhodium compounds showed oxidative bromination activity in homogenous reactions, only rhenium-promoted mesoporous zirconia has shown this activity under heterogeneous conditions (Table 7, entry 55).[399] Catalysts with the highest Re loading (up to 0.67 wt%) calcined at moderate temperature (630°C) have demonstrated the highest activity. SA values higher than those of the respective support material and mesoporous zirconia containing tungsten as active agent have been determined (Table 7, entry 55 and entry 4).[399] Re-assisted chlorination of phenol and iodination of phenol red has been reported as well.[399] The recyclability of the catalyst (four cycles) has been explained by Re-O-Zr condensation. Figure 15 illustrates the proposed, V-HPO-like mechanism involving Re-peroxo groups.

1.8   Supported Biomimetic Non-Transition Metal Catalysts

Besides transition metal compounds, metal-free systems have been reported as heterogeneous oxidative bromination catalysts as well. Surprisingly, the haloperoxidase-like activity of selenium and tellurium compounds is not limited to homogenous reactions.[272] Organo-Se or -Te complexes stabilized in silica gel ("xerogel") display oxidative bromination activity for the substrate 4-pentenoic acid (Table 7, entry 56, 57).[420,442] The product 4,5-dibromopentanoic acid can be cyclized subsequently to the corresponding bromolactone (Figure 16a). Notably, this bromolactone bears structural analogies to the natural AI-antagonist bromofuranone (cf. Figure 6 and Table 5, entry 6), but the potential antifouling qualities and the opportunities as a new potent natural-analogue dye have not been further explored. The covalently modified xerogel has been synthesized *via* nucleophilic substitution of a chlorine substituted silica precursor by diphenyl ditelluride or diphenyl diselenide, respectively (Figure 16a).

The proposed mechanism of the oxidative halogenation is shown in Figure 16b,c. Detty and coworkers[442] have suggested different oxidic forms of organotellurides and – selenides to be involved. Depending on the reaction with hydrogen peroxide, telluride is oxidized to tellurium oxide with subsequent hydration to dihydroxy tellurane (A). Hydroxytelluronium (B) and the halotelluronium species (C) have been assumed to be the catalytically active species in the two-electron oxidation of the halide (e.g. bromide). Organoselenides have shown a different mechanism and form hydroxy-perhydroxy selenanes (D) with hydrogen peroxide. Oxidized halide species are released subsequently or the halide exchanged compound (E) is formed.[442] A loss in activity has been observed after recycling (up to four times) due to a subsequent nucleophilic (Nu) attack at the Se/Te centers.[442] This leads to the formation of phenylchalcogenic acids (Nu = H_2O_2/OH^-) and phenylchalcogenic chloride (Nu = Cl^-) (Figure 16c) which might contribute to the oxidative bromination activity in solution. Cyclic ketones and lactams[421] or (hetero)aromatics[422] have been brominated with sodium bisulfate or sulfonated silica (Table 6, entry 58, 59) as Brønsted acids, *N*-bromosuccinimide (NBS) instead of bromide and H_2O_2 as oxidant. Zeolite (HZSM-5) bound NBS as "hidden" bromine source allowed bromination of aniline in CCl_4.[443]
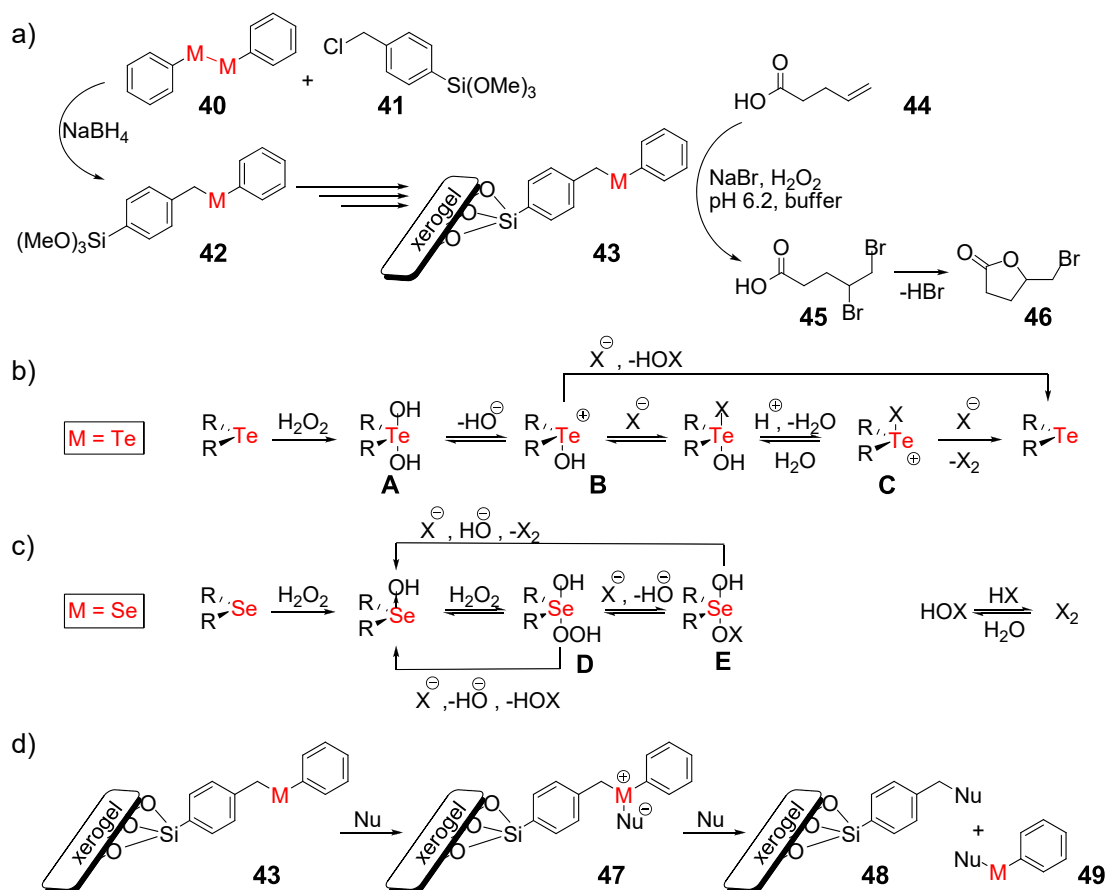
Figure 16. Chalcogenide xerogels. a) Synthesis of chalcogenide xerogel (M = Se or Te) **43** and the oxidative bromination of 4-pentoic acid **44** to bromofurane **46** with modified xerogel **43**. b, c) Proposed Se and Te intermediates, and d) proposed inactivation mechanism of the xerogel **43** (Nu = e.g. H_2O_2, OH, Cl). Illustration adapted from ref. [420,442].

1.9 Transition Metal Oxides as Heterogeneous HPO/HG-like Nanozymes

In analogy to vanadium containing enzymes and complexes, vanadium pentoxide (V_2O_5) is an active catalyst for the regioselective oxidative halogenation, specifically bromination[424,444] and iodination[425] of aromatic compounds even in the absence of acids (Table 6, entry 60–62).[423] The SA value of the *o*-cresol conversion is comparable to the highest values reported for immobilized enzymes. Regioselectivity is promoted by the substrate (charge-donating and/or steric hindrance) and depends on the source of bromide. For example, tetrabutylammonium bromide (TBAB) can stabilize Br_3^- species during the reaction.[423] Peroxovanadium(V) species have been believed to be the active species in the oxidation reaction of bromide. Subsequently, Rothenberg and Clark[444] have optimized the reaction conditions with respect to total costs, waste, risk and hazard factors

and have shown that HBr or Br_2 could be replaced by halide salts under acidic conditions. Strong acids as co-catalyst enhance the catalytic activity of V_2O_5 within the formation of active Br^+ species and the disproportionation of H_2O_2. Although the total costs, the amount of waste products, the required halide salts and acids are favorable for technical applications, increasing environmental and ecological awareness demand for non-toxic and sustainability solutions. In contrast to bulk metal oxides, nanomaterials are much more reactive because of favorable surface/volume ratio and optimized surface energies.[445] Different kinds of point or extended defects, intentionally or unintentionally introduced into the lattice, determine not only nucleation and growth, but specifically their chemical reactivity as well as their electrical, optical, and mechanical properties.[446] Notably, surface defects of metal oxides are the key to heterogeneous catalysis.[447] This is illustrated by the haloperoxidase-like activity of highly defective vanadium pentoxide nanowires[424] and cerium dioxide nanorods.[227]

V$_2$O$_5$ nanowires have SAs comparable to those of bulk V_2O_5 in bromination reactions. They show, however, catalytic activity even for micromolar H_2O_2 concentrations in phosphate buffer at neutral pH or even in seawater at ambient temperature (Table 7, entry 61), where bulk V_2O_5 is inactive.[424] Based on the kinetic parameters and the crystal structure, a surface-bound η^2-peroxo group has been proposed as transient active species in harmony with the proposed reaction mechanism for V-HPOs (Figure 17).[424]
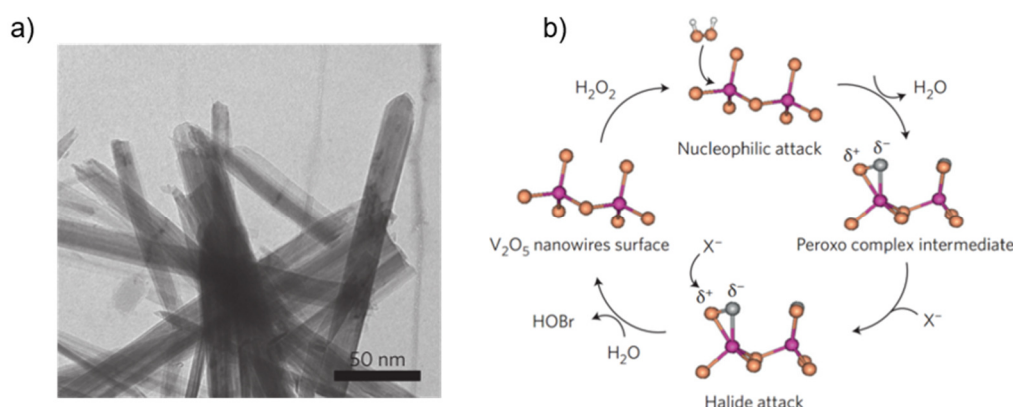
Figure 17. V_2O_5 nanowires. a) TEM image of V_2O_5 nanowires.[424] b) Proposed catalytic oxidative bromination mechanism with V_2O_5 nanowires. Reprinted with permission from ref. [424].

Besides being active in oxidative brominations, V_2O_5 nanowires catalyze iodination reactions as well. Iodination of dopamine leads to the formation of melanin with SA and TOF values that are nearly two times higher than those of the native enzyme.[425]

The structure of the product and the proposed reaction mechanism are shown in Figure 18. The synthetic biopolymer is analogous to the natural fibrillar and porous structure with spherical domains and diameters of ≈ 50 nm. The mechanism has been suggested to be based on the catalytic formation of hypoiodite/hypoidous acid (HOI) catalyzed by V_2O_5 nanowires. Dopamine is oxidized by the hypoiodite intermediate and undergoes subsequent cyclization, iodination and radical polymerization. The planar rings assemble to nanoplates *via* π-stacking and finally aggregate to clusters and filamental biopolymers.
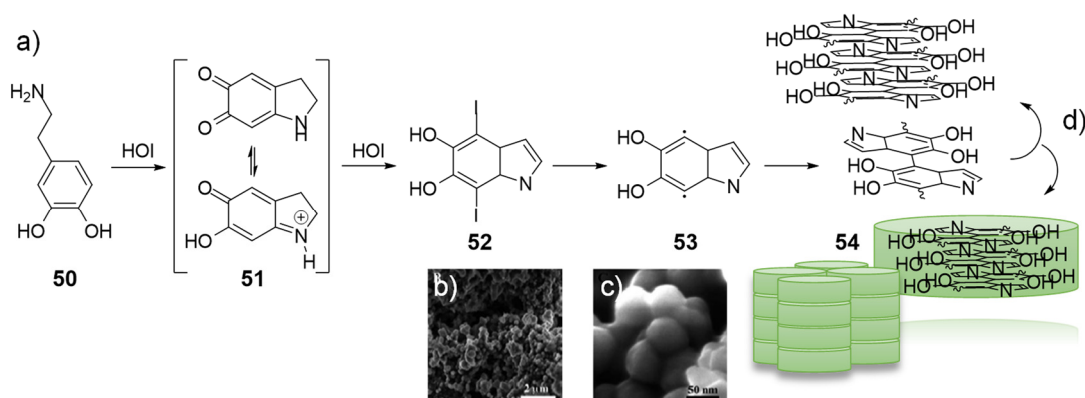
Figure 18. Oxidative iodination catalyzed by V_2O_5 nanowires. a) Proposed formation mechanism of melanin-like biopolymer **54** catalyzed by V_2O_5 nanowires, KI, H_2O_2 and dopamine.[425] b, c) SEM image displaying the fibrillary and porous structure of the spherical domains (diameter of $\approx$ 50 nm). d) Proposed structure of the resulting melanin-like biopolymer **54**. Reprinted with permission from ref .[425].

Although V_2O_5 is a potent haloperoxidase-like catalyst, the serious shortcomings for everyday applications are its toxicity and possible carcinogenicity under REACH safety criteria. This will retard the applications on a technical scale. In addition, the formation of soluble POMs leads to long-term leaching.

Nanocrystalline cerium dioxide (nano-ceria) is a viable alternative. From classic work on oscillating reactions, the Ce^{4+}/Ce^{3+} redox couple is known to catalyze the halogenation of malonic acid in the Belousov-Zhabotinsky reaction.[310] Furthermore, CeO_2 has been reported to be active in halogen exchange reactions and the O_2-dependent halogenation (oxyhalogenation) of methoxybenzenes (Table 7, entry 64).[427] These reactions have been carried out between 100 and 140°C in organo-halide solvents that simultaneously served as halogen source. A plausible mechanism has been proposed to be based on the redox potentials of the Ce^{4+}/Ce^{3+} (1.72 V), $Cl_2/2Cl^-$ (1.36 V), $Br_2/2Br^-$ (1.09 V), and $I_2/2I^-$ (0.54 V) redox couples, while fluorination is not possible ($F_2/2F^-$: 2.87

eV).[427,448] The halogenation proceed slowly under anaerobic conditions and can be accelerated in the presence of molecular oxygen (6 bar).[427] Ce^{3+} is re-oxidized under aerobic conditions (Figure 19b), and the oxidative halogenation reaction is stopped by radical scavengers. Reactions with acetylated arenes and substitution reactions with deuterated starting compounds have shown an inverse kinetic isotopic effect for chlorine and iodine which is typical for electrophilic aromatic substitutions.

The basic sites of nano-ceria facilitate a heterolytic cleavage of the organic halide. Subsequently, the halide anions are oxidized *via* single electron transfer reactions to the corresponding active hypohalous species. The halogenated end product is generated by electrophilic aromatic substitution (*via* σ-complexes/ Wheland intermediates). The proposed reaction mechanism is illustrated in Figure 19b.[427] The reaction can be described as a combination of an O_2-dependent halogenase and haloperoxidase-like mechanism. Particle size, surface area and morphology are very important, as bulk ceria or iron(III) oxide have not shown any activity. The exposed crystal planes determine the reactivity in the order cube < octahedra < nanorods.[427,449] The catalyst is inactivated by substitution of oxygen by halide in the CeO_2 structure (indicated by a color change from pale yellow to orange).[427,449] Another shortcoming of using molecular oxygen as oxidizing agent is the formation of volatile side products such as methanol and methyl bromide.[427,449]
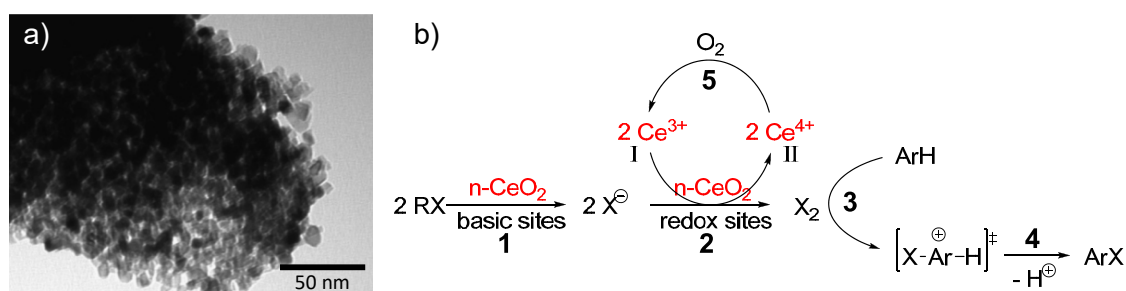
Figure 19. O_2-dependent halogenation reaction catalyzed by nanoceria. a) TEM image of ceria nanoparticles (diameter ≤ 10 nm). b) Proposed mechanism of the O_2-dependent halogenation reaction of electron-rich aromatic compounds (ArH) catalyzed by ceria nanoparticles (n-CeO_2) and organic halides (RX, X = Cl, Br, I). The basic sites of n-CeO_2 aid in the decomposition of the organic halide (1). The redox sites allow the oxidation by one-electron transfer reactions (2). The X_2 species oxidize the arenes *via* Wheland intermediates (3, 4). The catalyst is reactivated by O_2 (5, I-II). TEM image reprinted with permission from ref.[427].

The activity of nano-ceria has been extended from O_2-dependent halogenase-like to more controllable H_2O_2-dependent haloperoxidase-like reactions. Cerium dioxide nanoparticles have been shown to be functional mimics of halogenating enzymes in aqueous

media containing halide anions as halogen source, hydrogen peroxide instead of O_2 as co-oxidant, and phenol red as substrate.[227] The oxidative bromination reaction of phenol red to bromophenol blue allows a comparison with native enzymes and an analysis of the reaction kinetics to derive a reaction mechanism. The reaction follows a pseudo-third order kinetic (in total, Equation 14) with k_{gen} as general reaction constant, and $[S]$ and $[S]_0$ as substrate and initial substrate concentrations. Other specific kinetic parameters were determined by Lineweaver-Burk analysis.[227]

$$v = \frac{d[Br_4PR]}{dt} = k_{gen}[CeO_{2-x}]_0[NH_4Br]_0[H_2O_2] \qquad 14$$

Even for very low catalyst and substrate concentrations (25 µg mL^{-1} catalyst, 300 µM H_2O_2 and 25 mM halide salt, Table 7, entry 65) comparable to those being available for marine haloperoxidases in natural environments, CeO_{2-x} nanorods have shown a catalytic activity comparable to that of immobilized enzymes (Table 7, entry 2 and 65). The activity and the reaction rate can be increased by adjusting the reaction conditions, particularly, increasing the temperature and the concentrations of H_2O_2 and bromide and by increasing the defect density on the catalysts surface.[227] A radical mechanism has been proposed for the formation of halogenated ROS based on experimental data and calculations with high level methods,[227] which highlights the key role of Ce^{3+} and the Ce^{3+}/Ce^{4+} ratio. By virtue of the Ce^{4+}/Ce^{3+} redox potential, cerium can reversibly switch between its tetra- and trivalent states. As a result, ceria is non-stoichiometric with oxygen vacancies in the fluorite lattice.[227] Trivalent Ce^{3+} is associated with reactive defect sites in the CeO_{2-x} structure, which are suggested to be located preferentially at the particle surface (as anticipated from the ionic radii and demonstrated by XPS measurements).[227] A Ce^{3+} defect density of ≈ 0.5 wt% has been determined from magnetic susceptibility measurements. The proposed radical process contrasts with the mechanism suggested for vanadium, tungsten or rhenium compounds involving metal-η^2-peroxo-intermediates, but it is in accordance with the mechanism suggested for some natural heme-containing haloperoxidases.[141,143,450] The difference in the active halogen species (X_2[427] or HOX[227]) may be related to the co-oxidant. The degradation of celestine blue (CB) shows HOX to be the dominant species.[227]

Ceria nanorods preferentially expose their (110) facets. Quantum chemical calculations have been performed at various levels of theory (periodic calculations at the generalized gradient approximation– density functional theory (GGA-DFT) level together with calculations of small finite model compounds at the metahybrid-DFT level) including hydration (Ce^{4+} - OH^- and Ce^{3+} - H_2O coverage, Figure 20a, b). The results support the experimental findings on HOBr generation at Ce^{3+} defect sites in a radical reaction and the release of HOBr being the rate limiting step. This is compatible with the finding that natural antioxidants (like cysteine and ascorbic acid) slow down the reaction.[227]
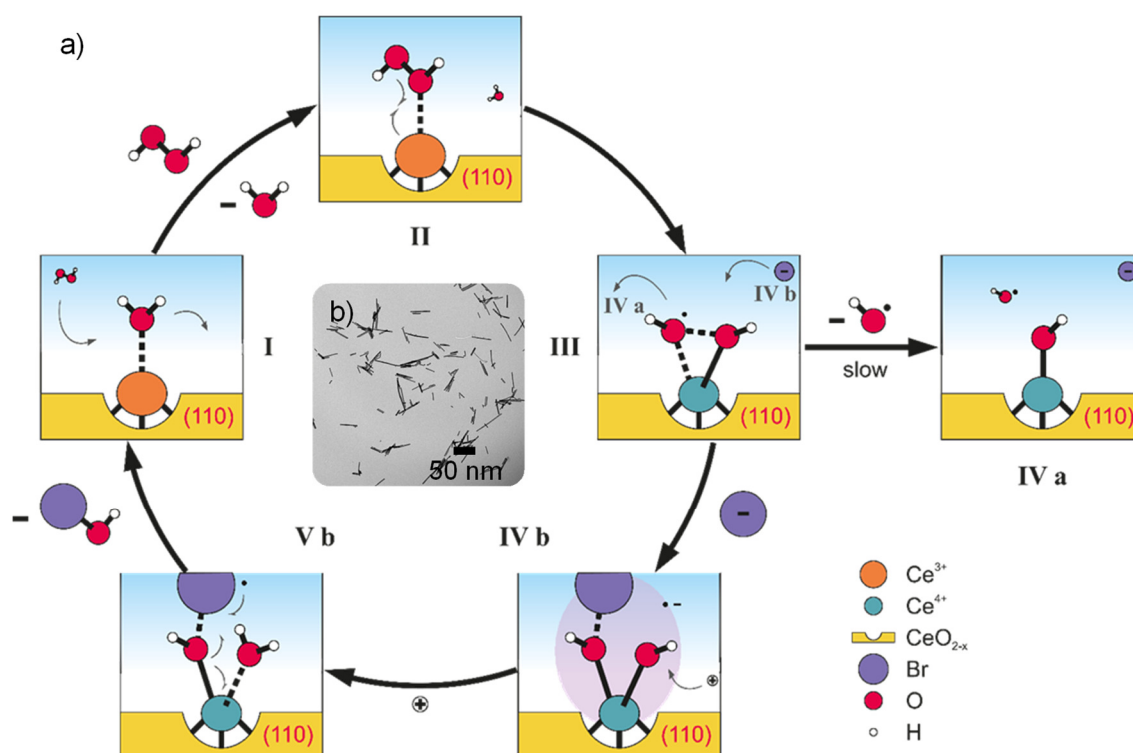
Figure 20. H_2O_2-dependent halogenation reaction catalyzed by nanoceria. a) Proposed catalytic bromination mechanism of the CeO_{2-x} nanorods. On a (110) model surface (I) the H_2O ligand can be exchanged against H_2O_2 (II) With a Gibbs free energy change ($\Delta G°$) close to zero this exchange is unlikely for low H_2O_2 concentrations. However, the exchange itself is favorable ($\Delta G°<0$) and becomes fully irreversible (more negative $\Delta G°$) for a (partial) dissociation of H_2O_2, which leads to an oxidation of the Ce^{3+} site with OH^- anion and $OH^•$ radical ligands (III). These two groups are bound to each other through a weak two-center three-electron bond. As both Ce-O distances in this species are essentially equal, the description involves two mesomeric boundary structures to account for the actual chemical bonding. A release of an $OH^•$ radical from this species into solution may occur, but it represents a step "uphill" in Gibbs free energy and is therefore slow (IVa). A Br^- anion can add to one of the O atoms to form to species which is best described as an anionic surface site (with two hydroxide ligands) where one of the OH^- anions interacts with a $Br^•$ radical (IVb). The other, non-interacting OH^- anion is protonated to restore a neutral surface site (V). Dissociation of the HOBr product finally regenerates the initial Ce^{3+} site (I). Although the final step is associated with a positive $\Delta G°$, it occurs because (i) the back reaction is energetically uphill as well and (ii) the concentration dependence of ΔG (= $\Delta G°+RTlnK$) makes ΔG favorable for low HOBr concentrations. b) TEM image of ceria nanoparticles. Reprinted with permission from ref. [227].

Marine haloperoxidases catalyze the halogenation of organic substrates *via* reactive HOBr intermediates. This leads to an inactivation of the bacterial signaling compounds. CeO_{2-x} nanorods emulate this reaction by catalyzing the conversion of bromide ions to reactive HOBr intermediates that target natural signaling compounds associated with bacterial quorum sensing and biofouling. This has been demonstrated for the bacterial signaling molecule 3-oxo-hexanoylhomoserine lactone (OHHL 19, a 3-oxo-AHL, Figure 21) which is halogenated to the mono- and di-brominated lactones within 30 – 150 min under ambient conditions with H_2O_2 and KBr as bromide source. The formation of the brominated lactone has been demonstrated by HPLC combined with mass spectrometry.[227]
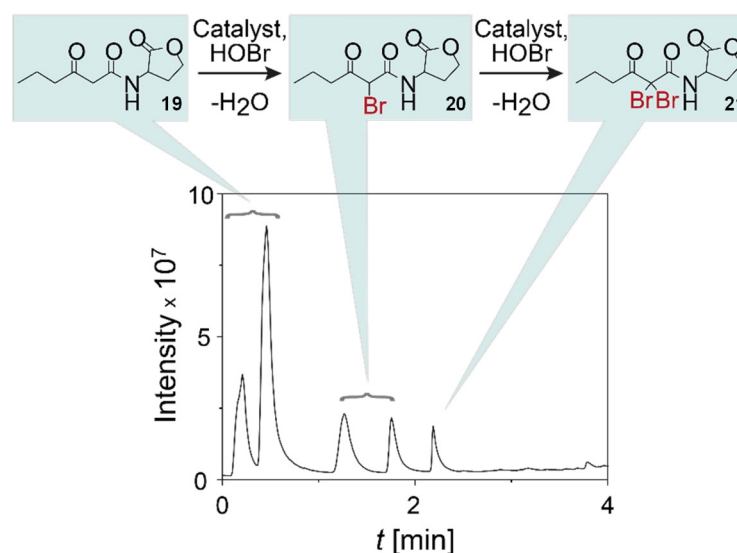
Figure 21. Oxidative bromination of signaling molecules. CeO_{2-x} nanorods catalyze the oxidative bromination of 3-oxo-hexanoylhomoserine lactone (OHHL **19**) to 2,2´dibromo-3-oxo-hexanoylhomoserine lactone **21** identified by HPLC/ESI-MS. The halogenated products are assigned to their specific signals in the total ion chromatogram. Reprinted with permission from ref. [227].

Additionally, sulfated ceria-zirconia (especially $SO_4^{2-}/Ce_{0.07}Zr_{0.93}O_2$) is a potent iodination catalyst. Phenol, aniline and their derivatives have been oxidatively halogenated by I_2 in PEG -200 resulting in high product yields (up to 97 % iodoaniline after 24h).[451] The activity has been attributed to the large surface area, the number of acidic sites and their acidity. Similarly, benzylic compounds such as dimethoxybenzene (DMB) are iodinated with I_2, H_2O_2 in the presence of ceria nanorods in high yields (up to 97 %, 0.5 h, mono-iodination),[426] but temperatures of 100°C and an excess of H_2O_2 are needed.

A Fenton-like decomposition of H_2O_2 at Ce^{3+} centers has been proposed (Figure 22), as the presence of hydroxyl radicals is demonstrated by electron paramagnetic resonance (EPR) spectroscopy with the spin trap agent 5,5-dimethyl-pyrroline N-oxide (DMPO). Four characteristic signals (ratio of 1:2:2:1) of the DMPO-OH spin adduct have been observed at $334.6 - 335.0$ B_0/mT and g-value of 1.992. Further EPR analysis has revealed that a decrease of the pH lead to an increase of the EPR response correlating with the amount of OH radicals. The pH required for oxidative iodination is lower than for bromination (pH ≤ 3.0[426] *versus* pH ≤ 7.0[227]). Increasing the pH to values ≥ 6.0 results in hydroxylated rather than iodinated products only (e.g. for benzene[426]).

Computational studies have suggested a stepwise reaction mechanism with four different iodine compounds[426] and iodites (I^+) as key species. A stepwise oxidation of one iodine molecule (I_2) to two HOI molecules that are involved in the actual oxidative iodination step (Figure 22) has been proposed. The electrophilicity of HOI is not sufficient to promote iodination, but protonation to H_2OI^+ under acidic conditions increases the reactivity and drives the reaction.[426]
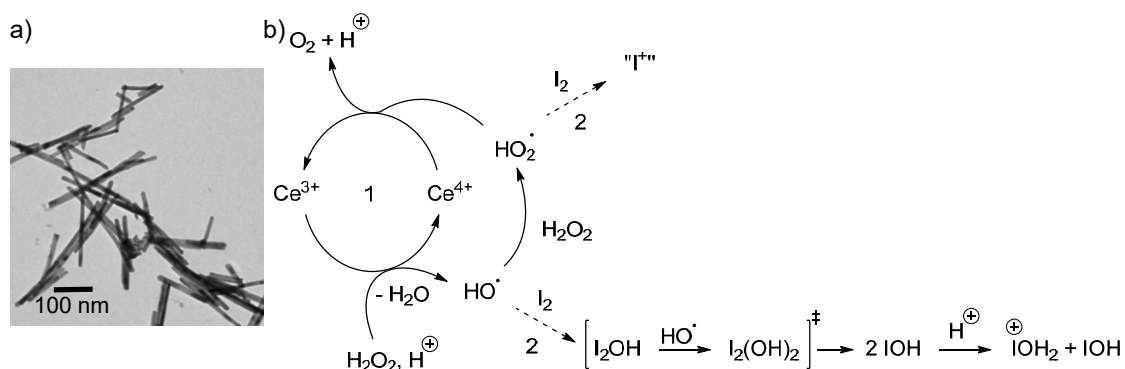
Figure 22. Oxidative iodination catalyzed by nanoceria. a) TEM image of ceria nanorods for oxidative iodination. Reprinted with permission from ref. [426]. b) Proposed formation mechanism of oxidized iodine species ("I$^+$") by a Fenton-like activity of $Ce^{4+/3+}$ (reaction 1). Hydroxyl radicals are formed by one-electron transfer reaction and oxidize I_2 *via* hydroxyl-iodite transition states (I_2OH, $I_2(OH)_2$), IOH. IOH is protonated in strong acidic media to the reactive species H_2OI^+ (reaction path 2). Singlet oxygen can be formed in side reactions with excess H_2O_2.[426]

1.10 Antimicrobial and Antifouling Agents

Enzymes are used in a variety of industrial applications and processes, including the food and beverage, textile, detergent or medical industries. Enzymes screened from natural origin are often engineered before entering the market place because their native forms do not meet the requirements for industrial application. Protein engineering is performed to design and construct new enzymes with tailored functional properties, including stability, catalytic activity, reaction product inhibition and substrate specificity.[362]

Haloperoxidases and halogenases can open environmentally benign routes to synthetic halogenated compounds for basic and materials science and are therefore useful in technical processes for organic synthesis, biosensing or as antifouling agents.[360,452,453] HOX formation is a key step in the synthesis of halogenated natural products[363,365,454] and precursor compounds for coupling reactions of the Sonogashira, Suzuki, Grignard or Wittig type.[455–457] The oxidizing properties of HOX can be used for the regio and enantioselective oxygenation of substrates,[69,105,458,459] oxidative cyclization, epoxidation[124] or sulfoxidation reactions.[256]

Currently, heme iron enzymes[69] are used depolymerization processes to obtain synthetic fuel.[460] Similarly, the bio-catalysis of sulfoxidation might find potential applications in the desulfurization process of diesel fuel,[461] and enzymatic biosensors with high selectivity and sensitivity are being developed.[462] Oxidative halogenation can be used for the chromogenic detection of halide[71,463–465] or peroxide contaminations.[466,467] With isotope-labeled substrates[130] HPOs allowed identifying the unknown origin of environmental or samples using isotope analysis.[130]

In addition, HPOs, H_2O_2, and halide constitute potent antimicrobial systems whose cytotoxic effect and antitumor properties have been demonstrated.[468–470] HPOs are involved in the synthesis and post-modification of many natural products and their analogues that proved to be potent drugs with anthelmintic, anti-inflammatory or antimicrobial activity.[74,76,365,471–481] Brominated cyclized sesquiterpenes,[482] acetogenin and antiviral compounds like thyrsiferyl acetate (protein phosphatase inhibitor) can be synthesized.[124,454] Bacteria and viruses might even be inactivated with a resistant mutant of vanadium chloroperoxidase.[483]

A series of reviews[73,74,77,78,123,207,471,484–487] and special journal series[76] highlight the pharmaceutical use of HPOs. By improved protein engineering methods, HPOs have

been modified genetically to be more effective at desired temperatures, pH or other manufacturing conditions that are detrimental to the enzyme activity otherwise (e.g. harsh chemicals). This makes them suitable and efficient for industrial and even home applications. Still, as heterogeneous catalysts nanoparticle enzyme mimics are easy to recover, to recycle[488] and may facilitate processes and reduce costs by replacing enzymes in mass applications, where these factors are essential.

Halogenating enzymes have proven useful in generating HOX and ROS species. The inactivation of spores, viruses and bacteria[66] by HPOs and HGs is a prime goal for their use as surface disinfectants,[489] sterilizing agents in laundry[490] with antimicrobial and bleaching properties, in industrial wastewater treatment[491] and on mammalian skin.[65] Barnett and coworkers have already filed a patent on the use of recombinant HPO as an antimicrobial agent in 1995,[158] and, more recently, HPOs have been established as disinfection agents in organic matrices.[483,492] The colonization of microorganisms that serve as food supply of higher organisms on surfaces exposed to water causes massive problems in the domestic, industrial, medical and marine sectors.[493] Thus, the development of antimicrobial coating systems is a challenging and outstanding example for the application of HPO mimics.

Microbial biofilms are ubiquitous in flora and fauna, and all structures and interfaces in contact with natural water suffer from biofouling due to the colonization of bacteria and aquatic organisms.[494] Figure 23 illustrates the process of marine biofouling at an interface exposed to seawater. In the first step, small adsorbed organic molecules like proteins and polysaccharides form a "conditioning film" as basis for the settlement and colonization of microorganisms (I), bacteria (II) and plants (IV). Within minutes the process becomes irreversible when the attachment of the bacteria to the surface is enhanced by extracellular adhesion molecules and polymers (III).
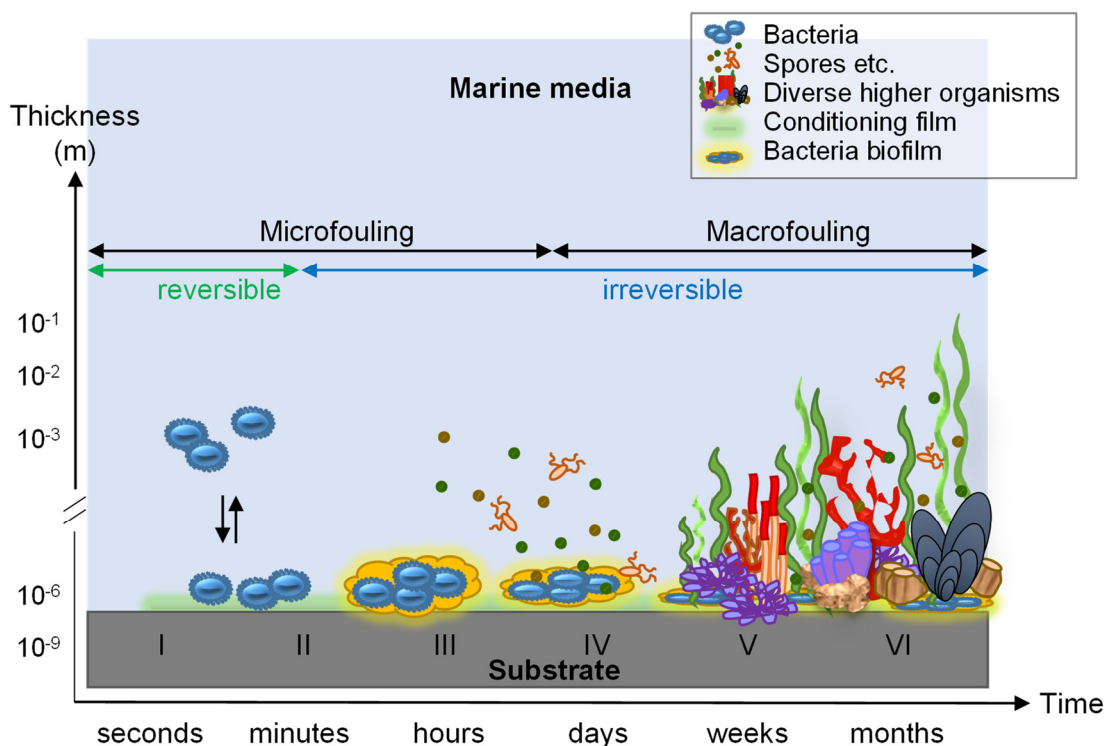
Figure 23. Model of the fouling process. (I) Conditioning film of adsorbed small organic/inorganic particles. (II) Reversible adhesion of bacteria. (III) Bacterial biofilm formation by covalent linkage due to expressed, extracellular adhesion molecules and polymers. (IV) Microfouling: slime formation *via* the incorporation of spores, germs and larvae of higher organisms (diatoms, barnacles, algae). (V, VI) Macrofouling: settlement and growth of soft foulers (green/brown/red macroalgae, tunicates, sponges, anemones) and hard foulers (barnacles, tubeworms, bryozoans, mussels). Adapted from ref. [495–497].

The term "biofilm" describes the covalent adhesion of unicellular microorganisms through interactions with the surrounding, e.g. *via* nutrient supply cycles. The biofilm formation improves the accessibility and attractiveness for the deposition of spores, germs and larvae of higher organisms yielding a slimy layer (IV). Subsequently, higher multicellular organisms like macroalgae or tunicates (soft foulers) grow dynamically out of the slime. Macrofouling (V) proceeds and animals with exoskeletons (hard foulants) can settle (VI).[495–497]

Biofilm formation is a major concern for applications ranging from biomedical implants, devices, food packaging to industrial and marine equipment.[498] Marine facilities, bridge piers, naval vessels, offshore wind parks and ship hulls are particularly affected, which leads to great economic losses.[140,425,452,453,494,498–500] Modern ship coatings aim to to minimize hull roughness owed by biofouling, because an increased roughness leads to increased drag, higher fuel consumption and increased greenhouse gas emis-

sions.[498,501,502] Current chemical antifouling coatings release copper and other co-biocides[497] including organic booster biocides like copper pyrithione[502] to impede the settlement, colonization and destruction of the metal surface by marine organisms.[503] Most biocides are harmful to the submarine world in general.[504,505] The usage of the organic biocide Irgarol® (cybutryn) has been prohibited 2016 in the course of the biocide-directive 98/8/EC[506] and the European implementing decision 2016/107.[507] Cybutryn has been banned because its degradation products have shown an increased persistence and toxicity compared to the starting compound.[506,508,509]

The re-evaluation of biocides is based on the impact assessment of the review of priority substances under directive 2000/60/EC and will affect all biocides on the market.[510] Therefore, a growing demand challenges scientists all over the world to develop economic, ecological and effective antifouling materials and coatings.

1.11 Biomimetic Antimicrobial and Antifouling Solutions

Following Nature's defense strategies against epibiont growth, physical and (bio)chemical antifouling strategies[495–498,501–503,511–516] have concentrated so far on engineered microtopographies ("sharkskin-effect"),[162,163] superhydrophobic[517] or superhydrophilic[495] surfaces, electrochemical defense,[518] natural product antifoulants,[519,520] and enzyme-based coatings.[503] Physical methods affect the interaction of marine fouling organisms with artificial surface topographies.[163,497]

An "unattractive" surface has only a loose connection to early stage foulers (phase I, Figure 23). The subsequent removal of bacteria is enhanced by flow mechanics and conditions,[163] and a mechanical surface cleaning is facilitated.[521] Silica-based protective coating formulations (e.g. *AquaFast* formulation) reduce the strength of biofilm adhesion after ≈ 7 weeks in a static immersion test in salt water (Melbourne, Florida, Figure 24).[521] A grooming process yields an almost clean coating.

Substrates under static conditions, e.g. in ship piers etc., suffer from instant fouling while cleaning is hard to manage. Once the biofilm has formed, other organisms will follow. Fouling of static marine structures such as oil production platforms, drilling rigs or wind parks from seaweed, barnacles, mussels etc. is prevented by securing a coated flexible sheet material (basalt or silicone rubber) to the underwater surface of the marine structure.[522] A flexible sheet material, useful as an antifouling cladding, is a fabric with

an outermost coated surface that consists of a silicone rubber/silicone oil mixture. It is produced by curing a room-temperature-vulcanizable silicone rubber with hydroxyl end groups in the presence of silicone oil.
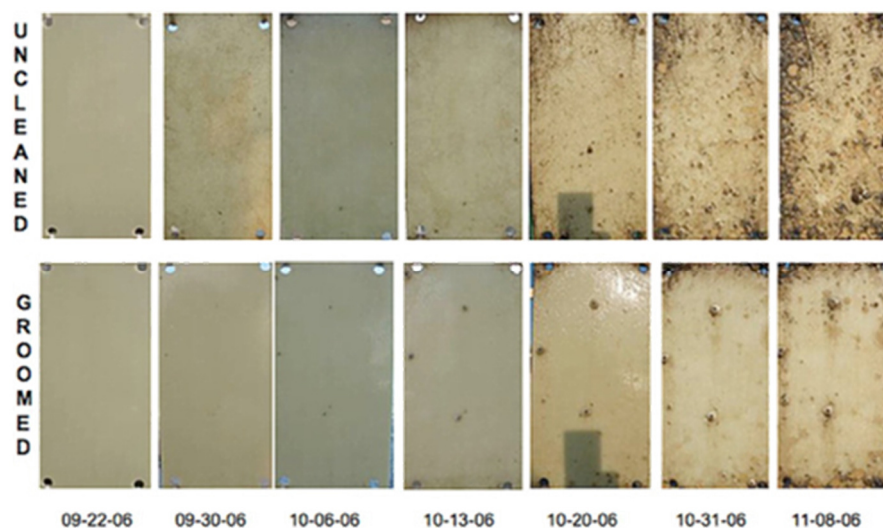
Figure 24. Static immersion test of a silica-based protective coating in salt water (Melbourne, Florida). The submerged, durable and smooth surface of the xerogel is resistant to strong biofilm adhesion. Reprinted with permission from ref. [521].

In an alternative approach, passive basalt filaments are applied as an antifouling coating fabric for flow around underwater surfaces. The fabric is fixed with adhesives on the substrate or the protected marine area. The basalt fabric may also be applied on the underwater surface by covering with tissues or ligaments or by braiding, where the surface of the antifouling coating is formed predominantly by free basalt fibers.[523,524] A related strategy is based on a hybrid pre-ceramic oxylane polymer, which has been designed to bind on the molecular level to bare-metal, hypalon, PVC, neoprene, painted, or gel-coated hulls of marine vessels and other marine structures to prevent the attachment and growth of barnacles and algae. The so-called gelcoat strategy works in a similar fashion. It consists of a two-part hybrid silicon-ceramic coating that infuses gelcoat with nano-particular ceramic-glass. The waxes, paints and polyurethane coatings (membranes) physically attach to the surface, while the nano-particle "glassifier" binds covalently to the gelcoat surface. This creates a mirror finish gelcoat that is self-cleaning, mold resistant, non-fading, non-skidding, hydrophobic. Moreover, it does not require any waxing.

Low Emission Antifouling Coatings

The basic concept in antifouling with biocide loaded coatings is a steady state release of biocides into the surrounding water that is required for preventing the settlement of marine organisms. Here, the antifouling activity is based only on the interaction between the biocide and fouling organisms on the coating. This scenario, however, does not properly describe the state of affairs on the paint surface during barnacle colonization, because there are synergistic effects between the embedded biocide in low concentrations and the mechanical properties of the coating. This has been demonstrated for preventing the deposition of barnacles. Low amounts (0.1 %) of the biocide Ivermectin embedded in a soft coating (similar as abrasive paint coatings) suppressed the attachment of adult barnacles completely, whereas no reduction in barnacle recruitment has been observed when Ivermectin is embedded in a hard polystyrene-derived coating.[525]

Both coatings suffer from initial fouling by settling barnacle larvae, but barnacle growth stopped after metamorphosis on the soft coating, although no difference in the biocide release rates has been observed (several ng/cm^2 per day). This shows that intoxication is triggered by the organism itself in contact with a coating containing an embedded biocide. Full biocide release is not indispensable because the reaction is shifted from the solid/water interface to the subsurface layers of the coating.

No Emission Antifouling Coatings

Nature has solved the problem of permanent constructions exposed to aqueous media by an active, biochemical defense strategy. Communities of bacteria can coordinate their behavior with three classes of signaling molecules that are used for communication within the organism to coordinate gene expressions to (i) generate adequate response behavior, (ii) signaling between the same or related species and (iii) signaling among different species. Bacteria can generate many different signal mediated interactions for different purposes with a limited number of molecules and a limited number of combinatorial rules. Bacterial sign-users share a set of syntactic rules to combine signs for a variety of interactional contexts (development, growth, mating, virulence, attack and defense, cf. Figure 5). The situational context of these interactions determines the signal semantics. The complementarity of these three levels of semiotic rules can be identified

in every sign-mediated interaction within and between organisms. This leads to the generation of intra- and intercellular processes that enable bacterial communities to generate memory. Stationary marine organisms like red and brown algae use this sophisticated and complex strategy against epibiont growth with a group of specialized enzymes that catalyze the synthesis of halogenated antifoulants or the oxidative halogenation of bacterial signaling compounds that prevent biofilm formation by interfering with cidal cell-to-cell communication[208] (*vide supra*). Thus, biofouling is defended at its lowest level, the microbial colonization.[166,184,204] Vanadium-dependent bromoperoxidases (V-BPOs) are the best-established group of enzymes.

Inspired by marine red algae, haloperoxidases[492,503] have been proposed as additives in antifouling paints more than 15 years ago.[71,158,202]Wever,[71] Barnett[158] and coworkers have filed patents for embedding native haloperoxidases in paint formulations to prevent biofouling.[71] Initial problems of enzyme stability and activity under non-physiological conditions are circumvented by making specially designed mutants.[146] "Biocoats" have been devised as new active hybrid materials based on a matrix or xerogel containing living microorganisms rather than pure enzymes. The bacteria produce antifouling substrates,[162] which extend the antifouling activity of the hybrid materials. However, the use of natural or recombinant enzymes or microorganisms raises the issue of production costs, long-term stability and the reaction conditions for proper activity.[259]

The use of haloperoxidase mimics in antifouling coatings is a low cost bioinspired alternative to overcome these shortcomings. Only a few, but promising HPO mimics have been developed in the laboratory and, more significantly, tested in the field. The use of modified xerogel coatings combines the physical and chemical antifouling characteristics[162,442] of porous silica coatings[521,526] with the haloperoxidase-like activity of the organo-selenium compounds.[442] Leaching has been encountered for phenylchalcogenic acids, and phenylchalcogenic chloride has been formed for low molecular weight organoselenium or tellurium compounds (Figure 16c).[420,442] This, however, turns into an advantage because active components can be released during the defense process.[420] A similar xerogel containing hydrogen peroxide and artificial sea water (ASW, with halides) has been successful as "hybrid" coating against the settlement of cypris larvae of the barnacle *Balanus amphitrite*, larvae of the tubeworm *Hydroides elegans* and of *Ulva zoospores*.[442] Hybrid titania/silica-derived xerogels impede the settlement of zoospores of the marine alga *Ulva linza* and sporelings (young plants) at pH 7-8 in the presence of

halides (bromide, chloride) and H_2O_2.[527] The activity of the xerogels (with Se or Ti) is connected to the haloperoxidase-like activity of the embedded compounds, more precise, to the formation of hypohalous acid in combination with a submerged, durable and smooth surface of the coating.[442,527] Lejars[497] and Nurioglu et al.[495] have presented a compilation of silica release coatings and their alternatives. The operating principle of active substances or particles incorporated in an antifouling device with haloperoxidase-like activity is shown in Figure 25. A variety of enzyme-like activities (e.g. peroxidase- and catalase-like) can be envisioned to impede biofouling.
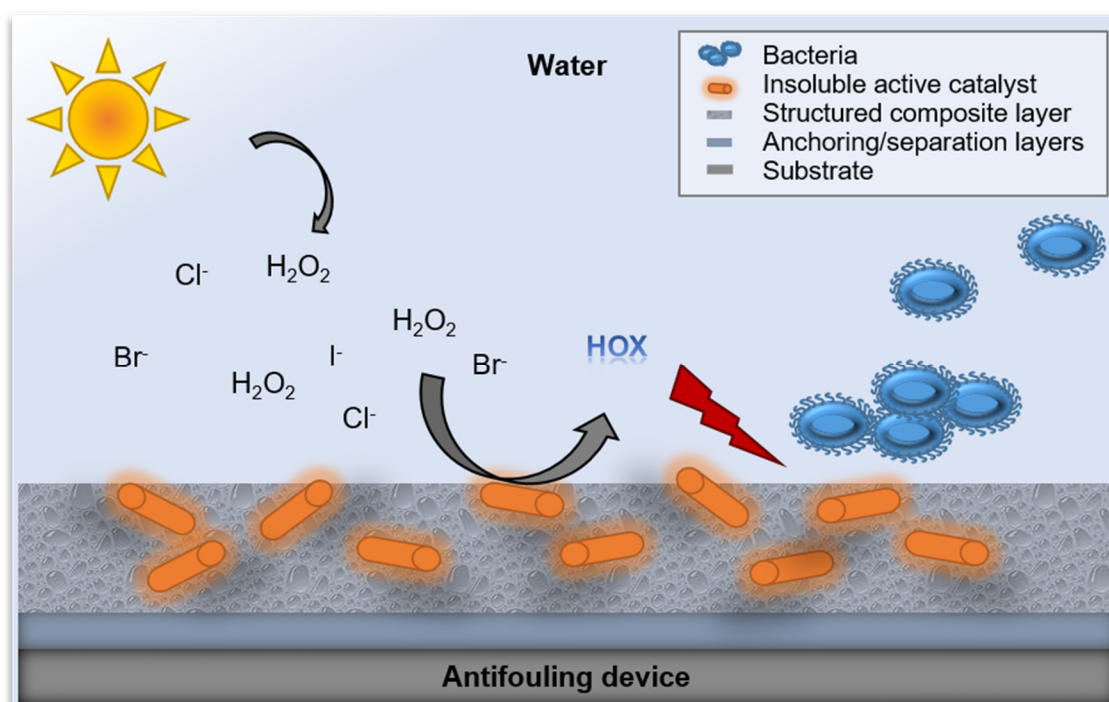
Figure 25. Sketch of antifouling formulation/device. The catalyst is incorporated in a porous matrix. In the presence of the haloperoxidase-mimic, HOX (X = Cl, Br, I) is formed that prevents fouling either through halogenation of signaling compounds or by direct oxidation. The substrates, bromide and hydrogen peroxide (formed under UV light) are present in water in the required (millimolar) amounts.

The illustration in Figure 25 is confined to HPO-like activity. An ideal antifouling formulation contains a durable biomimetic catalyst incorporated into an insoluble and stable, but porous matrix. The porosity provides sufficient surface area and allows mass transfer of hydrogen peroxide, halogenide and the substrate molecules. The products are released after the reaction and leave the catalysts in the matrix behind, where it can recover its activity. Besides haloperoxidase-like xerogels, several transition metal oxides

have shown oxidative bromination activity.[227,397,398,424,528,529] Many haloperoxidases employ vanadium(V) as cofactor, but molybdate(VI) shows higher catalytic activity towards halide oxidation in solution compared to vanadate(V). Density functional calculations have revealed that the oxodiperoxo species $[MoO(O_2)_2L]$ is catalytically more active than the dioxo-monoperoxo species $[MoO_2(O_2)L]$. Going along with that, the spatial environment of the V-HPO active site is tailored to a monoperoxo species. However, the reason for the inactivity of a hypothetical molybdenum bromoperoxidase might be that no peroxo species is formed in the first place because of the endothermic reaction with H_2O_2.[530] Still, oxides of molybdenum and tungsten exhibit excellent antimicrobial properties. Microbiological roll-on tests with *Staphylococcus aureus*, *Escherichia coli* and *Pseudomonas aeruginosa* have shown exceptional antimicrobial activities for anhydrous samples with large specific surface areas.[531–533] The proposed antimicrobial mechanism for transition metal oxides is based on local acidity, as supported by the identification of molybdenum oxide nanostructures with $Mo(=O)_2OH$ units by *in situ* Raman spectroscopy.[534] One might speculate that a haloperoxidase-like reactivity contributes to the observed antimicrobial properties of MoO_3 and WO_3, as indicated by antifouling steel surfaces after electrodeposition of nanoporous tungsten oxide films. The antimicrobial ability of these films has been demonstrated for modified naval construction steels and surgical instruments that have shown reduced marine algal film adhesion, *Escherichia coli* attachment and blood staining.[535]

The ability of V_2O_5 and CeO_{2-x} to emulate nature's chemical defense strategy against predation and epibiont growth has been demonstrated in the laboratory and in the field. V_2O_5 nanowires and CeO_{2-x} nanorods reduced bacterial adhesion and algal growth in hard (smooth) and soft (porous) paint formulations containing small amounts (2 wt%) of the metal oxide. Cultures containing the enzyme mimics, V_2O_5 or CeO_{2-x}, and both substrates, bromide and H_2O_2, showed virtually no bacterial colonization compared to controls. The bromination mechanism differs significantly for both oxides: Whereas the reaction for V_2O_5 involves a surface-bound η^2-peroxo group as for vanadium-dependent haloperoxidases, the halogenation *via* CeO_{2-x} follows a radical mechanism as observed for iron-heme haloperoxidases. Both metal oxides showed reduced algal growth in field test. Figure 26 shows test plates containing 2 wt% of V_2O_5 after immersing in the Atlantic Ocean in Portugal (stationary at a boat hull for 2 months) and with 2 wt% of CeO_{2-x} after immersing in the Maas in Belgium (stationary, at a boat pier, 2 months). Both examples

impressively demonstrate the antifouling activity of the haloperoxidase mimics catalysts in the field and compared to cuprous oxide, the current gold standard.

The antifouling activity of CeO$_{2-x}$ nanoparticles can be linked to native defense system of marine organisms. The use of natural intermediates such as HOBr or halogenated metabolites, which are different from conventional antifouling agents, target specific bacterial signaling and regulatory systems like 3-oxo-AHL. This represents a new strategy with the goal to emulate a natural defense system for preventing bacterial colonization or biofilm development.[227] A biomimicry approach that allows the substitution of conventional biocides or costly enzymatic preservation systems by a stable, non-toxic and highly abundant rare earth oxide represents a sustainable antifouling solution that maximizes damage in bacterial biofilms with minimal collateral effects to the environment.
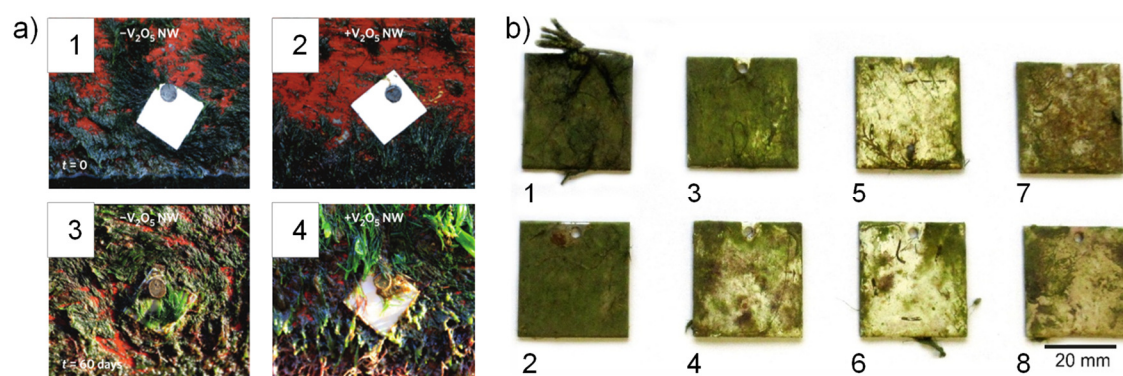
Figure 26. Representative digital images showing the antifouling activity in field test of V$_2$O$_5$ nanowires [424] and CeO$_{2-x}$ nanorods. [227] a) Antifouling activity in field test of V$_2$O$_5$ nanowires (nw) implemented in a commercially available paint for boat hulls.[424] Digital images of a stainless-steel plates (2×2 cm) covered with the paint formulation without (-V$_2$O$_5$ nw, a1,3) and with (+V$_2$O$_5$ nw, a2,4) V$_2$O$_5$ nanowires. a1,2) Immediately after fixation on a boat hull, a3,4) after 60 days immersion period in seawater. Severe natural biofouling has been observed at the painted stainless-steel plates in the absence (a3), but not in the presence of V$_2$O$_5$ nanowires (a4). Digital images reprinted with permission from ref. [424]. b) Commercially available antifouling paint (b3,5,7 hard and b4,6,8 soft formulation) with (b5,6) and without (b1-4, 7,8) cerium dioxide nanorods applied to stainless steel plates (4 x 4 cm).[227] Digital images (b1-b8) after static field immersion (52 days). Several control plates (b1,2 stainless steel, b3 native hard paint formulation, b4 native soft formulation, b7 hard paint formulation with copper oxide and b8 soft paint formulations with copper oxide) are displayed as well. The plates have been attached statically to a boat bridge with direct exposure to fresh water. After 52 days, the control plates without cerium dioxide nanoparticles (b1-4, 7,8) have shown heavy fouling in contrast to the plate with the cerium dioxide coating (b5 in soft and b6 in hard paint formulation). Here, the activity appears five times higher in comparison to Cu$_2$O. Digital images are reprinted with permission from ref. [227].

2

Metal Oxide Particles as Antifouling Materials

Identification and Application of Potential Active Haloperoxidase-like Catalysts in Collaboration with BASF SE

The following Chapter describes strategies, problems and possible solutions on the way to identify potential active haloperoxidase mimics. It is based on the concepts described in Chapter 1. Basic information about the paint formulation development, -preparation and analytical methods are described. Additionally, a short overview about tested materials in the course of the BASF collaboration project and the test strategies are given.

2.1   Groundbreaking: Bulk Vanadium Pentoxide

Vanadium pentoxide (V_2O_5) nanowires have been described to be functional active haloperoxidase mimics with mechanistic analogies to the native enzyme.[424] The upscaling process using pressure vessels deals with difficulties in industry, especially, occupational safety and high costs.

Nanowires were thus replaced by V_2O_5 bulk material which had been suggested to react similarly. Although, the bulk material´s activity was reduced compared to nanoparticles with equal volume because of the increased volume-to-surface ratio. However, this problem had been suggested to be overcome by the simplified sol-gel synthesis instead of autoclave-reactions with less waste products in combination with high purity. The material was supplied as an aqueous, orange paste avoiding hazardous vanadium containing dust. To examine the characteristics of the bulk material, the oxidative bromination of PR catalyzed by small aliquots of the V_2O_5 paste dried at 60°C for a few hours right before use was utilized (see Experimental Section, page 204). Thereby the chemical characteristics of the dried V_2O_5 powder obviously changed with time. Freshly dried powder and powder stored about one week and six months were compared.

The optical differences are highlighted in Figure 27a,b: the freshly dried powder as well as the prepared aqueous stock solutions (1 mg·mL^{-1}) appear dark orange. In contrast, the older the samples the more bleached to yellow.
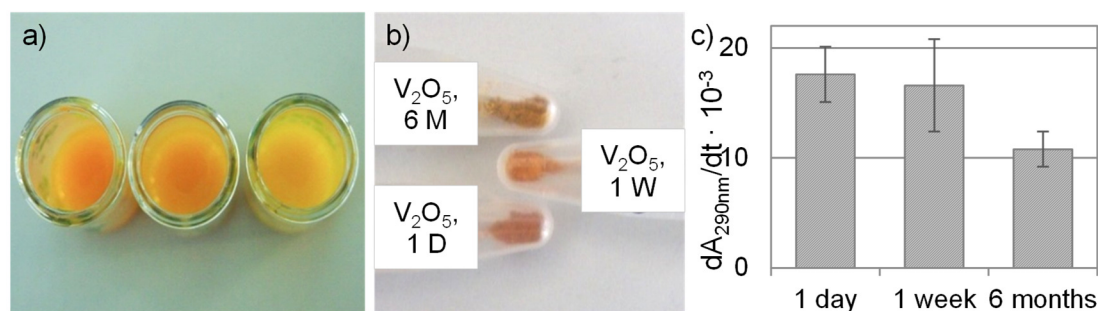
Figure 27. Comparison of V_2O_5 samples of varying ages. a) Digital images of aqueous stock suspensions (1 mg·mL^{-1}) made from one day, one week and 6 months old powders (from left to right). b) Corresponding educt powders. c) Comparison of the oxidative bromination activity of V_2O_5 powders (20 µg·mL^{-1}; MCD assay; absolute values of the absorbance at 290 nm *versus* time after 2h reaction time) aged for one day, one week and six months.

The catalytic activity of six months-old V_2O_5 powder in the oxidative halogenation reaction of MCD in Tris-SO_4 buffer (pH 8.3, see Experimental Section, page 188, 204) is roughly reduced by half compared to freshly prepared powders. The bar diagram (Figure 27c) compares the catalytic activity of V_2O_5 suspensions (20 µg·mL^{-1}) aged for two hours, which have been prepared from freshly dried, one week and six months old catalysts. Powders aged for one week show a comparable oxidative bromination activity.

However, the prepared stock suspensions showed a stable performance for up to two hours. To achieve a deeper understanding about the loss of catalytic activity, the dried powders and their aqueous suspensions have been analyzed. X-ray diffraction data implement phase pure orthorhombic and highly crystalline V_2O_5 for each dry-aged sample with almost identical crystallite sizes (Pawley fits: 113.38 nm (freshly dried), 118.72 nm (one week), 114.56 nm (six months), Figure 28 a-c). Bulk analysis *via* scanning electron microscopy (SEM, Figure 29a-d), transmission electron microscopy (TEM, Figure 29e-m) and FT-IR analysis (Figure 28d) do not show any macroscopic changes in the particle size (e.g. agglomeration, size distribution or increased water adsorption). BET analysis of the N_2 - physisorption data show comparable surface areas available for the heterogenous catalytic reaction of freshly dried and one-week old powder (10.52 m^2·g^{-1} and 10.98 m^2·g^{-1}, respectively) but a reduced area concerning the six months old one (9.64 m^2·g^{-1}). The analysis of the aqueous suspensions leads to interesting results.

Zeta potential measurements of all V_2O_5 powders with different aging times yielded in values that decreased with the material´s age: -38.4 mV (freshly dried) > -31.9 mV (one week) > -28.4 mV (six months). Each sample was recorded 25-times.

The trend of loss in the zeta potential within the aging time can be correlated to the decrease of the surface charge. This might have impact on the formation of hypobromite species *via* alterations in the catalytic circle. More precisely, variations in reaction potentials in general can influence the protonation reaction representing a key step in the catalytic cycle (see Introduction, page 29, 30).

Suspensions of the vanadium powders in D_2O have been analyzed *via* ^{51}V-NMR measurements relative to $VOCl_3$ as the reference material. The amplified, normalized and smoothed ^{51}V-NMR spectra of the corresponding V_2O_5 materials with different aging times are shown in Figure 30.
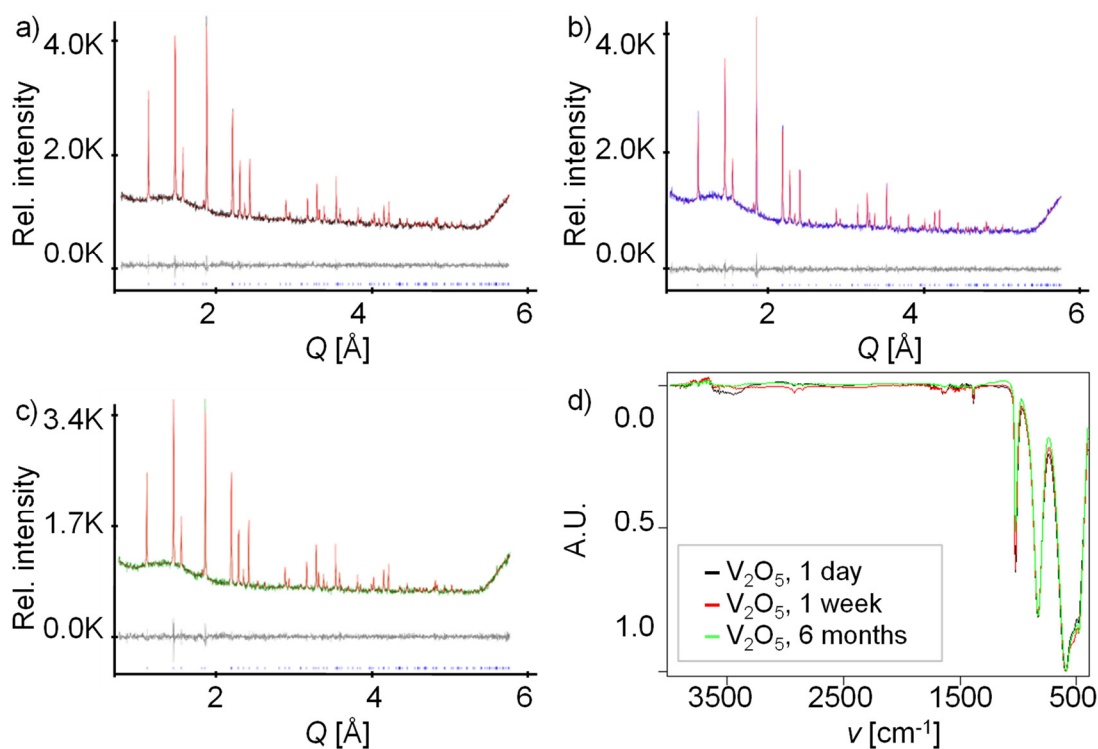
Figure 28. XRD and FT-IR analysis of V_2O_5 samples of varying ages. No difference occurs in XRD analysis of a) six months, b) one week and c) one-day old powder in analogy to d) FT-IR analysis (black: one day, red: one week and green: 6 months aged powders). The three specific vibrations of V=O are obvious in the range of 1100 to 500 cm^{-1}. Unexpectedly, no water signals coul be detected in the range of ca. 3500 cm^{-1}.

In general, the signals occur in a very negative range because of the high electron density results in a high shielding.[536–540] The main chemical shifts imply an increased occurrence of deprotonated decavanadate species ($[V_{10}O_{28}]^{6-}$ or $[H_2V_{10}O_{28}]^{4-}$)[536–540] (exp.: -427.13, -509.75, -528.81 ppm) with aging times of the powders. The two significant signals at -509.75 and -528.81 ppm indicate an octahedral geometry and are also known in some oxo-complexes of vanadium.[541,542] Polyoxovanadate species typically consist of such structural saturated "VO_6" octahedra (Figure 30 inlay) and they are therefore presumed to be catalytically inactive. The signal at -545 ppm has been assigned to low molecular compounds (e.g. $[VO_2]^+$)[541,542] which are formed at a low pH values.

This pH value was not achievable in the reaction mixture. However, such moieties could be a hint to variations in the local pH values near the catalyst´s surface as well as a linkage to the leaching process in general and to the formation of higher oxo-vanadium clusters. Oxidation state analysis demonstrated a maximum amount of 0.4 % of V(IV) species being in the range of impurities examined (ca. 0.3 %).

Impurities in the elemental composition of the V_2O_5 bulk material are assigned to other transition metals (mainly $M^{3+/6+}$), main group elements (mainly $M^{4+/5+}$) or different alkaline metals. However, the relevance of the mixed oxidation states of vanadium to catalytic reactions have become complex and further analysis like EPR measurements in combination with theoretical calculations will be required.
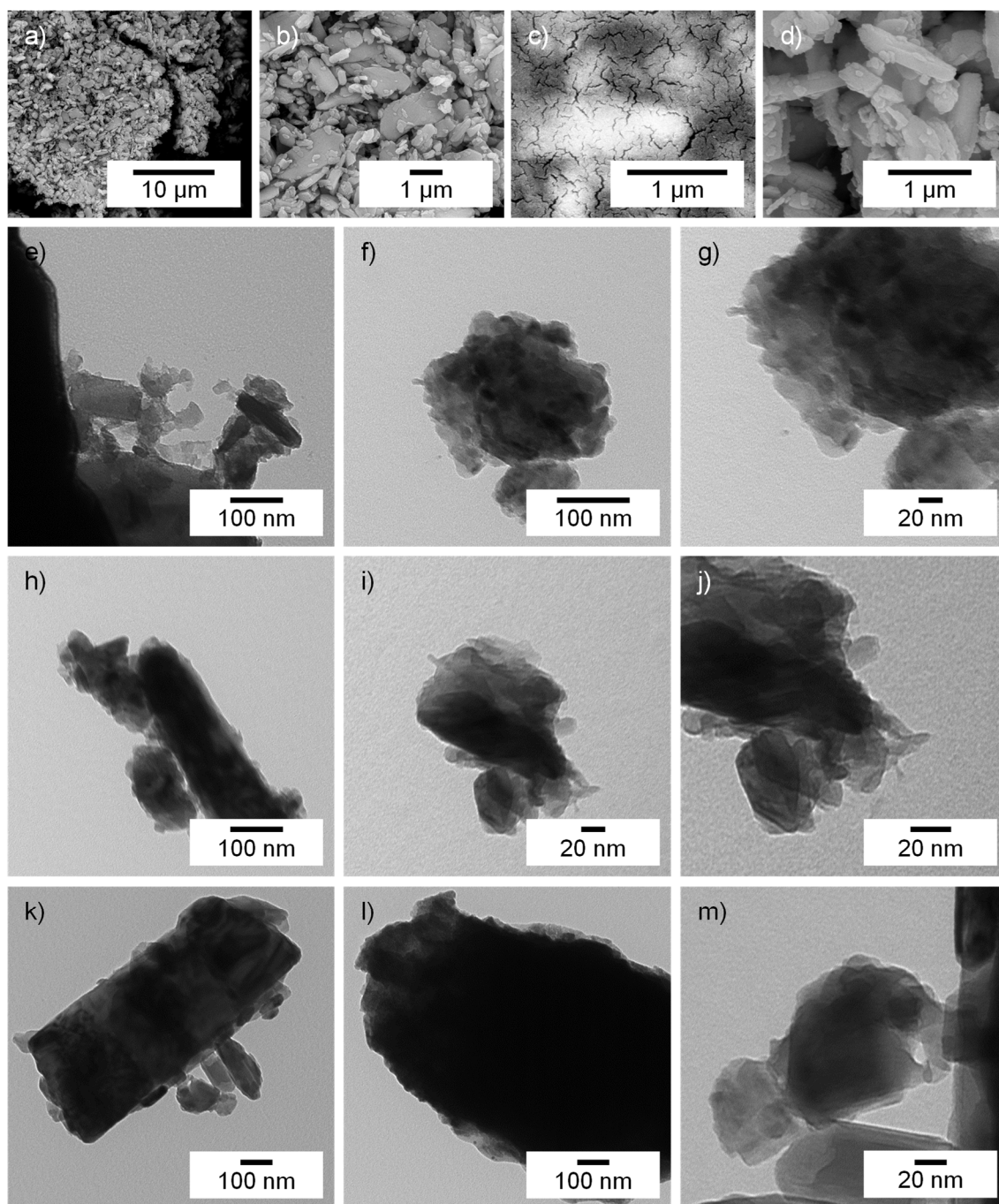
Figure 29. Representative SEM and TEM images of V_2O_5 powders of varying ages. SEM images of a), b) one week and c), d) six months old V_2O_5 powder. TEM images of e-g) one day, h-j) one week, k-m) six months old V_2O_5 powder.

In summary, the loss in performance of the V_2O_5 bulk material has been assigned to multistage processes modifying the catalyst´s surface, in particular, fluctuations in the surface charge and/or oxidation stages, dissolving processes concerning the formation of inactive, soluble polyoxovanadate clusters and possible migration/blocking by counter ions. Such inactivation processes seem not only affect the dried powders and aqueous stock solutions of the catalytic material, but the V_2O_5 paste as well.

A comparison of the analytical results after production of the paste with those made one year later demonstrated an increase of the hydrodynamic particle size and specific surface (data not shown). This further supported the suggestion that aging processes of the particles in the aqueous stock paste occurred that had led to agglomeration and inactivation. Reactivation approaches whereas the six months-aged V_2O_5 powder was annealed (2h at 60, 100 or 150°C) before the MCD assay did not succede. To address the leaching problem, approaches to fix transition metals on supporting materials were examined.
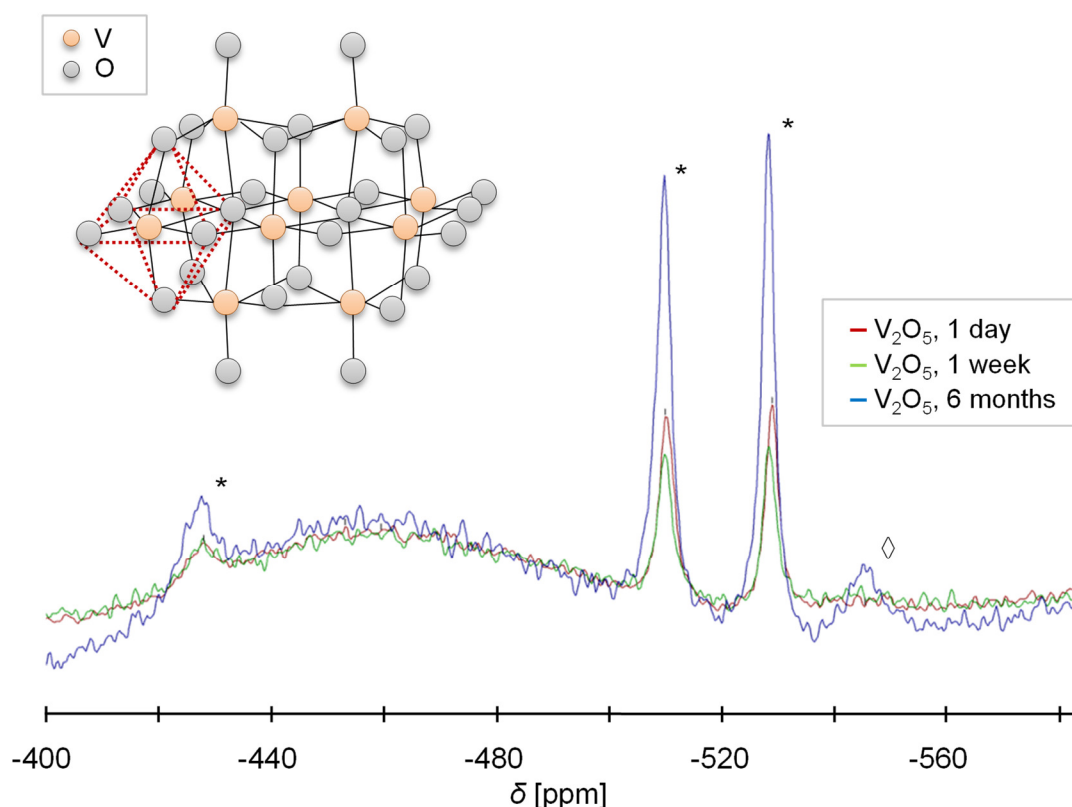
Figure 30. ^{51}V-NMR analysis of V_2O_5 powders of varying ages. Amplification of ^{51}V-NMR (normalized, smoothed) in D_2O of V_2O_5 powders aged for one day (red line), one week (green line) and six months (blue line). Signals at: -427.13, -509.75; -528.81; -545.45 ppm. The signals are assigned to decavanadate (*) and to low-molecular weight vanadium containing compounds (◊). Inlet: schematic structure of decavanadate.

2.2   Supporting Materials

PAN Polymers

Concerning the problems with bulk vanadium pentoxide, a "doping" with catalytically active species such as vanadate, molybdate and tungstate has been attempted. The finely dispersed catalysts at the surface of cheap and inert support materials provide the potential of enhanced catalytic activity in combination with reduced costs. Polyacrylonitriles of different molecular weights (X-PAN $\approx$ 50 000 g·mol^{-1} and N-PAN $\approx$ 80 000 g·mol^{-1}, offered by BASF) and different layered double hydroxides (e.g. doped Ni, Al-LDH) have been used. The materials are set as model organic/coordinative support systems in comparison to inorganic ionic carrier materials. Das and Boruah et al.[406] have reported molybdenum and tungsten peroxo species stabilized by nitrogen atoms of PAN´s nitrile groups ($[MO_2(O_2)(CN)_2]$-PAN, M=Mo or W) to be efficient and versatile catalysts for oxidative bromination with high turnover numbers.[406] The hypothetic structure of the PAN-transition metal intermediate in its active state is shown in Figure 31a.

The doping of the PAN polymers was achieved by mixing the polymers with the corresponding metal acid stock solutions (H_2WO_4 and H_2MoO_4, pH 5) and H_2O_2. Reproduction of the materials (see Experimental Section, page 185) resulted in hybrid components with similar performance in the oxidative bromination of phenol red to bromophenol blue as reported by Boruah et al.[406] However, the doping process was neither consistent nor reproducible and polymers with a Mo-loading between ca. 2 wt% and 64 wt‰ had been formed (see Experimental Section, page 185). Doping with tungstates appeared more difficult than with molybdates, and hybrid materials only with up to 18 wt‰ tungsten were achieved. Because of the insolubility of the polymer hybrid material, qualitative peroxidase (ABTS, see Experimental Section, page 205) and haloperoxidase (PR, see Experimental Section, page 207) dye assays were implemented. All reactions were started by addition of H_2O_2 and evaluated optically. Blank tests were performed using V_2O_5 as standard catalytic material and without any catalyst.

Shortly after H_2O_2 addition, V_2O_5 in acetate buffer oxidized ABTS (colorless) to the green ABTS$^{·+}$ (Figure 31b (5)). None of the Mo or W-doped polymers show peroxidase-like activity (Figure 31b). Reversely, V_2O_5 do not exhibit haloperoxidase-like activity under these reaction conditions (Figure 31b-f). Concentration-dependent haloperoxidase-like activities are observed for Mo or W polymer hybrids. The typical blue color of

the fourfold brominated bromophenol blue was first observed after 90 minutes reaction time in mixtures including 50 µg·mL^{-1} molybdenum content (adjusted from 1.4 wt% Mo@PAN) (Figure 31b (1-4)). As expected, reaction mixtures containing ≈ 4-5 µg·mL^{-1} (adjusted from 64 wt‰ Mo@PAN) needed a time period increased by a factor ≈ 15 (Figure 31c-f). However, both turnover rates fitted exactly with the catalytic activity of the native metal acids (Figure 31c-f).
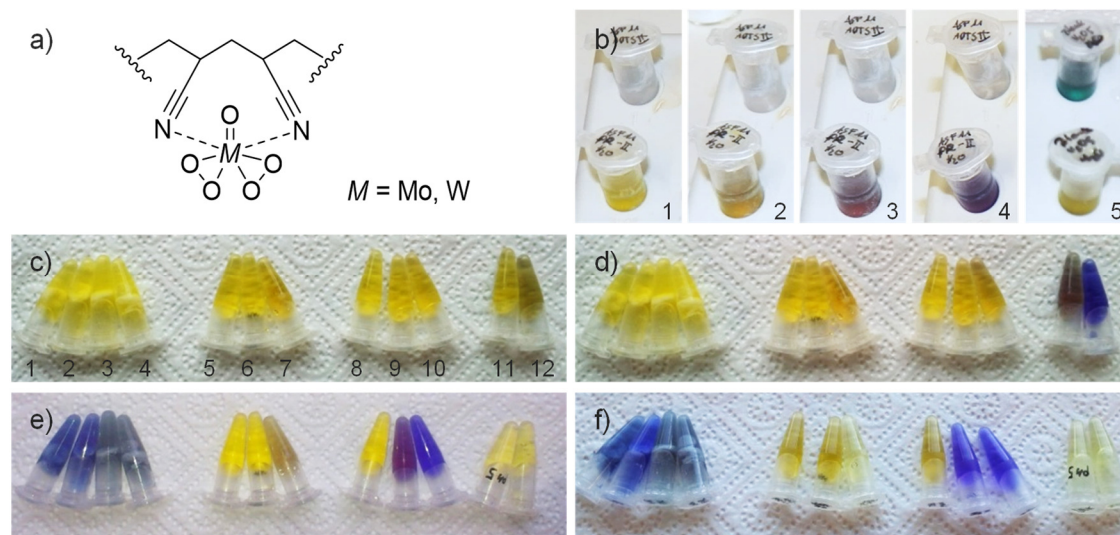
Figure 31. Qualitative peroxidase and haloperoxidase assays of polymer-transition metal hybrid catalysts. a) Hypothetic structure of the reactive PAN-diperoxomolybdate or -tungstate intermediate after H$_2$O$_2$ attack.[406] b) The oxidation of the colorless ABTS (700 µM) to the emerald green radical cation (row above) catalyzed by 1.4 wt% Mo@N-PAN (heterogenic, metal amount in reaction: 50 µg Mo·mL^{-1}) and 1 mM H$_2$O$_2$ in sodium acetate buffer (100 mM, pH 4.0) was followed in the time range of (1) 0 min, (2) 2 min, (3) 40 min and (4) 90 min. Within this time, no oxidation reaction is observed. Simultaneously, the oxidative bromination of yellow PR (50 µM) catalyzed by 1.4 wt% Mo@N-PAN (5 µg Mo·mL^{-1}), 25 mM NH$_4$Br and 300 µM H$_2$O$_2$ in H$_2$O to the blue-violet bromophenol blue was evaluated (row below). After (4) 90 min, the conversion to bromophenol blue is obvious. However, bulk V$_2$O$_5$ (20 µg·mL^{-1}) as reference material catalyzed the oxidation of ABTS within a few minutes but with respect to bromophenol blue no reaction occurred even after (5) 90 min. c-f) The oxidative bromination of yellow PR (50 µM) in aqueous solution (1 mL) containing 25 mM NH$_4$Br and 300 µM H$_2$O$_2$ to the blue-violet bromophenol catalyzed by diverse Mo/W doped polymeric catalysts and controls was followed in the time range of c) 60 min, d) 90 min, e) 1 day and f) 2 days. The catalysts are numbered in order (see c): 1) Mo@X-PAN (≈ 4-5 µg Mo·mL^{-1}), 2) Mo@N-PAN (≈ 4-5 µg Mo·mL^{-1}), 3) W@X-PAN (≈ 2 µg W·mL^{-1}), 4) W@N-PAN (≈ 2 µg W·mL^{-1}), 5) bulk V$_2$O$_5$ (5 µg·mL^{-1}), 6) bulk V$_2$O$_5$ (2 µg·mL^{-1}), 7) bulk V$_2$O$_5$ (50 µg·mL^{-1}), 8) no catalyst, 9) H$_2$MoO$_4$ (5 µg·mL^{-1}), 10) H$_2$WO$_4$ (2 µg·mL^{-1}), 11) H$_2$MoO$_4$ (50 µg·mL^{-1}), 12) H$_2$WO$_4$ (50 µg·mL^{-1}). Free molybdic (11) and tungstic acid (12, homogenous catalyst) catalyzed the reaction within 90 min analogue to Mo@N-PAN (heterogeneous catalyst, (b)) but bleached the dye afterwards (e, f). The Mo/W doped polymers (metal amount ≈ 5 µg·mL^{-1}) catalyzed the reaction within one to two days in analogy to their corresponding free acids without further bleaching. Bulk V$_2$O$_5$ (5, 6, 7) did not catalyze the oxidative halogenation but promoted bleaching (f (7); 50 µg·mL^{-1}).

Reactions containing tungsten as the catalytic material showed slightly increased reaction rates compared to molybdenum. This trend was confirmed by using free molybdic and tungstic acid (each: 50 µg·mL^{-1}) as active agents (Figure 31c-f). In addition, the homogenous catalysts showed excess reactivity by subsequental bleaching of the dye bromophenol blue (Figure 31e,f).[543] However, the haloperoxidase-like activity of the Mo/W polymer hybrid materials did not remain in cycle tests. Elemental analysis revealed a high leaching process of the transition metals in aqueous reaction conditions. A stabilization of transition metal acids in PAN polymers seemed to be not as efficient as expected and thus these materials were scrapped in the early product development and testing stage.

LDH

Sels et al.[397,544] reported nickel(II)-, aluminum(III)- layered double hydroxides (Ni, Al-LDHs) to be efficient catalysts in the oxidative bromination reaction of phenol red if doped with tungstate, molybdate or vanadate. The inorganic, hydrophilic carrier materials were synthesized in a co-crystallization step followed by an ion exchange doping process. Mainly, the chloride transition metal salts of tungsten, molybdenum and vanadium were used. Different LDH compositions were synthesized and adopted to further explore the effectiveness and reusability of LDHs as inorganic, hydrophilic carrier materials for the catalytically active species in haloperoxidase-mimetic studies.

X-ray diffraction patterns of the undoped, W, Mo, and V-doped LDH (Figure 32a) indicate an amorphous material with little crystalline parts. The assignment of the broad reflections has proved to be difficult and no difference among the three sample patterns, aside from intensity is detected. Crystal structures with analogies to magnesium aluminum hydroxide hydrate-like ($Mg_6Al_2(OH)_{18}$ · 4.5 H_2O) and to *Jamborite* ($Ni(OH)_2(NiOOH)$)-like compositions are assumed. The assumption is based on the similar ionic radii of $Mg^{2+} \approx Ni^{2+} \approx 78$ ppm.[428]

TEM images show similar layered structures that have agglomerated to larger particles. In accordance to the undoped material, all three doped samples emphasize a high particle size distribution as well (Figure 32b-f). No differences in XRD or TEM images of the (un)doped LDHs are recorded. The results of the elemental analysis of each sample indicate relatively low levels of doping, ranging from approximately 1-3 wt% (Table 8).

The elements listed from highest to lowest doping-level are tungsten, molybdenum, and lastly vanadium. The amount and relative ratio of Ni and Al remain constant (Table 8).
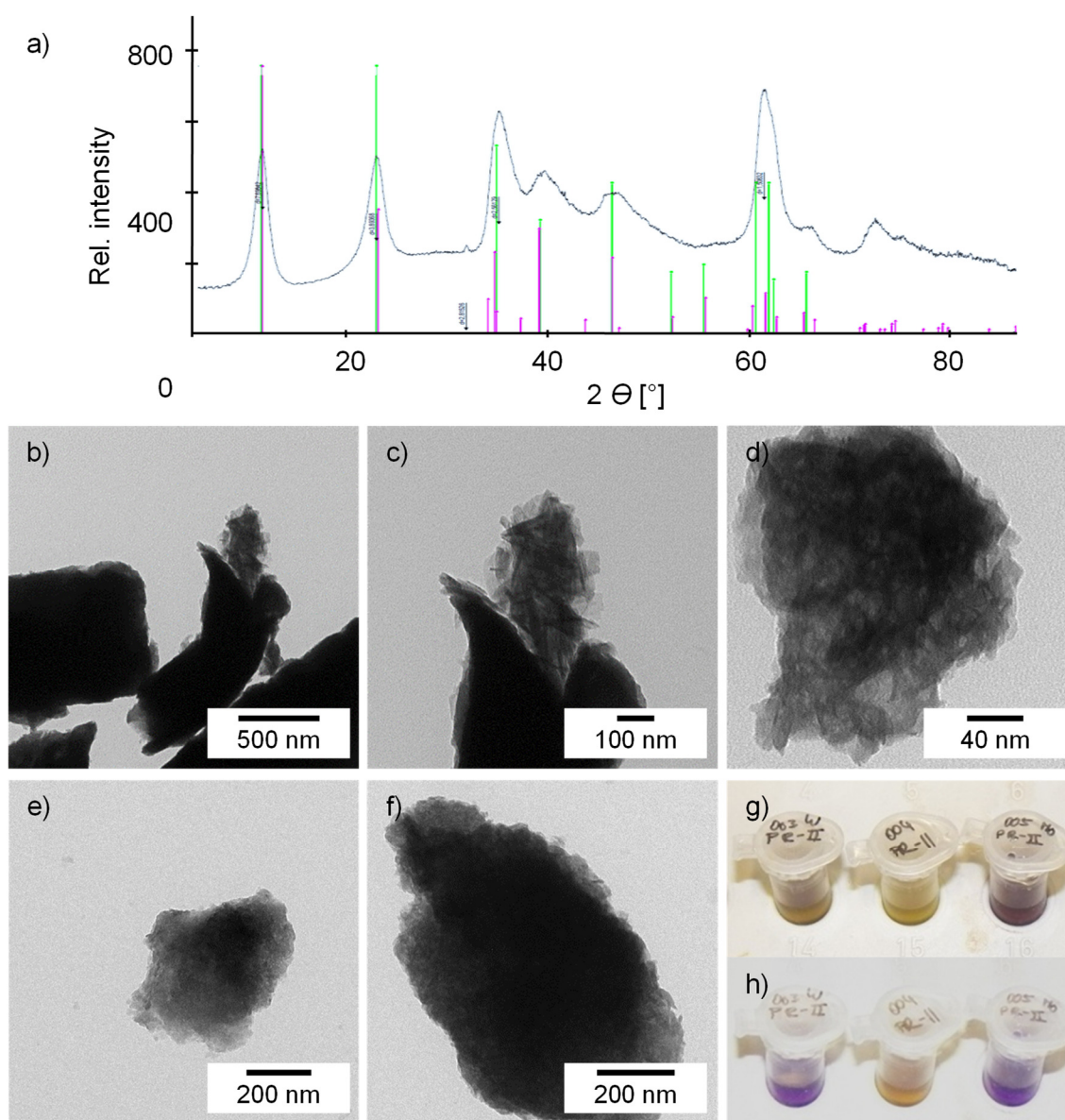
Figure 32. Analysis of Ni/Al-LDHs. a) XRD analysis of undoped Ni/Al-LDH. Structural analogy to "magnesium aluminium hydroxide hydrate"-like structures ($Mg_6Al_2(OH)_{18} \cdot 4.5\ H_2O$, green reference signals) and to *Jamborite*, syn ($Ni(OH)_2(NiOOH)$, pink reference signals). TEM images of NiAl-LDHs b-c) without doping and doped with d) MoO_4^{2-}, e) WO_4^{2-}, f) VO_3^{-}. Digital images of the qualitative (haloperoxidase) phenol red assay of 50 µg·mL^{-1} doped NiAl-LDHs (doping from left to right: W, V, Mo) after g) 90 min and h) one day.

The haloperoxidase activities of the doped LDHs were tested initially with monochlorodimedone (see Experimental Section, page 204). Due to sedimentation problems, the values could not be measured reliably and the qualitative phenol red and ABTS test systems were used instead. The doped materials did not enhance the formation of the

emerald green radical cation of ABTS (peroxidase-like reaction) compared to blanks but catalyzed the reaction to the violet-blue bromophenol blue. The activity was demonstrated by visual inspection of the qualitative PR assay firstly after 90 min (Figure 32g) and after one day (Figure 32h). Interestingly, the reaction rate was enhanced slightly for molybdenum over tungsten doping, and no reactivity for vanadate doping was recorded even after two days. Because of the toxicity of nickel and to further investigate LDHs as possible inorganic, hydrophilic carrier materials, the idea arose to synthesize alternative LDHs with a Mg/Al/Zn composition (see Experimental Section, page 185). Analysis of doped LDHs revealed an increased transition metal leaching under aqueous reaction conditions in analogy to the doped PAN materials. For this reason, the organic as well as the inorganic supporting materials were driven out of the focus of attention and further research mainly emphasized more stable, oxidic materials.

2.3   Excursus: Limitations of Spectrophotometric Test Methods

Turbid suspensions cause a high error and signal shifts because of strong particle scattering. Based on the assumption that the disturbing effects of the particles are constant for small periods of time, the error can be minimized mathematically.

To ensure and enhance comparability of optical assays with regards to instrumental and sample errors, standardized scripts for the quantitative assays, in particular, the MCD – haloperoxidase activity test, were developed. Test measurements using a constant MCD concentration (5 µM) in TRIS buffer (1 mL, 100 mM, pH 8.3) and a simultaneous variation in the V_2O_5 amount (0; 5 and 20 µg·mL^{-1}) as the opacifier were thus evaluated. All samples were prepared and measured three times. The raw absorption (A) data of each graph were transformed to their second derivatives and related datasets were averaged.

Figure 33 compares the non-processed and mathematically processed data of the three mean derived traces for each V_2O_5 concentration. The comparison between the non-processed signal curves (Figure 33a) shows significant differences between the signal state although equal MCD concentrations. The resulting shifts are assigned to particle scattering and are supposed to be minimized by the second derivatives (Figure 33b). The mean value determined from the peak maximum and minimum (≈ 0.0012 abs unit) corresponds to 5 µM MCD and is obtained for all reaction mixtures (*q.e.d*, Figure 33b).

Aqueous catalytic test systems are very complex and thus susceptible to signal distortions. Misinterpretation of values does not only depend on turbidity. The nature and components of the buffer system, salt concentrations, solubility and adsorption processes influence the output signal as well. Therefore, the mathematical data processing described above can not be used for longer reaction times.
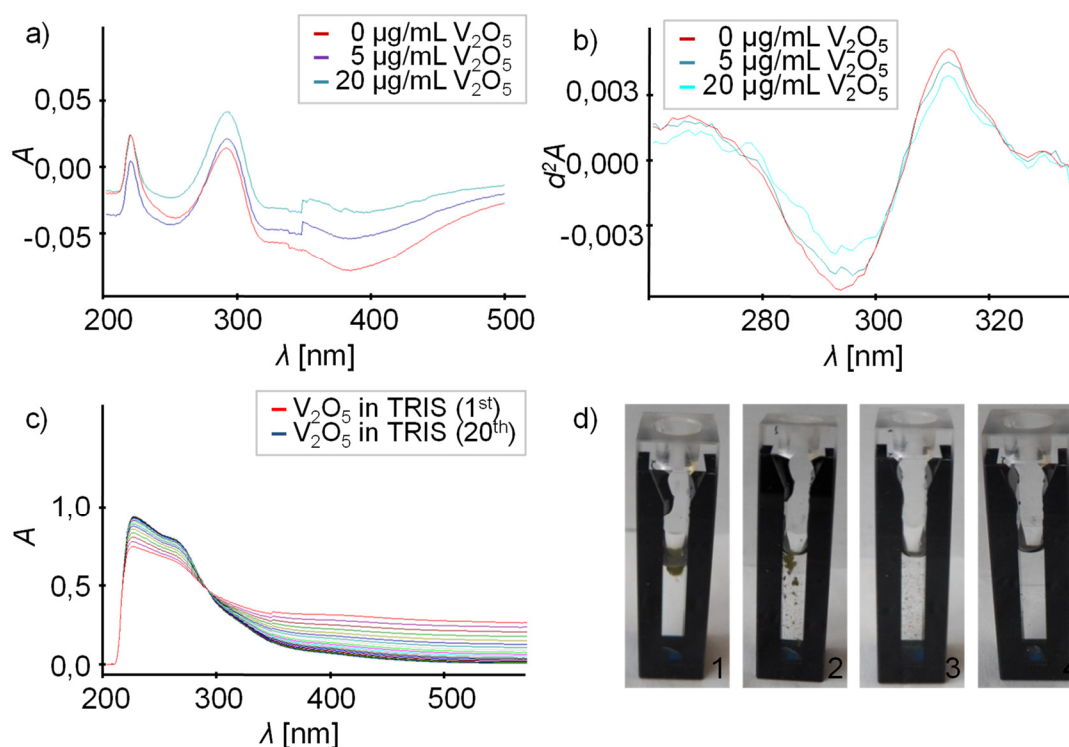
Figure 33. Mathematical data processing of compiled spectra with V_2O_5 as opacifier. a) Mean, superimposed absorbance spectra of the raw dataset of 5 µM MCD (red), 5 µM MCD + 5 µg mL^{-1} V_2O_5 (violet), 5 µM MCD + 20 µg mL^{-1} V_2O_5 (blue), λ = 200-500 nm. b) Magnification of the second derivatives of the datasets (filter size of the data points: 9; λ = 260-340 nm). c) Time-dependent measurement (20 min) of V_2O_5 particles in TRIS buffer, color code: first measurement (red) to last measurement (blue), scanning rate 600 nm/min. "Isosbestic point" at around 290 nm. d) Behavior of V_2O_5 particles (20 µg·mL^{-1}) in carbonate buffer containing 10 µM KBr, 5 µM MCD and 10 µM H_2O_2. d1-4) Agglomeration followed by partial solution of the particles within stirring and after d4) 15 minutes reaction time, almost all particles were dissolved. The remaining residue changed its color from yellow to grey-green possibly because of reduction processes.

The optical evaluation of a suspension of V_2O_5 (20 µg·mL^{-1}) in TRIS buffer (100 mM, pH 8.3) for 20 minutes shows strong interactions of the particles with the media (Figure 33c). Although a constant particle scattering in the range of 289 - 292 nm which corresponds to the absorbance required for the MCD assay (290 nm) have occurred, a distortion of the resulting signals can not be excluded completely. It is apparent that the V_2O_5 particles dissolve in the TRIS buffer within time (cf. Chapter 2.1).

In this context, changing the buffer system to carbonate buffer (100 mM, pH 8.4) forced agglomeration of V_2O_5 first, again followed by solution and reduction processes (cf. Figure 33d). Analogous results were observed when borate buffer (100 mM, pH 8.3) was used as reaction media. After reaction (20 μg·mL^{-1} V_2O_5, 10 μM KBr, 5 μM MCD, 10 μM H_2O_2), almost all particles were dissolved yielding a colorless solution. A new broad absorption (maximum at ≈ 262 nm) arose which implied the formation of vanadium borate.[545] This absorption band interfered with the MCD signal making quantitative and/or qualitative analysis impossible.

In conclusion, the optical dye assays represent an essential tool to detect and evaluate haloperoxidase-like reactions. Because of their complexity, these test systems are susceptible to errors. The components of a buffer system (here: TRIS, carbonate and borate) might interfere with the catalytic material. As chelate ligands they can force side reactions as dissolving processes, surface coverage or destabilization resulting in a reduced sensitivity to the MCD detection.

Minimizing such effects, deionized water or sea water as the reaction media were preferred. Additionally, the kinetic measurements were performed on spectrophotometers equipped with an integration sphere in combination with a magnet stirrer. Particle scattering was further reduced by using semi-micro quartz cuvettes with self-masking black walls and magnetic stirring capability (cf. Figure 33d). In addition, the stirring speed showed some influence on the reaction velocity and was optimized and standardized.

2.4   Developing Paint Formulations

The research, development and production of new products is always a challenge. Especially the design and implementation of new paint formulations imply a scientifically complex and complicated process coupled with market demands. Nowadays, external coatings created for marine applications can be subdivided into three main categories: 1) hard formulations for top coating (UV stability, glossiness and color; splash-water protection), 2) "soft" antifouling paint formulations (abrasive formulations with biocides for permanently water-subjected boat domains), 3) hard antifouling coatings (protective formulations for permanently water-subjected boat domains mainly based on physical defense, e.g. micro structuring, hydrophobic or hydrophilic coat surfaces). Typical paint matrices are optimized and customized for each single pigment (biocide).[495,501,502,512–515]

To meet these requirements, two given master-batches as paint formulations were used. For the implemented bacterial adhesion test system and later in field tests, the biocides (0.5, 1.0, 2.0, and 5.0 wt% of dry weight) were embedded in a commercial alkyd-based top coat (hard formulation, Toplac 001 white, International) and an abrasive, "Rosine" paint formulation provided by BASF. Because of that, a high degree of comparability between the different biocides was guaranted but lack particle specific optimization. The embedding process itself influenced highly the paint formulation and the performance. Taking a closer look at hard paint "Toplac" formulation mixtures, particles were added to the matrix by conventional stirring and ultra-sonification to reduce particle agglomeration.

Figure 34a-d illustrates the influence of the ultra-sonification time of a,b) 30 min and c,d) 1 min on particle blending (here 2.0 wt% Fe_2O_3 particles in Toplac) using optical methods as digital photography (Figure 34a,d) and light microscopy (Figure 34b,c) for each sample. As the reference, each sonificated paint formulation moiety is flanked by a formulation made of conventional Fe_2O_3 particle blending in Toplac (Figure 34a-d, superior moiety). Finely dispersed Fe_2O_3 particles enhance the color impression. The reddish color is maximum after 30 min of sonification (Figure 34a,b, bottom) and become visible after 1 min (Figure 34c,d, bottom). Figure 34b, c show laser microscopy analysis confirming these findings to be a result from a disintegration of agglomerates. Particles in a finely distributed form are suggested to go along with an increase in catalytically active centers. In contrast, ultra-sonification and the resulting heat input might negatively affect the paints. Therefore, the ultra-sonification time was limited to 1 – 5 min to ensure the paint integrity and to avoid cracks or demixing phenomena.
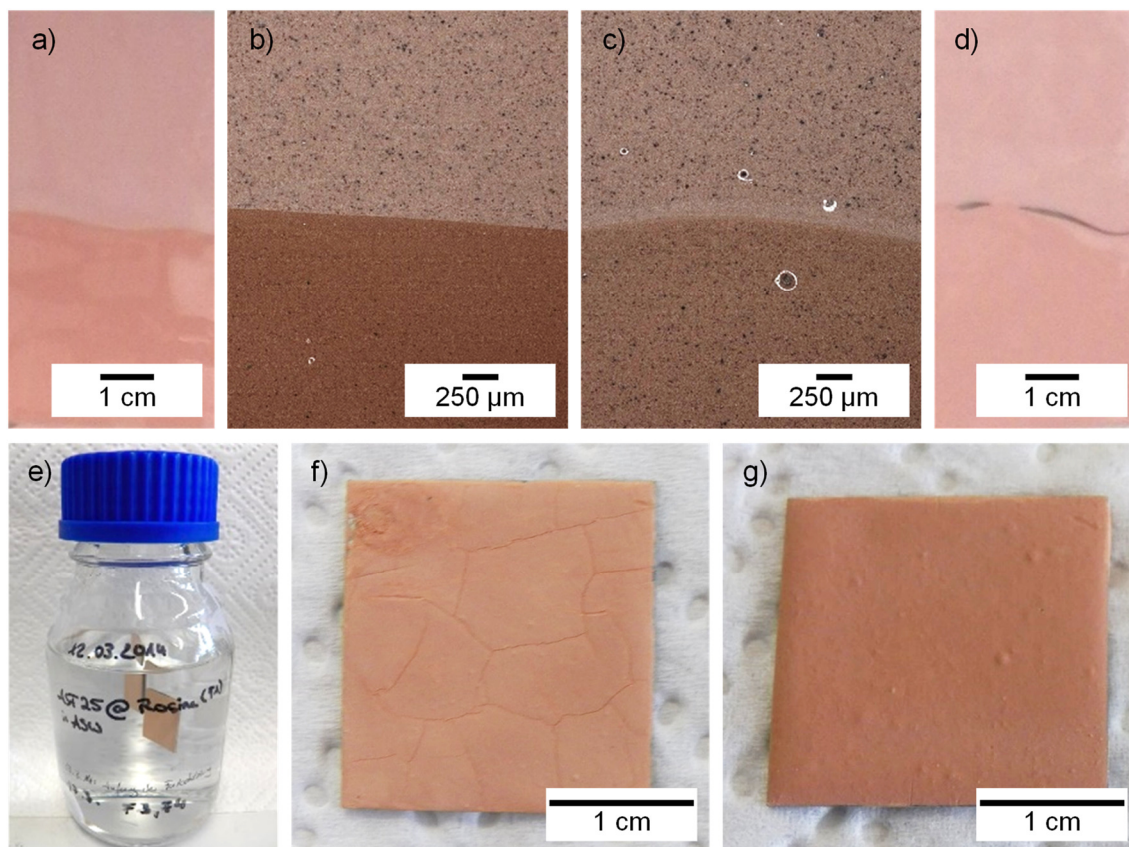
Figure 34. Fe$_2$O$_3$ particles embedded in different paint formulations. a-d) Influence of the mixing method when embedded into prefabricated hard paint formulation ("Toplac") using optical methods as digital photography (a,d) and light microscopy (b,c) for each mixture. Particle blending samples (2.0 wt% Fe$_2$O$_3$ particles in Toplac) were performed by ultra-sonification for a,b) 30 min and c,d) 1 min and are flanked by a formulation made of conventional Fe$_2$O$_3$ particle mixing in Toplac (superior moiety). e) Stability tests of an abrasive paint formulation containing Fe$_2$O$_3$ particles were performed by immersing coated steel plates for 5 days in sterile artificial sea water with gentle stirring. c) Example of a failed and d) example of a stable paint formulation.

Such problems did not affect the abrasive paint formulation directly as it was prepared from scratch instead of the particle addition to a pre-existing hard paint formulation. The resin-based, abrasive "soft" paint formulation was prepared by subsequent mixing the individual components (solvents, binder, softener, filler, adhesion promotor, dispersant, colorants and biocides) in a specific ratio, order and measure together. Here, the discovery of the specific amount of each component as the general valid norm was the main purpose to guarantee a stable, functional and comparable "master batch" for each kind of biocide. The paint stability was tested towards optimization processes in a laboratory water immersion test illustrated in Figure 34e-g. Test panels were coated with the formulations of interest (here Fe$_2$O$_3$ as biocide). After drying, the plates were subjected to artificial sea water for a couple of days (Figure 34e). After one week, the consistence of the coating was analyzed. Figure 34f shows a paint formulation which failed the test

due to fracture formation. In comparison, a smoother paint formulation with enhanced stability resulted (Figure 34g) as the amount of a filler material, an inorganic sulfate with swelling capacity, was increased.

With regards to the embedding of particles into the abrasive paint formulation, a suspension of biocides in organic solvents was easier to blend into the paint matrix than the raw powder. As a result, the enhanced surface smoothing reduced the bacterial adhesion compared to the conventional "powder embedding" (see Experimental Section, page 223, and Chapter 2.5). This is demonstrated impressively for $WO_3@TiO_2$ and Fe_2O_3 particles (Figure 35).
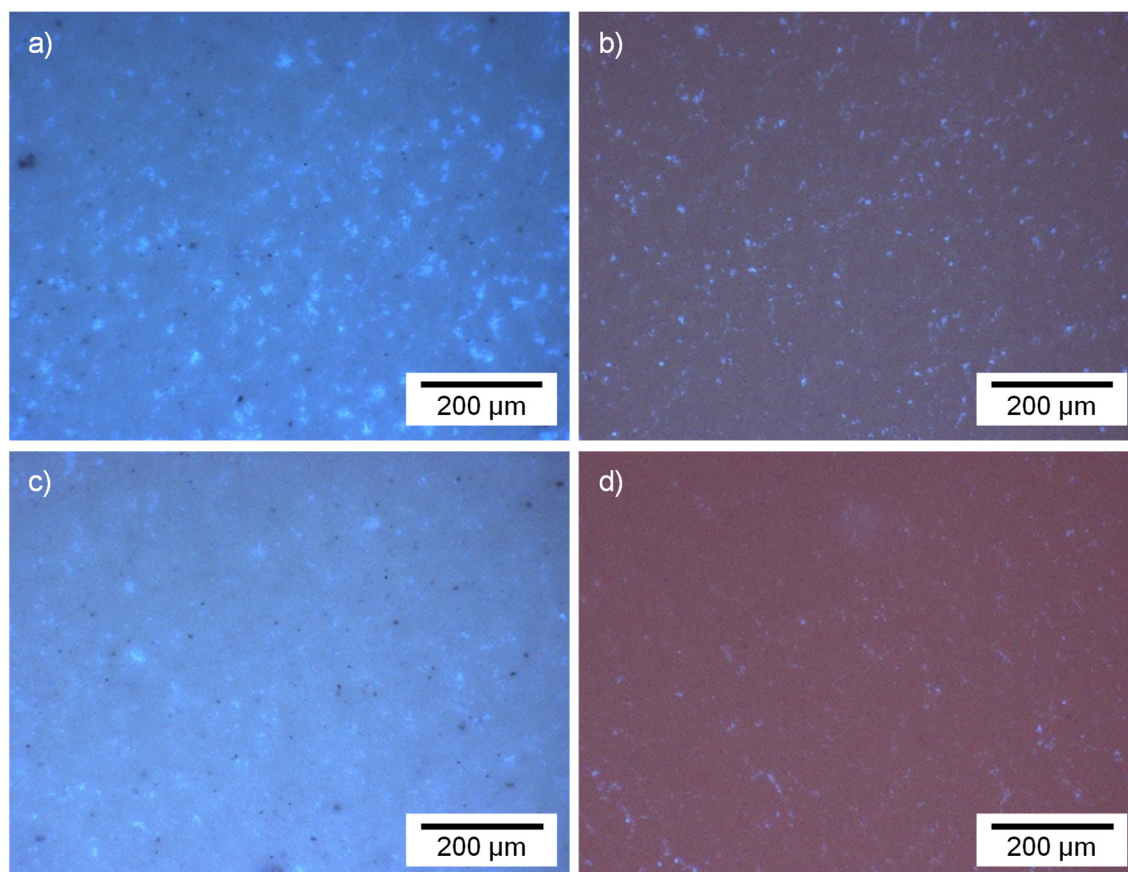
Figure 35. Decrease of bacterial adhesion by abrasive, resin-based paint optimization. Embedding of a) 2 wt% $WO_3@TiO_2$ powder, b) 2 wt% Fe_2O_3 powder, c) $WO_3@TiO_2$ (2 wt%) suspension, d) Fe_2O_3 (2 wt%) suspension. Implementing the particle suspension instead of raw powders yields an enhanced surface smoothing further impeding bacterial adhesion. For experimental details see Experimental Section, page 223, and Chapter 2.5.

Coating properties like abrasion resistance and coverage capacity are influenced by the layer thickness and surface quality.[546] In self-polishing, soft paint formulations they additionally determine the availability and, respectively, the total amount of the catalyst. Therefore, different height profile measurements have been performed by laser microscopy.

A stainless-steel plate being hand-coated with commercial Toplac (TL) without any biocide was analyzed as a reference. To evaluate the height difference from the precursor plate to the paint surface, an adhesive tape as a spacer was used. It was removed after the paint had been dried. The exemplified dataset of the laser height analysis reveals a smooth layer with a thickness up to 145 μm (Figure 36a).

In industrial scale, coats are prepared for example by dip coating or spray operations. This application methods minimize coat irregularities resulting from a variation in contact pressure or application velocity.[547] The resulting uniform coatings have been imitated in lab scale by motorized film applicators, in this case equipped with a spiral squeegee.[546] Different mechanical squeegeed hard (Toplac, TL) and soft (SF) paint formulation at stainless steel or PVC plates have been analyzed: i) WO_3/TL, ii) Fe_2O_3/ SF, iii) $WO_3@TiO_2$/TL and iv) Al/Cu/Mn-oxide/SF. The height profiles of Fe_2O_3/ SF and WO_3/TL are shown in Figure 36b and Figure 36c and the evaluation parameters are compiled in (Table 8). In general, the height of the squeegeed paint is lower than the hand-coated paint. The maximum height is limited by the squeegee used, here 150 or 300 μm, respectively. However, these values are never reached because of shrinkage processes. Paint shrinkage is manly affected by the volatile solvent content, amount of polymer and the soft-hard component ratio.

Thus, the paint composition is related to defined rheological properties, for example viscosity, density and surface tension. Toplac has a solvent content up to 50 %.[548] In combination with its high fluidity, the observed shrinkage of ≈ 73-80 % (Table 8) is realistic and seems to be unaffected by additional inserted particles (up to 2-5 wt%). The soft paint formulation has an amount of 20-40 % of solvent. The discrepancy compared to the thickness measured (Table 8, ≈ 65 or ≈ 26-44 μm) is suggested to result from the paint composition and compatibility between the different ingredients and substrates (stainless steel *versus* polyvinyl chloride (PVC) plate).
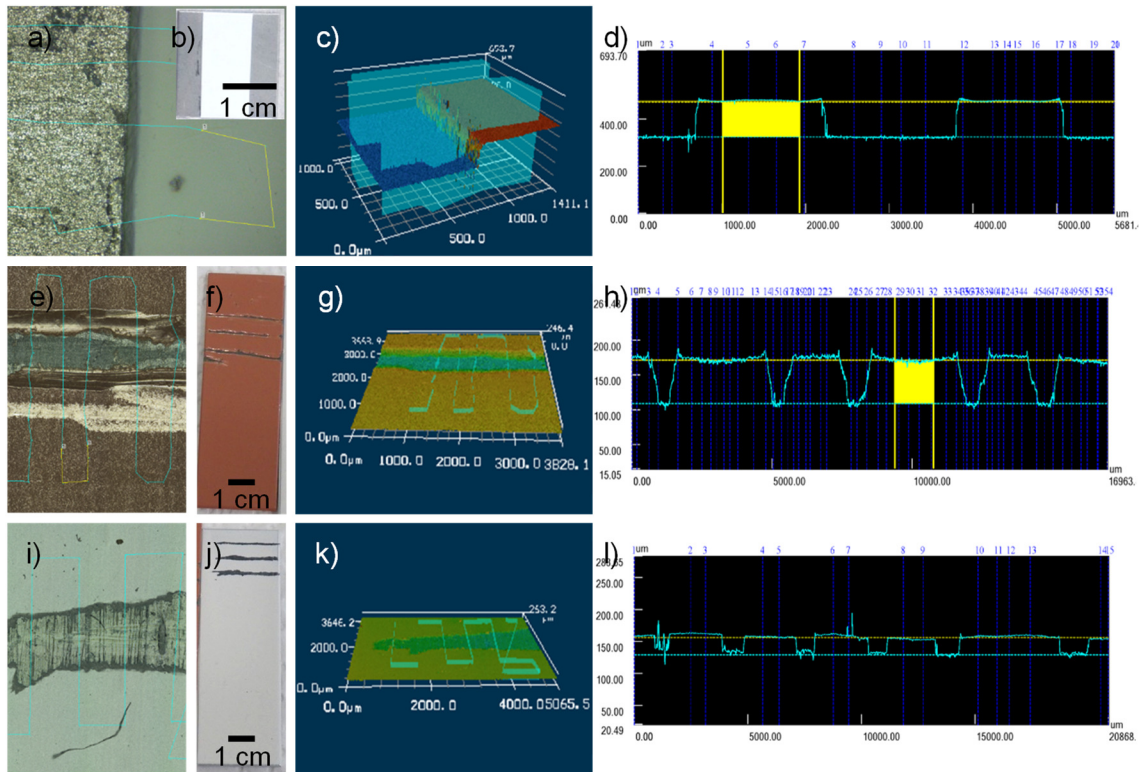
Figure 36. Height profile analysis of three different coated paint formulations. a-l) Each row provides a digital photograph of the coated sample and a light microscope picture of the analyzed area (10x magnification), a 3D height profile of the analyzed area revealing the smoothness of the paint (height increased from color code blue to red) and a 2D height profile of the analyzed area to evaluate the exact height value. Sample description: a) Hand-coated hard formulation paint without biocide. The Toplac sample without biocide was coated on a stainless-steel plate precursor and analysis had been performed after ripping off the spacings. b) A squeegeed soft paint formulation with biocide. The soft paint formulation containing iron oxide (red coating, 2 wt% Fe_2O_3) was coated on a PVC plate precursor. The paint was partially removed by scratching. c) A squeegeed hard formulation paint with biocide. The Toplac formulation containing tungsten oxide (white coating, 2 wt% WO_3) was coated on a PVC plate precursor. The paint was partially removed by scratching.

Table 8. Paint formulations and their structural analysis.

Coating on:	PVC, max. 150 µm high (150 µm squeegee; velocity 0.5 mm·s^{-1})		PVC, max. 300 µm high (300 µm squeegee, velocity 0.5 mm·s^{-1})	
Biocide (2-5 wt%)	WO_3	Fe_2O_3	WO_3@TiO_2	$(Al/Cu/Mn)O_x$
Formulation	Toplac	SF	Toplac	SF
Solvent content of formulation	25-50 %[548]	20-40 %	25-50 %[548]	20-40 %
Surface	Smooth, agglomeration possible	Rough	Smooth, agglomeration possible	Rough
Thickness	≈ 30 µm	≈ 65 µm	≈ 67-80 µm	≈ 26-44 µm
Shrinkage	80 %	57 %	73-78 %	85-91 %

In general, the height profiles provide also insights into the surface roughness (Figure 36, Table 8). The rougher a surface appeares, the more fouling organisms love to adhere.[163] The smooth surface of hard formulations (cf. Figure 36c) has been suggested to impede the bacterial adhesion in early stages. Therefore, the biocides and the formulation matrices have to be highly complementary. In a poor condition, the embedding of additional pigments in hard paint formulation results in agglomeration and/or a coverage of particles being not suitable for catalysis anymore. Particles which are highly compatible with hard formulations provide smooth, stable surfaces in combination with catalytic activity and a long coating lifetime. Self - polishing coatings appear rougher in their dried stages than the hard formulations. But in aqueous conditions they combine physical and chemical defense strategies against biofouling because of their soft, swellable and porous structure. Firstly, fouled superior coating layers can be ripped off easily by fluid dynamics while the ship is in service. Additionally, the surface coatings are said to provide always fresh biocidal substances either because of the self-cleaning process or due to freely diffusion and release processes within the paint formulation.[495,501,502,512–515] Because of this, soft paint formulations are the most frequently and conventionally used devices in marine industry.

2.5   Paint Formulations: Laboratory Performance Tests

The bacterial adhesion test system provided a further step in the material testing process. Potent haloperoxidase mimics identified by MCD or PR dye testing were embedded into different hard and soft paint formulations as described in Chapter 2.4. Coated test panels were then exposed to bacteria medium containing sea water concentrations of bromide and hydrogen peroxide as well. Within this lab testing, the catalytic activity of the biocide to form hypohalogenated species was evaluated against living systems.

Materials that show a lowered amount of adhered bacterial colonies compared to references might be good candidates for further field tests.

Hard paint formulations with a varying amount of bulk $VSbO_4$,[1] which were promising in previous MCD-haloperoxidase studies,[1] were investigated for their antimicrobial activity against *E. coli.*

---

[1] VSbO$_4$ material, analysis and test results provided by BASF.

Elemental and surface analysis of VSbO$_4$ reveal an excess of vanadium (molar ratio of V:Sb ≈ 3:1)[1] with a surface area of 71 m^2·g^{-1}.[1] X-ray diffraction analysis[1] (Figure 37a) indicates different crystalline composites: isotopic phase of antimony vanadium oxide (Sb$_{0.917}$V$_{0.917}$O$_4$, tetragonal), *Senarmontite* (syn-Sb$_2$O$_3$, cubic), *Valentinite* (syn-Sb$_2$O$_3$, orthorhombic) and eventually *Cervantite* (syn-Sb+3Sb+5O$_4$, orthorhombic).
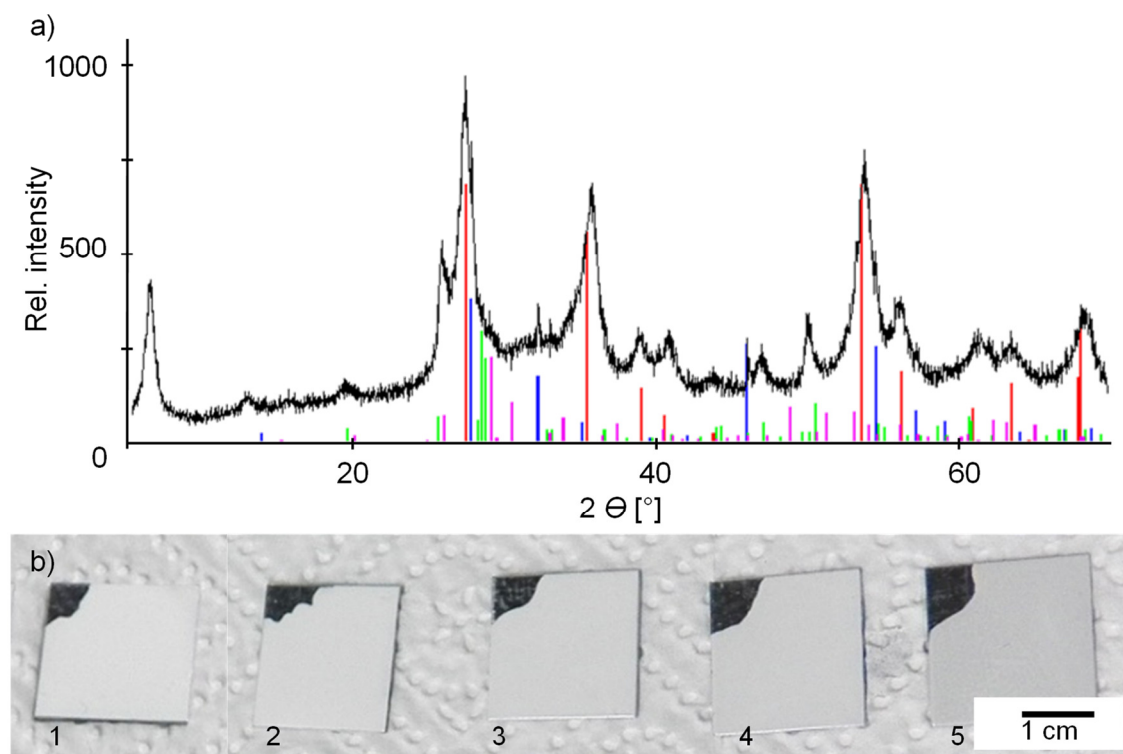
Figure 37. Analysis of VSbO$_4$. a) XRD analysis[1] of VSbO$_4$. Structures assigned to: tetragonal (Sb$_{0.917}$V$_{0.917}$)O$_4$ (red), cubic *Senarmontite*, syn (Sb$_2$O$_3$, blue), orthorhombic *Valentinite*, syn (Sb$_2$O$_3$, green) and possibly orthorhombic *Cervantite*, syn (Sb^{III}Sb^{V}O$_4$, pink). b) Painted steel plates before starting the bacterial adhesion tests with varying amount of VSbO$_4$: (1) 0.0, (2) 0.5, (3) 1.0, (4) 2.0 and (5) 5.0 wt% of dry weight.

A commercially available "Toplac" hard paint formulation was supplemented with 0.5 to 5.0 wt% VSbO$_4$ (determined by dry weight, see Experimental Section, page 223). Afterwards, 2x2 cm steel plates was painted by brushing, and dried for 5 days at room temperature. With increasing amount of the black VSbO$_4$ powder, the samples darkened slightly (Figure 37b). Plates coated by the paint formulation without biocide were provided as controls. All samples were supplied in duplicates. The dried painted steel plates were placed in sterile centrifugal tubes and exposed to bacteria growth media inoculated with *E. coli* at 37°C and soft agitation. After a short incubation time, sea water concentrations of KBr and H$_2$O$_2$ were added. To maintain the concentration of H$_2$O$_2$ and Br$^-$ in the media, these substrates were added sequentially minimum three times a day.
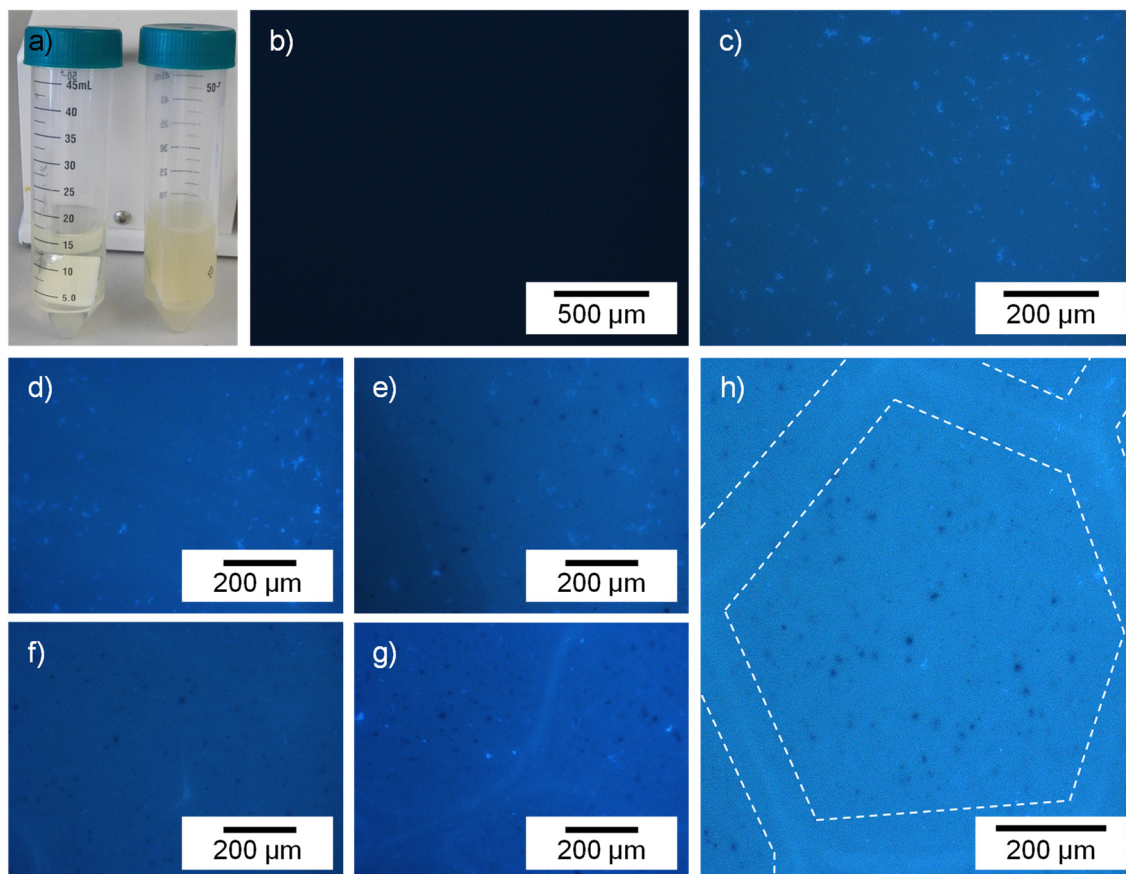
Figure 38. Results of the bacterial adhesion assay of VSbO$_4$. a) Control samples (painted steel plates without biocide) in LB reaction media after the bacterial adhesion tests. Left: negative control without biocide and without *E. coli,* right: positive control without biocide but with *E. coli*. Fluorescence images of the corresponding DAPI-stained control samples (magnification 20x) after reaction time (4 days) show b) no bacterial adhesion (negative control) and c) bacterial adhesion indicated by blue "dots" (positive control). Fluorescence images of the DAPI-stained samples with varying amount of VSbO$_4$ d) 0.5, e) 1.0, f) 2.0, g) 5.0 wt% indicate a concentration dependent reduction of bacterial adhesion up to 2.0 wt% VSbO$_4$. h) Fluorescence image of the DAPI-stained samples with 5.0 wt% VSbO$_4$ after bacterial adhesion assay (magnification 20x). VSbO$_4$ appeares as black "spots" within a honeycomb-like paint defect (framed by white dotted lines).

The control samples without biocides were supplemented to media without bacteria (negative control) and with bacteria inoculation (positive control). The added bacteria grew well in the yellow media yielding a turbid suspension. Digital photographs of both reaction mixtures are shown in Figure 38a right after the last addition of KBr and H$_2$O$_2$.

After the incubation time (3-4 days), the substrates were washed gently with pure media. Bacterial DNA was stained with the fluorescent dye 4,6-diamino-2-phenylindole (DAPI, 1 µg·mL^{-1}) and subsequently, the bacterial colonization upon the plates was analyzed by fluorescence microscopy.

The presence of bacterial colonies can be detected easily by the presence of bright blue "dots" or "clusters". For a general illustration, some fluorescence microscopic images of the corresponding DAPI-stained samples are demonstrated in Figure 38. With regards to the negative control sample (Figure 38b), blue fluorescent spots are not observable. In comparison, intense blue "dots" are visible in the positive control sample due to the presence of bacterial colonies (Figure 38c, *q. e. d.*). The evaluation of antifouling activity of the $VSbO_4$ containing paint formulations (0.5 to 5.0 wt%) is performed in relation to these controls. Representative digital images of the fluorescent samples with varying $VSbO_4$ amount are utilized in Figure 38d-g. The non-fluorescent, partially agglomerated $VSbO_4$ particles appear as black "spots" while the occasional light blue fluorescent "spots" indicate the presence of bacterial colonies.

An antifouling effect is already observed at a low concentration of 0.5 wt% $VSbO_4$ (Figure 38d) and maintains at higher concentrations. The sample containing 2.0 wt% $VSbO_4$ (Figure 38f) shows the best activity against bacterial surface adhesion indicated by the absence of blue fluorescent "spots". The sample containing a biocide amount of 5.0 wt% (Figure 38g) seems to have a lower antifouling activity. Agglomeration of particles or paint defects might have affected the biocide performance negatively: i) enhanced surface roughness promoting bacteria adhesion[163] and ii) reducing the availability of the catalytic material (cf. Chapter 2.4).

In this case, the decrease in activity of $VSbO_4$ might have resulted from a destabilization of the paint formulation with increasing amounts of additional particles. Thus, defects as tiny cracks or fissures have begun to form. Figure 38h highlights the hexagonal, honeycomb defect structures (framed by white dotted lines) that was found in a high amount throughout the whole sample. Bacteria adhered mainly at these edges and rims as it has been known for the preferred surface roughness[163] observable for many biocides mixed into the commercial Toplac paint formulation. Because of this, the amounts of additional particles used in these formulations have been limited to 2.0 wt%.

Gaining deeper insights about the catalytically active species, a ^{51}V-NMR kinetic study of $VSbO_4$ was performed in deuterated water within two days (d-H_2O, one recorded spectra in one hour). By mixing the particles in d-H_2O (23.5 mg in 1 mL), a green turbid suspension resulted. In analogy to V_2O_5 (Figure 30), signals of soluble vanadium oxide species were recorded. Figure 39 illustrates a selection of ^{51}V-NMR kinetic spectra.
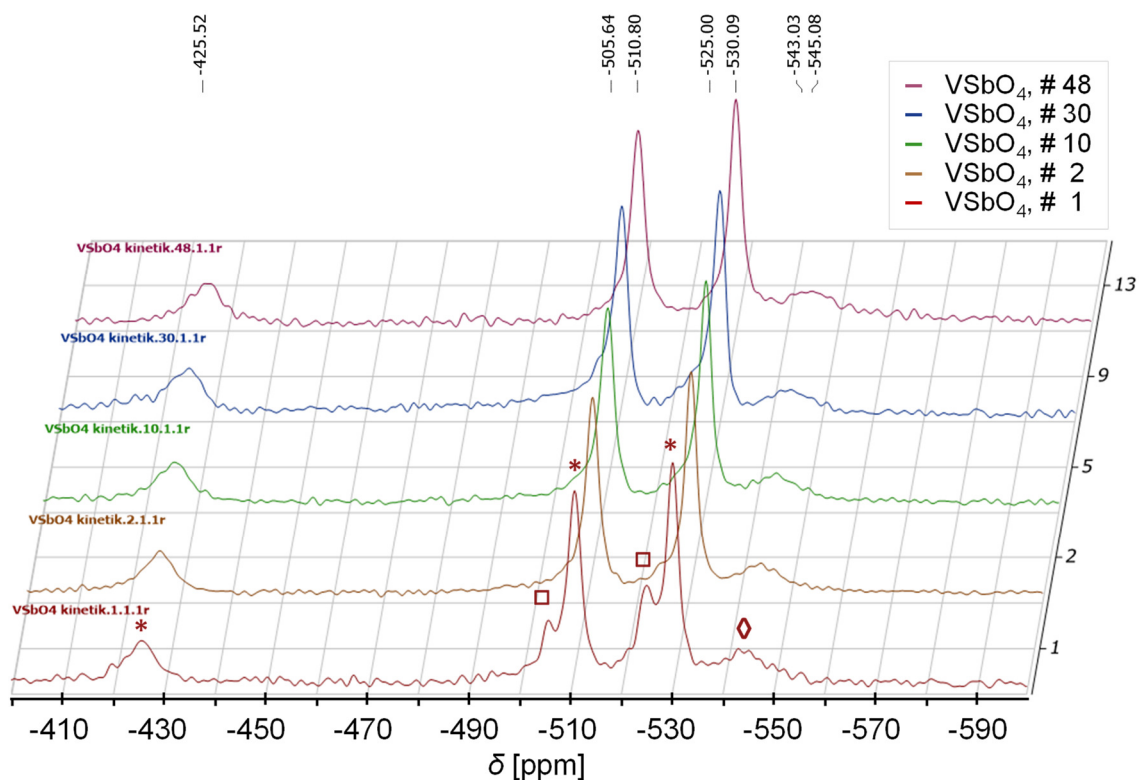
Figure 39. Stacking mode of a selection of ^{51}V-NMR kinetic spectra of VSbO$_4$ in D$_2$O. Record details: 32 scans/spectrum, one spectrum per hour, 48 spectra in total. The spectra were recorded according to the chemical shift of an external standard (VOCl$_3$). Normalized and smoothed spectra illustrated from bottom to top: spectrum number 1 (red), 2 (orange), 10 (green), 30 (blue), 48 (pink). Signals at: -425.52, -505.64, -510.80, -525.00, -530.09, -543.03, -545.08 ppm. Signals are assigned to decavanadate (*), low-molecular weight vanadium containing compounds (◊) and signals of unclear origin (□) disappearing in the course of the measurements.

The main signals are assigned to the decavanadate species and to low molecular vanadium containing compounds as discussed on page 92.[536,541,542] Compared to V$_2$O$_5$, the signals shift to more positive values (approximately +2 ppm) within variations in the chemical surrounding. It is hypothesized that this effect originates from the influence of antimony. Additionally, two signals at – 505.64 and -525.00 ppm are found in the first recorded spectrum disappearing afterwards.

This indicates further, less shielded species with an octahedral geometry and shifts with lower negative values: ≈ +4 ppm compared to the decavanadate signals. Their exact origin and their subsequent disappearance remain unclear. However, the detection of soluble vanadium containing species relates the antifouling activity of the paint formulation to leachable species in addition. It cannot be assigned properly whereas hindered bacterial adhesion have resulted from i) the toxicity of vanadium or antimony itself or ii) haloperoxidase-like activity of leached vanadium species or, most probable, iii) a combination of all effects.

Although the sterically and oxygen "saturated" decavanadate as active species can be excluded, preliminary stages in the formation of vanadium oxide clusters (c.f. NMR signals of unclear origin) might be potent catalysts. Although the bacterial adhesion assays are only qualitative and *E. coli* as standard laboratory bacteria do not necessarily appear in natural sea water, the results revealed highly reliable. Additionally, the findings correlated strongly with findings obtained in field tests. Therefore, the bacterial adhesion assay represents a great tool to identify potent biocides in natural-like environment.

In the course of the BASF project, a bundle of laboratory bacterial adhesion assays was performed to identify potent active antifouling agents. Varying amounts of biocides that were promising in previous MCD or PR haloperoxidase - studies were embedded and tested in both a commercial hard coating precursor (Toplac) and an abrasive soft paint formulation (provided by BASF). A general overview about the materials tested in the laboratory bacterial adhesion assays as discussed in detail for $VSbO_4$ is given in Table 9. Mainly, materials with transition metals as potent active species were focused as discussed in Chapter 1. The bacterial colonization at the coat surface was evaluated in relation to control samples being performed newly in each test campaign. On the one hand, increased bacterial adhesion was found in abrasive paint formulations being rough by definition. But on the other hand, the porous structure of abrasive paint formulations gave access to the biocides or biocidal products.

It is postulated that abrasive paint formulations are more active by using leachable, toxic species (V, W, Mo cf. V_2O_5, $VSbO_4$, WO_3, MO_3 etc. in Table 9) or diffusible biocidal intermediates as discussed for materials with potential HPO-like activity. Stable, hard formulations are said to hinder free diffusion of catalysts and their products. Therefore, they seem to be more suitable for insoluble substances with local, for example, peroxidase-like activity as provided by iron or manganese compounds (Table 9). This has been demonstrated for Cu_2O which is completely inactive in hard formulations (Table 9). The paint formulation stabilizes Cu_2O so that no active Cu^{2+} ions can be released. In contrast, Cu_2O is greatly active in soft paint formulations (Table 9) where the biocides are accessible for e.g. organic chelates extracting toxic Cu^{2+} out of the paint. Preliminary results have shown that vanadium, tungsten and molybdenum in their highest oxidation states are active in both, hard and soft formulations and, as discussed, a smoother surface enhanced the anti-adhesion effect.

Table 9. Summary of potential biocides tested with BASF cooperation. Activity levels in comparison to control samples: ✓✓✓ good activity, ✓✓ moderate activity, ✓ less active, – no activity.

Biocide	wt%	Activity in TL	Activity in RF
$VSbO_4$ darken slightly with wt%	0.5	✓	
	1	✓✓	
	2	✓✓✓	
	5	✓✓	
V_2O_5 @TiO_2	0.5	✓✓	-
	2	-	✓
V_2O_5 (bulk)	0.5		✓✓
	2	-	-
$VO(acac)_2$ green dots, very inhomogeneous, increased surface roughness	0.5; 1; 2	-	
$P/V_{(1:2)}$@αMoO_3 only active with V-excess	0.5	(✓)	
V @α MoO_3	0.5	-	
WO_3 diverse samples	2	✓	
	5	✓✓	-
WO_3@TiO_2 diverse supported W-amounts	0.5	-	✓
WO_3@TiO_2	2	✓✓	✓
WO_3@SiO_2 increased surface roughness	5	✓✓	✓
MoO_3	2		✓
	5	✓	
Mo @TiO_2 darken slightly with wt%, some roughness	0.5; 1;2	✓	
	5	✓✓	
$Mo/W/V$ @Al-Mg-LDH	2	-	
MnO_2 diverse samples	2	✓✓	✓
β-Mn_2O_3	2	✓	(✓)
Mn_3O_4 /Birnessite diverse samples	2	(✓)	✓✓
α & γ Fe_2O_3 some roughness	0.5; 2	✓✓	
α Fe_2O_3 some roughness	0.5	✓✓	✓
	2	-	
Fe_2O_3, Thyssen-Krupp HP	0.5	✓	-
	2	-	-
α Fe_2O_3	1	✓✓	✓
γ Fe_2O_3	1	✓✓	-
Fe_2O_3 (bulk)	0.5		-
	2	✓	✓✓
Cu_2O	10	(✓)	✓✓✓
$CuFe_2O_4$; $CuZnFe_2O_4$	2	✓	
60%Cu, 20%Al, 20%Mn	2	✓✓	✓✓
	5	-	-
$MnWO_4$; $ZnWO_4$	1	-	
Ag_2WO_4	5	✓	-

FeMn$_2$O$_4$	2	(✓)	-
CoMn$_2$O$_4$; NiMn$_2$O$_4$	5	✓	-
ZnMn$_2$O$_4$	2	✓	-
	5	✓✓	-
In$_2$GaZn$_2$O$_{6.5}$	5	-	-
Cs$_2$HPMo$_{11}$VO$_{40}$	2	-	(✓)
diverse compositions	5	✓	(✓)

This points to a combinatory effect of leachable biocidal species (polyoxometalates, heteropoly acids), haloperoxidase/peroxidase-like products, local toxicity of the metal and the surface character of the coat.

In contrast, vanadium(IV) occurring in vanadyl acetyl acetonate (Table 9) did not show any activity under these reaction conditions. Iron(III) oxide, some copper containing materials as Cu/Al/Mn mixed oxides and the tungsten doped TiO$_2$ samples were identified as promising potential additives at low concentrations. In particular, iron oxide species were proposed to have different catalytic activities.

Primary results in combination with bio-adhesion tests suggest γ-Fe$_2$O$_3$ to be slightly more effective than the pure α-phase.[549] However, such highly redox-active transition metals exhibit more peroxidase- than haloperoxidase-like activity. Titan or cerium dioxide as typical carrier materials might play a non-innocent role in heterogenous catalysis as they are photocatalytic active in addition.[550–552] Thus, these materials and their dopants can increase or diminish each another in respect to their catalytic activity.

Further, doping represents a "dilution" of active species and no antifouling effect was observed for Mo@TiO$_2$ and for the V, W, Mo-doped Mg/Al-layered double hydroxides. Increasing the amount of biocide in the paint formulation can partly counteract the antifouling effect by destabilizing the paint formulation.

Surface defects, enhanced roughness because of particle agglomeration and less exposed catalytic material are identified as the key aspects promoting biofilm formation. Increasing the amount of paint-compatible leachable materials or catalytic materials that produce diffusible compounds will lead to an enhancement in activity. The presented effects on antifouling paint performance depicted just a few out of many contributing factors. Paint optimization, customization as well as further research on additives that are catalytically active rather than simple being soluble and toxic will be the key aspects in near future.

In the following Chapter, the development of such a material is highlighted. Cerium dioxide nanoparticles combined high stability, insolubility, non-toxicity with exceptional haloperoxidase-like catalytic activity. The performance of the catalyst is described starting from the explanation of the catalytic mechanism up to in-field tests of different paint formulations.

3

Cerium Dioxide Nanorods

Haloperoxidase Mimicry by Cerium Dioxide Nanorods Combats Biofouling

"All structures in natural waters suffer from biofouling, the colonization of aquatic organisms that wreak havoc on shipping and offshore industry. Chemical antifouling coatings release toxins like copper and other co-biocides to retard the growth of algae and encrusting organisms. In contrast, Nature's defense strategy against epibiont growth relies on vanadium-dependent haloperoxidases (V-HPOs) and other halogenating enzymes which catalyze the oxidative halogenation of signaling compounds that prevent biofilm formation by interfering with bacterial cell-cell communication. Here we show that CeO_{2-x} nanorods emulate halogenating enzymes by catalyzing the conversion of bromide ions to reactive intermediates that target signaling compounds controlling bacterial quorum

sensing. This maximizes damage in bacterial biofilms with minimal collateral effects to the environment. Laboratory and field tests with paint formulations containing 2 wt% of CeO_{2-x} nanorods showed a reduction in biofouling comparable to Cu_2O, the most typical biocidal pigment. Nanoceria has the potential to be a non-toxic and sustainable substitute for conventional inorganic/organic biocides."

3.1   Introduction

"Marine organisms, that are under a constant threat of being overgrown by epibionts, have evolved chemical or physical antifouling strategies.[498,553] Marine algae have developed chemical mechanisms against microbial fouling by disrupting the quorum sensing, a process by which bacteria monitor cell density and regulate (among others) biofilm formation.[166,503] The algae *Corallina officinalis* and *Delisea pulchra* secrete vanadium haloperoxidases (V-HPOs),[147,394] a group of enzymes that plays a key role in the inactivation of cidal cell-to-cell communication[554] by catalyzing the oxidation of halides (Cl^-, Br^-, I^-) with hydrogen peroxide (H_2O_2) to the corresponding hypohalous acids (HOBr, HOCl).[133] The reactive HOX (X = Cl, Br) intermediates react in follow-up reactions to halogenated *N*-acyl homoserine lactones (AHLs), a class of signaling molecules involved in bacterial quorum sensing.[133,185,186] V-HPO in *D. pulchra* is located extracellularly on the algae surface where it thwarts the colonization of surface seaweed.[394,554] Functional recombinant V-HPOs have been produced[149] and HPOs have been proposed as additives in antifouling paints,[71,555] but the use of natural or recombinant enzymes raises the issues of production costs, long-term stability, and proper reaction conditions.

Current antifouling research focuses on the design of environmentally benign solutions including engineered microtopographies,[556,557] enzyme-based coatings,[503] or natural product antifoulants.[147] The biomimetic inhibition of biofouling, as observed in marine organisms, is a strategy for developing novel environmentally friendly and cost-effective antifouling technologies. Several η^2-peroxo compounds mimicking V-HPOs have been reported,[162,247,253,255,259,558] particularly vanadium complexes or V_2O_5 nanoparticles[424] with catalytic efficiency and selectivity in oxidative halogenation,[253,255] sulfoxidation,[259] and epoxidation[259] reactions. However, their large-scale application re-

mains highly questionable as vanadium compounds are mutagenic, carcinogenic and ter-
atogenic. They are classified as critical according to the REACH criteria,[275] and some
countries are threatening to ban even the use of copper in antifouling paints by 2020.[553]

Inspired by the catalytic activity of cerium oxide in oxidation/halogenation,[312]
the oxyhalogenation of activated arenes,[427] and role of the Ce^{3+}/Ce^{4+} redox couple in the
halogenation of malonic acid in the Belousov-Zhabotinsky reaction,[310] we acquire here
a deeper understanding of the intrinsic haloperoxidase activity of ceria nanoparticles to
combat biofouling.

By virtue of the $Ce^{3+/4+}$ redox potential, cerium can switch reversibly between its
tri- and tetravalent states. As a result, fluorite-type ceria (CeO_{2-x}) is non-stoichiometric
with oxygen vacancies.[559] Its success in chemical and electrochemical[550,559] catalysis is
connected not only to these unique redox and structural properties associated with oxygen
diffusion and oxygen storage/release capacity, but also to its abundance, stability and en-
vironmental compatibility. The redox cycling capabilities of nanoceria are comparable to
those of biological antioxidants, which makes it an efficient scavenger for reactive free
radical species. Ceria nanoparticles exhibiting peroxidase,[560] superoxide dismutase,[561]
and catalase activity[17] can remove reactive oxygen species (ROS) like superoxide (O_2^-)
or hydrogen peroxide (H_2O_2), e.g. as a protection against ischemic stroke even in an *in
vivo* animal model.[12]

Here we demonstrate that CeO_{2-x} nanorods exhibit an intrinsic haloperoxidase-
like activity by catalyzing the bromination of organic signaling compounds. CeO_{2-x} na-
norods show quorum-sensing-regulatory properties similar to natural or engineered vana-
dium haloperoxidases and halogenases.[71,158] Test panels with paint formulations con-
taining CeO_{2-x} nanoparticles in marine water show the strong inhibitory effect of the na-
noparticle enzyme mimic in natural environment."

3.2   Synthesis and Structural Characterization

"CeO_{2-x} nanorods were synthesized hydrothermally.[562] CeO_{2-x} crystallizes in the
fluorite structure type as confirmed by X-ray powder and electron diffraction (Figure 40
and Figure 41) as well as high-resolution transmission electron microscopy (HRTEM,
Figure 42a, b, Figure 41). The overview TEM image in Figure 42a shows rod-like parti-

cles with lengths ranging from 20 to 100 nm and lateral dimensions of ≈ 10 nm deter-

mined from lateral length and width analysis (Figure 41) resulting in a Brunauer-Emmett-

Teller (BET) surface area of 82.5 m^2g^{-1} (Experimental Section, page 190).
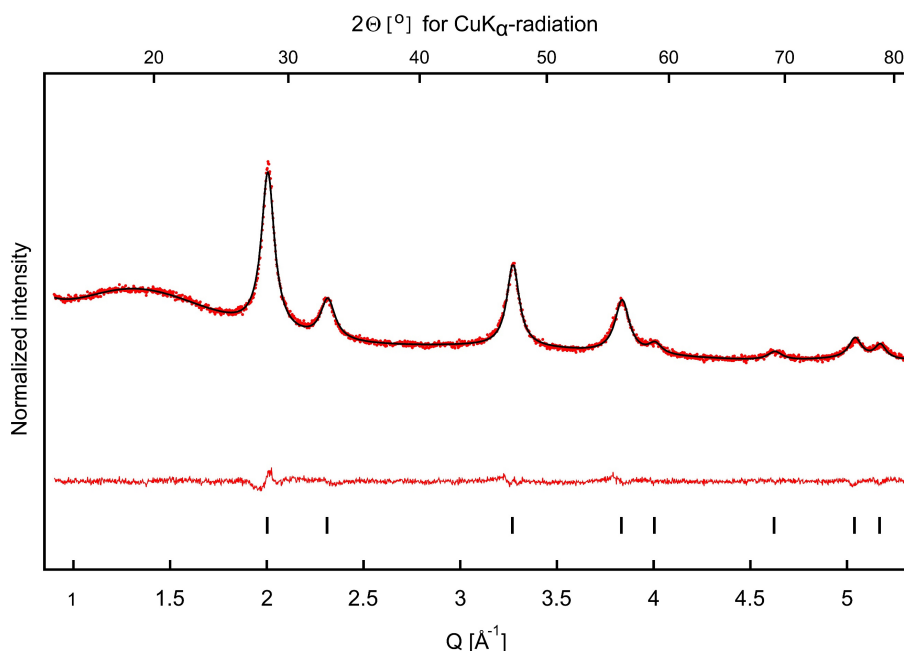
Figure 40. X-ray powder diffraction of CeO_{2-x} nanorods. Rietveld refinement (black line) on diffraction data (red dots) and difference between the measured and theoretical profile (red line) for the cubic CeO_2. The reflection position is given on a wavelength and technique independent scale in reciprocal space units or momentum transfer $Q = 4\pi \cdot \sin \theta / \lambda$ (bottom) and in terms of the Bragg angle 2θ (top).

The HRTEM image (Figure 42b) and 3D electron diffraction data (Figure 41)

show the nanorods to be polycrystalline with three crystallographically aligned single-

crystalline domains having $[1\bar{1}0]$ orientation along the nanorod. The polycrystalline con-

struction of the nanorods is evident form electron diffraction data and is additionally sup-

ported by the full pattern refinement of the X-ray diffraction data (Figure 41) with the

Rietveld method using the fundamental parameter approach for line profile modeling.[563]

Within this approach, the broadening of the reflection profile due to crystallite size, in

particular, the appearances of Fourier ripples in the lattice factor F_L (*hkl*) is modeled by

folding the line profile due to experimental setup with a Lorentzian line profile for crys-

tallite size broadening. The full width half maximum (FWHM) of the latter is given by

FWHM = $\lambda/(T\cdot\cos \theta)$, in which θ is the scattering angle, λ the wavelength of the mono-

chromatic X-rays and T the apparent crystallite size. The apparent crystallite size T refers

to a spherical crystallite, yet anisotropic crystal shapes may be modeled as well using *hkl-*

dependent corrections like spherical harmonics or quadratic forms. Using this approach, the (average) crystallite size was determined to 6.8(1) nm × 9.5(2) nm × 7.0(1) nm, corresponding to an aspect ratio of ≈ 1.5. Further information is compiled in the Experimental Section, page 188.
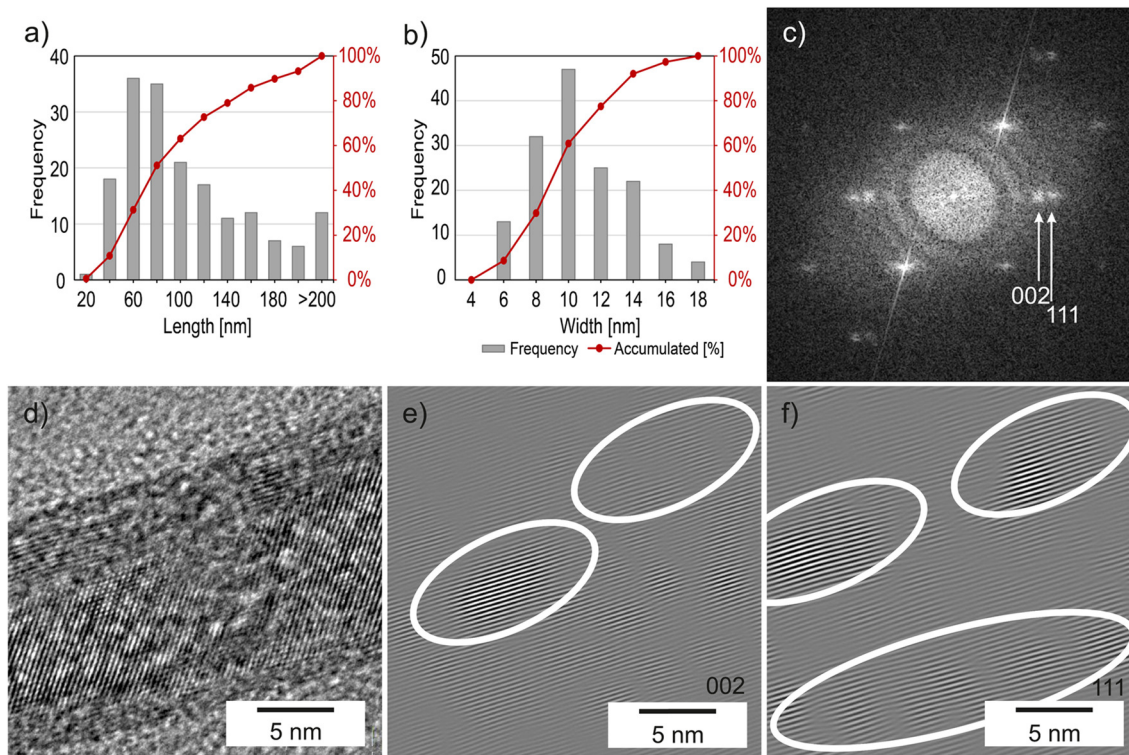
Figure 41. TEM analysis of CeO$_{2-x}$ nanorods. a) Length and b) width distribution diagrams of ceria nanorods based on approx. 150 individual particles. The fragile nanoparticles show a broad length distribution as they break easily during grinding. In contrast, the width distribution is narrow (6-12 nm for approx. 80 % of the particles analyzed). This correlates with a value of 10 nm for HR-TEM image shown in d). c) Electron diffraction pattern of a single nanoparticle to underline the splitting of the reflections (white arrows). Based on the HR-TEM image of a single nanorod d), the corresponding Fourier filtered images outline the 002 reflections: e) Originating from the inner part of the nanoparticle (higher contrast in the outer areas, white cycles), while the 111 reflections originate from the outer rims (f). The reverse Fourier transformation was used to generate the filtered images e) and f) because the phase information would be lost if electron diffraction data were used instead.
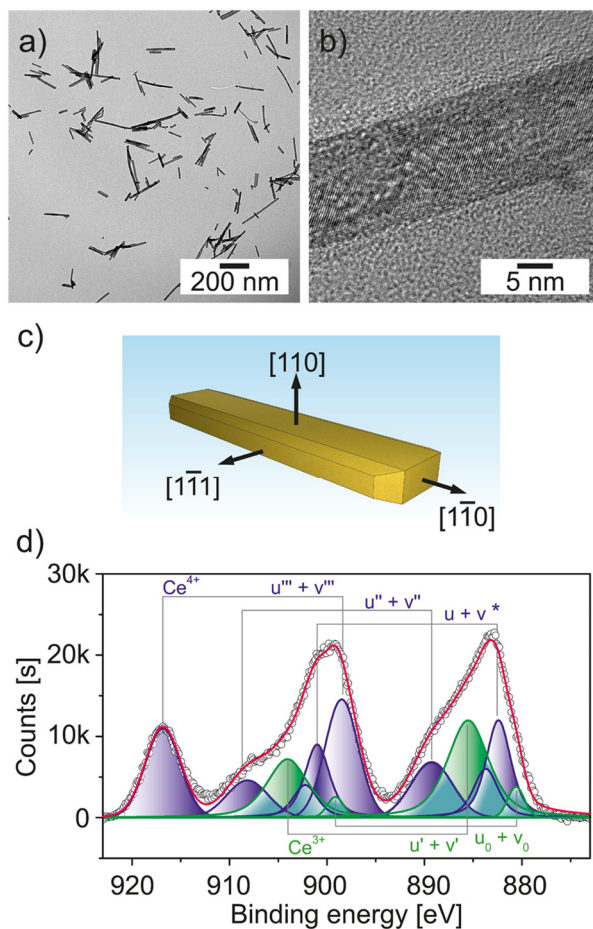
Figure 42. Defect structure of CeO_{2-x} nanorods. a) TEM image of CeO_{2-x} nanorods. b) HRTEM image of a single CeO_{2-x} nanorod. c) Morphology and exposed crystal surfaces of a single CeO_{2-x} nanorod. The triple construction of the nanorods is confirmed by a specific reflection splitting seen in electron diffraction data and lattice fringe images in HRTEM. The inner part of the nanorods is oriented with the [110] direction along the incident electron beam when placed on TEM grids, which suggests 110 type facets as bottom and top surfaces (see SI for details). d) XPS (Al-Kα) core level spectrum of the Ce 3d signals of the CeO_{2-x} nanorods with the corresponding peak fitting model (PFM) with deconvolution into three Voigt doublets corresponding to Ce^{4+} (u+v, u''+ v'' and u'''+ v'''. The asymmetry of the Ce^{4+} 3d u+v doublet was modelled as a sum of two constrained Voigt profiles (*) shifted by 1.30 eV towards higher binding energies and an intensity ratio of 0.50 with respect to the u+v doublet) and deconvolution into two Voigt doublets corresponding to Ce^{3+} ($u^0 + v^0$ and u' + v', all Voigt). The intensities indicate the preference of Ce^{3+} (36-45 %) for surface sites.

The presence of Ce^{3+} is indicated by the optical appearance (yellowish color, c.f. inset Figure 43d, *vide infra*). The Ce^{3+} content of ≈ 0.5 at% was quantified by superconducting quantum interference device (SQUID) magnetic susceptibility measurements (based on a magnetic moment of 2.54 μ_B for Ce^{3+} (100 %), details in the Experimental Section, page 191). High-resolution Ce 3d X-ray photoemission spectroscopy (XPS) (binding energy: 930-875 eV, Figure 42d) was used to estimate the portion of reactive

Ce^{3+} surface centers. The detailed description of the deconvolution method and the corresponding survey spectrum are presented in the Experimental Section, page 192. Complete deconvolution[564,565] of the peaks with respect to the 3d$_{5/2}$ and 3d$_{3/2}$ transitions of Ce^{4+} and Ce^{3+} (Figure 42d), yielded a relative amount of $\approx$ 36-45 % Ce^{3+} with respect to the surface integrals. In combination with the expected ionic radii of Ce^{4+} (111 pm) and Ce^{3+} (128 pm), this provides strong evidence that oxygen defects associated with Ce^{3+} predominantly occur at the particle surface rather than in the bulk. Thus, the catalytic activity appears to be correlated with the defect structure of CeO$_{2-x}$."

3.3   Haloperoxidase Activity

"The haloperoxidase-like activity of ceria nanorods was demonstrated using the phenol red bromination assay (Figure 43a) that involves the selective fourfold oxidative bromination of phenol red (PR, phenolsulfonphthalein) to bromophenol blue (Br$_4$PR, 3′,3″,5′,5″-tetrabromophenolsulfonphthalein), which can be monitored spectrophotometrically[247] from the absorption maxima of PR ($\varepsilon_{430} = 23900 \pm 100$ M^{-1}cm^{-1}) and Br$_4$PR ($\varepsilon_{590} = 72200 \pm 100$ M^{-1}cm^{-1}) in MilliQ water (cf. Experimental Section, page 207). Figure 43b shows typical time dependent scans recorded over 600 min in an aqueous reaction mixture (MilliQ-water, 18.2 MΩ·cm^{-1}, pH 5.6, room temperature) containing CeO$_{2-x}$ nanorods, PR and NH$_4$Br as bromide source. H$_2$O$_2$ was added to the mixture shortly before the measurements to trigger the reaction. Controls in the absence of Br$^-$, H$_2$O$_2$, PR, CeO$_{2-x}$ (or any combination) did not show any PR bromination (see Experimental Section, page 208). The formation rate of the bromination product Br$_4$PR is extracted from the absorbance at 590 nm (Figure 43c). Calibrations, blank tests and controls were performed to optimize the substrate concentrations and to confirm the kinetic parameters by varying the concentration of one substrate while keeping all other concentrations constant (a detailed description about the calculations is given in the Experimental Section, page 210).
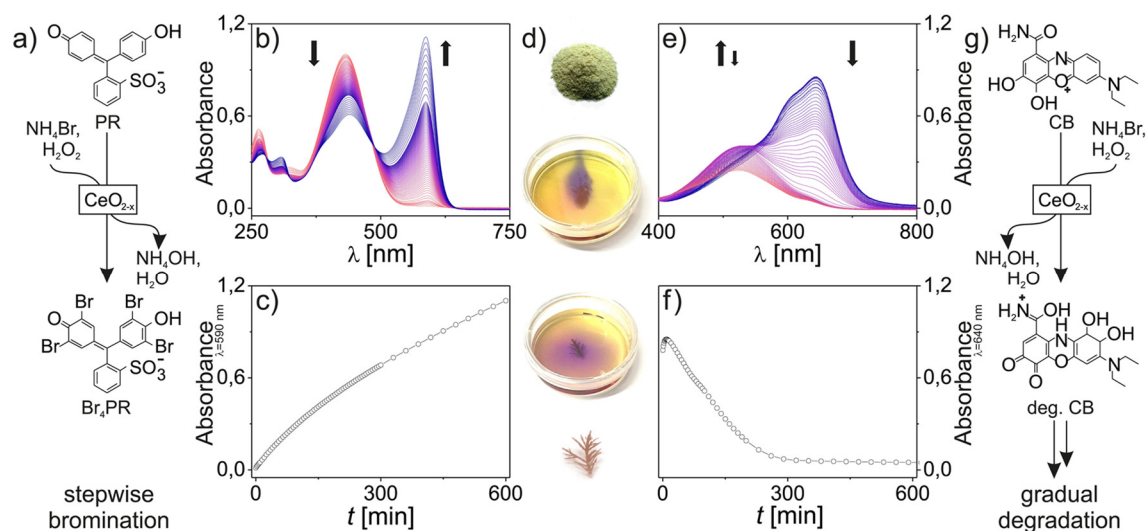
Figure 43. Illustration of the oxidative bromination reaction catalyzed by the CeO_{2-x} nanorods. a) Scheme of the oxidative bromination of phenol red (PR) to bromophenol blue (Br_4PR). b) Time dependent UV-Vis spectra showing the kinetics of the oxidative bromination of PR catalyzed by CeO_{2-x} nanorods (50 µM PR, 25 mM NH_4Br, 300 µM H_2O_2, 25 µg/mL CeO_{2-x}, 600 min, 23-25°C). c) Extracted kinetics from the absorbance at 590 nm. d) Oxidative bromination of PR catalyzed by CeO_{2-x} (2.1 mg, top) and by algal pieces of *C. officinalis* (7.1 mg, bottom, 50 µM PR, 25 mM NH_4Br, 300 µM H_2O_2) in a total volume of 4 mL and 100 min after addition of hydrogen peroxide. At pH ≈ 6 PR appears yellow, Br_4PR blue and partially brominated compounds (Br_xPR, x = 1, 2, 3) cause the color gradient. e) Time dependent UV-Vis spectra showing the kinetics of the oxidative degradation of celestine blue (CB) catalyzed by CeO_{2-x} nanorods (50 µM CB, 25 mM NH_4Br, 300 µM H_2O_2, 25 µg/mL CeO_{2-x}, 600 min, 23-25°C) and f) extracted kinetics from the absorbance at 640 nm indicating the formation of oxidized bromine species (e.g. HOBr). g) Illustration of the oxidative degradation of CB[246] catalyzed by CeO_{2-x} nanorods.

The kinetics (where k_{gen} is the general reaction constant, and [S] and [S]$_0$ are the substrate and initial substrate concentrations, respectively) follows the Equation $v = d[Br_4PR]/dt = k_{gen}[CeO_{2-x}]_0[NH_4Br]_0[H_2O_2]$. For experimental details and details concerning the calculations see Experimental Section, page 210. The reaction showed Michaelis-Menten behavior; the Michaelis-Menten constants (K_m) and the maximum reaction rates (v_{max}) were determined by Lineweaver-Burk linearization. For low substrate concentrations (CeO_{2-x}, H_2O_2 and NH_4Br) the values were plotted in logarithmic form to extract the specific reaction constants (k) and the reaction orders (a) using the initial rate method. A detailed description of the calculation method, plots and compiled kinetic parameters are given in the Experimental Section, starting with page 210.

The kinetic parameters with respect to H_2O_2 are within one order of magnitude, with respect to bromide (NH_4Br) two orders of magnitude higher to those found for the biological samples, particularly, a vanadium chloroperoxidase (V-CPO) mutant from

Curvularia inaequalis (K_m (H_2O_2) = 16 μM, K_m (Br⁻) = 3.1 mM)[566] and vanadium bromoperoxidase (V-BPO)[137] from *A. nodosum* (K_m (H_2O_2) = 22 μM, K_m (Br⁻) = 18.1 mM) or V_2O_5 (K_m (H_2O_2) ≈ 10 μM, K_m (Br⁻) = 0.2 mM).[424] CeO_{2-x} nanorods are stable at high H_2O_2 concentrations. The turnover frequency (TOF, k_{cat}) of ≈ 48.5 $μM_{Br4PR}$·min⁻¹ per m² of active surface is derived based on the BET surface area of the particles. This value corresponds to a k_{cat} ≈ 194 $μM_{HOBr}$·min⁻¹ per m² active surface (Experimental Section, page 214). An activation energy E_A ≈ 50 kJ·mol⁻¹ was determined from the temperature dependence of the reaction (5 to 55°C, Experimental Section, page 214).

As measurements in the dark and by daylight showed congruent results the reaction is not photocatalytic (Figure 44a-d). The effect of pH on the CeO_{2-x} nanorod bromination activity was assessed by varying the pH from 4.75 to 9.0 while keeping all other reaction conditions constant (Figure 44e). The catalytic activity of the CeO_{2-x} nanorods showed a pH optimum around pH 5.6, and it decreased with increasing pH. At pH 7.0 ≈ 50 % of the activity remained. This can be rationalized based on: (i) the oxidation potentials of CeO_{2-x} (related to its surface state) and H_2O_2 whose reactivity increases in the acidic regime and (ii) the pK_a values (determining the charge) of PR, (iii) protonation and stability of oxidized bromine species. In comparison, wild-type V-CPO (*C. inaequalis*) has its pH optimum at 5.5.[567] The reaction was independent of the bromide source (Figure 44f).
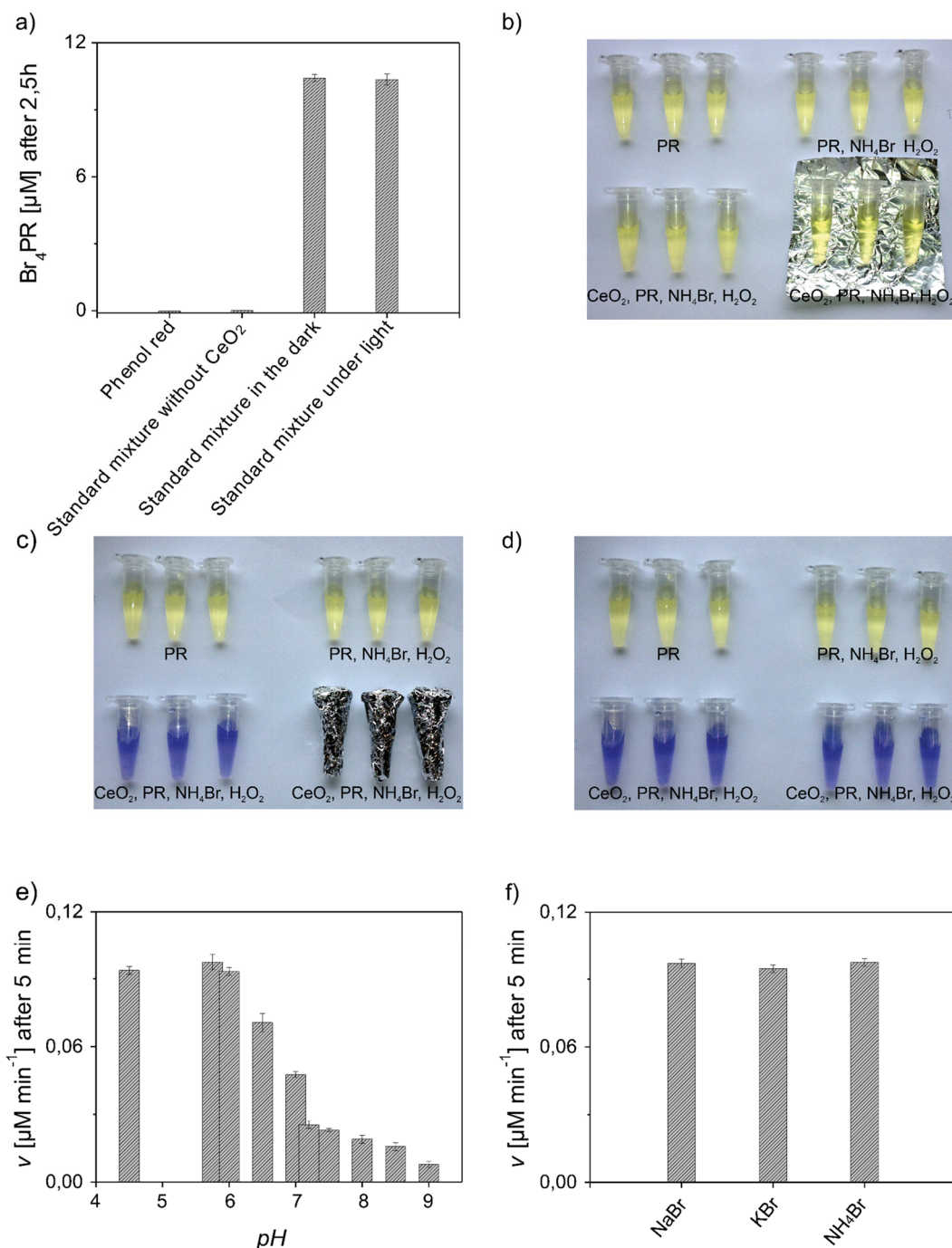
Figure 44. Effect of light, pH and bromide on the oxidative bromination of PR. a) Dependence on light (25 µg·mL^{-1} CeO$_{2-x}$ nanoparticles, 10 µM PR, 25 mM NH$_4$Br and 300 µM H$_2$O$_2$, r.t., 2,5h, reactions performed in triplicates) additionally illustrated by digital photographs of the reactions and controls (PR and reaction mixture without catalyst): b) Before the reaction. Three reaction vessels have been wrapped in aluminum foil to protect from light. c,d) After 2.5h reaction time. c) Samples wrapped and d) unwrapped. e) Dependence on pH adjusted with NaOH and acetic acid (25 µg·mL^{-1} CeO$_{2-x}$ nanoparticles, 50 µM PR, 25 mM NH$_4$Br and 300 µM H$_2$O$_2$, r.t., after 5 min, reactions performed in triplicates). f) Dependence on the bromide source (25 µg·mL^{-1} CeO$_{2-x}$ nanoparticles, 50 µM PR, 25 mM Br$^-$ salt and 300 µM H$_2$O$_2$, r.t., after 5 min, reactions performed in triplicates).

For any application, the stability of a catalyst is essential. Cycle tests (up to 12 cycles) were performed with CeO_{2-x} nanorods (0.1 mg·mL^{-1}), PR (10 µM), NH$_4$Br (25 mM) and H$_2$O$_2$ (300 µM) at room temperature and constant stirring (800 rpm). After each reaction cycle, the CeO_{2-x} nanorods were separated by centrifugation, washed with MilliQ water and treated again with PR, NH$_4$Br and H$_2$O$_2$ under identical experimental conditions. No loss of activity or change of morphology was observed (Figure 45). Leaching experiments (24 h), carried out under operating conditions in water (pH 5.6) and in standard bacterial growth media (pH 7.2) confirmed the long-term stability of the CeO_{2-x} nanorods with a solubility near the detection limit (by inductively coupled plasma mass spectrometry (ICP-MS), Experimental Section, page 194).[568]"
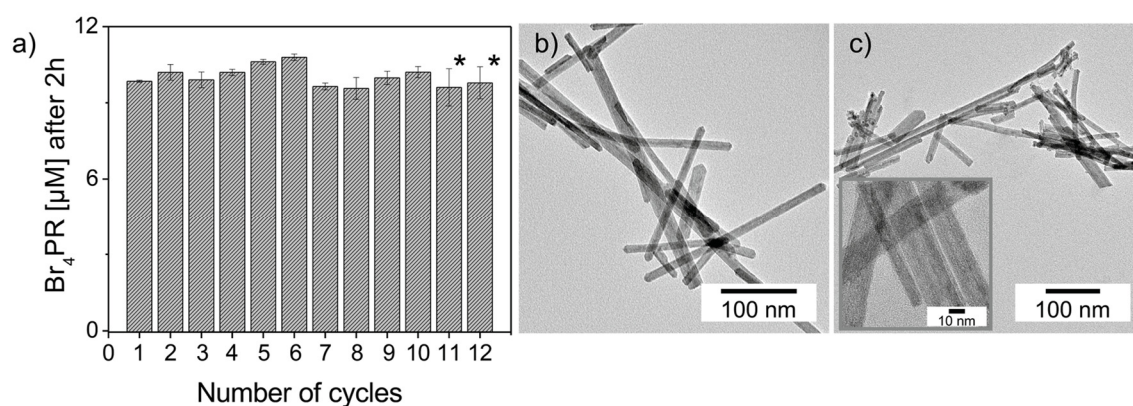
Figure 45. Reutilization test of CeO_{2-x} nanorods. a) Cycle test with CeO_{2-x} nanorods (100 µg·mL^{-1}), PR (10 µM), NH$_4$Br (25 mM) and H$_2$O$_2$ (300 µM). Ten reaction cycles were performed in triplicate. After using one of the three samples for TEM analysis (*, cf. c), the 11. and 12. cycle were measured in duplicate after a storage period of 17 days. The particle morphology in b) and c) remained unchanged after 10 cycles.

3.4   Reaction Mechanism

"The electrophilic attack on the aromatic system of PR and its stepwise bromination to Br$_4$PR were confirmed by time dependent mass spectrometry (Figure 46 and Experimental Section, page 195). After 60 min, the protonated molecule peaks of the PR substrate (*m/z* 355.1 [M+H]$^+$) and of its four bromination products (base peaks (*m/z*) of the proton adducts: BrPR 435.1, Br$_2$PR 513.0, Br$_3$PR 590.9, Br$_4$PR 670.8) were observed and assigned based on the structure of the isotopic patterns. After 24 h, the peak of the fourfold brominated product Br$_4$PR prevailed (cf. Experimental Section, page 195). A gradual color change from yellow (PR) to blue violet (Br$_4$PR) in MilliQ-water (pH ≈ 5.6)

showed the bromination reaction (after 100 min) with CeO_{2-x} nanorods ($\approx$ 0.5 mg mL^{-1}, Figure 43d, top) and pieces of the red alga *C. officinalis* ($\approx$ 1.8 mg mL^{-1}, Figure 43d, bottom and Figure 47), where the native haloperoxidase from *C. officinalis* is located extracellularly.[247] This allows visual monitoring of the formation of Br$_4$PR. Control measurements in the absence of substrates did not show any bromination of PR.
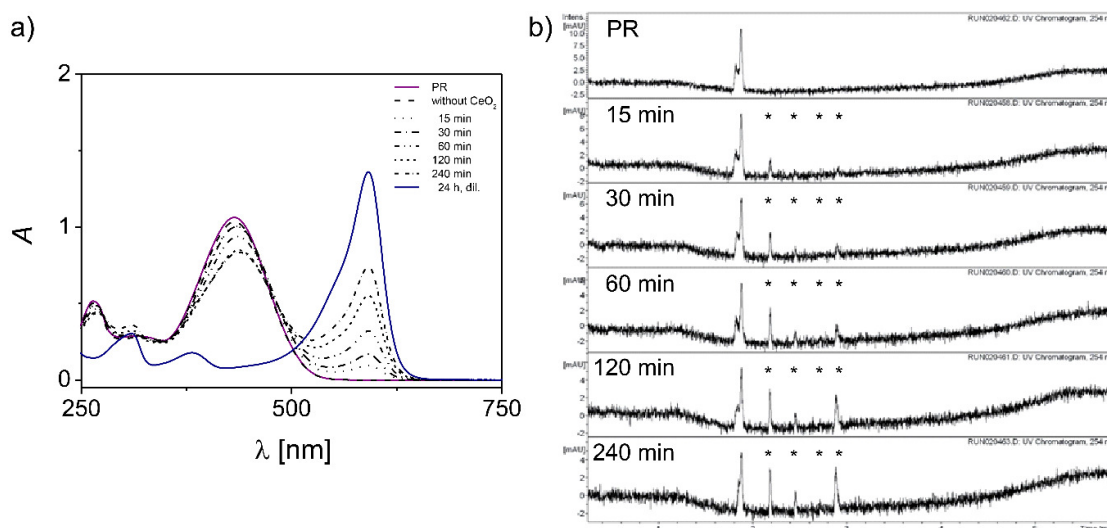
Figure 46. Time dependent UV-Vis spectra and corresponding UV chromatograms for the products of the oxidative bromination of PR. The reactions (aqueous reaction mixture (1 mL) containing CeO_{2-x} nanorods (25µg·mL^{-1}), NH$_4$Br (25 mM), PR (50 µM) and H$_2$O$_2$ (300 µM)) were run in triplicate for a specific period of time (15, 30, 60, 120, 240 min, 24 h; the given concentrations represent the final concentrations in the corresponding reaction mixtures). Afterwards, the reactions were terminated by removing the catalyst by centrifugation (14500 rpm, 3 min) and filtration (2.5 µm syringe filter). The supernatant was analyzed by a) absorption spectroscopy (solid line (——): control (50 µM PR), dashed line (-- --): standard reaction mixture (50 µM PR, 25 mM NH$_4$Br, 300 µM H$_2$O$_2$, 25µg·mL^{-1} CeO$_{2-x}$), dotted line (····): reaction after 15 min, dash-dot-dashed line (–·–): after 30 min, dash-dot-dot-dashed line (–··–): after 60 min, short dashed line (- - -): after 120 min, short dash-dotted line (- · -): after 240 min, short dash-dot-dotted line (- ·· -): after 24h (diluted 1:1)) and simultaneously by b) RP-HPLC/ESI-MS (method A) 0 – 240 min. * mark the retention time (absorption) of the several brominated products following BrPR<Br$_2$PR<Br$_3$PR<Br$_4$PR. Note: Mass spectrometry cannot predict the exact bromination site at the dye but as halogenation is preferred at reactive carbon sides, the structure was expected as mentioned in the main text. More precise RP-HPLC/ESI-MS data are given in Experimental Section, page 195.
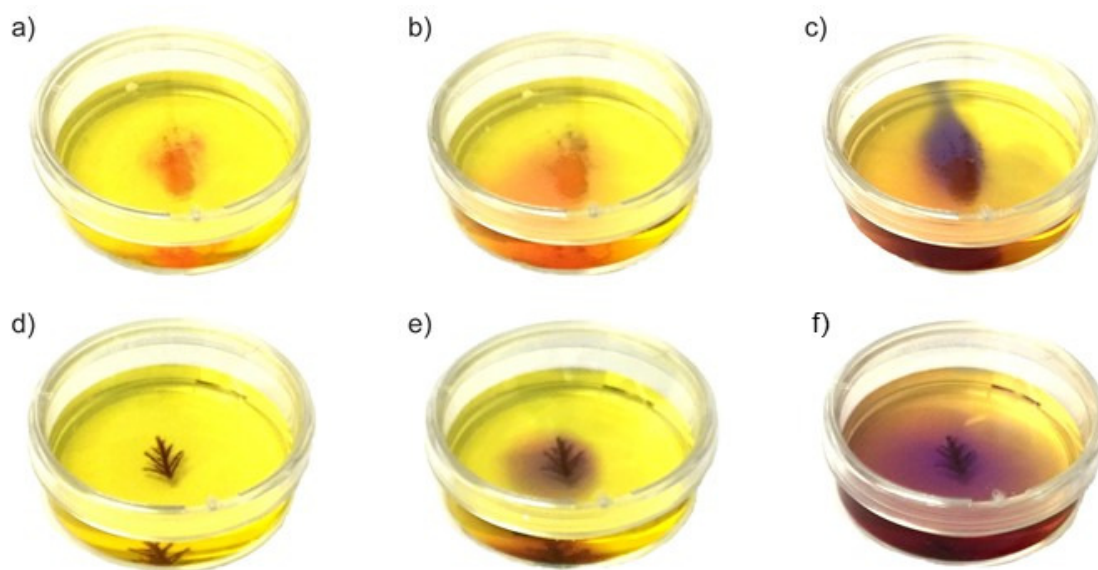
Figure 47. Oxidative bromination of PR catalyzed by CeO_{2-x} nanorods in respect to the natural haloperoxidase of *C. officinalis.* The oxidative bromination of PR catalyzed by a–c) cerium oxide nanoparticles (2.1 mg) and d–f) extracellularly located haloperoxidases of a piece of the marine red algae *C. officinalis* (7.1 mg) was monitored visually. Both were reacted with a standard reaction mixture (4 mL, pH 5.6, 50 µM PR and 25 mM NH_4Br without stirring at r.t.). H_2O_2 (300 µM) was added to start the reaction (a, d). After 10 min, CeO_{2-x} nanorods (b) as well as the algae (e) showed a significant formation of Br_4PR indicated by a gradual color change from yellow to blue-violet. The conversion is shown after 1 h reaction time (c, f).

The nature of the intermediary bromine species involved in the bromination of PR was probed with celestine blue (CB) which is bleached exclusively by oxidized halogen species like ClO^- and BrO^-, whereas it is not a substrate for any peroxidase activity and does not react with hydrogen peroxide and superoxide anions.[246] The bleaching of CB (50 µM) at 640 nm within 300 minutes (Figure 43e, f) showed that CeO_{2-x} nanorods catalyze the oxidation of bromide to $HOBr/BrO^-$. Liquid chromatography-mass spectrometry (LC-MS) analysis of the pink degradation product (A_{max} = 530 nm) yielded a *m/z* ratio of 362.1 as illustrated in Figure 43g and Experimental Section, page 195.

Further decay leads to low molecular weight species.[246] A radical mechanism for the generation of HOBr is suggested. Adding cysteine or ascorbic acid as natural antioxidants to the reaction mixture (NH_4Br, H_2O_2 and PR) in the presence of the CeO_{2-x} nanorods led to a strong decrease in the reaction rate, and the reaction was completely inhibited after adding equimolar amounts of the scavengers (Figure 48). The radical mechanism differs from that proposed for the vanadium,[247,253,255,259,558] tungsten[397] or rhenium[399] containing catalysts involving metal-η^2-peroxo intermediates. It is in accordance with the mechanism suggested for some natural heme containing halogenases.[69]
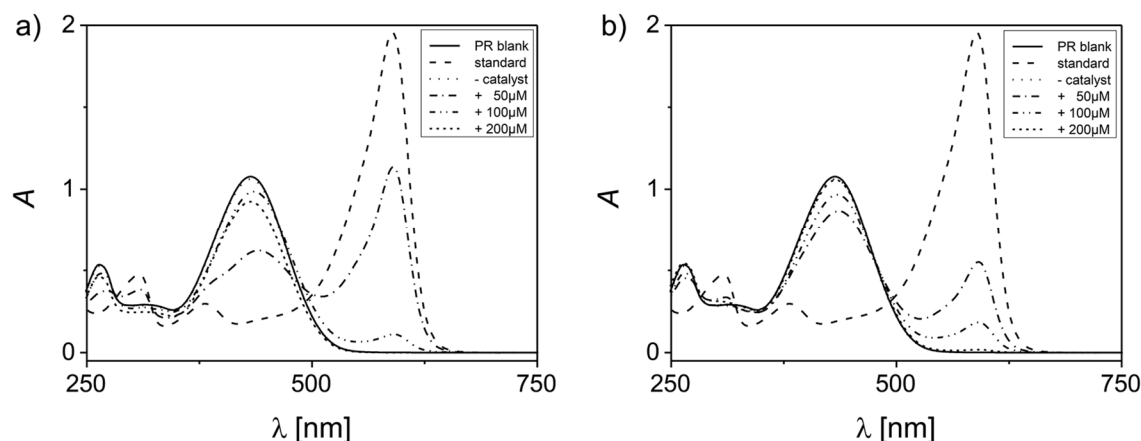
Figure 48. Effect of natural antioxidants. UV-Vis scanning kinetics of the oxidative bromination of PR catalyzed by CeO_{2-x} nanorods in the presence of the natural antioxidants a) cysteine and b) ascorbic acid at 23-25°C after 25 h and shaking at 800 rpm. Solid line (——): control (50 µM PR = 200 µM "active carbon"), dashed line (-- --): standard reaction mixture (50 µM PR, 25 mM NH_4Br, 300 µM H_2O_2, 25µg·mL^{-1} CeO_{2-x}), dotted line (· · ·): standard reaction mixture without catalyst (50 µM PR, 25 mM NH_4Br, 300 µM H_2O_2), dash-dot-dashed line (– · –): 50 µM, dash-dot-dot-dashed line (– · · –): 100 µM and short dashed line (- - -): 200 µM of natural antioxidant.

In contrast to CeO_{2-x} nanorods, bulk ceria (particle size ≈ 5 µm) showed little oxidative bromination activity indicating that the catalytic activity is correlated with the surface area and/or texture of nanoscale CeO_{2-x} (cf. Experimental Section, page 208). In general, the catalytic activity of nanoceria is attributed to its ability to undergo rapid redox cycles by releasing and storing oxygen,[559] where oxide defects and distinct crystallographic faces play a crucial role. These defects may serve as binding sites for reactive species.[559] If a CeO_2 structure model defines reactivity by the ease to release oxygen, the (100) surface has a lower oxygen vacancy formation energy than the (111) surface.[569] CeO_{2-x} nanorods preferentially expose their {110} facets (described as a reactive "hybrid-structure" between those observed on CeO_2(111) and CeO_2(100) by Mullins[569]) and a smaller portion of {111} facets (*vide supra*, Figure 42b, Figure 41). We suggest that surface defects and the stability of Ce^{3+} centers (cf. XPS analysis, Figure 42d) are responsible for the haloperoxidase-like activity of CeO_{2-x}.[562]

In studies on Fenton-type reactions[570] of spherical CeO_{2-x} nanoparticles with different particle sizes (≈ 4 nm, ≈ 6 nm, ≈ 8 nm), smaller particles with larger surface area were reported to be more reactive. The choice for nanorods combines the advantage of high yields - required for field tests - and high activity which can be related to the surface structure. Preliminary experiments showed mixed-valency to play an important role. Va-

lence-precise compounds like nano-CePO$_4$ or nano-CeVO$_4$ and bulk CeO$_2$ ($\approx$ 5 μm particles) had no activity, whereas mixed-valent compounds obtained by partial substitution of Ce by La showed enhanced turnover.

Quantum chemical calculations at various levels of theory (periodic calculations at the generalized gradient approximation-density functional theory (GGA-DFT) level and calculations of small finite model compounds at the metahybrid-DFT level, see Experimental Section, page 199 for details) were performed in order to rationalize this hypothesis and our experimental findings. Results obtained for Ce^{3+} defect sites at (110) and (111) model surfaces buttress the catalytic HOBr formation cycle illustrated in Figure 49 for the (110) surface. Hydration is expected to yield a coverage of every (110) surface Ce^{4+} site with an OH$^-$ and (for reasons of charge neutrality) an H$_2$O ligand on every Ce^{3+} site.

The calculations suggest the HOBr formation catalyzed by Ce^{3+} defect sites to be possible. As the release of HOBr appears to be the rate limiting step, intermediates involving Br• radicals on the ceria surface are conceivable. This also explains why natural antioxidants were observed to slow down the reactions, as a one electron transfer yields stable hydroxide terminated Ce^{4+} sites. A mechanism at two neighboring Ce^{3+} sites involving oxidation by H$_2$O$_2$ may be postulated but is (according to further calculations) not expected to be the origin of HOBr formation. A nucleophilic attack of Br$^-$ at Ce-bound H$_2$O$_2$ represents another mechanistic scenario, which would, however, not require Ce^{3+} sites but a strong Lewis-acidic surface. Such pathways were studied as well and could be excluded. Computational details and results for the (110) surface are given in the Experimental Section starting with page 199.

Figure 49. Proposed catalytic bromination mechanism of the CeO$_{2-x}$ nanorods. On a (110) model surface (I) the H$_2$O ligand can be exchanged against H$_2$O$_2$ (II) With a Gibbs free energy change (ΔG°) close to zero this exchange is unlikely for low H$_2$O$_2$ concentrations. However, the exchange itself is favorable (ΔG°<0) and becomes fully irreversible (more negative ΔG°) for a (partial) dissociation of H$_2$O$_2$, which leads to an oxidation of the Ce^{3+} site with OH⁻ anion and OH• radical ligands (III). These two groups are bound to each other through a weak two-center three-electron bond. As both Ce-O distances in this species are essentially equal, the description involves two mesomeric boundary structures to account for the actual chemical bonding. A release of an OH• radical from this species into solution may occur, but it represents a step "uphill" in Gibbs free energy and is therefore slow (IVa). A Br⁻ anion can add to one of the O atoms to form to species which is best described as an anionic surface site (with two hydroxide ligands) where one of the OH⁻ anions interacts with a Br• radical (IVb). The other, non-interacting OH⁻ anion is protonated to restore a neutral surface site (V). Dissociation of the HOBr product finally regenerates the initial Ce^{3+} site (I). Although the final step is associated with a positive ΔG°, it occurs because (i) the back reaction is energetically uphill as well and (ii) the concentration dependence of ΔG (= ΔG°+RTlnK) makes ΔG favorable for low HOBr concentrations.

Bacterial signaling molecules, specifically *N*-(3-oxo-acyl)homoserine lactones (3-oxo-AHL, Figure 50a) are susceptible to electrophilic halogenation at the C2 atom, as demonstrated by the V-HPO of *Laminaria digitata*.[71,554] CeO$_{2-x}$ nanorods catalyze the oxidative bromination and thus inactivation of 3-oxo-AHL *via* HOBr, forming mono- and dibromo-3-oxo-hexanoylhomoserine lactones (Figure 50a). After 150 min, a haloperoxidase-like activity could be demonstrated with true bacterial signaling compounds by verifying mono- and dibromo- 3-oxo-AHL by high performance liquid chromatography/ electrospray ionization mass spectrometry (HPLC/ESI-MS, Figure 50b and Experimental Section, page 195)."
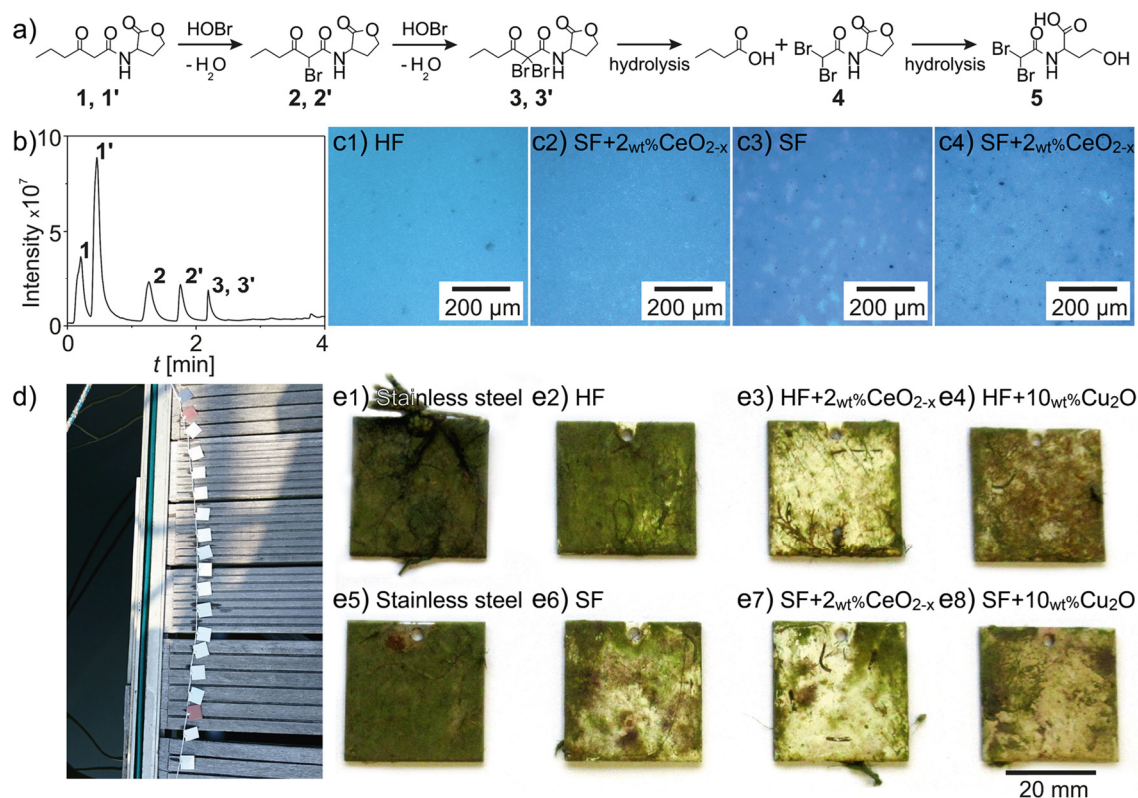
Figure 50. Summary of laboratory and offshore immersion field tests. a) The CeO$_{2-x}$ catalyzed oxidative bromination of 3-oxo-hexanoylhomoserine lactone 1 ($\equiv$ OHHL **19**) to 2,2′dibromo-3-oxo-hexanoylhomoserine lactone 3 ($\equiv$ DBHL **21**) and the subsequent basic hydrolysis to α,α-dibromoethanoyl-2-(4-hydroxy)butanoic acid 5 ($\equiv$ DAHL **22**, **23**). b) Total ion chromatogram (LC/ESI-MS) of the oxidative bromination reaction of the 3-oxo-acylhomoserine lactone (illustrated in a) catalyzed by CeO$_{2-x}$ nanorods (900 µM 3-oxo-AHL, 20 mM KBr, 20 mM H$_2$O$_2$, 100 µg/mL CeO$_{2-x}$) after 150 min at 30°C. The label numbers in the reaction scheme a) correlate with the numbering in b). Twin signals are due to partial hydrolysis of the lactone. The subsequent hydrolysis to α,α-dibromoethanoyl-2-(4-hydroxy)butanoic acid 5 could not be detected. c) Selected fluorescence images of *E. coli* colonies stained with DAPI (1 µg·mL^{-1}) on stainless steel plates (2 x 2 cm) covered with different paint formulations. c1) HF without biocide. c2) HF containing 2 wt% of CeO$_{2-x}$. c3) SF without biocide. c4) SF containing 2 wt% of CeO$_{2-x}$. d) Offshore immersion site (Belgium, Ophoven-Kinrooi, marina De Spaanjerd, Maas). Digital images of stainless steel plates (4 x 4 cm) covered with different paint formulations for boat hulls with and without CeO$_{2-x}$ nanorods. The plates were fixed statically to a boat bridge. e) Selected samples after 7 ½ weeks of the static field immersion. e1,5) Stainless steel plate, e2 & e6) HF & SF without biocide, e3 & e7) SF & HF containing 2 wt% of CeO$_{2-x}$, e4 & e8) SF & HF containing 10 wt% of Cu$_2$O. Abbreviations: HF, hard formulation and SF, soft formulation.

3.5   Antifouling Activity

"A straightforward application of the HPO properties of CeO_{2-x} is the design of stable antibacterial materials. Inspired by the previous use of HPO in water-based paints,[158] we probed the application of CeO_{2-x} nanorods as a paint additive to develop - highly demanded - antifouling paints with (i) high chemical stability, (ii) low cost, (iii) low environmental toxicity due to the insolubility of CeO_{2-x} in water, (iv) constant availability of the substrates (H_2O_2 and Br^-) which are required for a dynamic antibacterial activity (HOBr formation), and (v) intrinsic activity at substrate concentrations comparable to those encountered in marine environments.

Laboratory and static field tests were carried out with abrasive soft paint formulations (SF, self-polishing rosin formulation used for boat hull applications) and commercially available hard paint formulations (HF, silicone alkyd based paint with a minimum fraction of 25 % solvent mass) containing CeO_{2-x} nanorod additives. Rosin is a natural resin containing approx. 85-90 % acidic and 15-10 % neutral components, whose carboxyl groups react with the potassium and sodium ions in sea water.

The amount of CeO_{2-x} was estimated as 2 wt% of dry weight of the formulation, respectively, 0.6 g and 0.8 g with respect to 40 g HF and 40 g SF. After homogenization, the paints were applied onto stainless-steel plates, ca. 2×2 cm for the laboratory experiments, 4×4 cm for the field tests in Belgium. As controls, painted surfaces without additional additives were used. Identical paint formulations were used in laboratory and field tests. As a proof-of-principle, the static antifouling performance of the ceria nanorods was evaluated against gram-negative (*E. coli*) bacteria in laboratory bacterial adhesion experiments[424] under pH neutral conditions (Figure 50c). The paints and controls (identical, but (i) without CeO_{2-x} and (ii) with Cu_2O) were applied onto stainless steel plates in duplicate (Experimental Section, page 223). The concentrations (wt% of dry weight of the paint formulation) were chosen to compare the minimum amount of CeO_{2-x} nanorods or Cu_2O required to prevent a significant increase in bacterial colonization on soft paint formulations. Further information is provided in the Experimental Section starting with page 223.

The controls were immersed in media with (positive control, Figure 50c1, c3) and without (negative control, cf. Experimental Section starting with page 223) *E. coli*. After incubation, the plates were washed, and adhered bacterial colonies were stained with the

fluorescent dye 4′,6-diamidino-2-phenylindole dihydrochloride (DAPI, 1 µg mL^{-1}), indicated by the blue "spots" in the fluorescence microscopy images illustrated in Figure 50c and in the Experimental Section starting with page 223.

The smooth surface of the HF without CeO$_{2-x}$ nanorods (Figure 50c1) lead to a lower bacterial adhesion compared to the rough and porous SF (Figure 50c3). In the presence of CeO$_{2-x}$ nanorods bacterial adhesion on SF was greatly reduced (Figure 50c4), while adhesion on hard formulations (HF) remained low (Figure 50c2). Controls in the absence of one of the components (KBr, H$_2$O$_2$, CeO$_{2-x}$ nanorods) showed a dense bacterial population (Experimental Section starting with page 223) indicating that the CeO$_{2-x}$ nanorods alone do not exhibit any toxicity against bacteria. The presence of both substrates, H$_2$O$_2$ and Br$^-$, together with the intrinsic catalytic activity of the CeO$_{2-x}$ nanorods is essential for preventing bacterial adhesion. Since the SFs have a more porous structure than the corresponding HF that supports mass transfer, the laboratory experiments underpin the hypothesis that the antibacterial activity is caused by the intrinsic haloperoxidase activity of the CeO$_{2-x}$ nanorods (even embedded in a matrix) in the presence of Br$^-$ and H$_2$O$_2$.

Static immersion field tests were conducted using hard and soft paint formulations applied onto stainless steel (4 x 4 cm). H$_2$O$_2$ is formed in natural water exposed to sunlight in concentrations between 100 and 250 nM.[571] Static immersion field tests in fresh water were carried out in Belgium (Ophoven-Kinrooi, marina De Spaanjerd, Maas (Figure 50d and e), August-September 2015, bromide concentrations up to 2.5 µM).[572] Test plates treated with paint containing CeO$_{2-x}$ nanorods showed little indication of biofouling (Figure 50e3 (HF) and e7 (SF)). The control plates were covered densely with algae and increased biofouling was observed, indicating that during the test period of 51 days bacterial growth proceeded without delay (Figure 50e1, e5 (untreated steel plates), e2 (HF), e6 (SF)). Test plates treated with HF and SF coatings containing 10 % of Cu$_2$O (Figure 50e4, e8, antifouling paints may contain up to 50 % Cu$_2$O), the current antifouling gold standard, shows reduced algal growth for the CeO$_{2-x}$ nanorods compared to Cu$_2$O. To quantify the amount of settled algae, the test plates (Figure 50e1-e8) were analyzed quantitatively using the particle analysis function of the Fiji software package, which showed a relative decrease of algal population of ≈ 49 % for CeO$_{2-x}$ (HF, Figure 50e3 and Figure 51a3), ≈ 54 % for CeO$_{2-x}$ (SF, Figure 50e7 and Figure 51a7), ≈ 32 % for Cu$_2$O (HF, Figure 50e4 and Figure 51a4) and ≈ 47 % Cu$_2$O (SF, Figure 50e8 and Figure 51a8) (Figure 51).
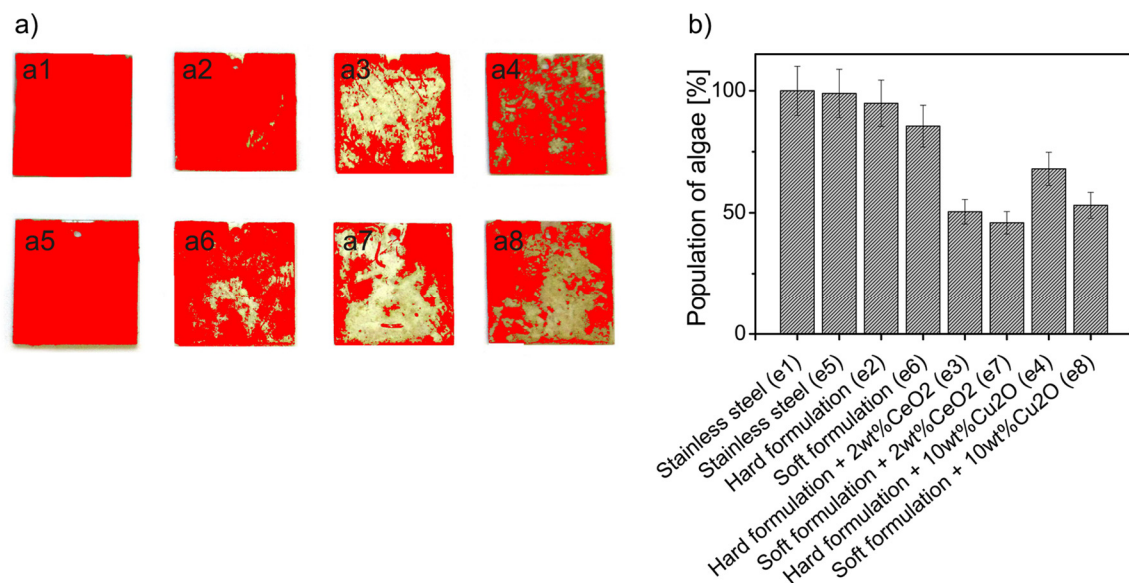
Figure 51. Quantification of algal growth. a) The test plates (Figure 50e1-e8 corresponding to the samples a1-a8) were analyzed using the particle analysis function of Fiji - an open source version of Image J. b) The relative fractions (total area analyzed/red pixel^2) are summarized in the bar chart. a1) is assigned to 100.0 % algae population and a2-a8) are set in proportion to a1) resulting in: a2) 94.9 %, a3) 50.5 %, a4) 68.0 %, a5) 98.9 %, a6) 85.5 %, a7) 45.9 %, a8) 53.1 %. The errors are approx. 10 %."

4

Further Scopes of Cerium Dioxide

Structural and Oxidation State Dependency of the Haloperoxidase-like Activity of Nanoceria

Nanoceria´s success in chemical,[559,573] electrochemical,[574,575] potential medical[576–579] applications has been strongly connected to the unique redox and structural properties associated with oxygen diffusion and reversible oxygen uptake/release capacity forced by the continuous change of Ce^{3+}/Ce^{4+} redox couples. Here, cerium can reversibly switch between its tri- and tetravalent states. As a result, ceria is non-stoichiometric with oxygen vacancies in the fluorite lattice.

Theoretical calculations by Nolan et al. have indicated that the surface stability of the low index surfaces of CeO_2 decreases with (111)>(110)>(100) going along with an

increase in relaxation energy (111)<(110)<(100).[580–582] Because of that, significant re-arrangements of surface atoms occurr resulting in a greater energy gain for (100).[580] The fully relaxed geometries of the surfaces are shown in Figure 52.[580–582]

With respect to the relaxation, alterations in Ce-Ce and Ce-O distances, the electronic band structures and thus the oxygen vacancy formation energies have been reported.[559,569,580–584] It has been found that the vacancy formation energy is lowest on the (110) surface followed by (100) and (111)[581] and, in general, is reduced on surfaces compared to bulk cerium oxide.[582] Furthermore, the surface stability as well as the regeneration of the catalyst depend also on bulk effects as oxygen mobility and oxygen migration through the lattice.[583,585,586] As these distinct crystallographic surfaces and their defect chemistry have been assigned to defined macroscopic crystal morphologies of ceria, the catalytic reactions and efficiency can be controlled by synthetic methods.[569,584,587–593] For more details, Huang and Gao have greatly reviewed the morphology-dependent surface chemistry and catalysis of CeO_2 nanocrystals.[449]

In general, the influence and correlation of macroscopic morphology and catalytic activity have been well studied in catalytic gas phase reactions. Concerning the gas phase oxidation reaction of CO to CO_2 catalyzed by cerium oxide nanoparticles, CeO_2 nanorods with (110) and (100) surfaces are distinguished to be more active than CeO_2 nanoparticles with an exposed (111) surface.[585,593–595] Cerium oxide cubes (100) are discussed to have better activity in the (reverse[596]) water–gas shift reaction,[597] for the dehydrogenation of ethylbenzene to styrene[588] and in the photocatalytic oxidation of volatile organic compounds.[598] With respect to oxygen adsorption[589] and oxygen storage capacity,[592] (110) and (100) planes have shown similar high reactivity and decreased activity for (111) planes.[589,592] As a consequence, the formation of oxygen defects in the structure is related to the Ce^{3+} fraction and stability. With regards to enzyme mimetic reactions catalyzed by cerium dioxide, especially the superoxide dismutase (SOD)-like reactions have been intensively studied.[599] The studies reveal that with increasing Ce^{3+} fraction the SOD mimetic activity of nanoceria increases as well.[17,561,600]

Inspired by these results, spherical, cubic and rod-like CeO_{2-x} particles were synthesized to compare their oxidative bromination catalytic activity in relation to morphology, exposed crystal planes and Ce^{3+} content (see Experimental Section, page 186).
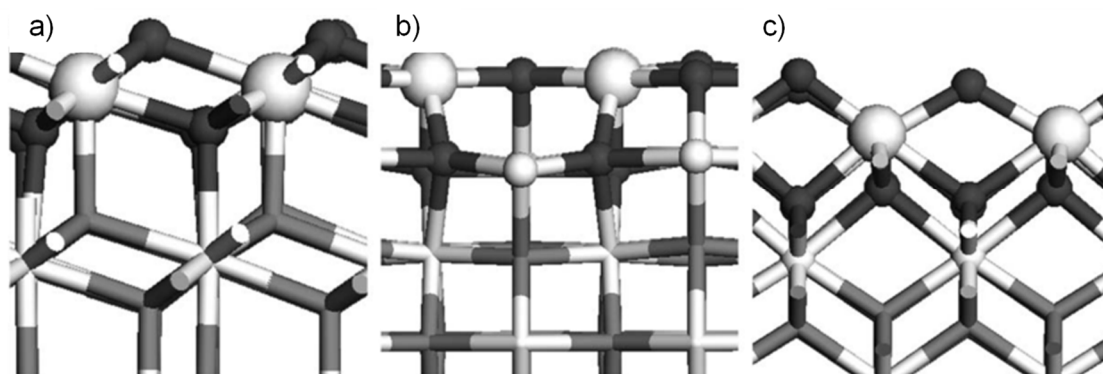
Figure 52. Front view of the defective surfaces of cerium dioxide: a) (111), b) (110) and c) (100) surfaces. The Ce^{3+} ions are denoted by the large, the Ce^{4+} ions are the small lightly shaded spheres, the oxygen ions at the surface and first subsurface layer are the darkly shaded spheres and the remaining oxygen ions are the grey shaded spheres. Provided with permission.[581]

All CeO_{2-x} nanoparticles consist of a face-centered cubic floruit-type structure confirmed by powder X-ray data (cf. Chapter 3) and high-resolution TEM imaging. The different morphologies of CeO_{2-x} highlighted by TEM and HR-TEM images (shown in Figure 53a-f) are additionally correlated to their corresponding XPS spectra (Figure 53g).

As discussed in Chapter 3, the pale, yellow cerium oxide nanorods were made of a dense but complex polycrystalline, triple rim-like structure (cf. page 123). The nanorods inhere a length ranging from 20 to 100 nm, with the average thickness of 15-20 nm and exhibit mainly {110} and {111} facets (Figure 41, Figure 53a, b). In contrast, cubic particles expose (100) surfaces at each of the six sites and the corners have a slightly rounded shape (Figure 53c, d). TEM-EDX measurements prove that all three samples contain cerium oxide and only CeO_{2-x} cubes show minor impurity of chloride-ions (Figure 54a). The main size of the cubic particles ranges around 12 - 30 nm although the particles showed a broad size distribution as reflected in the corresponding histogram (Figure 54b). Similar trends are found for the spherical particles having an approximate average size of 5 - 20 nm (Figure 53e, f). The increased agglomeration process made valid data analysis very difficult to ensure. In analogy to literature[593] and Figure 53f, respectively, the spherical nanoparticles can be described as truncated octa- and polyhedrons. In literature, they have been characterized by exposing {111} facets at each of the eight sites.[584,601–603]

Here, the small spherical particles showed smooth surfaces without any pronounced facets. Larger particles demonstrated the tendency to faceting, but did not reveal any preference for specific crystallographic orientation.
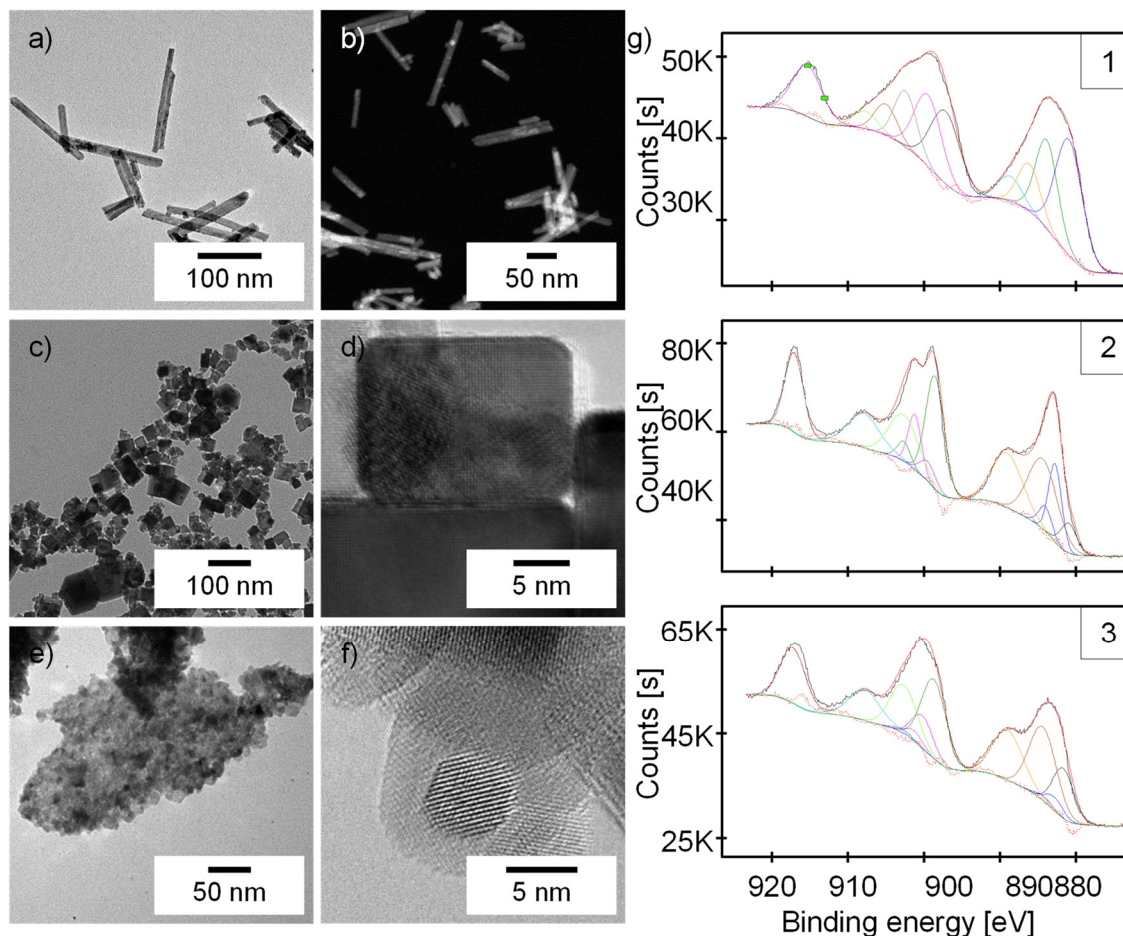
Figure 53. Structure and defect structure of CeO$_{2-x}$ nanorods. a-f) TEM images and HRTEM analysis different shaped CeO$_{2-x}$ nanoparticles: a, b) Nanorods (cf. Chapter 3). c, d) Nanocubes. e, f) Spherical nanoparticles. g) XPS (Al-Kα) core level spectra of the Ce 3d signals of the CeO$_{2-x}$ nanoparticles in accordance with the different morphologies. Deconvolution of the spectra was performed by using the corresponding peak fitting model (PFM) into three Voigt doublets corresponding to Ce^{4+} (u + v, u''+ v'' and u'''+ v''') and two Voigt doublets corresponding to Ce^{3+} (u^0 + v^0 and u' + v', all Voigt) as precisely described in Chapter 3. The intensities indicate the Ce^{3+} amount to be g1) up to 45 % for nanorods, g2) up to 33 % for nanocubes and g3) up to 44 % for spherical nanoparticles.

The optical appearances of the particles which represent an indication for the presence of Ce^{3+} differed. Nanorods and the spherical particles appeared similar pale yellow in contrast to the colorless cubes. The Ce^{3+} content going along with oxygen defects was estimated *via* XPS measurements (binding energy from 930 – 875 eV, Figure 53g) as described in Chapter 3. Complete signal deconvolution with respect to the 3d$_{5/2}$ and 3d$_{3/2}$ transitions of Ce^{3+} and Ce^{4+} (c.f. Chapter 3 and Experimental Section, page 192) yielded relative Ce^{3+} fractions of i) nanorods up to $\approx$ 45 % (cf. Chapter 3[227]), ii) cubes up to $\approx$ 33 % and iii) spherical particles up to $\approx$ 44 % concerning the surface integrals (Figure 53g).

Although the absolute values have to be handled carefully because of the mixed-valent ground state of CeO_2,[564,569,604–608] the trend in the Ce^{3+} amount and the optical appearance support the hypothesis that cubes have less oxygen defects.
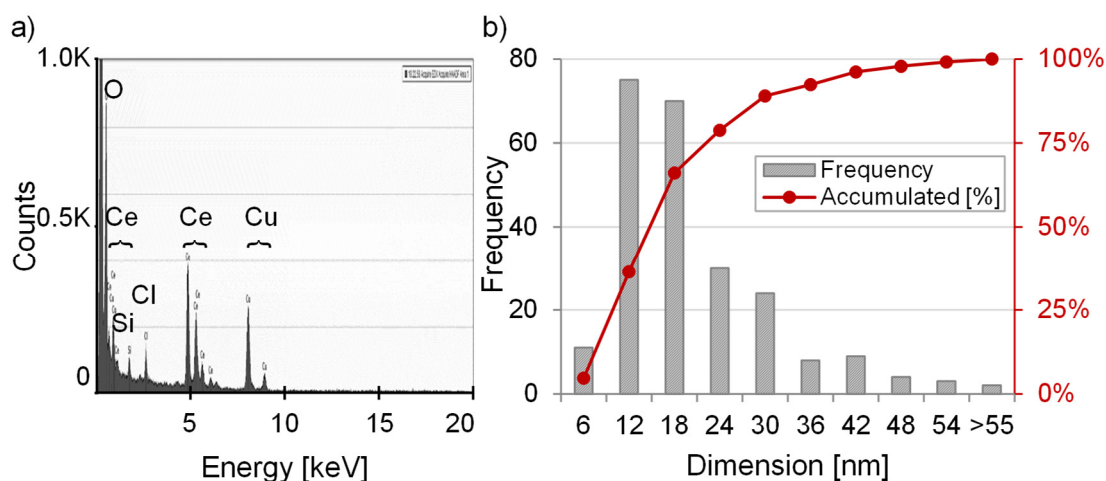
Figure 54. Analysis of CeO_{2-x} nanocubes. a) TEM-EDX spectra with signals resulting from Ce, O, Cl, and Si, Cu (TEM grid) and b) size distribution histogram.

As discussed in Chapter 3, the difference in the ionic radii of Ce^{4+} and Ce^{3+} ($\Delta \approx$ 27 ppm) strongly suggests surface defects to occur mainly at the particle surface.[227] Because of this, the catalytic activity in general seems to be not only dependent on the surface texture and defects, like edges, rims, corners but additionally on the exposed crystal planes correlating with oxygen defects.[609] The haloperoxidase-like activity of the cerium oxide nanoparticles with different morphologies was demonstrated using the PR bromination assay (Chapter 3 and Experimantal Section, page 207).

Thus, the reaction rate of the formation of bromophenol blue can be correlated to the predominantly exposed surfaces, oxygen defects as well as the inherent Ce^{3+}/Ce^{4+} ratio in aqueous media. To emphasize this point, schematic illustrations of the different morphologies of CeO_{2-x} and the (hypothesized) main crystallographic facets are shown in Figure 55a. The oxidative bromination activity of the different CeO_{2-x} morphologies (nanorods, -particles, -cubes) and their optical appearance is highlighted in Figure 55b. Depending on their synthesis (see Experimental Section, page 186), rod-shaped particles were synthesized in a yellow or colorless "mode". The formation of bromophenol blue was followed for 5 min at 590 nm and the fraction of Br_4PR was set in relation to the highly active, pale yellow nanorods (cf. Chapter 3).

The bar diagram evidently shows a direct correlation of the Ce^{3+} content expressed by the color impression and XPS measurements, which is connected to the particle shape *via* the exposed facets, respectively, and the catalytic activity. Interestingly, CeO_{2-x} spherical particles which can be synthesized easily in large scale exhibit catalytic activities comparable to the yellow nanorods. As the spherical particles have not revealed any preference for specific crystallographic orientation, it is hypothesized that, additionally, the activity is linked to particle surfaces tolerating oxygen defects in a high range independent of perfectly pronounced crystallographic planes.

It has been demonstrated in various experiments that the morphology, exposed crystallographic planes and oxygen defects are controlled and affected by the synthesis, selection of base and in addition, by the cerium educt salt.[449,570,587,610–612] In analogy to the results presented above, Jiang et al. have reported that EDX analysis of cubes and rods made of cerium(III) chloride reveals residual chlorine in the structure affecting the catalytic performance in photocatalytic test reactions.[598] With respect to this, further investigations concerning particle shape, Ce^{3+} content, exposed facets in combination with synthetic variations and elemental compositions of the products altering the haloperoxidase-like activity will be a very interesting topic.

However, annealing of colorless cubes or rods at 500°C in an ambient air atmosphere linked to oxygen loss did not increase the catalytic oxidative bromination activity. Reversely, pale yellow particles remained highly stable in their appearance and catalytic activity both aqueous and air conditions for years and were not further oxidized to colorless particles. The comparable activity of the synthesized, pale yellow CeO_{2-x} nanorods and particles was impressively demonstrated by in field tests in Belgium (cf. Chapter 3[227]). Algal growth at coated stainless-steel plates (2x2 cm) with hard and soft paint formulations containing 2.0 wt% pale yellow CeO_{2-x} nanorods or particles was significantly impeded compared to blank stainless-steel plates and coated plates with no biocide (Figure 55c, cf. Chapter 3[227]).

The embedding of cerium dioxide spherical particles has certain advantages over nanorods with respect to the easier synthesis and increased miscibility related to the particle shape. Thus, the abrasive soft paint formulation inhering CeO_{2-x} particles demonstrates analogous and even better results against biofouling than ceria nanorods (Figure 55).
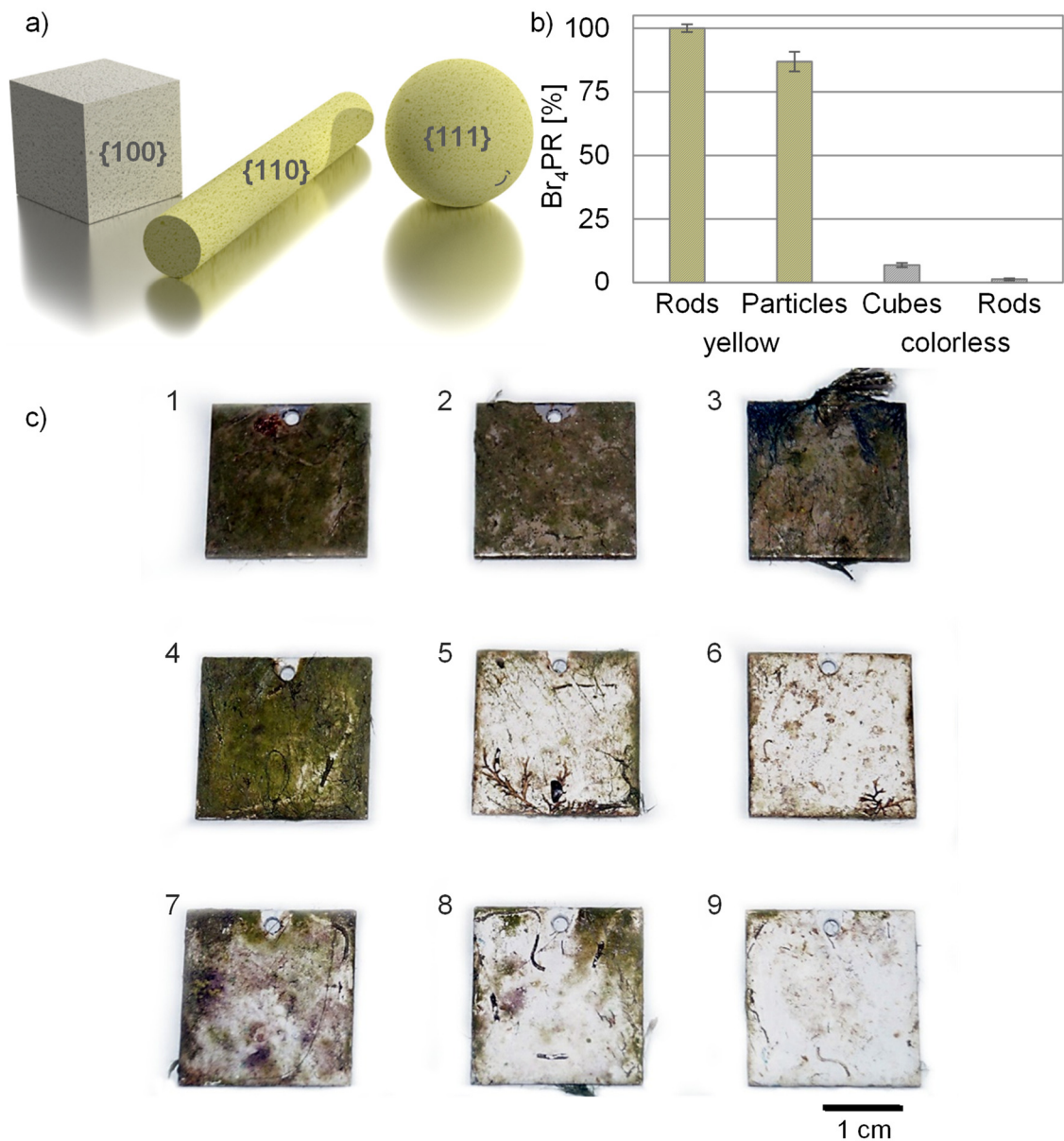
Figure 55. Comparison of the mode of action of different CeO_{2-x} nanoparticles. a) Schematic illustrations of the different morphologies including optical appearance of CeO_{2-x} nanoparticles and the (hypothesized) main crystallographic facets. b) Comparison of the oxidative bromination activity of the different CeO_{2-x} morphologies (pale yellow nanorods, -particles, and colorless nanocubes and -rods). The fraction of the Br_4PR formation after 5 min at 590 nm (25 $\mu g \cdot mL^{-1}$ nanoparticles, 25 mM NH_4Br, 50 μM PR and 300 μM H_2O_2 in 1 mL H_2O in total) is set in relation to the highly active, pale yellow nanorods. c) Results of the field tests in Belgium (cf. Chapter 3[227]). Algal growth at c1-3) stainless-steel plates, coated stainless-steel plates with hard paint formulations containing c4) no biocide, c5) 2.0 wt% pale yellow CeO_{2-x} nanorods, c6) 2.0 wt% pale yellow CeO_{2-x} spherical nanoparticles, and coated stainless-steel plates with soft paint formulations containing c7) no biocide, c8) 2.0 wt% pale yellow CeO_{2-x} nanorods, and c9) 2.0 wt% pale yellow CeO_{2-x} spherical nanoparticles. Algal growth at formulations with embedded pale yellow CeO_{2-x} nanorods or particles is significantly impeded compared to blank stainless-steel plates and coated plates without biocide.

Figure 56 compares several oxidation catalysts within their oxidative bromination efficiency with respect to the bromophenol blue formation (cf. Exerimental Section, starting with page 207) in the haloperoxidase-like test system after 2h reaction time. In comparison to commercial available oxidic materials, all pale yellow cerium dioxide nanomaterials show superior haloperoxidase-like activity in analogy to the self-synthesized ones, independent of their delivery form (Figure 56). In contrast, bulk cerium dioxide (colorless) exhibits only less activity. Titan dioxide, vanadium pentoxide (bulk) and zinc oxide (bulk and nanomaterials) have little activities comparable to bulk CeO_2. No Br_4PR formation has been found for MnO, Mn_3O_4, α-/γ-Fe_2O_3, Sb_2O_3, WO_2 and WO_3 (bulk) under these reaction conditions.
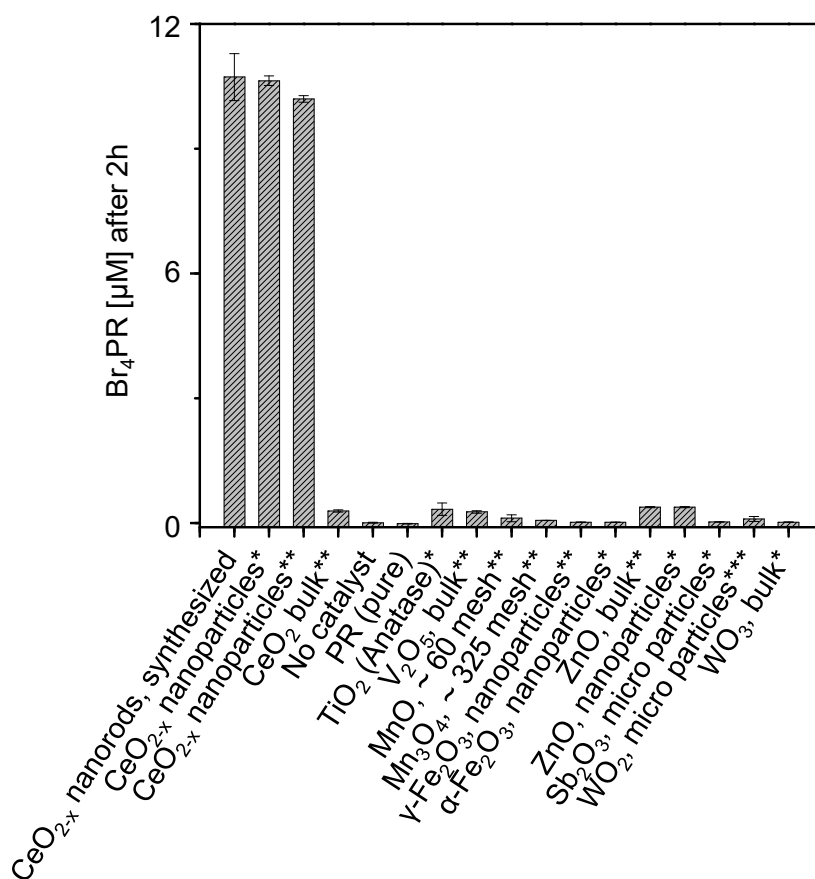
Figure 56. Oxidative bromination efficiency in the Br_4PR formation in µM of several, conventional metal oxides compared to different, pale yellow CeO_{2-x} nanoparticles after 2h reaction time. The catalytic activity of commercial available materials (purchased from *Alfa aesar, **Sigma Aldrich or ***ABCR) is compared against the activity of the self-synthesized, pale yellow CeO_{2-x} nanorods using the standard reaction mixture (25 µg·mL^{-1} catalyst, 25 mM NH_4Br, 10 µM PR and 300 µM H_2O_2 in 1 mL H_2O in total). Only commercial available, pale yellow CeO_{2-x} nanoparticles show analogous catalytic activities with no difference whether provided as suspension or as dried particles.

As discussed previously, the Ce^{3+} content is suggested to play the key role in the oxidative bromination catalytic activity of cerium oxide catalysts. This has been further demonstrated by doping experiments which have been performed in collaboration with Jens Hartmann as part of his bachelor thesis.[613] He has synthesized and analyzed different doped CeO_{2-x} and measured their catalytic activity against reference materials. Figure 57 shows the newly provisioned XPS spectra of the reference compounds a) $CeCl_3$, b) $CeVO_4$,[2] c) $CePO_4$,[2] d) $Ce(NO_3)_3$ and e) ceric ammonium nitrate $(NH_4)_2Ce^{IV}(NO_3)_6)$ to which the doped CeO_{2-x} has been compared to.

As mentioned earlier, all the XPS spectra reveal that "valence-precise" cerium containing salts in fact inhere a mixture of Ce^{3+} and Ce^{4+}. Complete deconvolution as described in Chapter 3 and page 192, yielded in a Ce^{3+} amount of a) 61 % for $CeCl_3$, b) 59 % for $CeVO_4$,[2] c) 53 % for $CePO_4$,[2] d) 53 % for $Ce(NO_3)_3$ and e) a Ce^{4+} amount of around 69 % for ceric ammonium nitrate (CAN). Although the exact values have to be handled carefully, the trend of Ce^{3+} amount i) discloses the stability and reliability of the chosen deconvolution method and ii) demonstrates that slight differences in the oxidation numbers cause high effects. Thus, $CeCl_3$, $CeVO_4$, $CePO_4$ and $Ce(NO_3)_3$ did not catalyze the oxidative bromination of PR but CAN acted as homogenous catalyst with activities analogous to CeO_{2-x} itself.[613] However, it could not be recovered or recycled.[613]

Compared to these materials as reference systems, Jens Hartmann has demonstrated impressively that i) a doping with Zr^{4+} (10 at%, ICP-MS) correlated with an enhanced Ce^{3+}/Ce^{4+} ratio[614] has resulted in a decreased activity and ii) a doping with La^{3+} (20 at%, ICP-MS) correlated with a lowered Ce^{3+}/Ce^{4+} ratio[614] has resulted in an increased activity (Figure 57f, thankfully provided by J.H.).[613] Additionally, he has pointed out that subsequent calcination steps at 500°C after synthesis have highly enhanced the catalytic performances of all catalysts in the following order $CeO_{2-x} \approx Ce_{0.8}La_{0.2}O_{2-x} > Ce_{0.9}Zr_{0.1}O_{2-x}$.[613] All these experiments point to a distinct but narrow window of an optimized Ce^{3+} fraction to be effective in haloperoxidase-like reactions. The reduced species seem to be in the range of the Ce^{3+} amount needed for SOD-like reactions.[17,561,600] However, XPS analysis of the doped materials and additional bio-adhesion studies will be required to confirm and to further analyze the "Ce^{3+}/Ce^{4+} ratio –

---

2 Synthesized and thankfully provided with permission by Jens Hartmann.[613]

hypothesis". Furthermore, the altering and optimization of the Ce^{3+}/Ce^{4+} ratio can be studied by copper,[615] iron,[616] vanadium[550] and nickel[550,609] doping as well that all have revealed extraordinary features in photocatalytic reactions.[617]
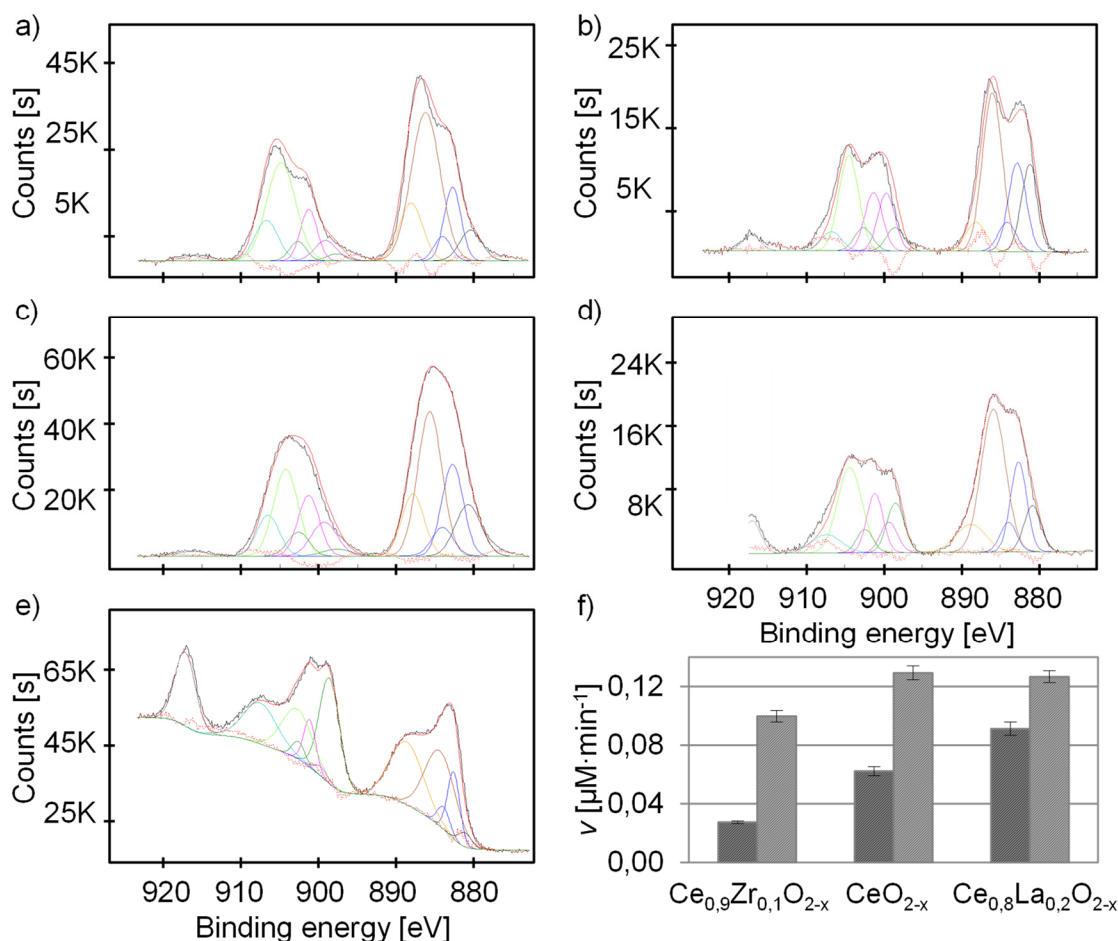
Figure 57. Illustration of the mixed valence state of cerium by XPS spectra of "reference materials" and the doping method to alter the Ce^{3+}/Ce^{4+} ratio. XPS (Al-Kα) core level spectra of the Ce 3d signals of a) $CeCl_3$, b) $CeVO_4$,[2] c) $CePO_4$,[2] d) $Ce(NO_3)_3$, e) CAN. Deconvolution of the spectra was performed by using the corresponding peak fitting model (PFM) into three Voigt doublets corresponding to Ce^{4+} (u + v, u''+ v'' and u'''+ v''') and two Voigt doublets corresponding to Ce^{3+} ($u^0 + v^0$ and u' + v', all Voigt) as precisely described in Chapter 3. The intensities indicate the Ce^{3+} fractions to be up to a) 61 % for $CeCl_3$, b) 59 % for $CeVO_4$,[2] c) 53 % for $CePO_4$,[2] d) 53 % for $Ce(NO_3)_3$, and a Ce^{4+} fraction to be up to e) 69 % for CAN. f) Influence of the Zr^{4+} and La^{3+} doping and annealing in comparison to pure CeO_{2-x} nanorods illustrated by the rate of the oxidative bromination of PR (20 µg·mL^{-1} catalyst, 25 mM NH$_4$Br, 10 µM PR and 300 µM H$_2$O$_2$ in 1 mL H$_2$O in total, 5 min). Color code: dark grey: particles as synthesized, light grey: annealed after synthesis. Bar diagram thankfully provided with permission by J. Hartmann.[613]

However, rod like particles are suspected of being harmful to health. Because of structural analogies of asbestos fibers, nanorods in general have been discussed to be lung toxic and to enforce lung cancer. German industrial safety regulations as the technical

rules for hazardous substances TRGS 559, 900, 905 and 910[618] being mandatory by German law and the European regulation (EG) 1272/2008 (CLP)[619] have determined rod-like particles being larger than 5 μm, thinner than 3 μm and with a length:width ratio of 3:1 as cancerogenic with specific occupational exposure limits ("level of acceptance": 10.000 fibers/m^3, "level of tolerance": 100.000 fibers/m^3 ($\equiv$ 0.1 fiber/mL).[618,619] This has been demonstrated in particular for CeO_2 nanorods with different lengths and aspect ratios by Ji et al. According to this study, short CeO_2 nanorods are non-toxic.[562,620] Due to that, ceria spherical nanoparticles have superior characteristics compared to nanorods: they agglomerate to highly stable porous "macroparticles" while remaining a high catalytic activity (Figure 53, Figure 55, Figure 56). However, cerium ions have been supposed to leach out because of chelating processes of living organisms[621–624] which might lead to additional toxic effects.

Gaining deeper insights into the toxicity of the particles, some fungal spores were supplemented to the particles at the "Institut für Biotechnologie und Wirkstoff - Forschung, IBWF".[625] The spores of *Magnaporthe grisea*[626,627] in aqueous and growth medium conditions, *Botrytis cinerea*[628] and *Phytophthora infestans*[629,630] (A1, D2) were studied and analyzed *via* light microscopy after 24 and 48h, respectively.

Fungal spores react very sensitive within environmental changes and effects.[631–635] In optimum conditions, the spores germinate and form enlarged penetration fibers which penetrate the surface cells of plants and allow the spores to infect their host.[636] These conditions were imitated in laboratory experiments. Figure 58a shows untreated and unhindered germination of *M. grisea* as the "negative control" (analogous digital photographs of *B. cinerea* and *P. infestans* are not shown to simplify the report).

As highly toxic materials, $Cu(OH)_2$ bulk particles (5 μg·mL^{-1}, IC_{100}, Figure 58b), V_2O_5 bulk particles (50 μg·mL^{-1}, IC_{95}, Figure 58c), WO_3 bulk particles (50 μg·mL^{-1}, IC_{100}, Figure 58d) added to spores of *M. grisea* in water (200 μL) are demonstrated as positive controls. Here, the spores remained in their original state and no transformation occurred. The inhibitory concentration (IC) is referred to the percentage value of the spore transformation inhibition. Interestingly, in aqueous conditions the toxicity of bulk $Cu(OH)_2$ was superior over WO_3 or V_2O_5 bulk particles by minimum factor of 10 (Figure 58b-d).

Figure 58e highlights *M. grisea* in water (200 μL) with maximum CeO_{2-x} nanoparticle concentration (50 μg·mL^{-1}) showing unhindered spore transformation. In growth media, none of the materials except $Cu(OH)_2$ (25-50 μg·mL^{-1}, not shown) demonstrated

an inhibitory effect. No toxicity of nanoceria itself could be detected in aqueous (*M. grisea,* Figure 58e) and growth media conditions (*M. grisea,* Figure 58f and *B. cinerea,* Figure 58g). Additionally, in aqueous conditions it seems that *M. grisea* have grown along the particles forming pearl necklace-like structures.
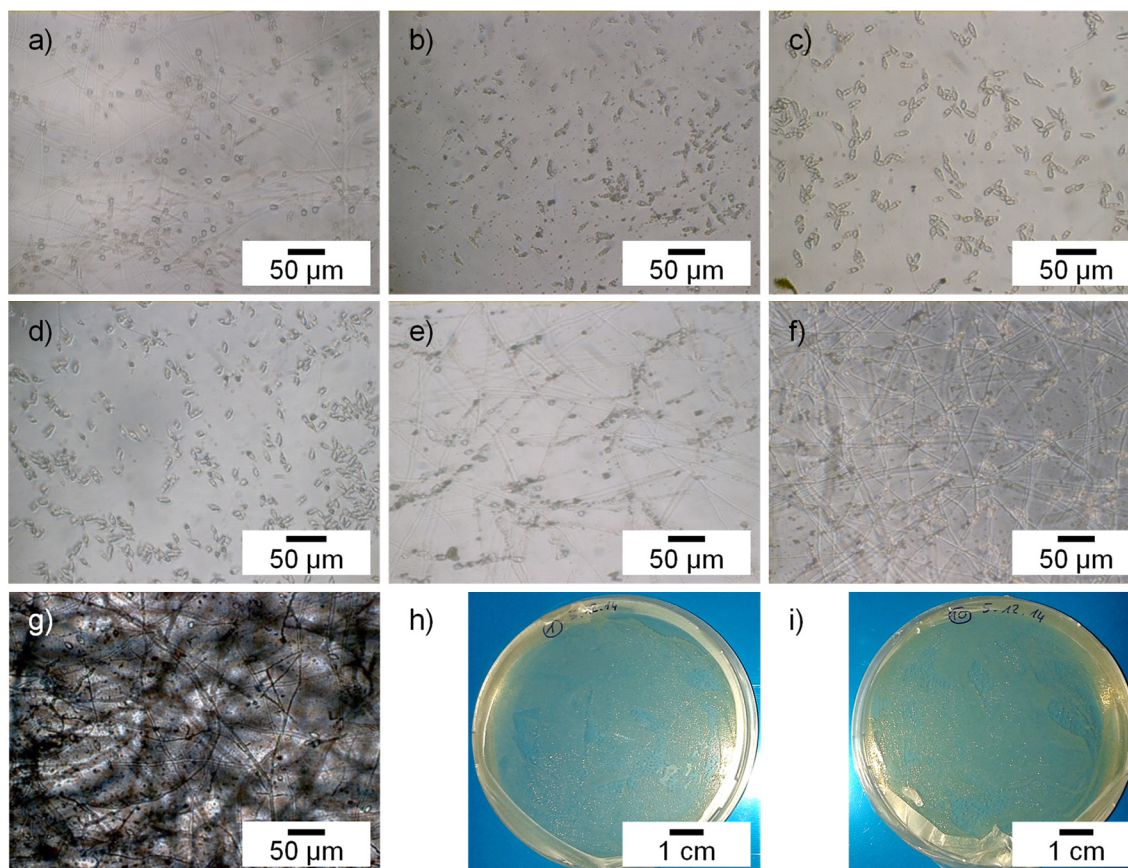
Figure 58. Demonstration of the non-toxicity of CeO_{2-x} nanoparticles by sprout inhibition and bacterial growth assays. Sprout inhibition was investigated in comparison to controls: a) *M. grisea* in 200 µL H_2O (negative control). b) *M. grisea* in 200 µL H_2O supplemented with 5 µg·mL^{-1} bulk $Cu(OH)_2$ (positive control with IC_{100}). c) *M. grisea* in 200 µL H_2O supplemented with 50 µg·mL^{-1} bulk V_2O_5 (positive control with IC_{95}). d) *M. grisea* in 200 µL H_2O supplemented with 50 µg·mL^{-1} bulk WO_3 (positive control with IC_{100}). e) *M. grisea* in 200 µL H_2O supplemented with 50 µg·mL^{-1} CeO_{2-x} spherical nanoparticles. f) *M. grisea* in 200 µL growth media supplemented with 50 µg·mL^{-1} CeO_{2-x} spherical nanoparticles. g) *P. infestans* (analogue to *B. cinera,* not shown) in 200 µL growth media supplemented with 50 µg·mL^{-1} CeO_{2-x} nanoparticles. An inhibitory effect of spore transformation is only detectable for $Cu(OH)_2$, V_2O_5 and WO_3 but not for CeO_{2-x} nano-particles. In growth media, none of the materials except $Cu(OH)_2$ (25-50 µg·mL^{-1}, not shown) demonstrated an inhibitory effect. All tests were performed in triplicates. Bacterial growth assays of h) pure *E. coli* at agar plates in comparison to i) *E. coli* treated singularly with 25 µg·mL^{-1} CeO_{2-x} nanoparticles, 25 mM KBr, and 300 µM H_2O_2 do not show any differences in bacterial growth and colonization. This provides the non-toxic effect of nanoceria itself, a constant supply of bromide and H_2O_2 to be necessary and an enzyme-mimic activity instead of killing organisms.

Proving the non-disruptive behavior of CeO_{2-x} nanoparticles, reaction mixtures containing bromide salt (25 mM), the catalyst (25 µg·mL^{-1}), H_2O_2 (300 µM) and *E. coli* (200 µL OVN) in growth media (15 mL) were plated at agar plates after a short incubation time at 37°C (3.5 h) in comparison to pure *E. coli* in growth media (see Experimental Section, page 228).

No difference in bacterial reproduction, growth and colonization coul be observed. This provides i) the non-toxic effect of nanoceria itself, ii) a constant supply of bromide and H_2O_2 to be necessary and that iii) the "anti-adhesion effect" can be correlated to a lowered surface attractiveness by the impediment of bacterial communication instead of killing organisms. Interestingly, preliminary results in sprout inhibition assays containing spores of *M. grisea,* CeO_{2-x} nanoparticles (25 µg·mL^{-1}), bromide salt (25 mM) and H_2O_2 (300 µM) in water (200 µL), revealed a decrease in spore transformation. However, the results are not presented here because a predominant effect of the H_2O_2 could not be excluded. It will be an interesting topic to re-evaluate these results with further control measurements proving the hindered spore germination originate from the haloperoxidase-like activity of CeO_{2-x} nanoparticles.

5

Conclusion

Starting in in the 20th century with the Belousov-Zhabotinsky reaction,[310,311,637] cerium and ceria compounds have followed an attractive career path as a result of the extraordinary, intrinsic features and properties in combination with high stability, non-toxicity, environmental compatibility and attractive prices to earth abundant resources. Because of that, cerium dioxide has become a widely and common used material in industry. It is typically used either as "inert" polishing and carrier material or as an "active" catalyst for example in photocatalysis and automobile industry.[638] Starting in the early 21th century, nano-sized cerium dioxide has enjoyed an increased amount of scientific interest showing catalytic and multi-enzyme-like properties with biomedical application potential.[576–579,639] In particular, cerium oxide has been investigated with respect to peroxidase-,[560] catalase-[17,640] and superoxide dismutase-like[561,600] activity correlated to cell protection against reactive oxygen species[577,578,639] as singlet oxygen, hydrogen peroxide, oxygen radical anions or irradiation,[641] protection against the process of aging[642] and against ischemic stroke in an *in vivo* animal model.[12]. In relation to the Belousov-

Zhabotinsky reaction, Van de Water et al.[643] have reported the bromination of phenol red catalyzed by of cerium(IV)-containing mesoporous silica (Ce-TUD-1) suggesting a radical mechanism without any deeper insights. In 2013, Leyva-Pérez et al. have described the oxygen-dependent halogenation activity of cerium dioxide regarding diverse electron-rich benzenes in organic solvents.[427]

Expanding the existing knowledge, this work demonstrates in conclusion that CeO_{2-x} nanorods and spherical nanoparticles are "functional analogues of halogenating enzymes by catalyzing the oxidative halogenation of organic substrates *via* reactive HOBr intermediates under laboratory (pH 5.6) and neutral conditions, and for marine Br^- and H_2O_2 concentrations. The reaction is associated with the Ce^{4+}/Ce^{3+} redox couple of nanoceria and follows a radical mechanism with an initial pseudo 3rd order reaction kinetic. The Ce^{4+}/Ce^{3+} ratio in CeO_{2-x} may be optimized for future applications by "doping" with other metals. Similar to natural bromoperoxidases (BPOs) and halogenases from algae,[158,558] CeO_{2-x} nanorods catalyze the oxidative bromination of the signaling compound *N*-(3-oxo-acyl)homoserine lactone (3-oxo-AHL) which impedes bacterial quorum sensing. As a result, CeO_{2-x} nanoparticles, even after embedding in paint formulations, show a higher antifouling activity than the commonly used cuprous oxide in field tests and may therefore lead to a reduction in biofouling. Reduced biofouling has a favorable effect on vessel speed, leads to a reduction of fuel and maintenance costs as well as greenhouse gas emissions.

The 3rd International Maritime Organization Greenhouse Gas study[644] estimates a global CO_2 emission of $\approx$ 33 Mio t/year for 2007-2012 with a 3.1 % contribution from shipping. The fuel consumption by vessels is estimated to $\approx$ 300 Mio t/year, with the frictional resistance as factor in the marine industry[645] and the costs of harm reduction suffered by non-indigenous species mitigation as $1.6 - 4$ % of the annual operational cost for vessels on European seas. Ceria may partially replace cuprous oxide, the most potent - but toxic - antifouling biocide. As ceria is a byproduct of lanthanide production, the costs of bulk ceria ($\approx$ 1000 \$ per ton) are only slightly higher than those of bulk Cu_2O ($\approx$ 500 \$ per ton) and make only a small contribution to the total costs, in particular, as much smaller amounts of ceria are needed compared to Cu_2O.

Microbial biofilms are ubiquitous on domestic, industrial, biomedical and other surfaces, and traditional biocides (strong oxidants, antibiotics, etc.) are increasingly problematic because of poor efficacy, non-target environmental impacts or the evolution of

resistance by micro-organisms. Because of their intrinsic catalytic characteristics, and environmental sustainability, CeO_{2-x} nanorods may find broad application in paints, textiles, polymer membranes for water desalination or filters for the reclamation of waste water, aquaculture systems, on bridge piers, naval vessels or in offshore windparks.

The use of natural intermediates such as HOBr or halogenated metabolites, which – different from conventional antifouling agents - target specific bacterial signaling and regulatory systems, represents a new strategy with the goal to emulate a natural defense system for preventing bacterial colonization or biofilm development. A biomimicry approach that allows the substitution of conventional biocides or costly enzymatic preservation systems by a stable, non-toxic and highly abundant rare earth oxide would be a big step towards a sustainable antifouling solution."

6

Outlook

On Future Antifouling Materials

Most antifouling solutions on the market today contain copper in combination with co-biocides. Even after years of research on alternative strategies, copper-based antifouling solutions still offer the best performance. They rely on the use of seawater insoluble cuprous oxide combined with various organic booster biocides (e.g., Irgarol 1051, diuron, SEA-NINETM, zinc pyrithione, zineb). Many studies, however, have shown clearly that copper compounds are toxic to a variety of non-target marine species like the embryo/larvae of the oyster, mussel and sea urchin. Cyanobacteria are highly sensitive to copper toxicity as well. Recent data have shown also that hatchery salmon are vulnerable to the olfactory neurotoxicity caused by copper. This leads to neurobehavioural response changes which are critical for a successful migration.[646] In essence, copper from antifouling sources has become a problem in the marine environment, especially in isolated

waters like marinas and harbors that have little water exchange and high levels of boating activity. It has been estimated that only in San Diego's Shelter Island Yacht Basin, approximately 2.5 tons of copper leach from the hulls of two thousand boats each year.[647]

The growing awareness of copper toxicity has led to changes in legislation. The Baltic Sea is an environmentally sensitive environment with a small diversity of aquatic species. Swedish authorities placed severe restrictions on the use of copper antifouling paints in the Baltic Coast of Sweden. Likewise, the copper loading in the inland aquatic environment of the Netherlands is uniquely high. The Dutch pesticide authorities decided to ban the use of copper-containing antifouling paints on all pleasure craft, especially in inland waters. In the United States, western states are leading the campaign against copper antifouling paints. The "California Department of Pesticide Regulation" reevaluated copper based paints and the daily mean copper release rate was set to 9.5 µg/cm^2 per day beginning on mid of 2018.[648] Washington regulated in 2011 the maximum amount of copper inside the antifouling paint to 0.5 % for recreational vessels with the beginning of 2020.[649]

Consequently, there is a need to develop new environmentally friendly antifouling solutions. The goal in the design of biocidal antifouling coatings is to provide a surface containing active biocides that (i) are stationary or (ii) are deactivated shortly after leaving the surface. Thus, biocides with a short half-life, either by biodegradation or deactivation are needed. There are several thousand fouling organisms in the waters of the world, broadly classified into hard (such as barnacles) and soft organisms (grasses, algae). An effective antifouling should have a broad activity spectrum which must be continuously available to protect against biofilm formation.

Although the interest in biofilm formation and particular in biofouling originates from its corrosive effects on manmade structures, it also occurs on the surfaces of living marine organisms and leads to problems in aquaculture of seaweeds and shellfish. Many sessile marine organisms do not possess any physical or mechanical means of defense against possible colonizers, or predators, but nevertheless resist colonization and overgrowth by epibionts (an organism that lives on the surface of another organism). Studying the natural defense strategies against fouling of organisms has led to biomimetic approaches that can be used to better understand the structure and function of biological systems as models or inspiration for the sustainable design and engineering of materials

and machines. Natural antifouling strategies developed by marine organisms can be classified into three categories: (i) chemical, (ii) physical/mechanical and (iii) behavioral. With a special focus on biofouling, two of them have been pursued for biotechnological applications, in particular, chemical defense and effects of surface topography. A successful large-scale approach to combat biofouling will have to make use of a combination of at least two of these strategies.

The ability of organisms to combat colonization of epibionts chemically is associated with the formation of secondary metabolites, commonly involved in chemical defense against predators, pathogens and, additionally, against fouling. The discovery of potent antifouling compounds such as brominated furanones, diterpenoids,[650] synoxazolidinones,[651] and pulmonarins[652] demonstrates the potential of natural products as a source of new antifouling compounds. However, the discovery of new lead compounds with antifouling activity and their development requires large quantities of these compounds for laboratory screening, field assays, and tests of paint formulations. The challenge of natural products is the scale-up for the coating market. There are several strategies to produce larger amounts of natural products.

(i) Natural products extracted from organisms collected in the field. Although this is the first step during development, it is prohibitive during up-scaled production due to the availability of natural resources.

(ii) *Natural products extracted from cultured organisms and plants*, for example, using aqua- or maricultures. In-sea cultures may be a cost-effective option for the supply of natural compounds. Culturing may be a successful strategy if the natural products are of microbial origin, but many organisms are very difficult to culture.

(iii) *Culturing of recombinant microorganisms* that are transfected with genes involved in the synthesis of the natural product. This is only practical if the desired natural product is a direct gene product as peptides.

(iv) *Chemical synthesis of natural products*. Many natural products are too complex and expensive to synthesize. The number of synthetic steps and the cost of initial reactants determine the yield of the final product and thus the success. Analogues of the natural product with similar bioactivity, but lower costs would be a viable alternative.

(v) *Employing haloperoxidases to generate the natural products in situ*. The main advantage of the biocatalyst would be that the required biocides are delivered on demand. Many bacterial pathogens use QS to regulate the timing and extent of virulence factor

production, thereby allowing them to amass until a sufficient population has been achieved to overwhelm the immune response of the hosts. As QS is dependent on small molecule signals and their relative concentration, there is substantial interest in developing chemical strategies that disable QS signaling networks or even prevent virulence. This "anti-virulence" strategy would not only be a pathway to suppress epibiont growth but also to mitigate bacterial infection in humans, animals, and plants.

Several opportunistic microorganisms have become resistant to current antimicrobial and antibiotic treatment. Therefore, strategies to inhibit QS have received significant attention. Such non-bactericidal approaches could also be robust to resistance development. The (non-halogenated) starting compounds for interference with QS are supplied by the colonizers themselves. This eliminates the need to synthesize many natural products as antimicrobial agents against different colonizers on spec. Moreover, there would be a constant supply of active biocides that are stationary in low concentration. The biocides are not only complexed and used shortly after leaving the surface, but also compounds of the ecosphere, present in the biological life cycle for millions of years.

(vi) *Employing nanoparticle haloperoxidase mimics to generate the natural QS inhibitors in situ*. This biomimicry approach to substitute conventional biocides or costly enzymatic preservation systems by cheap and very stable "heterogeneous catalysts" seems to be the most practical and sustainable solution.

Haloperoxidase mimics allow designing stable antibacterial materials with high chemical stability, low environmental toxicity due to the insolubility of ceria in water, costs, constant availability of the substrates (H_2O_2 and halide) which are required for a dynamic antibacterial activity (HOX formation), and intrinsic activity at substrate concentrations comparable to those encountered in aqueous environments. This reduces time, energy and produces less polluted water.

Because of their intrinsic catalytic characteristics and environmental sustainability oxide nanoparticles (e.g. CeO_{2-x}) may find broad application not only in antifouling paints, but also on bridge piers, naval vessels or in offshore windparks, in aquaculture systems,[653] polymer membranes for water desalination or filters for the reclamation of waste water,[654] drinking water pipes and clarification plants, cooling systems, or on textiles.[654] Biofouling in aquacultures is a well-known problem, whose severity depends on factors like biota in the region, temperature, light, salinity, tides and water transparency amongst others. Fouling on fish cages can cause a reduced water flow through the meshes,

clogging of the mesh and the increased excess weight. Water flow through nets can be reduced upon fouling and the diameter of the net twine can increase. Consequently, oxygen levels in the cage drop, whilst fish wastes and ammonia levels increase. Moreover, biofouling itself can act as a pathogen vector with serious consequences to fish health. The costs associated with biofouling can be very significant.

Similarly, biofouling leads to the use of higher operating pressure, frequent chemical cleaning, and shorter life times in reverse osmosis membranes. They are becoming increasingly popular for water purification applications that require high salt rejection such as brackish and seawater desalination. However, due to fouling by microorganisms, they have been unable so far to realize their full potential.

Many plants and fungi have coevolved and established regulated symbiotic associations with bacteria. Plant-associated proteobacteria possess AHL-mediated quorum-sensing systems.[655] Plants and fungi do not have active immune systems as mammals. They rely on chemical defense systems to cope with the bacteria in the environment. Since plants and fungi produce related chemical compounds to inhibit (or to stimulate) bacterial AHL-mediated communication,[656] similar strategies may be successful for suppressing fungal growth.

With a movement towards environmentally-friendly products, latest developments in the field of antifoulants include fouling-release coatings (silicone (PDMS), flour-silicones), fast polishing materials, contact activity, removable foils, on-demand systems, spiky coatings, surfaces with defined micro-structures, hydrogels and metallic layers including organo-metallic coatings and metal claddings. Biofilms are around virtually everywhere. They are present on practically all surfaces such as food packaging, door handles, push buttons, keyboards, and other elements made of plastic. In medicinal applications, they develop for example in catheter tubes or on surgical instruments. The main problem in connection with combatting these using biocides and antibiotics is the risk of the development of resistance.

The use of natural intermediates, formed *in situ* with non-toxic and highly abundant metal oxide enzyme mimics, which target specific bacterial signaling and regulatory systems, represents a new and efficient "green" strategy with the goal to emulate and utilize a natural defense system for preventing bacterial colonization or biofilm development.

7

Authorship Contributions

7.1   Authorship Contributions Chapter 1

Chapter 1 and the Outlook have been designed for a future review publication. For final and successful submission, further adjustments will be required and will be done by the co-authors. All pictures are presented with thesis-dependent permissions of the specific publishing groups listed at the end of the thesis. Taken parts are delimited by the name of the paper´s author and the specific reference.

Category 1

Conception and design of study:

K. Herget with support and proofreads from H. Frerichs, F. Pfitzner, N. Tahir and W. Tremel.

Acquisition of data and *Analysis and/or interpretation of data*:

Data acquisition and analysis had been done by each of the single authors of the papers cited. The selection of the papers cited to give a broad overview about this specific topic was done by K. Herget, H. Frerichs, F. Pfitzner, N. Tahir and W. Tremel.

Category 2

Drafting the manuscript: K. Herget, H. Frerichs, F. Pfitzner, N. Tahir and W. Tremel.

Revising the manuscript or specialized parts of the manuscript critically for important intellectual content: K. Herget, H. Frerichs, F. Pfitzner, N. Tahir and W. Tremel.

Category 3

Approval of the version of the manuscript to be published:

K. Herget, H. Frerichs, F. Pfitzner, N. Tahir and W. Tremel.

Figures and illustrations: Individual adaption prepared by K. Herget.

7.2   Authorship Contributions Chapter 3

The content of Chapter 3 and the Conclusion are taken and adapted from *"Haloperoxidase Mimicry by CeO$_{2-x}$ Nanorods Combats Biofouling", Adv. Mater.* 2017*, 29 (4),* 1603823. Taken parts are delimited by quotation marks.

Category 1

Conception and design of study:

K. Herget, W. Tremel.

Acquisition of data:

K. Herget – Synthesis, sample preparation, kinetic measurement and analysis, bio-antiadhesion tests, sample preparation for analysis methods and interpretation of results.

P. Hubach – Large-scale synthesis, analysis of leaching tests.

S. Pusch – HPLC/ESI-MS.

P. Deglmann– Theoretical calculations.

H. Götz – XPS measurements and analysis.

T.E. Gorelik – HRTEM measurements.

I.A. Gural'skiy – Support for kinetical analysis.

F. Pfitzner – Support for *E. coli* adhesion assays.

T. Link – Support for *E. coli* handling.

S. Schenk – Theoretical calculations.

M. Panthöfer – PXRD refinement.

V. Ksenofontov – SQUID measurement and analysis.

U. Kolb, T. Opatz, R. André, W. Tremel – Supervision and support.

Analysis and/or interpretation of data:

K. Herget, P. Hubach, S. Pusch, P. Deglmann, H. Götz, T.E. Gorelik, I.A. Gural'skiy, F. Pfitzner, T. Link, S. Schenk, M. Panthöfer, V. Ksenofontov.

Category 2

Drafting the manuscript: K. Herget, W. Tremel.

Revising the manuscript or specialized parts of the manuscript critically for important intellectual content: P. Hubach, S. Pusch, P. Deglmann, H. Götz, T.E. Gorelik, I.A. Gural'skiy, F. Pfitzner, T. Link, S. Schenk, M. Panthöfer, V. Ksenofontov, U. Kolb, T. Opatz, R. André, W. Tremel.

Category 3

Approval of the version of the manuscript to be published:

K. Herget, P. Hubach, S. Pusch, P. Deglmann, H. Götz, T.E. Gorelik, I.A. Gural'skiy, F. Pfitzner, T. Link, S. Schenk, M. Panthöfer, V. Ksenofontov, U. Kolb, T. Opatz, R. André, and W. Tremel.

Table of Contents figure: Prepared by K. Weldert

8

Permissions

**ELSEVIER LICENSE
TERMS AND CONDITIONS**

Jun 15, 2017

This Agreement between Karoline Herget ("You") and Elsevier ("Elsevier") consists of your license details and the terms and conditions provided by Elsevier and Copyright Clearance Center.

License Number	4130260757530
License date	Jun 15, 2017
Licensed Content Publisher	Elsevier
Licensed Content Publication	Journal of Molecular Biology
Licensed Content Title	X-ray structure determination of a vanadium-dependent haloperoxidase from Ascophyllum nodosum at 2.0 Å resolution11Edited by R. Huber
Licensed Content Author	M. Weyand,H.-J. Hecht,M. Kieß,M.-F. Liaud,H. Vilter,D. Schomburg
Licensed Content Date	Oct 29, 1999
Licensed Content Volume	293
Licensed Content Issue	3
Licensed Content Pages	17
Start Page	595
End Page	611
Type of Use	reuse in a thesis/dissertation
Portion	figures/tables/illustrations
Number of figures/tables /illustrations	1
Format	both print and electronic
Are you the author of this Elsevier article?	No
Will you be translating?	No
Order reference number	
Original figure numbers	Figure 7
Title of your thesis/dissertation	Metal Oxides as Enzyme Mimics
Expected completion date	Sep 2017
Estimated size (number of pages)	150
Elsevier VAT number	
Requestor Location	
Publisher Tax ID	
Total	0.00 USD
Terms and Conditions	

Permission of Figure 4b.

Permission of Figure 8.

**ELSEVIER LICENSE
TERMS AND CONDITIONS**

Jun 15, 2017

This Agreement between Karoline Herget ("You") and Elsevier ("Elsevier") consists of your license details and the terms and conditions provided by Elsevier and Copyright Clearance Center.

License Number	4130280516083
License date	Jun 15, 2017
Licensed Content Publisher	Elsevier
Licensed Content Publication	Polyhedron
Licensed Content Title	Polymer-grafted and neat vanadium(V) complexes as functional mimics of haloperoxidases
Licensed Content Author	Mannar R. Maurya,Nikita Chaudhary,Fernando Avecilla
Licensed Content Date	Jan 8, 2014
Licensed Content Volume	67
Licensed Content Issue	n/a
Licensed Content Pages	13
Start Page	436
End Page	448
Type of Use	reuse in a thesis/dissertation
Intended publisher of new work	other
Portion	figures/tables/illustrations
Number of figures/tables /illustrations	1
Format	both print and electronic
Are you the author of this Elsevier article?	No
Will you be translating?	No
Order reference number	
Original figure numbers	Figure 3
Title of your thesis/dissertation	Metal Oxides as Enzyme Mimics
Expected completion date	Sep 2017
Estimated size (number of pages)	150
Elsevier VAT number	
Requestor Location	
Publisher Tax ID	
Total	0.00 EUR
Terms and Conditions	

Permission of Figure 11a.

ACS Publications
Most Trusted. Most Cited. Most Read.

Title: MCM-41-Supported Oxo-vanadium(IV) Complex: A Highly Selective Heterogeneous Catalyst for the Bromination of Hydroxy Aromatic Compounds in Water

Author: Susmita Bhunia, Debraj Saha, Subratanath Koner

Publication: Langmuir

Publisher: American Chemical Society

Date: Dec 1, 2011

Copyright © 2011, American Chemical Society

PERMISSION/LICENSE IS GRANTED FOR YOUR ORDER AT NO CHARGE

This type of permission/license, instead of the standard Terms & Conditions, is sent to you because no fee is being charged for your order. Please note the following:

- Permission is granted for your request in both print and electronic formats, and translations.
- If figures and/or tables were requested, they may be adapted or used in part.
- Please print this page for your records and send a copy of it to your publisher/graduate school.
- Appropriate credit for the requested material should be given as follows: "Reprinted (adapted) with permission from (COMPLETE REFERENCE CITATION). Copyright (YEAR) American Chemical Society." Insert appropriate information in place of the capitalized words.
- One-time permission is granted only for the use specified in your request. No additional uses are granted (such as derivative works or other editions). For any other uses, please submit a new request.

If credit is given to another source for the material you requested, permission must be obtained from that source.

Permission of Figure 11b.

**ELSEVIER LICENSE
TERMS AND CONDITIONS**

Jun 15, 2017

This Agreement between Karoline Herget ("You") and Elsevier ("Elsevier") consists of your license details and the terms and conditions provided by Elsevier and Copyright Clearance Center.

License Number	4130281375256
License date	Jun 15, 2017
Licensed Content Publisher	Elsevier
Licensed Content Publication	Polyhedron
Licensed Content Title	Polymer-anchored peroxo compounds of molybdenum and tungsten as efficient and versatile catalysts for mild oxidative bromination
Licensed Content Author	Jeena Jyoti Boruah,Siva Prasad Das,Rupam Borah,Sandhya Rani Gogoi,Nashreen S. Islam
Licensed Content Date	Mar 22, 2013
Licensed Content Volume	52
Licensed Content Issue	n/a
Licensed Content Pages	9
Start Page	246
End Page	254
Type of Use	reuse in a thesis/dissertation
Intended publisher of new work	other
Portion	figures/tables/illustrations
Number of figures/tables /illustrations	1
Format	both print and electronic
Are you the author of this Elsevier article?	No
Will you be translating?	No
Order reference number	
Original figure numbers	Figure 1
Title of your thesis/dissertation	Metal Oxides as Enzyme Mimics
Expected completion date	Sep 2017
Estimated size (number of pages)	150
Elsevier VAT number	
Requestor Location	Karoline Herget
Publisher Tax ID	
Total	0.00 EUR
Terms and Conditions	

Permission of Figure 12a.

**SPRINGER LICENSE
TERMS AND CONDITIONS**

Jun 15, 2017

This Agreement between Karoline Herget ("You") and Springer ("Springer") consists of your license details and the terms and conditions provided by Springer and Copyright Clearance Center.

License Number	4130290347523
License date	Jun 15, 2017
Licensed Content Publisher	Springer
Licensed Content Publication	Journal of Inorganic and Organometallic Polymers and Materials
Licensed Content Title	Oxidation and Oxidative Bromination Reactions Catalyzed By a Reusable Polymer-Anchored Iron(III) Complex in Water at Room Temperature
Licensed Content Author	Sk. Manirul Islam
Licensed Content Date	Jan 1, 2013
Licensed Content Volume	24
Licensed Content Issue	2
Type of Use	Thesis/Dissertation
Portion	Figures/tables/illustrations
Number of figures/tables /illustrations	1
Author of this Springer article	No
Order reference number	
Original figure numbers	Figure 2
Title of your thesis / dissertation	Metal Oxides as Enzyme Mimics
Expected completion date	Sep 2017
Estimated size(pages)	150
Requestor Location	Karoline Herget
Billing Type	
Billing Address	
Total	0.00 EUR
Terms and Conditions	

Permission of Figure 14b,c.

Permission of Figure 17a,b and Figure 26a.

ROYAL SOCIETY OF CHEMISTRY LICENSE
TERMS AND CONDITIONS

Jun 15, 2017

This Agreement between Karoline Herget ("You") and Royal Society of Chemistry ("Royal Society of Chemistry") consists of your license details and the terms and conditions provided by Royal Society of Chemistry and Copyright Clearance Center.

License Number	4130291148148
License date	Jun 15, 2017
Licensed Content Publisher	Royal Society of Chemistry
Licensed Content Publication	Journal of Materials Chemistry
Licensed Content Title	V2O5 nanowires with an intrinsic iodination activity leading to the formation of self-assembled melanin-like biopolymers
Licensed Content Author	Filipe Natalio,Rute André,Sascha A. Pihan,Madalena Humanes,Ron Wever,Wolfgang Tremel
Licensed Content Date	Jul 11, 2011
Licensed Content Volume	21
Licensed Content Issue	32
Type of Use	Thesis/Dissertation
Requestor type	non-commercial (non-profit)
Portion	figures/tables/images
Number of figures/tables /images	2
Format	print and electronic
Distribution quantity	100
Will you be translating?	no
Order reference number	
Title of the thesis/dissertation	Metal Oxides as Enzyme Mimics
Expected completion date	Sep 2017
Estimated size	150
Requestor Location	Karoline Herget
	Ludwigshafen, 67071 Germany Attn: Karoline Herget
Billing Type	Invoice
Billing Address	Karoline Herget
	Ludwigshafen, Germany 67071 Attn: Karoline Herget
Total	0.00 EUR

Permission of Figure 18b,c.

ACS Publications
Most Trusted. Most Cited. Most Read.

Title: Oxyhalogenation of Activated Arenes with Nanocrystalline Ceria

Author: Antonio Leyva-Pérez, Diego Cómbita-Merchán, Jose R. Cabrero-Antonino, et al

Publication: ACS Catalysis

Publisher: American Chemical Society

Date: Feb 1, 2013

Copyright © 2013, American Chemical Society

PERMISSION/LICENSE IS GRANTED FOR YOUR ORDER AT NO CHARGE

This type of permission/license, instead of the standard Terms & Conditions, is sent to you because no fee is being charged for your order. Please note the following:

- Permission is granted for your request in both print and electronic formats, and translations.
- If figures and/or tables were requested, they may be adapted or used in part.
- Please print this page for your records and send a copy of it to your publisher/graduate school.
- Appropriate credit for the requested material should be given as follows: "Reprinted (adapted) with permission from (COMPLETE REFERENCE CITATION). Copyright (YEAR) American Chemical Society." Insert appropriate information in place of the capitalized words.
- One-time permission is granted only for the use specified in your request. No additional uses are granted (such as derivative works or other editions). For any other uses, please submit a new request.

If credit is given to another source for the material you requested, permission must be obtained from that source.

Permission of Figure 19a.

This Agreement between Karoline Herget ("You") and John Wiley and Sons ("John Wiley and Sons") consists of your license details and the terms and conditions provided by John Wiley and Sons and Copyright Clearance Center.

License Number	4130300171006
License date	Jun 15, 2017
Licensed Content Publisher	John Wiley and Sons
Licensed Content Publication	Advanced Synthesis & Catalysis
Licensed Content Title	Hydroxyl Radical Promotes the Direct Iodination of Aromatic Compounds with Iodine in Water: A Combined Experimental and Theoretical Study
Licensed Content Author	Peng Zhang,Dongqing Sun,Mingwei Wen,Jingkui Yang,Kebin Zhou,Zhixiang Wang
Licensed Content Date	Feb 23, 2012
Licensed Content Pages	10
Type of use	Dissertation/Thesis
Requestor type	University/Academic
Format	Print and electronic
Portion	Figure/table
Number of figures/tables	1
Original Wiley figure/table number(s)	Figure 1a
Will you be translating?	No
Title of your thesis / dissertation	Metal Oxides as Enzyme Mimics
Expected completion date	Sep 2017
Expected size (number of pages)	150
Requestor Location	Karoline Herget
Publisher Tax ID	
Billing Type	
Billing Address	
Total	0.00 EUR

Permission of Figure 22.

JOHN WILEY AND SONS LICENSE
TERMS AND CONDITIONS

Jun 15, 2017

This Agreement between Karoline Herget ("You") and John Wiley and Sons ("John Wiley and Sons") consists of your license details and the terms and conditions provided by John Wiley and Sons and Copyright Clearance Center.

License Number	4130300450953
License date	Jun 15, 2017
Licensed Content Publisher	John Wiley and Sons
Licensed Content Publication	ChemNanoMat
Licensed Content Title	Xerogel Coatings Produced by the Sol–Gel Process as Anti-Fouling, Fouling-Release Surfaces: From Lab Bench to Commercial Reality
Licensed Content Author	Michael R. Detty,Rosaria Ciriminna,Frank V. Bright,Mario Pagliaro
Licensed Content Date	Jun 25, 2015
Licensed Content Pages	7
Type of use	Dissertation/Thesis
Requestor type	University/Academic
Format	Print and electronic
Portion	Figure/table
Number of figures/tables	1
Original Wiley figure/table number(s)	Figure 5
Will you be translating?	No
Title of your thesis / dissertation	Metal Oxides as Enzyme Mimics
Expected completion date	Sep 2017
Expected size (number of pages)	150
Requestor Location	Karoline Herget
Publisher Tax ID	
Billing Type	
Billing Address	
Total	0.00 EUR
Terms and Conditions	

Permission of Figure 24.

**JOHN WILEY AND SONS LICENSE
TERMS AND CONDITIONS**

Jun 15, 2017

This Agreement between Karoline Herget ("You") and John Wiley and Sons ("John Wiley and Sons") consists of your license details and the terms and conditions provided by John Wiley and Sons and Copyright Clearance Center.

License Number	4130300676662
License date	Jun 15, 2017
Licensed Content Publisher	John Wiley and Sons
Licensed Content Publication	Biochemistry and Molecular Biology Education
Licensed Content Title	Red seaweed enzyme-catalyzed bromination of bromophenol red: An inquiry-based kinetics laboratory experiment for undergraduates
Licensed Content Author	Piyachat Jittam,Patcharee Boonsiri,Chamras Promptmas,Namkang Sriwattanarothai,Nattinee Archavarungson,Pintip Ruenwongsa,Bhinyo Panijpan
Licensed Content Date	Mar 24, 2009
Licensed Content Pages	7
Type of use	Dissertation/Thesis
Requestor type	University/Academic
Format	Print and electronic
Portion	Figure/table
Number of figures/tables	1
Original Wiley figure/table number(s)	Table AII
Will you be translating?	No
Title of your thesis / dissertation	Metal Oxides as Enzyme Mimics
Expected completion date	Sep 2017
Expected size (number of pages)	150
Requestor Location	Karoline Herget
Publisher Tax ID	
Billing Type	
Billing Address	
Total	0.00 EUR

Permission of Table 6.

Permission of Figure 20, 21, 26b, Chapter 3 and, partly, of the Conclusion.

ELSEVIER LICENSE
TERMS AND CONDITIONS

Jul 22, 2017

This Agreement between Karoline Herget ("You") and Elsevier ("Elsevier") consists of your license details and the terms and conditions provided by Elsevier and Copyright Clearance Center.

License Number	4154320756945
License date	Jul 22, 2017
Licensed Content Publisher	Elsevier
Licensed Content Publication	Surface Science
Licensed Content Title	The electronic structure of oxygen vacancy defects at the low index surfaces of ceria
Licensed Content Author	Michael Nolan,Stephen C. Parker,Graeme W. Watson
Licensed Content Date	Dec 5, 2005
Licensed Content Volume	595
Licensed Content Issue	1-3
Licensed Content Pages	10
Start Page	223
End Page	232
Type of Use	reuse in a thesis/dissertation
Portion	figures/tables/illustrations
Number of figures/tables /illustrations	1
Format	both print and electronic
Are you the author of this Elsevier article?	No
Will you be translating?	No
Original figure numbers	Figure 2
Title of your thesis/dissertation	Metal Oxides as Enzyme Mimics
Expected completion date	Sep 2017
Estimated size (number of pages)	150
Requestor Location	Karoline Herget
Publisher Tax ID	GB 494 6272 12
Total	0.00 EUR
Terms and Conditions	

Permission of Figure 52.

9

Experimental Section

9.1   Materials

Cerium(III) chloride heptahydrate (99.9 %), celestine blue ("Mordant Blue 14", 80 %), coumarin (≥99 %), 2,2′-azino-bis(3-ethylbenzothiazoline-6-sulfonic acid) diammonium salt (ABTS, ≥98 %), phenol red (BioReagent), ethylenediaminetetraacetic acid (EDTA), sterile-filtered seawater from Gulf Stream in the Gulf of Mexico, Na_3PO_4, NaOH, KBr, NaBr, LiBr, tris(hydroxymethyl)aminomethane (Tris base/Trizma base/THAM), bulk cerium(IV) oxide (< 5 μm, 99.9 %), cerium(IV) oxide nanoparticles (<25 nm, 10 %w solution), bulk vanadium pentoxide (99.9 %), manganese(II) oxide (≈ 60 mesh, 99 %), manganese(II,III) oxide (≈ 325 mesh, 97 %), γ-iron(III) oxide nanopowder (<50 nm), zinc oxide (≥ 99.0 %), zinc oxide nanopowder (<100 nm, ≈ 80 %), copper iron oxide nanopowder (<100 nm, 98.5 %) and copper zinc iron oxide nanopowder (<100 nm, 98.5 %) were purchased from Sigma Aldrich.

Cerium(III) nitrate hexahydrate (99.5 %, REacton®), cerium(IV) oxide nanopowder (15-30 nm, >99.5 %), cerium(IV) ammonium nitrate (>98 %), titan(IV) oxide (anatase, ≈ 325 mesh, 99.9 %), α-iron(III) oxide nanopowder (<20-60 nm, 99 %), antimony(III) oxide (1.1 - 1.8 micron powder, >99.6 %) and tungsten(VI) oxide, 2-chloro-5,5-dimethyl-1,3-cyclohexanedione (MCD, 98 %, $\varepsilon_{290\ nm}$ =20.2 $mM^{-1}cm^{-1}$) and 2,3-dimethoxytoluene (2,3-DMT, >98 %) were purchased from Alfa Aesar. 4′,6-Diamidino-2-phenylindole dihydrochloride powder (DAPI, ≥98 %), hydrogen peroxide (30 %, ROTI-PURAN®, d = 1.11 g·mL^{-1}, $\varepsilon_{240\ nm}$ = 43.6 $mM^{-1}cm^{-1}$), LB-Medium (Luria/Miller) were purchased from Carl Roth. NH_4Br (99 %) and tungsten(IV) oxide (150 micron, 99.9 %) are supplied by abcr.

E. coli (Top 10) are thankfully provided by Thorben Link (group of Prof. Dr. W. Müller, Universitätsmedizin). The silicone alkyd-based, hard formulation paint was purchased from International Yachtfarben (Akzo Nobel, "Toplac Snow White 001", YKB000, International Paint Ltd.; EG – safety data sheet, version 2, 17/07/12) and the abrasive paint formulation (resin-based) was thankfully provided by BASF. *Corallina officinalis* was purchased from the Alfred-Wegener-Institut, Helmholtz-Zentrum für Polar- und Meeresforschung, Biologische Anstalt Helgoland, Germany.

All reagents and solvents were of analytical grade and used as received. Stock solutions, reaction mixture and synthesis were prepared in deionized "MilliQ" water (18.2 MΩ·cm, 25°C, pH ≈ 5.6).

9.2   Synthesis

Doped PAN

The reaction was performed in on-tenth of the approach published.[406,657] In general, the metal acid (H_2MoO_4 or $H_2WO_4 \cdot 2H_2O$; 0.472 mmol (1/10 of original amount)) was dissolved in a minimum of cold H_2O_2 solution (30 wt%, $\approx$ 2 mL) at room temperature. The time needed to obtain a clear solution varies with respect to the used metal acid from 1-3 days. Afterwards, the solution was cooled by using an ice bath and the pH (ca. 1-2) was adjusted to 5 by drop-wise addition of concentrated NaOH solution. Subsequently, the PAN polymer (0.1 g) was added to the cooled reaction mixture. The ice bath had been allowed to melt and the reaction mixture was stirred up to one week. Then, the turbid suspension was filtered, washed with a small amount of water (ca. 3 mL) and pre-cooled acetone (2x 5mL). The raw product was dried at 40-60°C for one day. After work up, colorless or slightly yellow product powders were received. Elemental analysis resulted in: 2.1 wt% Mo@X-PAN, 1.4 wt% Mo@N-PAN (both synthesized by BASF) and 64 wt‰ Mo@X-PAN, 75 wt‰ Mo@N-PAN, 18 wt‰ W@X-PAN and 17 wt‰ W@N-PAN (synthesized by K. Herget). Because of the difficulties of measuring the PAN polymers by UV/Vis spectroscopy (water-insoluble and adherence at the cuvette), qualitative dye assays were emphasized. The stock solutions of the PANs were prepared in DMSO.

Doped LDH

The reaction was performed as published.[397,544] All solutions were prepared with deionized H_2O that was degassed by sonication in an argon atmosphere for approximately one hour. Degassed H_2O (200 mL) was given to a 1L three-necked flask. Afterwards, the pH was adjusted to pH 8 by the addition of 1M NaOH. The prepared aqueous stock solutions of $NiCl_2 \cdot 6\ H_2O$ (120 mL, 708 mM, 2.43 Equation) and $AlCl_3 \cdot 6\ H_2O$ (120 mL, 292 mM, 1.00 Equation) were mixed prior to addition *via* a dropping funnel (combined greenish solution, 0.354 M $NiCl_2$ and 0.156 M $AlCl_3$ in 240 mL). Under an inert atmosphere (argon balloon), the metal solution was added dropwise at a rate of approximately 120 mL/hour, resulting in a turbid, green suspension. The pH was monitored with a pH electrode at short intervals and kept at approximately 8.0 ± 0.5 by the addition of 1 M NaOH (4g in 100 mL; ca. 300 mL in total). After complete addition of the metal solution,

the green suspension (pH 8) was stirred overnight at room temperature. Then, the green precipitate was filtered, washed several times with water and dried at 80°C overnight. The sample was ground, yielding a green powder, and prepared for XRD and TEM analysis. Elemental analysis by BASF resulted in 7.2 g aluminum and 38.0 g nickel per 100 g sample. An analogues procedure was performed to synthesize of MgAl-LDH[397,398,658] the addition of a solution of 0.3 M (4.36 g in 60 mL water) $AlCl_3 \cdot 6H_2O$ and 0.7 M (8.539 g in 60 mL) $MgCl_2 \cdot 6H_2O$ to basic H_2O (50 mL, pH 10.4). The pH during reaction was kept at 10 ± 0.5 with 1M NaOH.

In a general doping procedure, the pre-synthesized LDH (ca. 500 mg) was added to a 250 mL round bottomed flask containing a stirred solution of the corresponding doping metal salt in H_2O (1.9 mM in 50 or 20 mL, doping material: $Na_2WO_4 \cdot 2 H_2O$, KVO_3 or $Na_2MoO_4 \cdot 2 H_2O$) at r.t. The suspension was stirred at r.t. in an inert atmosphere (argon) for one day. After approx. 24 hours, the green, turbid suspension was transferred in aliquots to a plastic tube (50 mL) and centrifuged at 9000 rpm for 5-10 min until entire contents were collected. In a repetitive procedure, the doped LDHs were washed with H_2O (2x 25 mL). Afterwards, the greenish powders were dried at 80°C overnight. After drying, samples were ground and yields (> 960 mg) determined. Elemental analysis of the doped LDH resulted in a doping amount, for example, of 1.9 g molybdenum; 3.3 g tungsten and 0.9 g vanadium each in combination of 7.2 g Al/38.0 g Ni per 100 g sample.

Cerium Oxide Nanoparticles

CeO$_2$ nanorods, yellow

CeO_{2-x} nanorods were synthesized following ref.[562,592]. An aqueous solution of NaOH (100 mL, 9.0 M, 37.8 g) was directly poured into a rapidly stirred solution of cerium(III) nitrate hexahydrate (20 mL, 5.2 g, 0.05M) in MilliQ-water. After being heavily stirred for 30 min, the lilac suspension was transferred into a stainless-steel autoclave (total volume: 270 mL) and heated to 100°C for 24 hours. The lilac product was separated from the turbid suspension by centrifugation (3000 rpm, 10 min), washed five times with MilliQ-water (15 mL each). After drying at 60°C overnight, the resulting yellow product was carefully hand ground. The yield (>70 %) was determined gravimetrically.

CeO$_2$ nanorods, colorless

CeO$_2$ nanorods were synthesized as published.[562] Cerium(III) chloride hexahydrate (0.373 g, 0.05M) in 15 mL MQW was poured into 5 mL of an aqueous Na$_3$PO$_4$ solution (0.025 g, 0.02M) with rapid stirring. The resulting white suspension was stirred for 15 minutes and afterwards transferred into a stainless-steel autoclave with Teflon inlay (total volume: 25 mL) and heated at 220°C for 15 hours. The resulting colorless product was separated from the turbid suspension by centrifugation (9000 rpm, 10 minutes), washed several times with water (20 mL) and dried at 60°C for minimum 12 hours. The resulting colorless product (yields >70 %) was carefully grinded.

CeO$_2$ spherical nanoparticles, yellow

EDTA (2.925 g, 0.005 mol) was poured into a rapidly stirred solution of cerium(III) nitrate hexahydrate (2.182 g, 0.01 mol) in 100 mL MQW. Afterwards, aqueous NH$_3$ solution (25 vol%) was added until a yellow solution (pH 5) was reached. The water was evaporated to yield a yellow, hygroscopic residue which was then transferred to a ceramic crucible. After a drying step (100°C, 5h), the residue was heated in a muffle furnace to 250°C (5°C/min,), plateau: 1h at 200 nL/h air, then heated further to 500°C (2.5°C/min), plateau: 1.5h at 200 nL/h air. The resulting yellow product (yields >70 %) was carefully grinded.

CeO$_2$ nanocubes, colorless

CeO$_2$ nanocubes were synthesized as published.[562] Cerium(III) chloride hexahydrate (0.373 g, 0.05M) in 15 mL MQW was poured into an aqueous Na$_3$PO$_4$ solution (5 mL, 0.025 g, 0.02M) with rapid stirring. The resulting white suspension was stirred for 15 minutes and afterwards transferred into a stainless-steel autoclave with Teflon inlay (total volume: 25 mL) and heated at 220°C for 15 hours. The resulting white product was separated from the turbid suspension by centrifugation (9000 rpm, 10 minutes), washed several times with water (20 mL) and dried at 60°C for minimum 12 hours. The resulting colorless product (yields >70 %) was carefully grinded.

9.3   Methods

Powder-X-Ray Diffraction Patterns

X-ray diffractograms of the samples were obtained with a step size of 0.0025° on a Siemens D5000 powder diffractometer equipped with a Braun M50 position-sensitive detector, Ge (220) monochromator, and using Cu-K$_\alpha$ ($\lambda = 1.5405$ Å) radiation (for details see Table 10). XRD patterns were recorded in the *2θ* range of 10-90° at ambient temperature. The XRD samples were prepared on a Scotch®tape. All intensities in Figure 40 could be indexed to a fluorite type CeO_2 (space group: Fm3m) with lattice constant a = 5.411 Å, which agrees with the JCPDS file for CeO_2 (JCPDS 34-394). Full pattern profile fits applying the fundamental parameter approach were performed using TOPAS academic V5 (Figure 40).

Table 10: Details concerning Rietveld refinement (cf. Figure 40).

Section	Subsection	Detailed description
General information	Diffractometer	Siemens D5000 with Braun M50 position sensitive detector
	Sample preparation	Powder fixed between two stripes of 3m Scotch tape
	Measuring mode	Transmission, ω-2Θ, step size 0.025°, step time 4s, scanning rate 0.375°/min
	Wavelength /Å	1.540596, Ge (220) monochromator
	Measuring range	$10 \leq 2\Theta$ /° ≤ 90; $0.71 \leq Q$ /Å-1 ≤ 5.77
	Refinement range	$12.5 \leq 2\Theta$ /° ≤ 85; $0.9 \leq Q$ /Å-1 ≤ 5.5
	Temperature /K	298K
	Profile fit	Rietveld refinement according to reported crystal structure models
	Background	Chebyshev
	Profile function	Fundamental parameters approach, crystallite size anisotropy modeled in quadratic correction (*)
	Program	TOPAS Academic V5
	Total no. of parameters / background	24/17
	R$_{wp}$	1.71
	GoF	0.25
CeO_2 Cerianite	Space group	Fm-3m
	Cell parameter /Å	5.4363(3)
	Crystallite size /nm	6.8(1) nm × 9.5(2) nm × 7.0(1) nm, according to axes
	Wyckoff positions	Ce: 4a, O: 8c
	B$_{eq}$	1.0(1)

(*) individual crystallite (CS$_{\underline{h}}$) sizes are computed for each reflection (*hkl*) according to the quadratic form $CS_h = 1/norm \{\underline{h}^T \times \underline{C}_{ij} \times \underline{h}\}$ in which $\underline{h}$ is the reciprocal lattice vector corresponding to (*hkl*). $\underline{C}_{ij} = (\underline{a}_i)^{1/2} \times (\underline{a}_j)^{1/2}$ is the symmetric second rank tensor of the square roots of the crystallite dimensions in direction *i* and *j* in the basis of the crystal lattice.

Transmission Electron Microscopy

The TEM samples were prepared by dispersing the nanoparticle powders in ethanol, placing a droplet onto a holey-carbon coated copper grid and drying at ambient temperature. The low-magnification imaging was performed using a Philips EM420 (LaB_6 source, 120kV) and a Zeiss Leo 906E (tungsten source, 120kV). High-resolution TEM imaging and electron diffraction were done using a FEI TECNAI F30 TEM (field-emission gun, 300kV). HRTEM (and Fourier transformations) as well as 3D electron diffraction data of a single CeO_{2-x} nanorod (thickness ≈ 7 nm, Figure 41) indicated the presence of polycrystalline and complex, "triple-rim" structured particles by the apparent splitting of certain reflections. The complex Fourier pattern (3D electron diffraction data, respectively) could be described as an overlay of two nets of reflections – one representing the [110] and the other – [112] diffraction pattern. The alignments of the diffraction patterns resulted in an overlap of the 220 reflections and the 111 and 002 reflections pointed in the same direction. Because the interplanar distances of 111 and 002 of the cubic CeO_2 structure were slightly different, a pair of two separate reflections was observed. With respect to the 111 reflection, the Fourier filtered image expressed the particle areas of the periphery, and the filtered image from the 002 reflection corresponded to the inner part of the particle. Assuming the particles lay flat on the supporting film, the top and bottom part of the particles´ cores exposed {110} facets (Figure 41). The side blocks were oriented with the [111] direction towards the sides. However, the facets formed at the side areas of the nanorods could not be assigned properly. No direct evidence for {100} facets which in general dominate in cubic cerium oxide could be found. Additionally, the exact crystallographic relationship of the interface between the inner and the outer parts could not be allocated. Along the nanorod axis, the lattices matched exactly by exposing (110)-type lattice planes. A complex inclined interface at the interfaces orthogonal to the rod axis was assumed because a theoretical lattice mismatch determined to be > 20 % would be not realistic.

Nitrogen Adsorption Measurements

A specific amount of CeO_{2-x} nanorods were transferred into a piston measuring cell and screwed with the device. Nitrogen adsorption measurements were performed using the Brunauer/Emmett/Teller evaluation method (BET) (Equation 15) on a Quantachrome gas adsorption instrument Autosorb-6B using nitrogen (28.0134 g·mol^{-1}) as the analysis gas at 77.4 K for a time period of about 843.9 min (cross section: 16.200 Å², liquid density: 0.808 g/cc) where P and P_0 are the equilibrium and saturation pressure of the adsorbates at the temperature of adsorption, w is the weight of gas adsorbed and S is the BET constant.

The software associated with the device (Quantachrome ASiQwin 3.0) was used to analyze the recorded data resulting in a BET surface area of 82.5 m^{2}g^{-1}.

$$\frac{1}{w\left(\frac{P_0}{P} - 1\right)} = 1 + S\left(\frac{P}{P_0}\right)$$

15
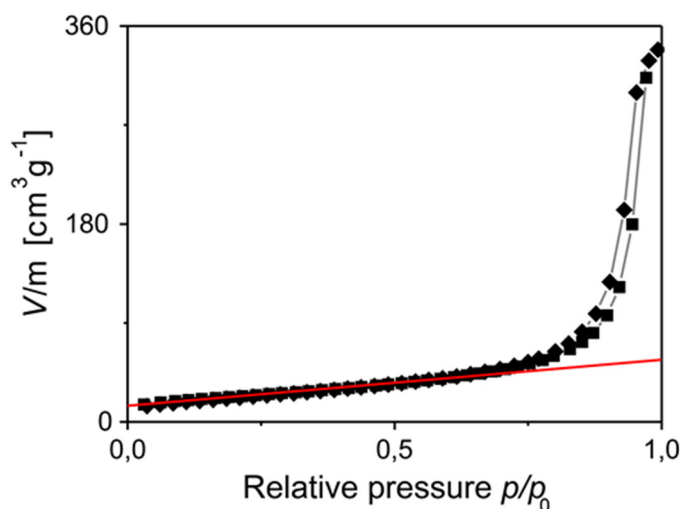
Figure 59. Physisorption isotherm of CeO_{2-x} nanorods. A surface area of to 82.5 m^{2}g^{-1} for the CeO_{2-x} nanorods has been determined using the BET (Brunauer/Emmett/Teller) method within the linear range of 0-0.3 relative pressure (p/p$_0$) and volume per mass (V/m) of the adsorption curve (red line: slope: 41.838, intercept: 0.3832, correlation coefficient R: 0.999941, C constant: 110.177), ◆ adsorption, ■ desorption.

Fourier Transform Infrared Spectroscopy

Nicolet iS10 FT-IR spectrophotometer (Thermo Scientific) was used in the range of 550-4000 cm^{-1} with a resolution of 4 cm^{-1}.

Spectrophotometric Measurements

Kinetic measurements were performed on a JASCO Cary 300 spectrophotometer (instrument version 12) equipped with an integration sphere in combination with a magnet stirrer. To avoid a loss of intensity from the scattered light, the transmitted beam was forwarded to an integration sphere installed after the cuvette. The scanning kinetic measurements and antioxidant assays were performed on a Cary 5G spectrophotometer equipped with a magnetic stirrer. In both cases, a 1.3 mL semi-micro quartz cuvette with self-masking black walls and magnetic stirring capability (Agilent, product number 6610015400) was used. The software associated with the device was used primary to analyze the recorded data (determination of slopes) and Origin 7.5 was applied for graphic evaluations.

Magnetic Susceptibility Measurements

Magnetic susceptibility measurements were carried out with a Quantum-Design MPMS-XL-5 SQUID (superconducting quantum interference device) magnetometer at 200 K and variable magnetic field up to 5 T. Pascal's constants was used for diamagnetic correction. The magnetic susceptibilities of CeO_{2-x} nanorods and bulk CeO_2 which was considered as a standard Ce^{3+}-free compound were compared, at $T = 200$ K and a magnetic field $H = 5$ T. Taking into account the magnetic moments of Ce^{3+} ($\mu_{eff} = 2.54$ μ_B),[659–661] the amount of Ce^{3+} in CeO_{2-x} nanorods was determined to ≈ 0.5 at% as follows (Equation 16-19) where χ_{dia} : diamagnetic contribution to the magnetic susceptibility in $cm^3 \cdot mol^{-1}$; M: magnetisation of the sample in emu; M_{hold}: correction of the sample holder at in emu; H: magnetic field strength in Oersted; M_{CeO2}: molar mass of CeO_2 in $g \cdot mol^{-1}$; m_{CeO2}: weight of CeO_2 samples in g; χ_{mol} : molar magnetic susceptibility in $cm^3 \cdot mol^{-1}$: -1,42696E-4 $cm^3 \cdot mol^{-1}$ and -1,6299E-4 $cm^3 \cdot mol^{-1}$ at $T = 200$ K for CeO_{2-x} nanorods and standard CeO_2, correspondently.

$$\chi_{mol} = (M + M_{hold})\chi_g + |\chi_{dia}| \qquad\qquad 16$$

$$\chi_{mol} = (M + M_{hold})\frac{M_{CeO_2}}{Hm_{CeO_2}} + |\chi_{dia}| \qquad\qquad 17$$

$$\chi_{mol,theo}(Ce^{3+}) = \left(\frac{\mu_{eff}(Ce^{3+})}{2.828}\right)^2 / T = 40.334 \cdot 10^4 \, cm^3 mol^{-1} \qquad\qquad 18$$

$$Ce^{3+} = \frac{\chi_{mol}(CeO_{2-x}) - \chi_{mol}(CeO_{2,bulk})}{\chi_{mol,theo}(Ce^{3+})} \qquad\qquad 19$$
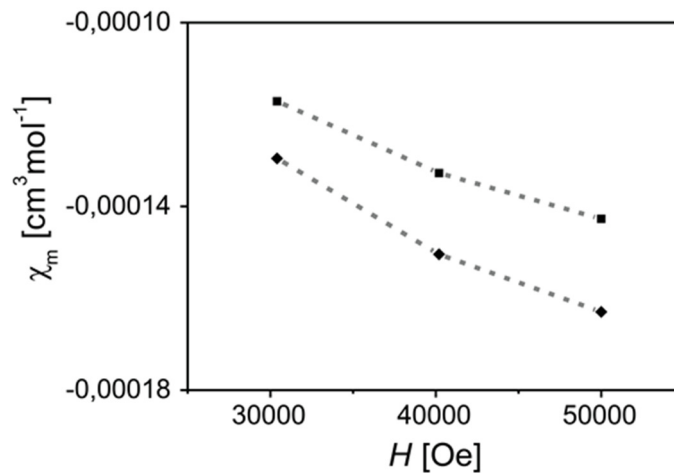
Figure 60. Magnetic measurements. Magnetic susceptibility of CeO_{2-x} nanorods and bulk CeO_2 *versus* magnetic field strength at T = 200 K. ◆ bulk CeO_2, ■ CeO_{2-x} nanorods.

X-Ray Photoelectron Spectroscopy

The surface composition of CeO_{2-x} nanorods was determined by X-ray photoelectron spectroscopy (XPS) on a 5600 ESCA (XPS) spectrometer (Physical Electronics GmbH) with monochromatic Al-K$_\alpha$ radiation (1486 eV at 250.0 W). The pass energy of the analyzer system was set to 58.7 eV and all acquisitions are done with an energy resolution of 0.125eV. The base pressure during XPS analysis was 10^{-9} mbar. All binding energies were referenced to the binding energy of C (1s, 284.8 eV). Deconvolution of the XPS spectra was carried out using MultiPak (version 9.6) software. The complex signals

were deconvoluted into 10 peaks (Table 11) with respect to physical constrains arising from the final-state occupation of the Ce 4f level, namely $3d_{3/2}$ (910-895 eV)[662] and $3d_{5/2}$ (895-875 eV)[662] spin-orbit coupling (3d multiplet splitting assigned to 18.5 ± 0.5 eV), ratio of intensities (3:2), iterative Shirley (background) and a Gauss/Lorenz peak type. According to ref. [565] the asymmetric peaks u and v are also modelled by a sum of two symmetric peaks with constrained parameters.

Table 11 shows an overview of the initial and final configurations corresponding to the specific transitions couples as well as the designation used in the following. The signals u', v' and u^0, v^0 correspond to the transitions of Ce^{3+} creating charge imbalance, oxygen vacancies and unsaturated chemical bonds on the catalyst surface.[564,565,663–667] Thus, the value of surface Ce^{3+} can be approximated to 36-45 % (Equation 20).[605] The corresponding survey spectrum is shown in Figure 61.

$$\%Ce_{(5/2)}^{3+} = \frac{A_{Ce_{(5/2)}^{3+}}}{A_{Ce_{(5/2)}^{3+}} + A_{Ce_{(5/2)}^{4+}}} \times 100$$

20

Table 11. Quantitative XPS analysis. The XPS spectrum of CeO_{2-x} nanorods contains 2 doublets (u, v) corresponding to two final state configurations: $3d^9\,4f^1\,(5d\,6s)^4$ and $3d^9\,4f^2\,(5d\,6s)^3$ for Ce^{3+}, while in the case of Ce^{4+} 3 doublets corresponding to $3d^9\,4f^0\,(5d\,6s)^5$, $3d^9\,4f^1\,(5d\,6s)^4$ and $3d^9\,4f^2\,(5d\,6s)^3$ final states are observed.[564,667,668]

Oxidation state	Initial configuration	Final configuration	Notation
Ce^{4+}	$3d^{10}\,4f^0\,V^n$	$3d^9\,4f^2\,V^{n-2}$	u''', v'''
		$3d^9\,4f^1\,V^{n-1}$	u'', v''
		$3d^9\,4f^0\,V^n$	u, v
Ce^{3+}	$3d^{10}\,4f^1\,V^n$	$3d^9\,4f^2\,V^{n-1}$	u', v'
		$3d^9\,4f^1\,V^n$	u^0, v^0
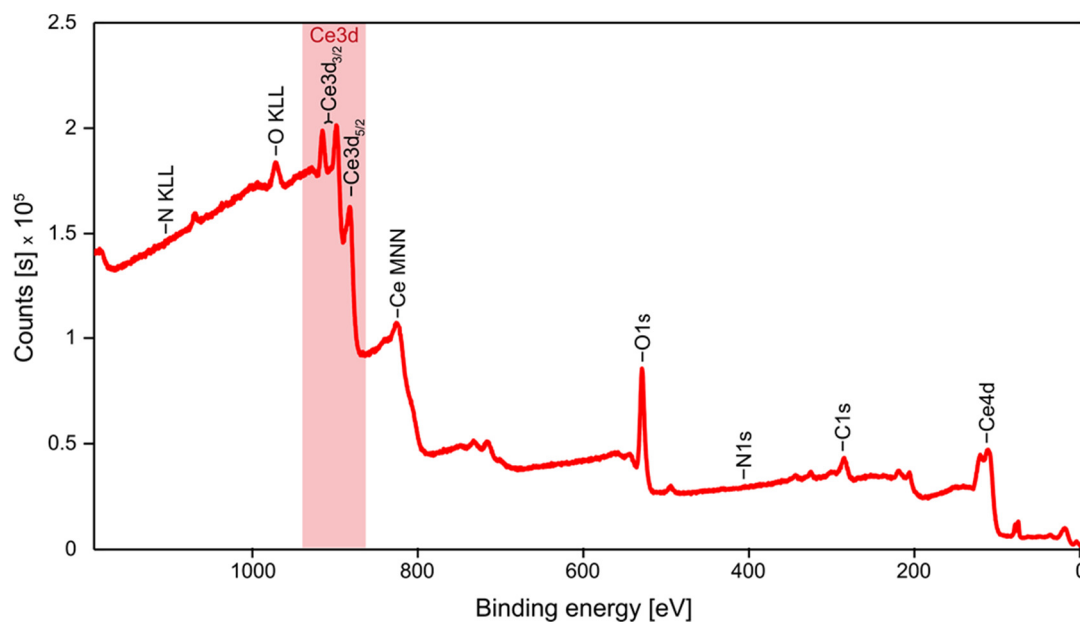
Figure 61. XPS survey spectrum of CeO$_{2-x}$ nanorods. Acquisition conditions: Al-Kα (mono), 250.0 W, 45.0°, 187.85 eV. The atomic amount of the elements has been determined to 36.06 at% C1s, 0.00 at% N1s, 55.26 at% O1s and 8.68 at% Ce3d. The relative ratio O/Ce have resulted in 6.4 (theoretical value: ≤ 2 with respect to the stochiometric formula). The highlighted region (red, core level spectrum of the Ce 3d signals, 920-870 eV) has been used instead in "multiplex" acquisition mode with higher energy resolution (0,125 eV) to examine the relative amount of Ce^{3+} at the surface of the CeO$_{2-x}$ nanorods as described in Figure 42.

Inductively Coupled Plasma Mass Spectrometry

Inductively coupled plasma mass spectrometry (ICP-MS) was used to analyze the cerium content for stability measurements of CeO$_{2-x}$ nanorods in water and in LB medium. In a typical leaching experiment, 100 mg of the CeO$_{2-x}$ nanorods were suspended in 2 mL of MilliQ-water or in 2 mL of LB medium, respectively, for 24 hours at room temperature with gentle stirring (50 rpm). After sedimentation and a rough filtration process (0.2 μm syringe filter), the resulting filtrates were dialyzed against MilliQ-water (500 mL, dialysis membrane: Nadir 5104.1, 25-30 Å, purchased from Carl Roth) for 24h. The volume was reduced to ca. 1.3 mL and the cerium content (^{140}Ce) was analyzed by ICP-MS (mass spectrometer Agilent 8800 equipped with a Meinhard spray system, external calibration, 1200 W) referred to a blind sample resulting in 1 mg Ce /kg water and < 1 mg Ce /kg LB medium.

Reversed Phase High-Performance Liquid Chromatography

Reversed phase high performance liquid chromatography was used to determine (i) the bromination of PR (aqueous reaction mixture (1 mL) containing CeO_{2-x} (25 µg·mL^{-1}), NH_4Br (25 mM), PR (50 µM) and H_2O_2 (300 µM) with a simultaneous analysis of the supernatants by optical (UV-Vis) absorption spectroscopy, see "PR-Haloperoxidase Assay"), (ii) degradation of celestine blue (see "Celestine Blue Assay") and (iii) bromination of 3-oxo-AHL (see "Lactone Assay"). All the reactions were run in triplicates. After the specific time period, the reactions were terminated by removing the catalyst by centrifugation (14500 rpm, 3 min) and filtration (2.5 µm syringe filter).

The supernatants (products of the activity assays) were analyzed by reversed phase high performance liquid chromatography coupled with electrospray ionization-mass spectrometry (RP-HPLC/ESI-MS) was performed on a 1200 series HPLC system with a UV diode array detector coupled with a LC/MSD trap XCT mass spectrometer (Agilent Technologies). An Ascentis Express C_{18} column (pore size: 2.7 µm, length: 3 cm, diameter: 2.1 mm; Supelco) was used at a temperature of 40°C. The capillary voltage was set to 3500 V and the capillary exit voltage was set according to the respective target mass. Mixtures of acetonitrile (MeCN) and water (with 0.1 % formic acid, FA) were used as eluents at a total flow rate of 1.0 mL·min^{-1}. The following gradient methods were used: Method A: H_2O (+ 0.1 % FA) / MeCN = 10:90 isocratic (0.0 - 0.2 min), 10:90 to 90:10 (0.2 - 4.0 min), 90:10 (4.0 - 6.0 min); Method B: H_2O (+ 0.1 % FA) / MeCN = 5:95 isocratic (0.0 - 0.2 min), 5:95 to 95:5 (0.2 - 4.0 min), 95:5 (4.0 - 6.0 min).
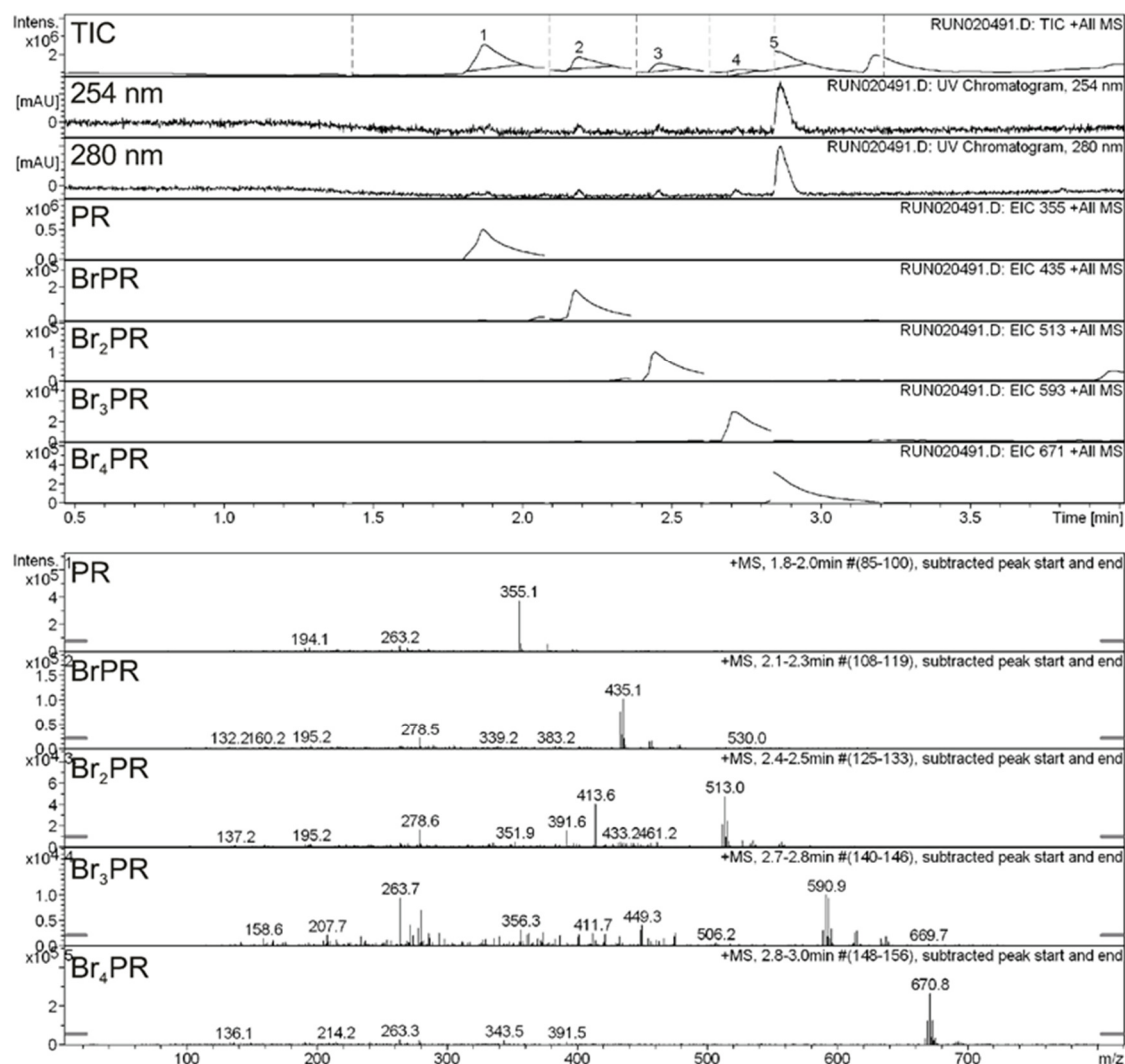
Figure 62. RP-HPLC/ESI-MS analysis. I. UV chromatograms and corresponding mass spectra of the oxidative bromination of PR after 24h. After 24h reaction time (CeO$_{2-x}$ nanoparticles (25μg·mL^{-1}), NH$_4$Br (25 mM), PR (50 μM) and H$_2$O$_2$ (300 μM)), Br$_4$PR was predominantly generated (main absorbance at 254 and 280 nm). The stepwise oxidative bromination of PR was proven by the specific bromine pattern for mono (BrPR)-, di (Br$_2$PR)-, tri (Br$_3$PR)- and tetra-brominated (Br$_4$PR) products (H$^+$ salts). Note: Mass spectrometry could not predict the exact bromination site at the dye, but as halogenation was preferred at reactive carbon sites (the four *o*-positions of the phenolic units), the structure was expected as mentioned in the main text. Abbreviations: TIC/EIC total/ extracted ion chromatogram.
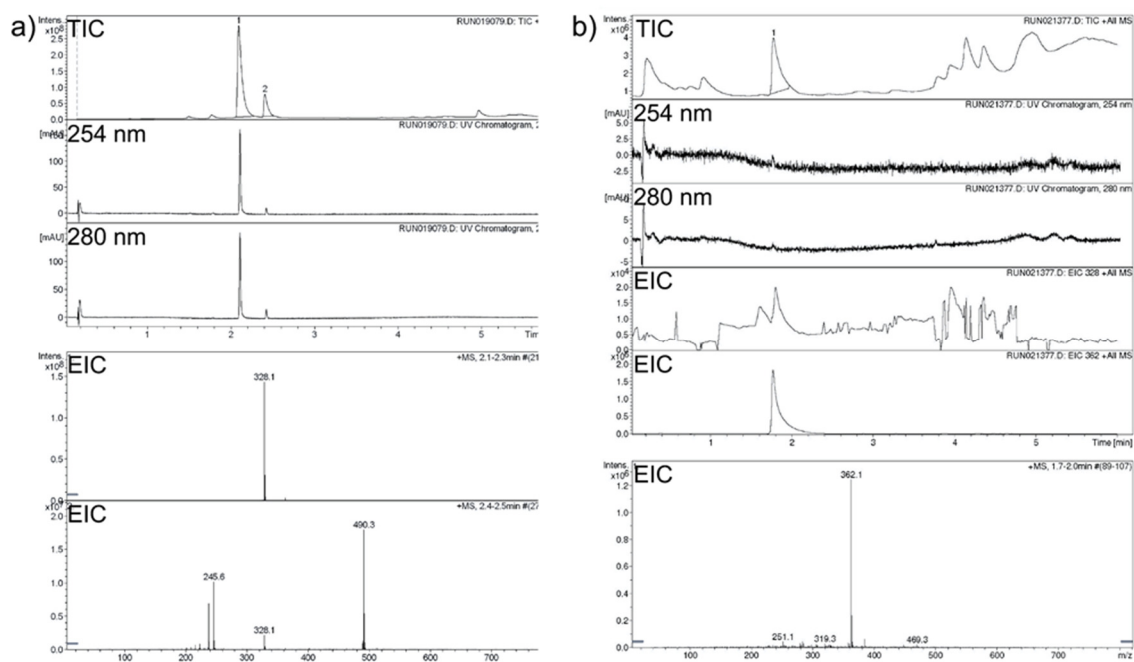
Figure 63. RP-HPLC/ESI-MS analysis. II. UV chromatograms and corresponding mass spectra of the degradation of Celestine blue. RP-HPLC/ESI-MS analysis of CB a) before and b) after reaction. The reaction mixture consisted of CeO$_{2-x}$ nanoparticles (25µg·mL^{-1}), NH$_4$Br (25 mM), CB (50 µM) and H$_2$O$_2$ (300 µM)) and CB was bleached (main absorbance at 254 and 280 nm) within 36 h. The pink oxidized intermediate formed (*m/z* 362.1) was further degraded to low weight molecular species over time. Note: The assumed structure of the oxidized compound was taken from ref. [246]. Abbreviations: TIC/EIC: total/ extracted ion chromatogram.

Figure 64. RP-HPLC/ESI-MS analysis. III. UV chromatograms and corresponding mass spectra of the oxidative bromination of 3-oxo-AHL **19**. Blank reactions without catalyst (KBr (20 mM), 3-oxo-AHL (900 µM) and H_2O_2 (20 mM)) after a) 2.5h and b) after 5h showed no bromination of 3-oxo-AHL. c) blank reaction after 5 h, d) reaction after 5h. All reactions (aqueous reaction mixture (1 mL) containing CeO_{2-x} nanorods (200 µg·mL^{-1}), KBr (20 mM), 3-oxo-AHL (900 µM) and H_2O_2 (20 mM)) were run in duplicate for a) 2.5 h and b) 5 h. The oxidative bromination of 3-oxo-AHL was proven by the specific bromine pattern for mono- and dibrominated products (H^+ and K^+ salts). Note: Mass spectrometry could not predict the exact bromination site at the dye but as halogenation was preferred at reactive carbon sides, the structure was expected as mentioned in the main text.

Quantum Chemical Calculations

All periodic calculations were performed with the CP2K software, V. 3.0 (available from https://www.cp2k.org). Here, the PBE functional was used in combination with a DZVP-SR-GTH basis set. Solvation effects were taken into account using a general Poisson solver algorithm in combination with a dielectric constant of 80.[669] For Ce, a DZV-GTH-q30-2 basis set[670] was used. The pseudopotentials were of GTH-PBE-type as delivered in the CP2K distribution. For calculations of finite systems, the TURBO-MOLE program suite was used.[671] Structure optimizations were performed at the BP86/def-SV(P) level using the solvation model COSMO with a dielectric constant of infinity. Final single point calculations were done at the BP86/def-TZVP level including aqueous solvation with the COSMO-RS model[672] and using standard formulae from statistic thermodynamics to compute Gibbs free energies. The calculations of finite systems served to derive how SCF-energy differences ΔE translate into Gibbs free energies ΔG (Figure 48), as the computation of vibrational spectra is very time consuming for the periodic models and there is no COSMO-RS interface in CP2K. The species "H^+" was modelled by using HBr instead of Br^- as reactant where protonation had taken place; the strong acidity of HBr ($pK_a = -9$) as a proton source was taken into account by adding +83.7 $kJ \cdot mol^{-1}$ to ΔE of reactions with the HBr model reactant which corresponds to a pH of 7.

Altogether, the calculations suggested that HOBr formation catalyzed by Ce^{3+} sites was possible, and the particular advantage of the catalytic system represented its favored reaction with H_2O_2 and subsequently with Br^-, as thus these two rare reactants were efficiently brought together in spite of their very low / low concentration. The actual HOBr release represented the rate limiting step of the catalytic cycle, so that species with formal Br radicals on the ceria surface were quite probable and long-lived; this also explains why radical scavengers had been observed to slow down catalysis, as a one electron transfer would yield stable hydroxide terminated Ce^{4+} sites. Other mechanisms of HOBr formation could be postulated that involve H_2O_2 disproportionation to form singlet oxygen as the active oxidant, which could, for example, be catalyzed by two neighboring Ce^{3+}. Also, a nucleophilic attack of Br^- at coordinated H_2O_2 represented a mechanistic scenario, which would, however, not require Ce^{3+} sites but rather a maximally Lewis-acidic surface. Parts of such pathways were studied as well and could be excluded because (i) the O-O cleavage step as part of H_2O_2 disproportionation at two neighboring Ce(III)

sites was extremely exothermic. A least, on a hydrated (110) surface it would be irreversible and thus not allowed for catalytic HOBr formation, and (ii) nucleophilic substitution looked actually like a viable pathway at the GGA-DFT level of theory. However, meta-hybrid GGA calculations clearly showed that GGA-DFT strongly underestimated the activation barrier of such reactions.
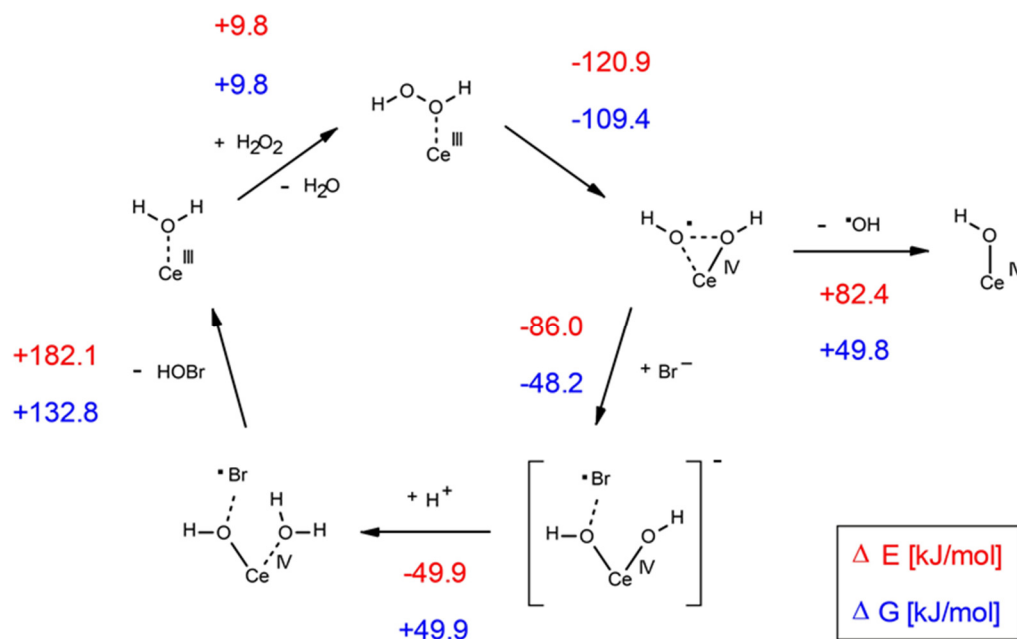
Figure 65. Quantum chemically predicted catalytic cycle for HOBr formation at a hydrated (110) surface model with one Ce(III) defect. At such surfaces (illustrated in detail in Figure 66), the H_2O ligand can be exchanged against H_2O_2. If the Gibbs free energy change (ΔG) of this exchange is close to zero, the exchange will be very unlikely at low H_2O_2 concentration. However, this step becomes irreversible (highly negative ΔG) upon a (partial) dissociation of H_2O_2 leading to Ce-oxidation and, formally, yielding a hydroxide anion and a hydroxyl radical as ligands. These two groups are bound to each other *via* a weak two-center-three-electron bond as both Ce-O distances exhibited in this species inhere the same length. The structure described represents one of two mesomeric boundary intermediates that account for the actual chemical bonding. In principle, in solution the release of an OH radical will be possible but represents a step "uphill" in both energy and Gibbs free energy. Thus, it will require an enlarged time period in which the rare species Br$^-$ can attack one of the O atoms. The resulting species can be described best as a negative charged surface site (due to its two hydroxide ligands) with one of the hydroxide anions interacting with a Br radical. Subsequently, the non-interacting hydroxide anion is protonated easily yielding a neutral surface site again. Here, the HOBr dissociation leads to the regeneration of the initial Ce^{3+} site. Although this step is associated with a very high ΔE and a significantly positive ΔG, it will finally take place because (a) the back reaction is highly energetic as well and (b) within the educt concentrations present in the medium, particularly, the negligible HOBr amount, the ΔG will not be that unfavorable as suggested here. The given Gibbs free energies are refered to standard conditions of 1 mol$\cdot$L^{-1}.
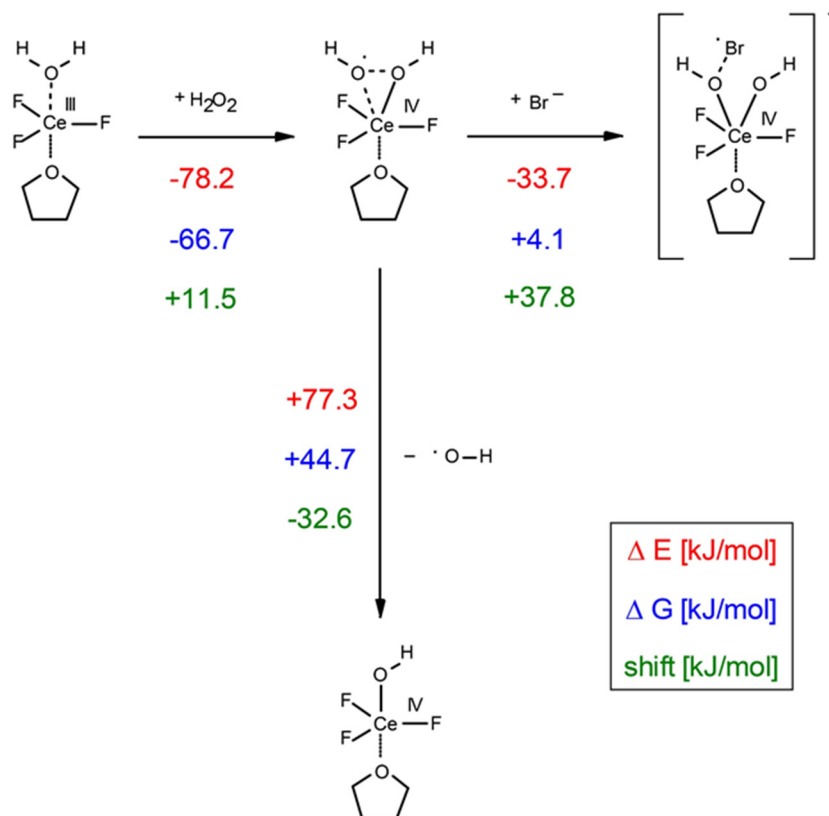
Figure 66. Quantum chemical study of the HOBr formation cycle for a small molecular model. Calculations using a small Ce^{3+} model compound are performed to clarify the transferability of ΔE from periodic quantum chemistry to ΔG in water at 25°C. As a model compound, $CeF_3(THF)(H_2O)$ has been chosen. The shifts derived from the difference between ΔE and ΔG are used in Figure 65 to predict the ΔG on a real CeO_2 surface. Only a few representative examples to derive these shifts are considered to evaluate, for example, the exchange of H_2O by H_2O_2 without H_2O_2 dissociation assuming $\Delta G = \Delta E$ as a reliable estimate.
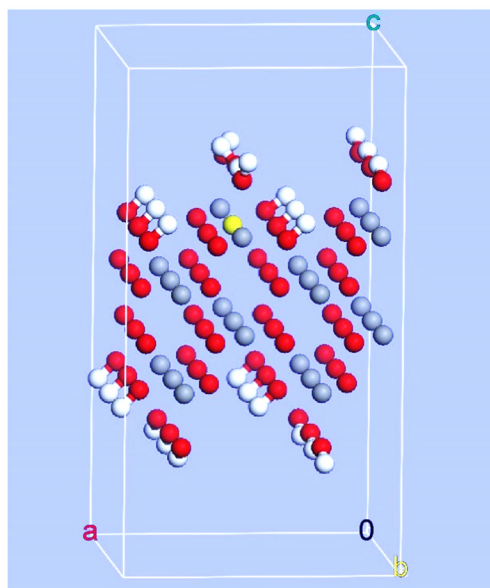
Figure 67. Periodic computational model for a hydrated CeO_2 (110) surface with one Ce^{3+} defect. Color coding: H – white, O – red, Ce^{4+} – grey, Ce^{3+} – yellow. The Ce^{3+} site carries an H_2O instead of an (OH)- goup maintaining the overall charge neutrality of the system.

9.4   Assays

The catalytic activity was determined by photometric analysis, optical absorption spectroscopy (UV-Vis) and high-performance liquid chromatography.

Stock Solutions

The *TRIS-SO₄ buffer* (100 mM) was prepared by dissolving 12.12 g of TRIS base in 1 L H_2O. The pH was adjusted to 8.0 – 8.5 with H_2SO_4 (conc.). The buffer was stored under room temperature for several weeks. It was discarded when a formation of micro-organisms was observed.

The *sodium acetate buffer* (100 mM) was prepared by mixing 1.24 g sodium acetate and 5.10 g acetic acid in 1L H_2O. The buffer was stored under room temperature for several weeks. It was discarded when a formation of microorganisms was observed.

The *LB-Medium* (Luria/Miller) had been prepared without any antibiotics as described in the manual (25 g in 1L deionized H_2O) and afterwards sterilized *via* steam sterilization in an autoclave. The sterilized, unopened media was stored in the dark under room temperature for several months. It was discarded after approximately three months or/and when a formation of microorganisms was observed.

Borate buffer (100 mM, pH 8.3) was prepared by dissolving 281.33 mg borax ($Na_2B_4O_7 \cdot 10\ H_2O$) and 427.77 mg H_3BO_4 in 100 mL H_2O (cf. Henderson-Hasselbalch Equation, pKa = 9.14).

The colorless stock solution of *MCD* (100 µM; 1.7 mg in 100 mL H_2O) was stored for several weeks in the fridge. Its concentration was controlled prior the measurements by UV-Vis ($\varepsilon(MCD)_{290\ nm} \approx 20.2\ M^{-1}cm^{-1}$).

Although it could be stored in the fridge, the slightly green stock solution of *ABTS* (10 mM; 54.9 mg in 10 mL H_2O) was prepared freshly before use. Its concentration was controlled prior the measurements by UV-Vis ($\varepsilon_{[ABTS2-],\ 340nm} \approx 36.6\ mM^{-1}cm^{-1}$).

The red stock solution of *PR* (1 mM; 8.8 mg in 25 mL H_2O) could be stored in the fridge for several months. Its concentration was controlled prior the measurements by UV-Vis ($\varepsilon_{PR,\ 436\ nm} \approx 20.0\ mM^{-1}cm^{-1}$).

The *DAPI* solution was prepared in a H_2O/glycerin (1:1) mixture providing a good distribution along the coated plate´s surface. Additionally, the prepared colorless solution could be stored in the freezer without loss in activity. The DAPI solution used for staining

(1 µg·mL^{-1} in H$_2$O/glycerin, 1:1) was prepared by dilution series of a 1 mg·mL^{-1} stock solution.

The *KBr* stock solution (1 M) was prepared by dissolving 4.76 g in 40 mL H$_2$O and stored in the fridge for several weeks. The *KBr* stock solution (100 mM) for the MCD assay was prepared by dissolving 0.30 g in 25 mL H$_2$O or by dilution.

The *NH$_4$Br* stock solution (1 M) was prepared by dissolving 3.92 g in 40 mL H$_2$O and stored in the fridge for several weeks.

The *NaBr* stock solution (1 M) was prepared by dissolving 4.12 g in 40 mL H$_2$O and stored in the fridge for several weeks.

The *LiBr* stock solution (1 M) was prepared by dissolving 2.15 g in 25 mL H$_2$O and stored in the fridge for several weeks.

The stock solutions of *H$_2$O$_2$* (10 mM; 20 µL of 30 wt% H$_2$O$_2$ or 50 mM; 100 µL of 30 wt% H$_2$O$_2$ in 20 mL H$_2$O each) had to be prepared freshly minimum each day. The H$_2$O$_2$ stock concentration used (10 mM) was validated spectrophotometrically[673] by following the intensity of its absorption band centered at 240 nm (ε(H$_2$O$_2$)$_{240\ nm}$ $\approx$ 43.6 M^{-1}cm^{-1}).

The inorganic, *catalytic material* was suspended freshly every day in H$_2$O (1 mg·mL^{-1}, considered to the total mass of the particles) by sonication (a few seconds). Guaranteeing an equal catalyst amount for each reaction mixture, the catalyst suspension was stirred during sample collection for the dye assays. The stock solution of polymeric catalysts e.g. doped PAN samples was prepared in DMSO (0.5 mg·mL^{-1}) with a resulting metal content of $\approx$ 50, 5 or 2 µg in the final reaction mixtures (1 mL).

The overnight culture of *E. coli* was prepared by inoculation of 20 mL LB media with 1-2 "inoculating beads". After being gently shaken at 37°C overnight, the bacterial suspension was directly used and residuals afterwards discarded by steam sterilization. The "inoculating beads" can be re-prepared by the addition of 1 mL of overnight culture and glycerin to ca. 10 beads. After being gently shaken, the supernatant was completely removed and the "inoculating beads" were stored in a freezer at -80°C.

MCD – Haloperoxidase Assay

The oxidative halogenation of monochlorodimedone (MCD) in the presence of H_2O_2 and a halogen source represented one of the most commonly used haloperoxidase screening assays. The formation of the dihalogenated MCD-derivative could easily be monitored: The decrease in the UV absorption of native MCD at 290 nm ($\varepsilon(MCD)_{290\ nm}$ $\approx 20.2\ M^{-1}cm^{-1}$) was directly proportional to the halogenating activity. To maintain the reaction pH around 8.0 to 8.5, TRIS sulfate base (100 mM) as the buffer system or water could be used. Sea water-like concentrations of H_2O_2 (100 µM in reaction mixture) and bromide (1 mM in reaction mixture of KBr, NaBr or NH$_4$Br for example) were present in the final reaction mixture. The catalytic material suspension was added in the concentration needed after the baseline of the adsorption experiment had been recorded following by H_2O_2. Blank tests were performed using V_2O_5 as the standard material and without any catalyst. A typical reaction mixture was made of 910 µL TRIS-SO$_4$ or H_2O, 20 µg mL^{-1} catalytic material (20 µL of a 1 mg·mL^{-1} stock suspension), 10 µL KBr (100 mM stock solution), 50 µL MCD (100 µM stock solution) and, after baseline-record, 10 µL H_2O_2 (10 mM stock solution). The mixture was stirred during reaction. The decrease in absorbance at 290 nm was followed for three minutes. However, the problems with the MCD dye system were discussed previously. Additionally, increasing the concentration in MCD emerged in irreproducible results. Ideally, the activity of the catalyst correlate linearly with the decrease in absorption. Using the model of a first order kinetic, the absolute value in slope obtained from the linear region of the UV-Vis plot (Δt: 3min, absorbance *versus* time) represented the reaction rate by using the Lambert-Beer relation. Before performing the MCD tests, the particles themselves were tested to determine if they show any absorption or interaction with the buffer or dye.

ABTS – Peroxidase Assay

Peroxidase-like activity of catalytic material was determined by using the qualitative (and quantitative) ABTS assay. Because of the strong color changes, the chromophore could easily be followed spectrophotometrically as well as optically. Sometimes, different notations of ABTS related compounds had been used in current literature.[674] Depending on the protonation degree of ABTS, two species were distinguished: i) fully deprotonated (ABTS^{2-}, pH > 5, $\varepsilon_{[ABTS2-], pH\ 5-7,\ 340nm}$ ≈ 36.6 mM^{-1}cm^{-1}) and ii) simply protonated (HABTS$^-$, pH < 3, $\varepsilon_{[HABTS-], pH\ 0-1,\ 310nm}$ ≈ 20.9 mM^{-1}cm^{-1}) (Figure 68).[675] In general, a reaction pH of about 4 was preferentially used. Under the reaction conditions, only slightly protonated ABTS occurred and absorbance/extinction coefficient was related to ABTS^{2-}.[675] Single electron oxidation reaction of ABTS^{2-} by the catalyst and H$_2$O$_2$ yielded the emerald green, soluble persistent radical ABTS$^{•-}$ which absorbance was directly proportional to the peroxidase-like activity. With respect to analysis, the absorbance at 417 nm was used in general. No HABTS$^•$ was formed because of its high acidity and the extinction coefficient of ABTS$^{•-}$ was applied ($\varepsilon_{[ABTS•-], pH\ 0,\ 417\ nm}$ ≈ 34.7 mM^{-1} cm^{-1}).[675] Further oxidation (or disproportionation) resulted in pale-yellow ABTS^0 ($\varepsilon_{[ABTS0], pH\ 0,\ 518\ nm}$ ≈ 36.0 mM^{-1} cm^{-1}) (Figure 68).[674,675]

To maintain the reaction pH at 4.0, sodium acetate buffer (100 mM, pH 4.0) was used. In the qualitative assay, 0.7 mM ABTS (70 µL of a 10 mM stock solution) and 50 (or 100) mg·mL^{-1} catalytic material (50 (or 100) µL of a 1 mg·mL^{-1} stock solution) were mixed into 880 (or 730) µL buffer. Subsequently, the reaction was started by adding 1 mM H$_2$O$_2$ (100 µL of a 10 mM stock solution) and optically followed. Within these reaction conditions, the reaction rate was increased to a few minutes by active catalysts. In quantitative, spectrophotometric reactions, the amounts of H$_2$O$_2$ and catalyst were decreased to 100 µM (10 µL of a 10 mM stock solution) and 20 mg·mL^{-1} (20 µL of a 1 mg·mL^{-1} stock suspension) in 900 µL acetate buffer, respectively. Blank tests were performed using V$_2$O$_5$ as the standard material and without any catalyst. With regards to polymeric catalysts (e.g. doped PAN samples), 100 µL the material (stock solution: 0.5 mg·mL^{-1} in DMSO; metal concentrations in the reaction mixture ≈ 50, 5 or 2 µg) had been added instead.
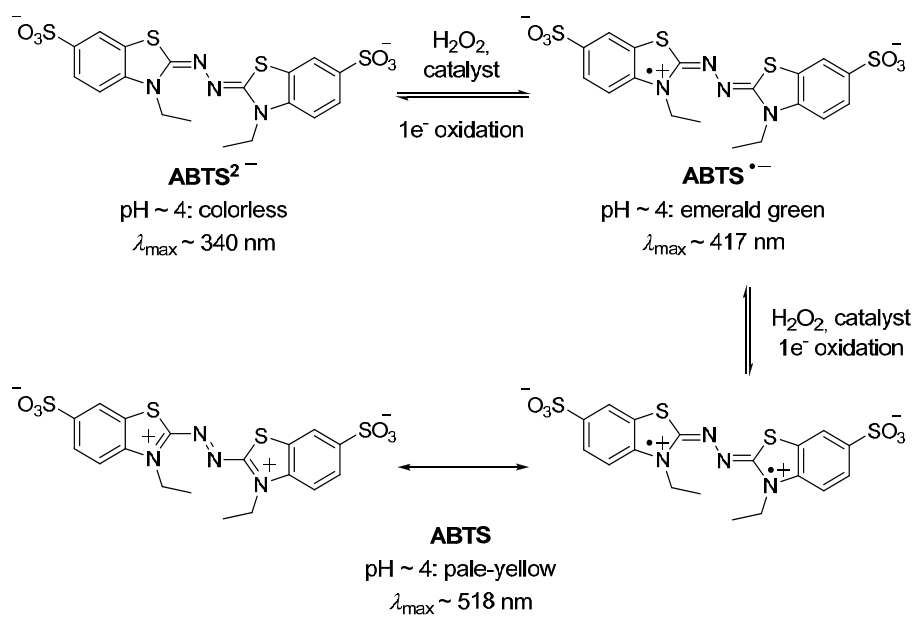
Figure 68. Illustration of the ABTS oxidation reaction catalyzed by peroxidase or peroxidase mimics at pH ≈ 4.

PR – Haloperoxidase Assay

Haloperoxidase-like activity of catalytic material was determined by using the qualitative (and quantitative) phenol red assay. Phenol red (phenolsulfonphthalein) represented a common pH indicator (Figure 69a). Additionally, the yellow dye (at pH ≈ 6-7, $\varepsilon_{436nm} = 20.0$ mM^{-1}cm^{-1})[225] could be oxidatively brominated by H_2O_2, bromide and a suitable catalyst at the *ortho* positions of phenol residues *via* an electrophilic aromatic substitution (Figure 69b). Because of the strong color changes, this test systems could easily be followed qualitatively/optically or quantitatively by UV-Vis. Based on this reaction, the haloperoxidase-like activity of catalytic materials was determined by the formation of the four-fold brominated bromophenol blue (5',5''-dibromophenolsulfonphthalein,[676] $\varepsilon_{590nm} = 72200$ Lmol^{-1}cm^{-1}).[227] For reaction conditions used (pH > 4.6, 298 K) the bromination of the yellow phenol red yielded a blue-purple compound[409,677] (at pH < 3, bromophenol blue appeared green/yellow).

a)

b)
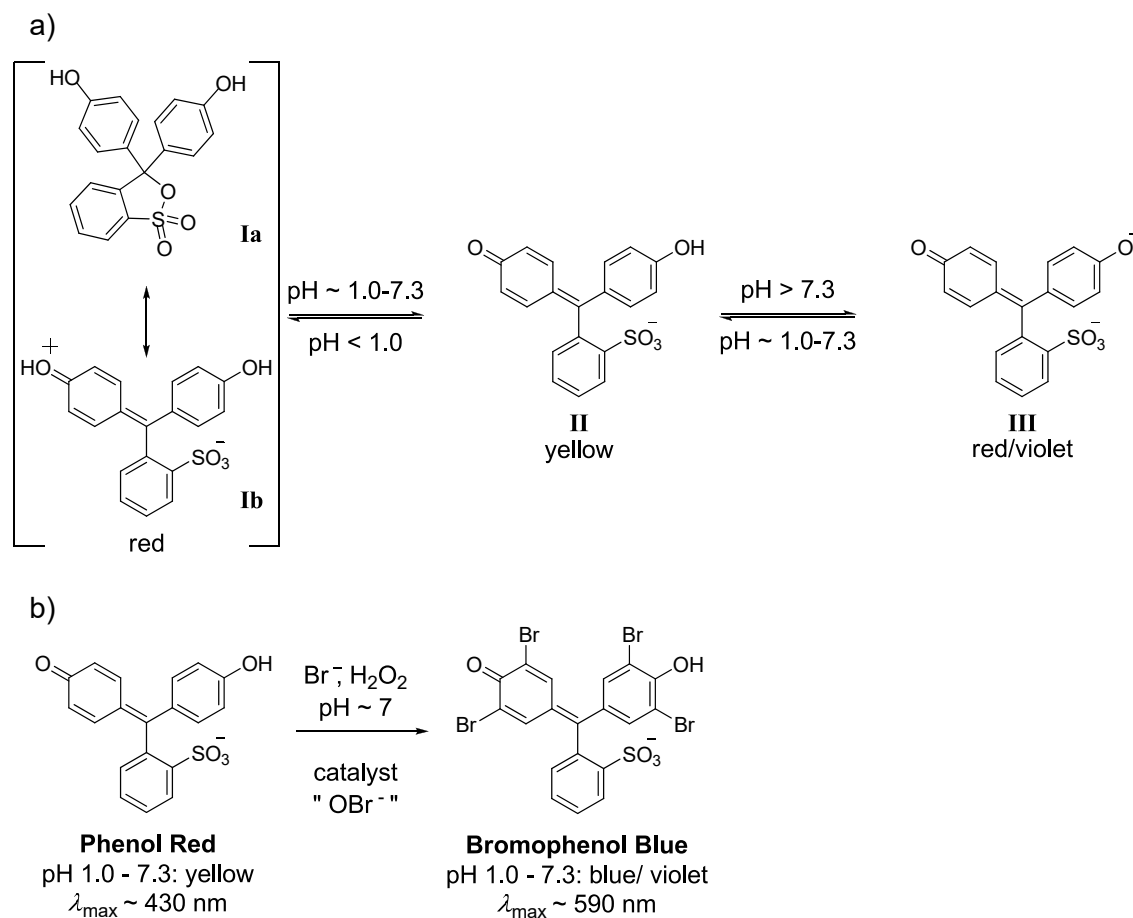
Figure 69. Illustration of the structure and oxidative bromination reaction of phenol red. a) pH dependency.[678] b) Reaction to bromophenol blue catalyzed by haloperoxidase or haloperoxidase mimics.[409,676,677] The equilibrium of the open and closed ring structure of phenol red is only illustrated for structure I. It can also occur concerning compound II, but is less likely for III.

Qualitative PR-Haloperoxidase Assay

In the qualitative assay, typically performed in transparent 1.5 mL reaction vials, the aqueous reaction mixture (1 mL in total) contained 50 µM PR (50 µL of a 1 mM stock solution), 50 (or 100) mM NH_4Br (50 (or 100) µL of a 1 M stock solution) and 50 (or 100) mg·mL^{-1} catalytic material (50 µL (or 100 µL) of a 1 mg·mL^{-1} stock suspension). Subsequently, the reaction was started by addition of 5 mM H_2O_2 (100 µL of a 50 mM stock solution) and monitored optically. Under these reaction conditions, the reaction rate increased to 1-2 hours by active catalysts. Blank tests were performed using V_2O_5 as the standard material and without any catalyst. In comparison to polymeric catalysts (e.g. doped PAN samples), 100 µL the material (stock solution: 0.5 mg·mL^{-1} in DMSO; metal concentrations in the reaction mixture ≈ 50, 5 or 2 µg) were added.

Quantitative PR-Haloperoxidase Assay

Concerning the quantitative assay, the reaction mixture typically contained 50 or 10 µM PR (50 or 10 µL of a 1 mM stock solution), 25 mM NH_4Br (25 µL of a 1 M stock solution) and 25 µg·mL^{-1} catalytic material (25 µL of a 1 mg·mL^{-1} stock solution) and 300 µM H_2O_2 (30 µL of a 10 mM stock solution) in 1 mL H_2O in total (pH ≈ 5.6). The reaction was traced spectrophotometrically, for example, for 300 minutes in the range of 220-720 nm followed ("scanning kinetic").

In particular, the catalytic activity of the ceria nanoparticles in oxidative bromination was determined according to the procedure described by Colpas et al.[247] and Chen et al.[262] First test experiments were performed about 600 min. They revealed that a constant slope dA/dt is present for the first ≈ 120 min. In all following experiments only 5 min kinetics was monitored which is representative for the whole process. In order to determine the optimal concentrations of all reactants, several calibrations were carried out (590 nm, pH 5.6, 23-25°C). The conditions of the corresponding test experiments are summarized in Table 12 (experiments a-d). Control experiments in the absence of Br$^-$, H_2O_2, PR, CeO_{2-x} or any combination did not show any PR bromination (Figure 70).
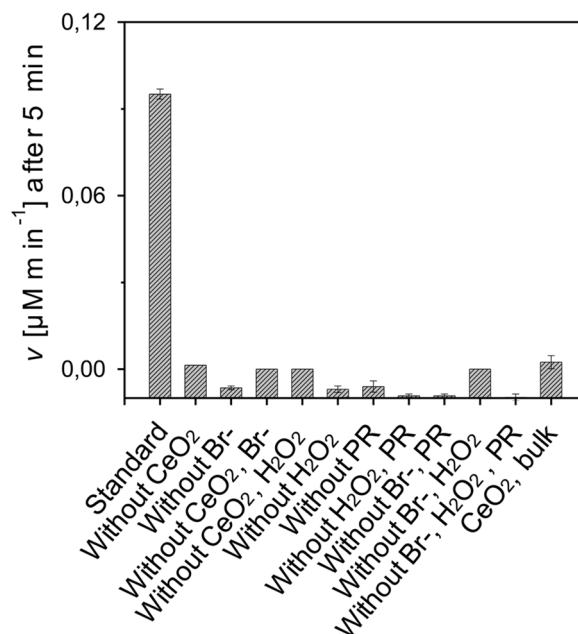
Figure 70. Control samples of the oxidative halogenation reaction of PR. The standard reaction mixture contained CeO_{2-x} nanoparticles (25 µg·mL^{-1}), PR (50 µM), NH_4Br (25 mM) and H_2O_2 (300 µM), r.t.); in all other mixtures at least one of the substrates was absent. Obviously, Br_4PR formation occurrs only in the presence of all substrates. Control samples of bulk CeO_2 show much lower activity compared to CeO_{2-x} nanorods.

Table 12. Summary of the selected substrate concentrations used in Figure 71. The individual values of concentrations are given as in the reaction mixture (1 mL total volume).

Experiment	CeO_{2-x}	H_2O_2	NH_4Br	PR
A	2 – 100 µg·mL^{-1}	2 mM	20 mM	50 µM
B	25 µg·mL^{-1}	0.02 – 5 mM	20 mM	50 µM
C	25 µg·mL^{-1}	300 µM	0.5 – 150 mM	50 µM
D	25 µg·mL^{-1}	300 µM	25 mM	0.5 – 50 µM
E	2 – 75 µg·mL^{-1}	300 µM	25 mM	50 µM
Optimized parameters	25 µg·mL^{-1}	300 µM	25 mM	50 µM

H_2O_2 was added to the mixture immediately prior to the measurements to trigger the reaction. For each measurement, blank tests and controls were performed (cf. Figure 60); each measurement was carried out several times until the slopes (dA_{590nm}/dt,) remained constant over 5 min. The optimized substrate concentrations were determined as given in Table 12. Additionally, several kinetic parameters were calculated: (i) the Michaelis Menten constant (K_m) and (ii) the maximum reaction rate (v_{max}) by Lineweaver-Burk linearization, (iii) reaction orders and (iv) reaction constants by logarithmic correlations, (v) the turn over frequency (TOF, k_{cat}) and (vi) the overall activation energy (E_A). In a series of kinetic experiments, the concentration of one reactant was varied whereas the

concentrations of others were kept constant (see details in Table 12). Table 13 summarizes the determined kinetic parameters. The specific calculations, plots and results are described and summarized below.

Table 13. Compiled kinetic parameters for the oxidative bromination of phenol red.

Substrate	K_m[a)] (μM)	v_{max}[a)] ($\mu M \cdot min^{-1}$)	k[b)] (min^{-1})	a[b)]
H_2O_2	261.1 ± 0.6	$1.0 \cdot 10^{-1} \pm 5.9 \cdot 10^{-3}$	$1.3 \cdot 10^{-3} \pm 8.1 \cdot 10^{-4}$	1
NH_4Br	350175.0 ± 0.2	$1.5 \cdot 10^{-0} \pm 3.2 \cdot 10^{-1}$	$1.3 \cdot 10^{-5} \pm 3.8 \cdot 10^{-6}$	1
PR	1.1 ± 0.2	$1.1 \cdot 10^{-1} \pm 2.1 \cdot 10^{-3}$	$1.4 \cdot 10^{-1} \pm 2.9 \cdot 10^{-2}$	0
CeO_{2-x}*			$5.0 \cdot 10^{-4} \pm 3.6 \cdot 10^{-6}$	1

Parameters obtained from a) Lineweaver Burk linearization and b) by logarithmic plotting. Abbreviations: K_m Michaelis Menten constant, v_{max} maximum velocity, k reaction constant, a pseudo reaction order.
* determined with the optimized parameters, 25 mM NH_4Br, 50 μM PR, 300 μM H_2O_2 in 1 mL reaction volume, respectively. The errors of K_m, v_{max} and k are considered using the law of error propagation ($\Delta y = \delta y/\delta x_1 \cdot \Delta x_1 + \delta y/\delta x_2 \cdot \Delta x_2 + \dots$).

Calculations on Haloperoxidase-like Reaction Mechanism

Kinetic Parameters

To evaluate the kinetic parameters with respect to the Br_4PR concentration, the dA_{590nm}/dt values were converted to the equivalent $d[Br_4PR]/dt$ values using the Lambert-Beer law with an extinction coefficient of Br_4PR (ε_{Br4PR}) determined to be 72200 $M^{-1}cm^{-1}$ (Equation 21).

$$[Br_4PR] = \frac{A_{590}}{d \cdot \varepsilon_{Br_4PR}}$$

21

$$v_0 = \frac{d[Br_4PR]}{dt} = const + \frac{v_{max} \cdot [S]}{K_m + [S]}$$

22

$$\frac{1}{v_0} = \frac{1}{d[Br_4PR]/dt} = \frac{K_m}{v_{max}} \cdot \frac{1}{[S]} + \frac{1}{v_{max}}$$

23

Figure 71 (a-d, left) shows kinetic curves at variations of the concentrations of CeO_{2-x}, H_2O_2, NH_4Br and PR when all others were fixed (Abbreviations: v_{max}: maximum reaction rate, K_m: Michaelis-Menten constant, k: reaction rate constant, a: pseudo reaction order). The values show (i) a Michaelis-Menten-like behavior (fit: blue line, Equation 22) and (ii) a linear dependence (fit: dark grey, dashed line) within the relevant data range (marked by fitting bars). The enzymatic parameters (except for CeO_{2-x}, *vide infra*) were calculated by Lineweaver-Burk linearization (Equation 23, Figure 71 a-d, middle). The reaction constants and orders were determined from logarithmic correlations (cf. Equation 24-27, Figure 71 a-d, right). After optimizing each substrate concentration (red squares), the CeO_{2-x} concentration was varied using the optimized parameters (Figure 71 d). The turnover frequency (TOF, k_{cat}) and the overall activation energy (E_A, Figure 72) were extracted from these data.

Variation of the CeO_{2-x} particles (Figure 71a) led to an apparent "saturation"; in fact, this is caused by an intense scattering of the particles for concentrations > 290 µM which distort the absorbance even when using an integration sphere installed behind the stirring cuvette. Thus, the optimum concentration of the CeO_{2-x} particles was taken as 25 µg·mL^{-1} (145 µM, red squares). The absence of scattering effects with 25 µg·mL^{-1} was confirmed by control measurements after removing the catalyst by centrifugation before the UV-Vis measurements.

Variation of the H_2O_2 concentration (Figure 71b) led to saturation kinetics as the accessibility of the catalyst surface. An analogous dependence was found for the *variation of the bromide concentration* (Figure 71c). Based on the linear dependence of the absorption, the optimum concentrations of H_2O_2 and NH_4Br were determined as 300 µM and 25 mM (red squares).

Variation of the concentration of PR revealed a different behavior, and the change in the reaction rate was more complex (Figure 71d). At low concentrations, a fast turnover of PR occurred due to kinetic reasons. For higher PR concentrations, the reaction rates decreased because diffusion effects become predominant and multiple bromination of a single molecule is less likely than mono-bromination of several molecules.

For the determination of the reaction orders and constants the method of initial reaction rates (low substrate concentrations) were used to simplify the analysis, which follows a higher order reaction otherwise.

Equation 24 expresses the formation rate of bromophenol blue with k as the reaction constant and a, b… as the reaction orders. The reaction constants include the reaction parameters of the back reaction, the dissociation, adsorption and desorption rates, and the formation rates of the partially brominated intermediates, which could not be separated or assigned from the UV-Vis measurements. The analysis could be simplified by regarding only the range of small concentrations of the component S (which may be PR or NH_4Br or H_2O_2 or CeO_{2-x}) for an excess of all other substrates and the initial rates only (Equation 26). In this case the formation rate of Br_4PR depends only on the component S as limiting factor. Equation 25 can be reduced to Equation 26 with k as a total reaction constant (including all constant parameters) and x as reaction order with respect to S. Logarithmic plots (Equation 27) were used (Figure 71, middle part) to extract the rate constants and reaction orders for each substrate given in Table 13.

$$PR + 4\,NH_4Br + 2\,H_2O_2 \xrightarrow{\;CeO_{2-x}\;} Br_4PR + 4\,NH_4OH \qquad 24$$
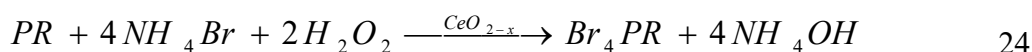
$$v = \frac{d[Br_4PR]}{dt} = k_1[PR]^a \cdot k_2[NH_4Br]^b \cdot k_3[H_2O_2]^c \cdot k_4[CeO_{2-x}]^d \qquad 25$$

$$v = \frac{d[Br_4PR]}{dt} = k \cdot [S]^x \qquad 26$$

$$\log\!\left(\frac{d[Br_4PR]}{dt}\right) = \log(v) = x \cdot \log([S]) + \log k \qquad 27$$
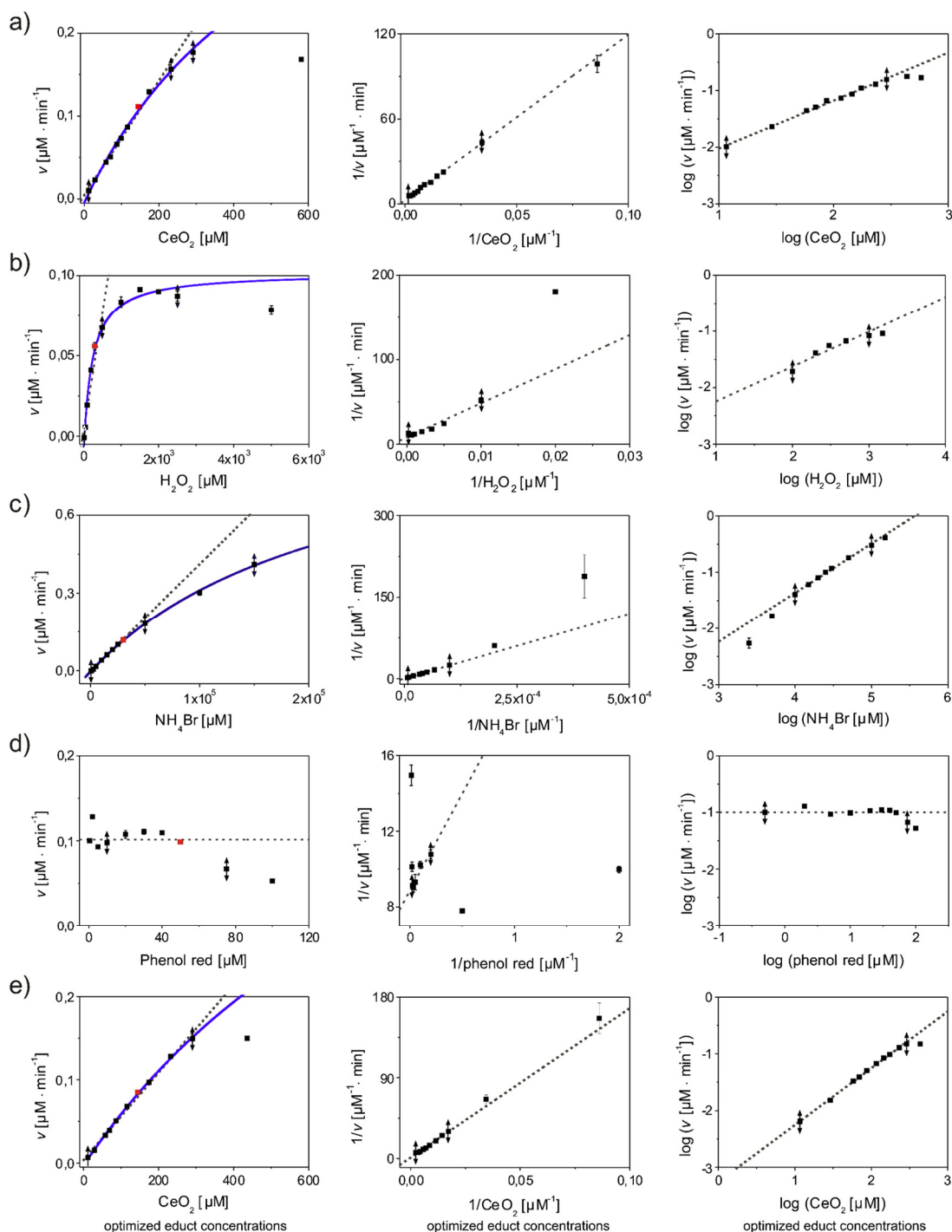
Figure 71. Kinetics of the fourfold oxidative bromination of PR as a function of the substrate concentrations as compiled in Table 11. a-e) The kinetics as a function of the selected substrate concentrations while others are fixed are illustrated in the left column. The values are fitted linearly (dark grey, dashed line to $y = A + Bx$) and to the Michaelis-Menten equation (blue line, $y = A + Bx/(C+x)$ with $B = v_{max}$ and $C = K_m$). The fit range is illustrated by fitting bars. The corresponding Lineweaver-Burk linearizations are shown in the middle column (linear fit: dark grey, dashed line, $y = A + Bx$ with $A = 1/v_{max}$ and $B = K_m/v_{max}$) and the corresponding logarithmic correlations are illustrated in the right column (linear fit: dark grey, dashed line, $y = A + Bx$ with $A = log(k)$ and $B = a$). d) The kinetic for PR variation appears highly complicated and is fitted linearly at a "stable state" as marked in the graph. In general, red squares highlight the individual optimized concentrations of NH_4Br (25 mM), PR (50 µM) and H_2O_2 (300 µM) used in experiment e) catalyzed by an optimized CeO_{2-x} nanorod amount (25 µg·mL^{-1}). Abbreviations: cf. main text.

Turnover Frequency

The turnover frequency (TOF = k_{cat}) was calculated as the maximum formation rate per minute (v_{max}) of PR at optimized substrate concentrations (0.1 $\mu M_{Br4PR}\cdot min^{-1}$, Table 13) for molar concentrations of the catalyst (Equation 27) and a concentration of 145 μM CeO_{2-x} (25 $\mu g\cdot mL^{-1}$/ 172.11 $g\cdot mol^{-1}$) and yield to $6.9\cdot 10^{-4}$ min^{-1}. As the oxidative bromination of PR requires the oxidation of four Br^-, the TOF with respect to the HOBr concentration is $2.8\cdot 10^{-3}$ min^{-1}.

$$TOF = k_{cat} = \frac{v_{max}}{[CeO_{2-x}]_0} \qquad\qquad 28$$

As only the particle surface is available for catalysis, the TOF is determined by the surface area, which was determined from BET adsorption isotherms. An active surface of $2062.1\cdot 10^{-6} m^2$ (82.483 $m^2\cdot g^{-1}$/25 μg particles in the reaction mixture) lead to 48.5 $\mu M_{Br4PR}\cdot min^{-1}$ per m^2 CeO_{2-x} and to 194 $\mu M_{HOBr}\cdot min^{-1}$ per m^2 CeO_{2-x}, respectively.

General Kinetic Model – Determination of k_{gen} and E_A

The kinetics was pseudo-first order by each of NH_4Br, H_2O_2 and CeO_{2-x} and pseudo-zero order by PR (Figure 71 and Table 13). The overall oxidative bromination of PR at the initial state can be regarded as pseudo-third order reaction with k_{gen} as the overall reaction constant (Equation 28). For a pseudo-third order reaction, some approximations had to be made to extract the general reaction constant k_{gen}: (i) The concentration of the catalyst remained constant during the reaction and its concentration is given by the initial quantity of cerium oxide $[CeO_{2-x}]_0$ = 145 μM, (ii) As $[NH_4Br] \gg [PR]$, the ammonium bromide concentration is given by the initial concentration ($[NH_4Br]_0$). (iii) As the formation of one Br4PR molecule consumes four NH_4Br and two H_2O_2 molecules (Equation 24), the change in the Br4PR concentration is related to the H_2O_2 consumption by $d[Br_4PR]$ = - ½ $d[H_2O_2]$ and $[H_2O_2]_t$ = $[H_2O_2]_0$ - ½ $[Br_4PR]_t$.

$$v = \frac{d[Br_4PR]}{dt} = k_{gen}\cdot[CeO_{2-x}]\cdot[NH_4Br]\cdot[H_2O_2] \qquad\qquad 29$$

This leads to Equation 30 and integration (Equation 31 – 35) yields the Equation for the overall reaction constant (k_{gen}).

$$v = \frac{d[Br_4PR]}{dt} = -\frac{1}{2} \cdot \frac{d[H_2O_2]}{dt} = k_{gen} \cdot [CeO_{2-x}]_0 \cdot [NH_4Br]_0 \cdot [H_2O_2] \qquad 30$$

$$\int_{[H_2O_2]_0}^{[H_2O_2]_t} \frac{d[H_2O_2]}{[H_2O_2]} = 2\int_0^t k_{gen} \cdot [CeO_{2-x}]_0 \cdot [NH_4Br]_0 \, dt \qquad 31$$

$$\ln \frac{[H_2O_2]_0}{[H_2O_2]_t} = 2k_{gen} \cdot [CeO_{2-x}]_0 \cdot [NH_4Br]_0 t \qquad 32$$

$$\ln[H_2O_2]_t = \ln[H_2O_2]_0 - 2k_{gen} \cdot [CeO_{2-x}]_0 \cdot [NH_4Br]_0 t \qquad 33$$

$$\ln\left([H_2O_2]_0 - \frac{1}{2}[Br_4PR]_t\right) = \ln[H_2O_2]_0 - 2k_{gen} \cdot [CeO_{2-x}]_0 \cdot [NH_4Br]_0 t \qquad 34$$

$$k_{gen} = \frac{\ln\left([H_2O_2]_0 / [H_2O_2]_0 - \frac{1}{2}[Br_4PR]_t\right)}{2[CeO_{2-x}]_0 \cdot [NH_4Br]_0 t} \qquad 35$$

The kinetics of optimized reactions that are given in Figure 71e was analyzed with this kinetic model (Equation 34, Figure 72). The optimized reaction was repeated at different temperatures (5, 15, 25, 35, 45, 55°C) and analyzed with Equation 35 (Table 14, Figure 72a). Variable temperature experiments revealed the Arrhenius constant (ln A) equal to 13.4±1.6 and the activation energy E_A equal to 49.7±0.4 kJ·mol^{-1} (Figure 72b). The general reaction constants k_{gen} were determined with respect to the concentration of CeO_{2-x} varied (2-75 µg·mL^{-1}, 590 nm, pH 5.6, 23°C) (black points, Figure 72c). The k_{gen} determined at different concentrations of CeO_{2-x} and at different temperatures are shown in Figure 72c. As one can see, the k_{gen} was practically independent on the CeO_{2-x} concentration (black points) and its values lay within the range 1.1·10^{-3} to 1.2·10^{-3} L^2·mmol^{-2}·h^{-1} (2 − 50 µg·mL^{-1} CeO_{2-x}). The average value of k_{gen} determined at 23°C was 1.1·10^{-3}±1.5·10^{-4} L^2·mmol^{-2}·h^{-1}. The reproducibility of the kinetics confirmed the mathematical model described by Equations 24-35. Temperature-dependent experiment revealed a considerable dependence of k_{gen} on temperature (Figure 72c – red points) in accordance with an Arrhenius model.

Table 14. Values of the general reaction constants (k_{gen}) depending on temperature variations. Concentrations of Br$_4$PR generated at different temperatures (5 – 55°C) after 1 h of reaction time and estimates of k_{gen} via Equation 35.

T (°C)	[Br$_4$PR] after 1 h (mM)	k_{gen} (L^2· mmoL^{-2}· h^{-1})
5	1.0	$2.2 \cdot 10^{-4}$
15	3.7	$8.4 \cdot 10^{-4}$
25	6.0	$1.4 \cdot 10^{-3}$
35	11.0	$2.6 \cdot 10^{-3}$
45	19.3	$4.5 \cdot 10^{-3}$
55	29.0	$6.8 \cdot 10^{-3}$
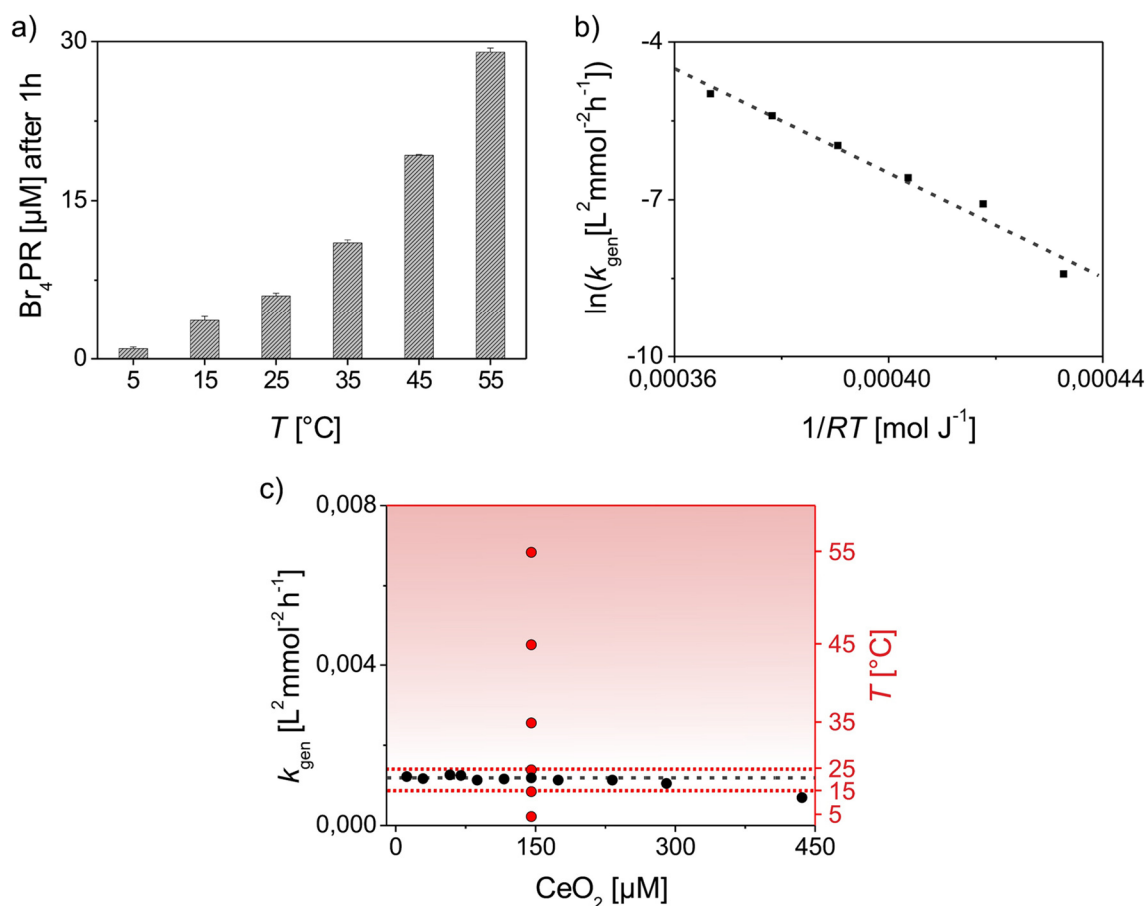
Figure 72. Activation energy determination based on the Br$_4$PR concentrations formed at 5 – 55°C after 1h of reaction time and estimates of $k_{gen(t)}$. a) Illustrates the temperature dependence (5, 15, 25, 35, 45, 55°C) of the oxidative bromination of PR after 1h of reaction time (CeO$_{2-x}$ nanoparticles (25 µg·mL^{-1}), PR (50 µM), NH$_4$Br (25 mM) and H$_2$O$_2$ (300 µM)). Based on this data, $k_{gen(t)}$ is estimated (Equation 35, Table 14). b) Arrhenius plot for the oxidative bromination of PR between 5–55°C to assign the overall activation energy (E$_A$) to $\approx$ 50 kJ·mol^{-1}. c) Comparison of the values of $k_{gen(t)}$ obtained from temperature-dependent measurements (●) and $k_{gen(t)}$ obtained from the kinetics (●, absorbance versus catalyst concentration) underlying the established values of Figure 71e and graphical evaluation following Equation 34, not shown.

Calculations of TOF and SA Values of Diverse Catalysts

Table 15. Precise description of the evaluation of TOF and SA values of Table 7 in respect to the details given in the assigned paper and (TOF [1/h] = mol(Br^{ox})/(mol(cat)·h); SA [mmol/g·h] = mmol(Br^{ox})/(g(cat)·h)). The entries and references match to the numbers in Table 7. Molar masses used in g mol^{-1}: Mo 95.95, Cr 52.00, Fe 55.85, Cu 63.55, Ti 47.87, V 181.88, Ce 172.11, ZrO$_2$ 123.22, H$_3$PW$_{12}$O$_{40}$ (PTA) 2880.05, H$_4$SiW$_{12}$O$_{40}$ (STA) 2878.17, H$_3$PMo$_{12}$O$_{40}$ (PMA) 1825.49, H$_4$SiMo$_{12}$O$_{40}$ (SMA) 1823.61.

# [Ref.]	Catalyst (support)	Reaction details
5 [400]	Zr (ZrO$_2$)	200 mg (1.623 mmol), dye: 2mmol (conv.: 48.84% 1Br), 5h $$TOF_{ZrO2} = \frac{2mmol \cdot 48.84\%}{1.623mmol \cdot 5h} = 0.12\frac{1}{h}$$ $$SA_{ZrO2} = \frac{2mmol \cdot 48.84\%}{200mg \cdot 5h} = 0.98\frac{mmol}{g \cdot h}$$
6 [395]	Al. Si (HZSM)	200 mg, dye: 2mmol (conv.: 55% 1Br, 18% 2Br), 5h $$SA_{HZSM} = \frac{2mmol \cdot (55\% + 18\% \cdot 2)}{200mg \cdot 5h} = 1.82\frac{mmol}{g \cdot h}$$
7 [395]	Al, Si (HY)	200 mg, dye: 2mmol (conv.: 75% 1Br), 5h $$SA_{HY} = \frac{2mmol \cdot 75\%}{200mg \cdot 5h} = 1.50\frac{mmol}{g \cdot h}$$
8 [401]	V(IV)O complex (polymer)	20 mg, dye: 2mmol (conv.: 31% 1Br, 55% 2Br and 28% 1Br, 65% 2Br), 1h [TOF$_{given}$ 31.5-38.8 1/h] $$SA_{V(IV)O} = \frac{2mmol \cdot (31\% + 55\% \cdot 2)}{200mg \cdot 1h} = 141.00\frac{mmol}{g \cdot h}$$ $$SA_{V(IV)O} = \frac{2mmol \cdot (28\% + 65\% \cdot 2)}{200mg \cdot 1h} = 158.00\frac{mmol}{g \cdot h}$$
9 [402]	V(V)O$_2$ complexes (PS)	30 mg, dye: 10mmol (conv.: 73% = 7.3 mmol, thereof: 81.4% 1Br, 15.8% 2Br), 2h [TOF$_{given}$ 100.0-104.3 1/h] nW=12·nPTA=12·(200mg·15%)/2880.05g/mol=0.125 mmol $$SA_{V(V)O2} = \frac{7.3mmol \cdot (81.4\% + 15.8\% \cdot 2)}{30mg \cdot 2h} = 137.48\frac{mmol}{g \cdot h}$$
10 [403]	V(V)O$_2$ complexes (PS)	5 mg, dye: 5mmol (conv.: 96% = 4.8 mmol, thereof: 81% 1Br, 6% 2Br, 13 3Br), 2h [TOF$_{given}$ 2254 1/h] $$SA_{V(V)O2} = \frac{4.8mmol \cdot (81\% + 6\% \cdot 2 + 13\% \cdot 3)}{5mg \cdot 2h} = 633.60\frac{mmol}{g \cdot h}$$
11 [404]	V(V)O$_2$ complexes 1.3–1.4 wt% V (PS)	20 mg, dye: 10mmol (conv.: 85.2% = 8.52 mmol, thereof: 90.4% 1Br and conv.: 81.7% = 8.17 mmol, thereof: 89.6% 1Br), 2h [TOF$_{given}$ 775 and 800 1/h] $$SA_{V(V)O2} = \frac{8.52mmol \cdot 90.4\%}{20mg \cdot 2h} = 192.55\frac{mmol}{g \cdot h}$$ $$SA_{V(V)O2} = \frac{8.17mmol \cdot 89.6\%}{20mg \cdot 2h} = 183.01\frac{mmol}{g \cdot h}$$
14 [405]	V(IV)O complex, 0.65 wt%V (MCM-41)	25 mg, dye: 5mmol (conv.: 99% 1Br), 3.5h [TOF$_{given}$ 448 1/h] $$SA_{V(IV)O} = \frac{5mmol \cdot 99\%}{25mg \cdot 3.5h} = 56.57\frac{mmol}{g \cdot h}$$

15 [396]	V(V)O$_2$ complexes (HY)	20 mg, dye: 2mmol (conv.: 34% and 26.8% 1Br), 3.5h [TOF$_{given}$ 52 and 67 1/h] $$SA_{V(V)O2} = \frac{2mmol \cdot 34\%}{20mg \cdot 4h} = 8.50 \frac{mmol}{g \cdot h}$$ $$SA_{V(V)O2} = \frac{2mmol \cdot 26.8\%}{20mg \cdot 4h} = 6.70 \frac{mmol}{g \cdot h}$$
16 [406]	WO$_2$(O$_2$)(CN$_2$) (PAN)	$\approx$ 200 mg, dye: 0.04mmol Br$_4$PR (nHOBr = 4·nBr$_4$PR), 1.33h $$TOF_{WO3(O2)(CN)2}(HOBr) = TOF_{WO3(O2)(CN)2}(Br_4PR) \cdot 4 = 274.00 \frac{1}{h}$$ $$SA_{WO3(O2)(CN)2} = \frac{0.04mmol \cdot 4}{200mg \cdot 1.33h} = 0.62 \frac{mmol}{g \cdot h}$$
21 [407]	WO$_4^{2-}$ (NiAl-LDH (Taktovite))	80 mg (4mM W), dye: 360 mM (in 10mL; 3.6 mmol) (conv.: 96 or 99%, in each case 93% 1Br, 25 (r.t.) or 10 min (35°C) nW=12·nPTA=12·(200mg·15%)/2880.05g/mol=0.125 mmol $$TOF_{W@LDH} = \frac{360mM \cdot 96\% \cdot 93\%}{4mM \cdot \frac{25}{60}h} = 192.84\frac{1}{h}$$ (r.t.) $$SA_{W@LDH} = \frac{(360mM \cdot 10mL) \cdot 96\% \cdot 93\%}{80mg \cdot \frac{25}{60}h} = 96.42 \frac{mmol}{g \cdot h}$$ (r.t.) $$TOF_{W@LDH} = \frac{360mM \cdot 99\% \cdot 93\%}{4mM \cdot \frac{10}{60}h} = 497.18\frac{1}{h}$$ (35°C) $$SA_{W@LDH} = \frac{(360mM \cdot 10mL) \cdot 99\% \cdot 93\%}{80mg \cdot \frac{10}{60}h} = 248.59 \frac{mmol}{g \cdot h}$$ (35°C)
22 [408]	15 wt% H$_3$PW$_{12}$O$_{40}$ (ZnAl-LDH)	200 mg, dye: 2mmol (conv.: 67% = 1.34 mmol, thereof: 93% 1Br, 7% 2Br), 5h nW=12·nPTA=12·(200mg·15%)/2880.05g/mol=0.125 mmol $$TOF_{W@LDH} = \frac{1.34mmol \cdot (93\% + 7\% \cdot 2)}{0.125mmol \cdot 5h} = 2.29\frac{1}{h}$$ $$SA_{W@LDH} = \frac{1.34mmol \cdot (93\% + 7\% \cdot 2)}{200mg \cdot 5h} = 1.43 \frac{mmol}{g \cdot h}$$
24 [410]	15 wt% H$_4$SiW$_{12}$O$_{40}$ (ZrO$_2$)	200 mg, dye: 2mmol (conv.: 92% 1Br), 5h nW=12·nSTA=12·(200mg·15%)/2878.17g/mol=0.125 mmol $$TOF_{W@ZrO2} = \frac{2mmol \cdot 92\%}{0.125mmol \cdot 5h} = 2.94\frac{1}{h}$$ $$SA_{W@ZrO2} = \frac{2mmol \cdot 92\%}{200mg \cdot 5h} = 1.84 \frac{mmol}{g \cdot h}$$
25 [410]	15 wt% H$_3$PW$_{12}$O$_{40}$ (ZrO$_2$)	200 mg, dye: 2mmol (conv.: 93% = 1.86 mmol, thereof: 99% 1Br, 0.3% 2Br), 5h nW=12·nPTA=12·(200mg·15%)/2880.05g/mol=0.125 mmol $$TOF_{W@ZrO2} = \frac{1.868mmol \cdot (99\% + 0.3\% \cdot 2)}{0.125mmol \cdot 5h} = 2.96\frac{1}{h}$$ $$SA_{W@ZrO2} = \frac{1.868mmol \cdot (99\% + 0.3\% \cdot 2)}{200mg \cdot 5h} = 1.85 \frac{mmol}{g \cdot h}$$
26 [400]	15 wt% H$_3$PW$_{12}$O$_{40}$ (ZrO$_2$)	200 mg, dye: 2mmol (conv.: 93.4% = 1.868 mmol, thereof: 99.7% 1Br, 0.3% 2Br), 5h; nW=12·nPTA=12·(200mg·15%)/2880.05g/mol=0.125 mmol $$TOF_{W@ZrO2} = \frac{1.868mmol \cdot (99.7\% + 0.3\% \cdot 2)}{0.125mmol \cdot 5h} = 3.0\frac{1}{h}$$ $$SA_{W@ZrO2} = \frac{1.868mmol \cdot (99.7\% + 0.3\% \cdot 2)}{200mg \cdot 5h} = 1.87 \frac{mmol}{g \cdot h}$$

27 [411]	12 wt% $H_3PW_{12}O_{40}$ (ZrO$_2$)	5 wt%·≈10g suspension ≅ 500 mg catalyst, dye: 18 mmol (conv.: 99% 1Br), 1.5h nW=12·nPTA=12·(500mg·12%)/2880.05g/mol=0.250 mmol $$TOF_{W @ ZrO_2} = \frac{18\,mmol \cdot 97\%}{0.250\,mmol \cdot 1.5h} = 46.56\,\frac{1}{h}$$ $$SA_{W @ ZrO_2} = \frac{18\,mmol \cdot 97\%}{500\,mg \cdot 1.5h} = 23.28\,\frac{mmol}{g \cdot h}$$
28 [412]	15 wt% $H_4SiW_{12}O_{40}$ (TiP)	200 mg, dye: 2mmol (conv.: 97%, 1Br), 5h nW=12·nSTA=12·(200mg·15%)/2878.17g/mol=0.125 mmol $$TOF_{W @ TiP} = \frac{2\,mmol \cdot 97\%}{0.125\,mmol \cdot 5h} = 3.10\,\frac{1}{h}$$ $$SA_{W @ TiP} = \frac{2\,mmol \cdot 97\%}{200\,mg \cdot 5h} = 1.94\,\frac{mmol}{g \cdot h}$$
29 [412]	15 wt% $H_3PW_{12}O_{40}$ (TiP)	200 mg, dye: 2mmol (conv.: 98%, 1Br), 5h nW=12·nPTA=12·(200mg·15%)/2880.05g/mol=0.125 mmol $$TOF_{W @ TiP} = \frac{2\,mmol \cdot 98\%}{0.125\,mmol \cdot 5h} = 3.14\,\frac{1}{h}$$ $$SA_{W @ TiP} = \frac{2\,mmol \cdot 98\%}{200\,mg \cdot 5h} = 1.96\,\frac{mmol}{g \cdot h}$$
30 [402]	Mo(VI)O$_2$ complex (PS)	30 mg, dye: 10mmol (conv.: 92% = 9.2 mmol, thereof: 83.4% 1Br, 14% 2Br), 2h [TOF 213.3 1/h] $$SA_{Mo @ PS} = \frac{9.2\,mmol \cdot (83.4\% + 14\% \cdot 2)}{30\,mg \cdot 2h} = 170.81\,\frac{mmol}{g \cdot h}$$
31 [413]	Mo(VI)O2 complex (PS)	15 mg, dye: 5mmol (conv.: 96% = 4.8 mmol, thereof: 49% 1Br, 47.5% 2Br), 2h nMo=0.45 mmol Mo/g PS-complex·15 mg PS-complex = 6.75·10^{-3}mmol $$TOF_{Mo @ PS} = \frac{4.8\,mmol \cdot (49\% + 47.5\% \cdot 2)}{6.75 \cdot 10^{-3}\,mmol \cdot 2h} = 512.00\,\frac{1}{h}$$ $$SA_{Mo @ PS} = \frac{4.8\,mmol \cdot (49\% + 47.5\% \cdot 2)}{15\,mg \cdot 2h} = 230.40\,\frac{mmol}{g \cdot h}$$
32 [406]	Mo(VI)O$_2$(O$_2$)(CN)$_2$ (PAN)	≈ 100 mg, dye: 0.04mmol Br$_4$PR (nHOBr = 4·nBr$_4$PR), 1.33h $$TOF_{Mo @ PAN}(HOBr) = TOF_{Mo @ PAN}(Br_4PR) \cdot 4 = 240.00\,\frac{1}{h}$$ $$SA_{Mo @ PAN} = \frac{0.04\,mmol \cdot 4}{100\,mg \cdot 1.33h} = 1.20\,\frac{mmol}{g \cdot h}$$
33 [414]	Mo(VI)O$_4$$^{2-}$ 9.9 % Mo (MgAl-LDH)	250 mg, dye: 1mmol (conv.: 80% 1Br), 20 min nMo=(250 mg·9.9%)/95.95g/mol=0.258 mmol $$TOF_{Mo @ LDH} = \frac{1\,mmol \cdot 80\%}{0.258\,mmol \cdot \frac{20}{60}h} = 9.30\,\frac{1}{h}$$ $$SA_{Mo @ LDH} = \frac{1\,mmol \cdot 80\%}{250\,mg \cdot \frac{20}{60}h} = 9.60\,\frac{mmol}{g \cdot h}$$
35 [408]	15 wt% $H_3PMo_{12}O_{40}$ (ZnAl-LDH)	200 mg, dye: 2mmol (conv.: 82% = 1.64 mmol, thereof: 96% 1Br, 4% 2Br), 5h nMo=12·nPTA=12·(200mg·15%)/1825.49g/mol=0.197mmol $$TOF_{Mo @ LDH} = \frac{1.64\,mmol \cdot (96\% + 4\% \cdot 2)}{0.197\,mmol \cdot 5h} = 1.66\,\frac{1}{h}$$ $$SA_{Mo@LDH} = \frac{1.64\,mmol \cdot (96\% + 4\% \cdot 2)}{200\,mg \cdot 5h} = 1.71\,\frac{mmol}{g \cdot h}$$

36 [410]	15 wt% $H_4SiMo_{12}O_{40}$ (ZrO$_2$)	200 mg, dye: 2mmol (conv.: 80% = 1.6 mmol, thereof: 98% 1Br, 2% 2Br), 5h nMo=12·nSMA=12·(200mg·15%)/1823.61g/mol=0.197mmol $$TOF_{Mo@ZrO2} = \frac{1.6\,mmol \cdot (98\% + 2\% \cdot 2)}{0.197\,mmol \cdot 5h} = 1.67\frac{1}{h}$$ $$SA_{Mo@ZrO2} = \frac{1.6\,mmol \cdot (98\% + 2\% \cdot 2)}{200\,mg \cdot 5h} = 1.63\frac{mmol}{g \cdot h}$$
37 [410]	15 wt% $H_3PMo_{12}O_{40}$ (ZrO$_2$)	200 mg, dye: 2mmol (conv.: 86% 1Br), 5h nMo=12·nPMA=12·(200mg·15%)/1825.49g/mol=0.197 mmol $$TOF_{Mo@ZrO2} = \frac{2\,mmol \cdot 86\%}{0.197\,mmol \cdot 5h} = 1.75\frac{1}{h}$$ $$SA_{Mo@ZrO2} = \frac{2\,mmol \cdot 86\%}{200\,mg \cdot 5h} = 1.72\frac{mmol}{g \cdot h}$$
38 [395]	5 wt% Mo (ZSM)	200 mg, dye: 2mmol (conv.: 67% 1Br, 22% 2Br), 5h nMo=(200mg·5%)/95.95g/mol=0.104 mmol $$TOF_{Mo@ZSM} = \frac{2\,mmol \cdot (67\% + 22\% \cdot 2)}{0.104\,mmol \cdot 5h} = 4.27\frac{1}{h}$$ $$SA_{Mo@ZSM} = \frac{2\,mmol \cdot (67\% + 22\% \cdot 2)}{200\,mg \cdot 5h} = 2.22\frac{mmol}{g \cdot h}$$
39 [412]	15 wt% $H_4SiMo_{12}O_{40}$ (TiP)	200 mg, dye: 2mmol (conv.: 72% = 1.44 mmol, thereof: 81% 1Br, 19% 2Br), 5h nMo=(200mg·15%)/1823.61g/mol=0.197 mmol $$TOF_{Mo@TiP} = \frac{1.44\,mmol \cdot (81\% + 19\% \cdot 2)}{0.197\,mmol \cdot 5h} = 1.74\frac{1}{h}$$ $$SA_{Mo@TiP} = \frac{1.44\,mmol \cdot (81\% + 19\% \cdot 2)}{200\,mg \cdot 5h} = 1.71\frac{mmol}{g \cdot h}$$
40 [412]	15 wt% $H_3PMo_{12}O_{40}$ (TiP)	200 mg, dye: 2mmol (conv.: 83% = 1.66 mmol, thereof: 80% 1Br, 20% 2Br), 5h nMo=(200mg·15%)/1825.49g/mol=0.197 mmol $$TOF_{Mo@TiP} = \frac{1.66\,mmol \cdot (80\% + 20\% \cdot 2)}{0.197\,mmol \cdot 5h} = 2.02\frac{1}{h}$$ $$SA_{Mo@TiP} = \frac{1.66\,mmol \cdot (80\% + 20\% \cdot 2)}{200\,mg \cdot 5h} = 1.99\frac{mmol}{g \cdot h}$$
43 [395]	Ti (IV) (TS1)	200 mg, dye: 2mmol (conv.: 61% 1Br, 14% 2Br), 5h $$SA_{TS1} = \frac{2\,mmol \cdot (61\% + 14\% \cdot 2)}{200\,mg \cdot 5h} = 1.78\frac{mmol}{g \cdot h}$$
45 [331]	4 wt% Ti(IV)O$_2$ (ZrP)	200 mg, dye: 2mmol (conv.: 82% 1Br), 5h nTi=(200mg·4%)/47.87g/mol=0.167 mmol $$TOF_{Ti@ZrP} = \frac{2\,mmol \cdot 82\%}{0.167\,mmol \cdot 5h} = 2.01\frac{1}{h} \quad ; \quad SA_{Ti@ZrP} = \frac{2\,mmol \cdot 82\%}{200\,mg \cdot 5h} = 1.64\frac{mmol}{g \cdot h}$$
46 [331]	4 wt% Ti(IV)O$_2$ (TiP)	200 mg, dye: 2mmol (conv.: 94% = 1.88 mmol, thereof: 80% 1Br, 20% 2Br), 5h nTi=(200mg·4%)/47.87g/mol=0.167 mmol $$TOF_{Ti@TiP} = \frac{1.88\,mmol \cdot (80\% + 20\% \cdot 2)}{0.167\,mmol \cdot 5h} = 2.70\frac{1}{h}$$ $$SA_{Ti@TiP} = \frac{1.88\,mmol \cdot (80\% + 20\% \cdot 2)}{200\,mg \cdot 5h} = 2.26\frac{mmol}{g \cdot h}$$
47 [416]	Zr(IV)/SO$_4^{2-}$ (SBA-15-620)	50 mg, dye: 0.5mmol (conv.: 90%, 1Br), 4h $$SA_{Zr@SBA} = \frac{0.5\,mmol \cdot 90\%}{50\,mg \cdot 4h} = 2.25\frac{mmol}{g \cdot h}$$

48 [395]	Cr, 5 wt% (ZSM)	200 mg, dye: 2mmol (conv.: 83% 1Br), 5h nCr=(200mg·5%)/51.996g/mol=0.192 mmol $$TOF_{Cr@ZSM} = \frac{2mmol \cdot 83\%}{0.192\,mmol \cdot 5h} = 1.73\,\frac{1}{h}$$ $$SA_{Cr@ZSM} = \frac{2mmol \cdot 83\%}{200mg \cdot 5h} = 1.66\,\frac{mmol}{g \cdot h}$$
49 [417]	Fe(III) com-plex 3.66 % Fe (PS)	50 mg, dye: 10mmol (conv.: 98% 1Br), 3h nFe=(50mg·3.66%)/55.85g/mol=0.033 mmol $$TOF_{Fe@PS} = \frac{10\,mmol \cdot 98\%}{0.033\,mmol \cdot 3h} = 98.99\,\frac{1}{h}$$ $$SA_{Fe@PS} = \frac{10\,mmol \cdot 98\%}{50mg \cdot 3h} = 65.33\,\frac{mmol}{g \cdot h}$$
51 [395]	5 wt% Fe (ZSM)	200 mg, dye: 2mmol (conv.: 56% 1Br, 22% 2Br), 5h nFe=(200mg·5%)/55.845g/mol=0.179 mmol $$TOF_{Fe@ZSM} = \frac{2mmol \cdot (56\% + 22\% \cdot 2)}{0.179\,mmol \cdot 5h} = 2.23\,\frac{1}{h}$$ $$SA_{Fe@ZSM} = \frac{2mmol \cdot (56\% + 22\% \cdot 2)}{200mg \cdot 5h} = 2.00\,\frac{mmol}{g \cdot h}$$
52 [418]	Cu(II) (PS)	15 mg, dye: 2mmol (conv.: 97% 1Br), 2h nCu=0.37 mmol Cu/g PS-complex·15 mg PS-complex = 5.55·10⁻³mmol $$TOF_{Cu@PS} = \frac{2mmol \cdot 97\%}{5.55 \cdot 10^{-3}\,mmol \cdot 2h} = 174.77\,\frac{1}{h}$$ $$SA_{Cu@PS} = \frac{2mmol \cdot 97\%}{15mg \cdot 2h} = 64.67\,\frac{mmol}{g \cdot h}$$
53 [419]	Cu(II) com-plex (SiO₂)	50 mg, dye: 2mmol (conv.: 99% 1Br), 1.5h nCu=0.045 mmol Cu/g complex·50 mg complex = 2.25·10⁻³mmol $$TOF_{Cu@SiO2} = \frac{2mmol \cdot 99\%}{2.25 \cdot 10^{-3}\,mmol \cdot 1.5h} = 586.67\,\frac{1}{h}$$ $$SA_{Cu@SiO2} = \frac{2mmol \cdot 99\%}{50mg \cdot 1.5h} = 26.40\,\frac{mmol}{g \cdot h}$$
54 [395]	5 wt% Cu (ZSM)	200 mg, dye: 2mmol (conv.: 61% 1Br, 12% 2Br), 5h nCu=(200mg·5%)/63.546g/mol=0.157 mmol $$TOF_{Cu@ZSM} = \frac{2mmol \cdot (61\% + 12\% \cdot 2)}{0.157\,mmol \cdot 5h} = 2.17\,\frac{1}{h}$$ $$SA_{Cu@ZSM} = \frac{2mmol \cdot (61\% + 12\% \cdot 2)}{200mg \cdot 5h} = 1.70\,\frac{mmol}{g \cdot h}$$
56 [442]	Se, 2.5 mol% (xerogel)	$k_{obs} = 1.27 \cdot 10^{-5}\,\frac{1}{s}$, Insertion of 2 Br into the substrate molecule yield: $$TOF_{Se@Xerogel} = 2 \cdot k_{obs} = 9.14 \cdot 10^{-3}\,\frac{1}{h}$$
57 [442]	Te, 2.5 mol% (xerogel)	$k_{obs} = 5.71 \cdot 10^{-5}\,\frac{1}{s}$, Insertion of 2 Br into the substrate molecule yield: $$TOF_{Te@Xerogel} = 2 \cdot k_{obs} = 0.041\,\frac{1}{h}$$
58 [421]	NaHSO₄ (SiO₂)	100 mg, dye: 1mmol (conv.: 93% 1Br), 0.5h $$SA_{NaHSO4@SiO2} = \frac{1mmol \cdot 93\%}{100\,mg \cdot 0.5h} = 18.60\,\frac{mmol}{g \cdot h}$$
59 [422]	H₂SO₄ (SiO₂)	15 mg, dye: 1mmol (conv.: 83% 1Br), 0.5h $$SA_{H2SO4@SiO2} = \frac{1mmol \cdot 83\%}{15mg \cdot 0.5h} = 110.67\,\frac{mmol}{g \cdot h}$$

60 [423]	V (V_2O_5)	91 mg, dye: 1mmol (conv.: 92% 1Br), 1.5h $nV=nV_2O_5\cdot2=0.5\ mmol\cdot2 = 1.0\ mmol$ $$TOF_{V2O5} = \frac{1mmol\cdot 92\%}{1.0mmol\cdot 1.5h} = 0.61\frac{1}{h}$$ $$SA_{V2O5} = \frac{1mmol\cdot 92\%}{91mg\cdot 1.5h} = 6.74\frac{mmol}{g\cdot h}$$
61 [424]	V (V_2O_5nw)	20 µg, v_{max}=0.05µM$_{HOBr}$/min, 1mL $nV=nV_2O_5\cdot2=(20\mu g/181.88g/mol)\cdot2 = 0.22\ \mu mol$ $$TOF_{V2O5} = \frac{0.05\mu M\ \cdot 1mL}{\frac{1}{60}h\cdot 0.22\mu mol} = 0.014\frac{1}{h}$$ $$SA_{V2O5} = \frac{0.05\mu M\ \cdot 1mL}{\frac{1}{60}h\cdot 20\mu g} = 0.15\frac{1}{h}$$
62 [425]	V (V_2O_5nw)	1 mg, dye: 25mM·1mL=0.025mmol (assumption: conv.: 100% 1Br), 1 min $nV=nV_2O_5\cdot2=(1mg/181.88g/mol)\cdot2 = 0.011\ mmol$ $$TOF_{V2O5} = \frac{0.025\,mmol}{0.011mmol\cdot\frac{1}{60}h} = 136.36\frac{1}{h}$$ $$SA_{V2O5} = \frac{0.025mmol}{1mg\cdot\frac{1}{60}h} = 1500.00\frac{mmol}{g\cdot h}$$
63 [426]	Ce (CeO_2nr)	50 mg, dye: 1mmol (conv.: 97% 1Br), 0.5h $nCe=50mg/172.11g/mol=0.291\ mmol$ $$TOF_{CeO2} = \frac{1mmol\cdot 97\%}{0.291mmol\cdot 0.5h} = 6.67\frac{1}{h}$$ $$SA_{CeO2} = \frac{1mmol\cdot 97\%}{50mg\cdot 0.5h} = 38.80\frac{mmol}{g\cdot h}$$
64 [427]	Ce (CeO_2 np)	80 mg, dye: 0.063mmol (conv.: 90% 1Br), 20h $nCe=80mg/172.11g/mol=0.465\ mmol$ $$TOF_{CeO2} = \frac{0.063mmol\cdot 90\%}{0.465mmol\cdot 20h} = 0.61\cdot 10^{-2}\frac{1}{h}$$ $$SA_{CeO2} = \frac{0.063mmol\cdot 90\%}{80mg\cdot 20h} = 0.035\frac{mmol}{g\cdot h}$$
65 [227]	Ce (CeO_2nr)	25 µg, v_{max}=0.4µM$_{HOBr}$/min, 1mL, $nCe=25\mu g/172.11g/mol=0.145\ \mu mol$ $$TOF_{CeO2} = \frac{0.4\mu M\ \cdot 1mL}{\frac{1}{60}h\cdot 0.145\mu mol} = 0.17\frac{1}{h}$$ $$SA_{CeO2} = \frac{0.4\mu M\ \cdot 1mL}{\frac{1}{60}h\cdot 25\mu g} = 0.96\frac{mmol}{g\cdot h}$$

Celestine Blue Assay

The formation of HOBr was demonstrated by the reaction of CB (50 µM, λ_{max} = 640 nm) with CeO_{2-x} nanorods (25 µg·mL^{-1}), NH_4Br (25 mM) and H_2O_2 (300 µM) in a total volume of 1 mL MilliQ-water (final concentrations) for 900 min at 25 ± 2°C. The reactions were terminated by removing the catalyst by centrifugation (14500 rpm, 3 min) and filtration (2.5 µm syringe filter), and the supernatant was analyzed by RP-HPLC/ESI-MS (method A).

Lactone Assay

The degradation of the quorum sensing molecules by oxidative bromination was followed by time dependent reverse high-performance liquid chromatography coupled with electrospray ionization-mass spectrometry. Several reaction mixtures (1 mL total volume) containing 900 µM 3-oxo-AHL, 20 mM KBr, 20 mM H_2O_2 and CeO_{2-x} nanorods (200 µg·mL^{-1}) were measured after 2.5h and 5h of reaction time. The reactions were terminated by removing the catalyst by centrifugation (14500 rpm, 3 min) and filtration (2.5 µm syringe filter), and the supernatant was analyzed by RP-HPLC/ESI-MS (method B).

Bacterial Adhesion Assay

Paint formulations containing the active catalysts prior identified in haloperoxidase-like dye assays were tested for their antibacterial activity against *E. coli* in the presence of H_2O_2 and Br$^-$. For the paint preparation, the particles were embedded either in a commercially available hard formulation ("Toplac") or/and in a soft paint formulation ("Rosine") provided by BASF. The amount of the catalyst (0.5, 1.0, 2.0 or 5.0 wt%) was evaluated in relation to the dry mass of the coating. With respect to Toplac, the weight amount was estimated by the mass of the paint precursor minus 25 wt% solvent mass (note: 25 wt% represented the minimum solvent mass in the Toplac paint formulation given in the MSDS).[548] The powders were dispersed by stirring and by ultrasonication (only a few seconds) yielding an almost homogenous paint formulation. Afterwards, 2x2 cm steel plates were painted directly with no previous treatment and dried for 5-7 days at room temperature. Plates with the paint precursor were prepared as blank samples. All samples were performed in duplicate. The dried, painted steel plates were sterilized by

UV irradiation (340 nm) for 15 min on each side. Afterwards, the plates were put into centrifugal tubes which had been sterilized with ethanol and dried at 60°C previously. The samples were exposed to 15 mL LB (Luria/Miller, 25 g·L^{-1}) media. Subsequently, the media was inoculated with *E. coli* (200 µL of an overnight culture of TOP10) and incubated for approximately 1 h at 37°C with soft agitation (160 rpm). Afterwards, KBr (1 mM, 150 µL of a 100 mM stock solution) and H_2O_2 (100 µM, 150 µL of a 10 mM stock solution) were then added sequentially every 3-4 hours (except during the night) over a period of 4 days at 37°C with soft agitation (160 rpm). Repeated additions of KBr and H_2O_2 were necessary to maintain the concentration of H_2O_2 and Br$^-$ in the media. Several sets control experiments were run in parallel: (i) plates coated with the paint precursor without additives incubated in pure LB media without bacteria ("negative control"), (ii) plates coated with formulations including 10 wt% (dry weight) of Cu_2O ("second negative control"), (iii) plates coated with the paint precursor without additives incubated in LB media with *E. coli* ("positive control"), (iv) plates coated with formulations including additives incubated in LB media with *E. coli* without adding KBr and H_2O_2 ("second positive control"). The blank samples were treated in exactly the same way as the samples containing a biocidal paint formulation. After the test period, the plates were gently washed with pure LB media (200 µL).

Bacterial DNA was stained with 4,6-diamidino-2-phenylindole (DAPI, in sterile water/glycerin (1:1), 1 µg·mL^{-1}). The staining was allowed to take effect for at least one hour in the dark. Note: a better outcome (e.g. facilitated microscope focusing) could be obtained when the stained samples were stored cool and in the dark (e.g. in a fridge) overnight before analysis. Fluorescence analysis was performed using an Olympus AHBT3 light microscope, together with an AH3-RFC reflected light fluorescence attachment. The presence of bacterial colonies was easily detected by the presence of bright blue "dots" or "clusters". After incubation in the reaction media, the samples were slightly sticky. Nevertheless, this did not influence the DAPI - staining and the fluorescence microscopy. The Toplac paint formulations themselves glowed and occasionally, problems arose within focusing. In addition to the resolution of the microscope used (10x), single bacteria imaging was not possible making these tests purely qualitative. However, the fluorescent signals were clearly seen in the oculars of the microscope, but could be difficult to detect in the pictures, making them at times misleading. Only representative fluo-

rescence images were shown to simplify the report. No blue fluorescence spots were observed in the negative DAPI-stained control samples. In comparison, intense blue fluorescence "dots" were present in the positive control sample due to the presence of bacterial colonies (*q. e. d.*). The bacterial colonization at the surface of all paint formulations tested was evaluated in relation to the control samples which were performed newly in each test campaign.
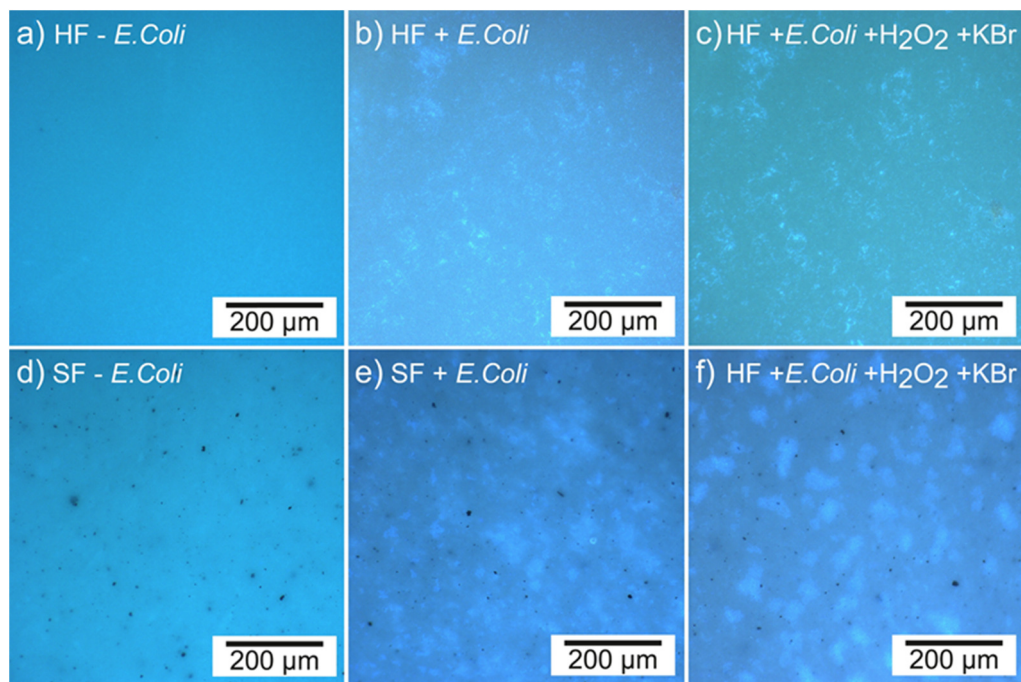
Figure 73. Bacterial adhesion assay – blank samples. Fluorescence images of paint formulations without biocide stained with DAPI (1 µg·mL^{-1}) to detect *E. coli* colonies. a) HF subjected to growth media without bacteria (negative control). b) HF subjected to growth media with bacteria (positive control). c) HF subjected to growth media containing bacteria, H_2O_2, KBr (positive control). d) SF subjected to growth media without bacteria (negative control). e) SF subjected to growth media with bacteria (positive control). f) HF subjected to growth media containing bacteria, H_2O_2, KBr (2. positive control). No bacteria have been detected in the negative controls (a, d) and no difference of the bacteria colonization of the positive control (b, e) in comparison the sample containing H_2O_2 and KBr (c, f) have been seen (*q.e.d.*). Abbreviations: HF hard formulation, SF soft formulation.
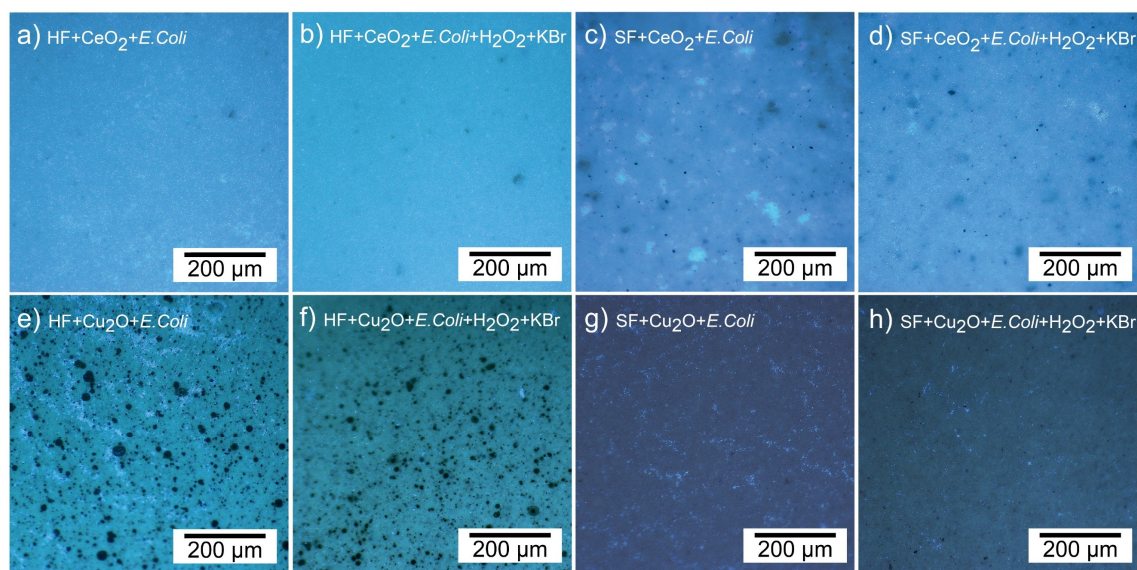
Figure 74. Bacterial adhesion assay: CeO$_{2-x}$ compared to Cu$_2$O. Fluorescence images of *E. coli* colonies stained with DAPI (1 µg·mL^{-1}) on stainless steel plates (2 x 2 cm) covered with paint formulations with cerium oxide or copper(I) oxide as biocides. a) HF containing 2 wt% of CeO$_{2-x}$ subjected to bacteria (positive control). b) HF containing 2 wt% of CeO$_{2-x}$ subjected to growth media containing bacteria, H$_2$O$_2$, KBr. c) SF containing 2 wt% of CeO$_{2-x}$ subjected to bacteria (positive control). d) SF containing 2 wt% of CeO$_{2-x}$ subjected to growth media containing bacteria, H$_2$O$_2$, KBr. e) HF containing 10 wt% of Cu$_2$O subjected to bacteria (positive control). f) HF containing 10 wt% of Cu$_2$O subjected to growth media containing bacteria, H$_2$O$_2$, KBr. g) SF containing 10 wt% of Cu$_2$O subjected to bacteria (positive control). h) SF containing 10 wt% of Cu$_2$O subjected to growth media containing bacteria, H$_2$O$_2$, KBr. In general, an increased number of small, isolated bacteria colonies have been formed on HF compared to SF as indicated by smaller blue "dots". A decrease in bacterial adhesion is apparent in Cu$_2$O and CeO$_2$ containing formulations in the order SF > HF. Abbreviations: HF hard formulation, SF soft formulation.
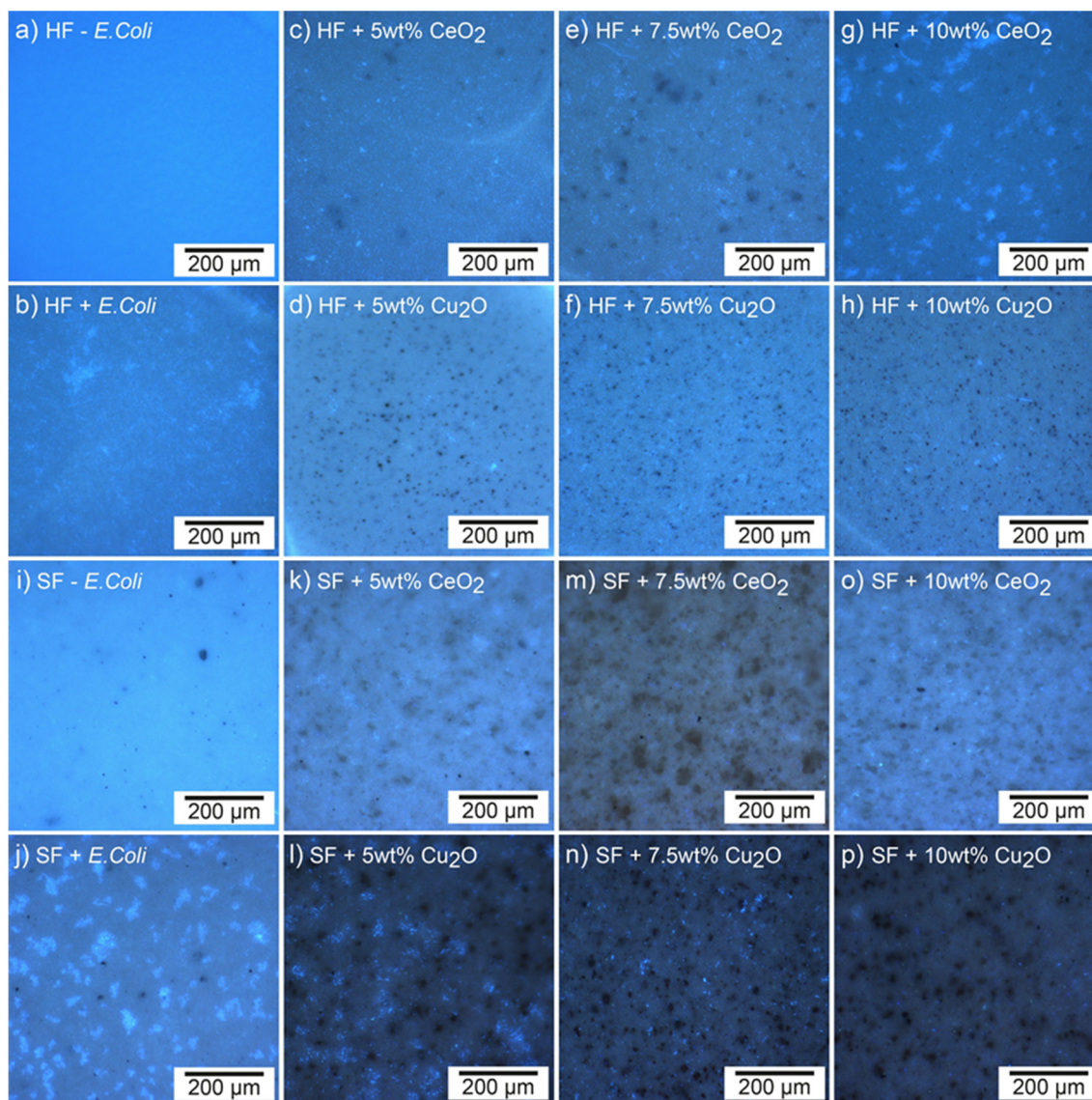
Figure 75. Bacterial adhesion assay: Dependence on CeO_{2-x} concentration compared to Cu_2O. Fluorescence images of *E. coli* colonies stained with DAPI (1 $\mu g \cdot mL^{-1}$) on stainless steel plates (2 x 2 cm) covered with paint formulations with CeO_{2-x} or Cu_2O as biocides in HF and SF. a) HF without biocide and bacteria (negative control). b) HF without biocide subjected to bacteria (positive control). c,d) HF containing 5 wt%, e,f) 7.5 wt% and g,h) 10 wt% biocide subjected to growth media containing bacteria, H_2O_2, and KBr. i) SF without biocide and bacteria (negative control). j) SF without biocide subjected to bacteria (positive control). k,l) HF containing 5 wt%, m,n) 7.5 wt% and o,p) 10 wt% biocide subjected to growth media containing bacteria, H_2O_2, and KBr. In HF, bacterial colonization has occured in all samples (c-h) whereas the increased surface roughness due to CeO_{2-x} containing samples have led to an increased amount of bacterial colonization. For Cu_2O containing hard formulations, only bacterial lawns have occured due to the smoother surface. In soft paint formulations, bacterial adhesion is highly reduced in all samples containing reactive species compared to the positive control (j). For CeO_{2-x}, no concentration dependence has been observed. 2 wt% ceria seems to catalyze the formation of a sufficient amount of reactive species to reduce bacterial adhesion. A concentration dependence has been observed for Cu_2O, because a sufficiently large amount of Cu^{2+} ions has to be formed and leak out of the formulation to inhibit bacterial colonization. A minimum amount of 10 wt% Cu_2O is required to obtain a bacteria-free surface. Abbreviations: HF hard formulation, SF soft formulation.

Bacterial Growth Assays

In contrast to the adhesion assay, bacterial growth assays focused on the repro-duction rate of bacteria. A typical reaction mixture contained bacteria (*E. coli*), the bro-mide source, the pure catalytic material and hydrogen peroxide in growth media as de-scribed for the bacterial adhesion assay. The reaction mixture was incubated at 37°C with soft agitation for a time period depending on demand/analytical method. No further addi-tion of KBr and H_2O_2 was necessary. Determining if the catalyst really had influenced the bacterial reproduction rate, the reaction mixtures could either be followed spectrophoto-metrically at 600 nm because of the absorbance of aromatic amino acids or could be plated on agar plates. With respect to the first method, the increase in the optical density (OD_{600}) was followed for several hours in 30 min steps. The measured absorbance was directly correlated to the bacterial reproduction rate (multiplication approximately every 20 minutes). However, this assay should only be used with respect to homogenous biocides, whereas harmful shear forces could be excluded. With respect to the second method, agar plates had to be prepared beforehand. For the preparation of agar plates, agar - LB me-dium (40 g in 1L H_2O) was sterilized *via* steam sterilization. Being cooled to $\approx$ 50°C, it was filled into petri dishes about ½ of the total volume of the dish under sterile conditions (sterile bench). After hardening, the dishes were closed, wrapped with Scotch Tape© and stored in the fridge. In general, the agar plates could be stored for several weeks but using them as soon as possible should be preferred. The reaction mixture for the growth test for both OD_{600} experiments or agar plates inoculation (cf. bacterial adhesion assay) contained 200 µL *E. coli* overnight culture, 500 µg·mL^{-1} catalytic material (500 µL of a 1 mg·mL^{-1} stock solution), 1 mM KBr (50 µL of a 100 mM stock solution) and 100 µM H_2O_2 (50 µL of a 10 mM stock solution) in 5 mL LB media in total.

Additionally, several blank samples in LB media were prepared containing: i) pure *E. coli*, ii) *E. coli* + catalyst, iii) *E. coli* + KBr, iv) *E. coli* + H_2O_2, and v) *E. coli* + KBr + H_2O_2. For the agar plate experiment, the reaction mixtures were incubated at 37°C with soft agitation (160 rpm) for 3.5 hours. Afterwards, 10 µL (or 50 µL) of the reaction mix-tures were plated on re-warmed agar plates, for example, by drawing "stripes". The pre-pared, closed-up plates were incubated for 10 minutes at room temperature. Then, the samples were turned upside down and incubated at 37°C for ca. 8 hours. Bacterial growth was monitored and documented at every hour by photographic shots.

10

Curriculum Vitae

Persönliche Daten

Geburtsdatum/ -ort ██████████████████

Staatsangehörigkeit ████

Sprachen ████████████████████████████

Akademische Ausbildung

██████ █████

██████ ████████████████████
████████████

██████ ████████████████████
████████████████
██████████████

██████ ████████████████████
████████████████
██████████

██████ ████████████████████
██████ ██

██████ ██████████
█ ████████████
██████ ████████
██████ ████████
██████ ████████████████
██████████████████

██████ ██████████

Forschungs- und Arbeitserfahrung

█████ ████████████████████
████████████
█████ █████████████████
████████████████
████████████

Akademische Tätigkeiten

Weiterbildungen und Konferenzteilnahmen

Persönliche Interessen

11

References

[1]   A. Bruggink, E. C. Roos, E. de Vroom, *Org. Process Res. Dev.* **1998**, *2*, 128.

[2]   D. A. Estell, T. P. Graycar, J. V. Miller, D. B. Powers, J. A. Wells, J. P. Burnier, P. G. Ng, *Science.* **1986**, *233*, 659.

[3]   V. J. Jensen, S. Rugh, in *Methods Enzymol.*, **1987**, pp. 356–370.

[4]   L. Sedlaczek, *Crit. Rev. Biotechnol.* **1988**, *7*, 187.

[5]   A. Dinçer, A. Telefoncu, *J. Mol. Catal. B Enzym.* **2007**, *45*, 10.

[6]   S. Elleuche, C. Schröder, K. Sahm, G. Antranikian, *Curr. Opin. Biotechnol.* **2014**, *29*, 116.

[7]   R. Breslow, L. E. Overman, *J. Am. Chem. Soc.* **1970**, *92*, 1075.

[8]   M. Raynal, P. Ballester, A. Vidal-Ferran, P. W. N. M. van Leeuwen, *Chem. Soc. Rev.* **2014**, *43*, 1734.

[9]   R. Breslow, *Artificial Enzymes*, Wiley-VCH Verlag GmbH & Co. KGaA, Weinheim, FRG, **2006**.

[10]   M. J. Wiester, P. A. Ulmann, C. A. Mirkin, *Angew. Chem. Int. Ed.* **2011**, *50*, 114.

[11]   K. Fan, C. Cao, Y. Pan, D. Lu, D. Yang, J. Feng, L. Song, M. Liang, X. Yan, *Nat. Nanotechnol.* **2012**, *7*, 459.

[12]   C. K. Kim, T. Kim, I. Y. Choi, M. Soh, D. Kim, Y. J. Kim, H. Jang, H. S. Yang, J. Y. Kim, H. K. Park, S. S. P. Park, S. S. P. Park, T. Yu, B. W. Yoon, S. H. Lee, T. Hyeon, *Angew. Chem.* **2012**, *51*, 11039.

[13]   R. Ragg, F. Natalio, M. N. Tahir, H. Janssen, A. Kashyap, D. Strand, S. Strand, W. Tremel, *ACS Nano* **2014**, *8*, 5182.

[14]   R. M. Yusop, A. Unciti-Broceta, E. M. Johansson, R. M. Sanchez-Martin, M. Bradley, *Nat. Chem* **2011**, *3*, 239.

[15]   H. Wei, E. Wang, *Chem. Soc. Rev.* **2013**, *42*, 6060.

[16]   Y. Lin, J. Ren, X. Qu, *Acc. Chem. Res.* **2014**, *47*, 1097.

[17]   T. Pirmohamed, J. M. Dowding, S. Singh, B. Wasserman, E. Heckert, A. S. Karakoti, J. E. S. King, S. Seal, W. T. Self, *Chem. Commun.* **2010**, *46*, 2736.

[18]   J. Fan, J. J. Yin, B. Ning, X. Wu, Y. Hu, M. Ferrari, G. J. Anderson, J. Wei, Y. Zhao, G. Nie, *Biomaterials* **2011**, *32*, 1611.

[19]   J. Mu, L. Zhang, M. Zhao, Y. Wang, *ACS Appl. Mater. Interfaces* **2014**, *6*, 7090.

[20]   T. Baran, T. Inanan, A. Menteş, *Carbohydr. Polym.* **2016**, *145*, 20.

[21]   L. Song, C. Huang, W. Zhang, M. Ma, Z. Chen, N. Gu, Y. Zhang, *Colloids Surfaces A Physicochem. Eng. Asp.* **2016**, *506*, 747.

[22]   X. Liu, Q. Wang, H. Zhao, L. Zhang, Y. Su, Y. Lv, *Analyst* **2012**, *137*, 4552.

[23]   R. Guo, Y. Wang, S. Yu, W. Zhu, F. Zheng, W. Liu, D. Zhang, J. Wang, *RSC Adv.* **2016**, *6*, 59939.

[24]   D. Salvemini, D. P. Riley, S. Cuzzocrea, *Nat. Rev. Drug Discov.* **2002**, *1*, 367.

[25]   W. Wang, X. Jiang, K. Chen, *Chem. Commun.* **2012**, *48*, 7289.

[26]   T. D. Schladt, K. Schneider, H. Schild, W. Tremel, *Dalton Trans.* **2011**, *40*, 6315.

[27]   T. Sun, Y. S. Zhang, B. Pang, D. C. Hyun, M. Yang, Y. Xia, *Angew. Chem.* **2014**, *126*, 12520.

[28]   R. Ragg, M. N. Tahir, W. Tremel, *Eur. J. Inorg. Chem.* **2016**, *2016*, 1906.

[29]   A. C. Rosenzweig, C. A. Frederick, S. J. Lippard, P. Nordlund, *Nature* **1993**, *366*, 537.

[30]   R. L. Lieberman, A. C. Rosenzweig, *Nature* **2005**, *434*, 177.

[31]   A. S. Hakemian, A. C. Rosenzweig, *Annu. Rev. Biochem.* **2007**, *76*, 223.

[32]   R. A. Himes, K. D. Karlin, *Curr. Opin. Chem. Biol.* **2009**, *13*, 119.

[33]   M. H. Groothaert, P. J. Smeets, B. F. Sels, P. A. Jacobs, R. A. Schoonheydt, *J. Am. Chem. Soc.* **2005**, *127*, 1394.

[34]   S. Grundner, M. A. C. Markovits, G. Li, M. Tromp, E. A. Pidko, E. J. M. Hensen, A. Jentys, M. Sanchez-Sanchez, J. A. Lercher, *Nat. Commun.* **2015**, *6*, 7546.

[35]   H. Wu, C. Tian, X. Song, C. Liu, D. Yang, Z. Jiang, *Green Chem.* **2013**, *15*, 1773.

[36]   C. Rodriguez, I. Lavandera, V. Gotor, *Curr. Org. Chem.* **2012**, *16*, 2525.

[37]   R. W. Estabrook, K. M. Faulkner, M. S. Shet, C. W. Fisher, in *Methods Enzymol.*, **1996**, pp. 44–51.

[38]   V. Reipa, M. P. Mayhew, V. L. Vilker, *Proc. Natl. Acad. Sci. U. S. A.* **1997**, *94*, 13554.

[39]   J. H. Kim, D. H. Nam, C. B. Park, *Curr. Opin. Biotechnol.* **2014**, *28*, 1.

[40]   F. Hollmann, I. W. C. E. Arends, K. Buehler, *ChemCatChem* **2010**, *2*, 762.

[41]   F. Hollmann, K. Hofstetter, T. Habicher, B. Hauer, A. Schmid, *J. Am. Chem. Soc.* **2005**, *127*, 6540.

[42]   F. Hollmann, A. Taglieber, F. Schulz, M. T. Reetz, *Angew. Chem. Int. Ed.* **2007**, *46*, 2903.

[43]   M. M. Grau, J. C. Van Der Toorn, L. G. Otten, P. Macheroux, A. Taglieber, F. E. Zilly, I. W. C. E. Arends, F. Hollmann, *Adv. Synth. Catal.* **2009**, *351*, 3279.

[44]   A. Taglieber, F. Schulz, F. Hollman, M. Rusek, M. T. Reetz, *ChemBioChem* **2008**, *9*, 565.

[45]   A. K. Udit, M. G. Hill, V. G. Bittner, F. H. Arnold, H. B. Gray, *J. Am. Chem. Soc.* **2004**, *126*,

10218.

[46]   S. Unversucht, F. Hollmann, A. Schmid, K.-H. van Pée, *Adv. Synth. Catal.* **2005**, *347*, 1163.

[47]   F. E. Zilly, A. Taglieber, F. Schulz, F. Hollmann, M. T. Reetz, *Chem. Commun.* **2009**, *2*, 7152.

[48]   D. H. Peterson, H. C. Murray, S. H. Eppstein, L. M. Reineke, A. Weintraub, P. D. Meister, H. M. Leigh, *J. Am. Chem. Soc.* **1952**, *74*, 5933.

[49]   J. T. Groves, *Proc. Natl. Acad. Sci. U. S. A.* **2003**, *100*, 3569.

[50]   W. Liu, J. T. Groves, *J. Am. Chem. Soc.* **2010**, *132*, 12847.

[51]   W. Liu, J. T. Groves, *Acc. Chem. Res.* **2015**, *48*, 1727.

[52]   W. Liu, J. T. Groves, *Angew. Chem. Int. Ed.* **2013**, *52*, 6024.

[53]   W. Liu, X. Huang, J. T. Groves, *Nat. Protoc.* **2013**, *8*, 2348.

[54]   D. L. Zechel, S. P. Reid, O. Nashiru, C. Mayer, D. Stoll, D. L. Jakeman, R. A. J. Warren, S. G. Withers, *J. Am. Chem. Soc* **2001**, *123*, 4350.

[55]   D. O'Hagan, H. Deng, *Chem. Rev.* **2015**, *115*, 634.

[56]   D. O'Hagan, C. Schaffrath, S. L. Cobb, J. T. G. Hamilton, C. D. Murphy, *Nature* **2002**, *416*, 279.

[57]   H. M. Senn, D. O'Hagan, W. Thiel, *J. Am. Chem. Soc.* **2005**, *127*, 13643.

[58]   S. L. Neidleman, J. Geigert, *Endeavour* **1987**, *11*, 5.

[59]   J. Fauvarque, *Pure Appl. Chem.* **1996**, *68*, 1713.

[60]   P. Ratnasamy, A. P. Singh, in *Handb. Heterog. Catal.*, Wiley-VCH Verlag GmbH & Co. KGaA, Weinheim, Germany, **2008**, pp. 3564–3578.

[61]   H. A. Wittcoff, B. G. Reuben, J. S. Plotkin, *Industrial Organic Chemicals, 3rd Edition*, John Wiley & Sons, Inc., Hoboken, NJ, USA, **2013**.

[62]   S. Purser, P. R. Moore, S. Swallow, V. Gouverneur, *Chem. Soc. Rev.* **2008**, *37*, 320.

[63]   M. G. Campbell, T. Ritter, *Org. Process Res. Dev.* **2014**, *18*, 474.

[64]   S. P. Marsden, *Contemp. Org. Synth.* **1997**, *4*, 118.

[65]   C. Johansen, *Antimicrobial Composition Containing a Haloperoxidase, a Hydrogen Peroxide Source, a Halide Source and an Ammonium Source, US 6.818.212 B2*, **2004**.

[66]   B. E. Christensen, M. Allesen-Holm, M. Gjermansen, *Methods for Killing Spores and Disinfecting or Sterilizing Devices, US 2009/0104172 A1*, **2009**.

[67]   R. André, F. Natalio, W. Tremel, R. Wever, A. Hartog, *Use of Vanadium Pentoxide Particles as a Biocide, EP 2 671 449 A1*, **2015**.

[68]   N. F. Fischer, C. Dobner, M. Bräu, *Use of Vanadium-Containing Particles as Biocides, US 2016/0113283 A1*, **2016**.

[69]   M. Hofrichter, R. Ullrich, *Appl. Microbiol. Biotechnol.* **2006**, *71*, 276.

[70]   J. Littlechild, M. Isupov, in *Recent Adv. Redox Act. Plant Microb. Prod.* (Eds.: C. Jacob, G. Kirsch, A. Slusarenko, P.G. Winyard, T. Burkholz), Springer Netherlands, Dordrecht, **2014**, pp. 425–446.

[71]   R. Wever, H. L. Dekker, J. W. P. M. Van Schijndel, E. G. M. Vollenbroek, *Antifouling Paint Containing Haloperoxidases and Method to Determine Halide Concentrations, WO 1995/27009*, **1995**.

[72]   J. W. Blunt, B. R. Copp, R. A. Keyzers, M. H. G. Munro, M. R. Prinsep, *Nat. Prod. Rep.* **2015**, *32*, 116.

[73]   E. Shannon, N. Abu-Ghannam, *Mar. Drugs* **2016**, *14*, 81.

[74]   R. C. F. Cheung, T. B. Ng, J. H. Wong, Y. Chen, W. Y. Chan, *Appl. Microbiol. Biotechnol.* **2016**, *100*, 1645.

[75]   H. Malve, *J. Pharm. Bioallied Sci.* **2016**, *8*, 83.

[76]   A. M. S. Mayer, A. D. Rodríguez, O. Taglialatela-Scafati, N. Fusetani, *Mar. Drugs* **2013**, *11*, 2510.

[77]   A. M. Mayer, M. Nguyen, D. J. Newman, K. B. Glaser, *FASEB J.* **2016**, *30*.

[78]   J. W. Blunt, B. R. Copp, R. A. Keyzers, M. H. G. Munro, M. R. Prinsep, *Nat. Prod. Rep.* **2016**, *33*, 382.

[79]   H. S. Soedjak, J. V. Walker, A. Butler, *Biochemistry* **1995**, *34*, 12689.

[80]   D. Rehder, *Chemie unserer Zeit* **2010**, *44*, 322.

[81]   C. Leblanc, H. Vilter, J.-B. Fournier, L. Delage, P. Potin, E. Rebuffet, G. Michel, P. L. Solari, M. C. Feiters, M. Czjzek, *Coord. Chem. Rev.* **2015**, *301–302*, 134.

[82]   J. S. Martinez, G. L. Carroll, R. A. Tschirret-Guth, G. Altenhoff, R. D. Little, A. Butler, *J. Am. Chem. Soc.* **2001**, *123*, 3289.

[83]   F. H. Vaillancourt, E. Yeh, D. A. Vosburg, S. Garneau-Tsodikova, C. T. Walsh, *Chem. Rev.* **2006**, *106*, 3364.

[84]   U. von Gunten, *Water Res.* **2003**, *37*, 1443.

[85]   H. S. Soedjak, A. Butler, *Inorg. Chem.* **1990**, *29*, 5015.

[86]   D. C. Crans, J. J. Smee, E. Gaidamauskas, L. Yang, *Chem. Rev.* **2004**, *104*, 849.

[87]   G. Xu, B.-G. Wang, *PLoS One* **2016**, *11*, e0154619.

[88]   P. G. Furtmüller, M. Zederbauer, W. Jantschko, J. Helm, M. Bogner, C. Jakopitsch, C. Obinger, *Arch. Biochem. Biophys.* **2006**, *445*, 199.

[89]   J. P. Henderson, J. W. Heinecke, in *Handb. Environ. Chem.*, **2003**, pp. 201–214.

[90]   S. Banerjee, P. G. Furtmüller, C. Obinger, *Biotechnol. J.* **2011**, *6*, 231.

[91]   S. P. Porterfield, C. E. Hendrich, *Endocr. Rev.* **1993**, *14*, 94.

[92]   J. Arnhold, J. Flemmig, *Arch. Biochem. Biophys.* **2010**, *500*, 92.

[93]   C. C. Winterbourn, A. J. Kettle, *Free Radic. Biol. Med.* **2000**, *29*, 403.

[94]   C. C. Winterbourn, *Toxicology* **2002**, *181–182*, 223.

[95]   E. L. Thomas, M. B. Grisham, M. M. Jefferson, M. Margaret Jefferson, in *Methods Enzymol.*, **1986**, pp. 569–585.

[96]   E. L. Thomas, *Infect. Immun.* **1979**, *25*, 110.

[97]   A. G. J. Ligtenbarg, R. Hage, B. L. Feringa, *Coord. Chem. Rev.* **2003**, *237*, 89.

[98]   R. Renirie, C. Pierlot, J.-M. Aubry, A. F. Hartog, H. E. Schoemaker, P. L. Alsters, R. Wever, *Adv. Synth. Catal.* **2003**, *345*, 849.

[99]   A. U. Khan, *Biochem. Biophys. Res. Commun.* **1984**, *122*, 668.

[100] J. R. Kanofskys, H. Hoogland, R. Wever, S. J. Weiss, *J. Biol. Chem.* **1988**, *263*, 9692.

[101] H. Rosen, S. J. Klebanoff, *J. Biol. Chem.* **1977**, *252*, 4803.

[102] A. Butler, J. V Walker, *Chem. Rev.* **1993**, *93*, 1937.

[103] M. Weyand, H.-J. Hecht, M. Kieß, M.-F. Liaud, H. Vilter, D. Schomburg, *J. Mol. Biol.* **1999**, *293*, 595.

[104] R. R. Everett, H. S. Soedjak, A. Butler, *J. Biol. Chem.* **1990**, *265*, 15671.

[105] V. M. Dembitsky, *Tetrahedron* **2003**, *59*, 4701.

[106] C. S. Neumann, D. G. Fujimori, C. T. Walsh, *Chem. Biol.* **2008**, *15*, 99.

[107] A. Butler, J. N. Carter-Franklin, *Nat. Prod. Rep.* **2004**, *21*, 180.

[108] C. Wagner, M. El Omari, G. M. König, *J. Nat. Prod.* **2009**, *72*, 540.

[109] J. Geigert, T. D. Lee, D. J. Dalietos, D. S. Hirano, S. L. Neidleman, *Biochem. Biophys. Res. Commun.* **1986**, *136*, 778.

[110] H. Lund, L. Kalum, M. Hofrichter, P. Sebastian, *Epoxidation Using Peroxygenase, WO 2013/144105 A1*, **2013**.

[111] J. M. Albrich, C. A. McCarthy, J. K. Hurst, *Proc. Natl. Acad. Sci.* **1981**, *78*, 210.

[112] C. C. Winterbourn, *Biochim. Biophys. Acta* **1985**, *840*, 204.

[113] M. P. Lesser, *Annu. Rev. Physiol.* **2006**, *68*, 253.

[114] C. Leblanc, C. Colin, A. Cosse, L. Delage, S. La Barre, P. Morin, B. Fiévet, C. Voiseux, Y. Ambroise, E. Verhaeghe, D. Amouroux, O. Donard, E. Tessier, P. Potin, *Biochimie* **2006**, *88*, 1773.

[115] A. Wuosmaa, L. Hager, *Science* **1990**, *249*, 160.

[116] R. Wever, M. A. van der Horst, *Dalt. Trans.* **2013**, *42*, 11778.

[117] C. Paul, G. Pohnert, *Nat. Prod. Rep.* **2011**, *28*, 186.

[118] L. P. Hager, D. R. Morris, F. S. Brown, H. Eberwein, *J. Biol. Chem.* **1966**, *241*, 1769.

[119] K.-H. van Pée, *Arch. Microbiol.* **2001**, *175*, 250.

[120] N. Ohsawa, Y. Ogata, N. Okada, N. Itoh, *Phytochemistry* **2001**, *58*, 683.

[121] U. R. Thorenz, M. Kundel, L. Müller, T. Hoffmann, *Anal. Bioanal. Chem.* **2012**, *404*, 2177.

[122] J. N. Carter-Franklin, J. D. Parrish, R. A. Tschirret-Guth, R. D. Little, A. Butler, *J. Am. Chem. Soc.* **2003**, *125*, 3688.

[123] D. J. Faulkner, *Nat. Prod. Rep.* **1998**, *15*, 113.

[124] J. N. Carter-Franklin, A. Butler, *J. Am. Chem. Soc.* **2004**, *126*, 15060.

[125] D. G. Fujimori, C. T. Walsh, *Curr. Opin. Chem. Biol.* **2007**, *11*, 553.

[126] G. W. Gribble, *Chemosphere* **2003**, *52*, 289.

[127] S. J. Crockford, *Integr. Comp. Biol.* **2009**, *49*, 155.

[128] L. Wang, X. Zhou, M. Fredimoses, S. Liao, Y. Liu, *RSC Adv.* **2014**, *4*, 57350.

[129] J. Ihssen, M. Schubert, L. Thöny-Meyer, M. Richter, *PLoS One* **2014**, *9*, 1.

[130] C. M. Reddy, L. Xu, N. J. Drenzek, N. C. Sturchio, L. J. Heraty, C. Kimblin, A. Butler, *J. Am. Chem. Soc.* **2002**, *124*, 14526.

[131] G. W. Gribble, *Mar. Drugs* **2015**, *13*, 4044.

[132] J. M. Winter, M. C. Moffitt, E. Zazopoulos, J. B. McAlpine, P. C. Dorrestein, B. S. Moore, *J. Biol. Chem.* **2007**, *282*, 16362.

[133] A. Butler, M. Sandy, *Nature* **2009**, *460*, 848.

[134] M. Sundaramoorthy, J. Terner, T. L. Poulos, *Chem. Biol.* **1998**, *5*, 461.

[135] M. N. Isupov, A. R. Dalby, A. A. Brindley, Y. Izumi, T. Tanabe, G. N. Murshudov, J. A. Littlechild,

J. Mol. Biol. **2000**, *299*, 1035.

[136] N. Itoh, A. K. M. Q. Hasan, Y. Izumi, H. Yamada, *Eur. J. Biochem.* **1988**, *172*, 477.

[137] E. de Boer, R. Wever, *J. Biol. Chem.* **1988**, *263*, 12326.

[138] K. M. Manoj, *Biochim. Biophys. Acta* **2006**, *1764*, 1325.

[139] R. A. Tschirret-Guth, A. Butler, *J. Am. Chem. Soc.* **1994**, *116*, 411.

[140] H. B. Dunford, *Peroxidases and Catalases: Biochemistry, Biophysics, Biotechnology and Physiology*, **2010**.

[141] E. I. Solomon, A. Decker, N. Lehnert, *Proc. Natl. Acad. Sci.* **2003**, *100*, 3589.

[142] L. C. Blasiak, F. H. Vaillancourt, C. T. Walsh, C. L. Drennan, *Nature* **2006**, *440*, 368.

[143] A. K. Vardhaman, P. Barman, S. Kumar, C. V. Sastri, D. Kumar, S. P. de Visser, *Chem. Commun.* **2013**, *49*, 10926.

[144] M. Sundaramoorthy, J. Terner, T. L. Poulos, *Structure* **1995**, *3*, 1367.

[145] K. Kühnel, W. Blankenfeldt, J. Terner, I. Schlichting, *J. Biol. Chem.* **2006**, *281*, 23990.

[146] J. W. P. M. Schijndel, P. Barnett, J. Roelse, E. G. M. Vollenbroek, R. Wever, *Eur. J. Biochem.* **1994**, *225*, 151.

[147] M. Sandy, J. N. Carter-Franklin, J. D. Martin, A. Butler, *Chem. Commun.* **2011**, *47*, 12086.

[148] J. M. Winter, B. S. Moore, *J. Biol. Chem.* **2009**, *284*, 18577.

[149] Z. Hasan, R. Renirie, R. Kerkman, H. J. Ruijssenaars, A. F. Hartog, R. Wever, *J. Biol. Chem.* **2006**, *281*, 9738.

[150] J. N. Carter, K. E. Beatty, M. T. Simpson, A. Butler, *J. Inorg. Biochem.* **2002**, *91*, 59.

[151] W. Hemrika, R. Renirie, S. Macedo-Ribeiro, A. Messerschmidt, R. Wever, *J. Biol. Chem.* **1999**, *274*, 23820.

[152] R. Wever, R. Renirie, in *Peroxidases Catalases Biochem. Biophys. Biotechnol. Physiol.*, **2010**, pp. 363–385.

[153] R. Gupta, G. Hou, R. Renirie, R. Wever, T. Polenova, *J. Am. Chem. Soc.* **2015**, *137*, 5618.

[154] G. Zampella, P. Fantucci, V. L. Pecoraro, L. De Gioia, *Inorg. Chem.* **2006**, *45*, 7133.

[155] G. Zampella, J. Y. Kravitz, C. E. Webster, P. Fantucci, M. B. Hall, H. a. Carlson, V. L. Pecoraro, L. De Gioia, *Inorg. Chem.* **2004**, *43*, 4127.

[156] U. von Gunten, Y. Oliveras, *Environ. Sci. Technol.* **1998**, *32*, 63.

[157] M. J. Clague, A. Butler, *J. Am. Chem. Soc.* **1995**, *117*, 3475.

[158] P. Barnett, D. H. Hondmann, S. Lambertus Henricus, P. F. Ter Steeg, R. Wever, *Enzymatic Antimicrobial Compositions, WO 1995/27046*, **1995**.

[159] C. Johansen, *Antimicrobial Peroxidase Compositions, WO 1997/42825*, **1997**.

[160] C. Johansen, C. C. Fuglsang, *Enzymatic Preservation of Water Based Paints, US 7.063.970 B1*, **2006**.

[161] B. A. Annous, P. M. Fratamico, J. L. Smith, *J. Food Sci.* **2009**, *74*, R24.

[162] M. R. Detty, R. Ciriminna, F. V. Bright, M. Pagliaro, *Acc. Chem. Res.* **2014**, *47*, 678.

[163] F. W. Y. Myan, J. Walker, O. Paramor, *Biointerphases* **2013**, *8*, 30.

[164] T. B. Rasmussen, M. Manefield, J. B. Andersen, L. Eberl, U. Anthoni, C. Christophersen, P. Steinberg, S. Kjelleberg, M. Givskov, *Microbiology* **2000**, *146*, 3237.

[165] L. Gram, R. de Nys, R. Maximilien, M. Givskov, P. Steinberg, S. Kjelleberg, *Appl. Environ. Microbiol.* **1996**, *62*, 4284.

[166] S. Dobretsov, M. Teplitski, V. Paul, *Biofouling* **2009**, *25*, 413.

[167] S. Kjelleberg, P. Steinberg, M. Givskov, L. Gram, M. Manefield, R. De Nys, *Aquat. Microb. Ecol.* **1997**, *13*, 85.

[168] D. Smith, J.-H. Wang, J. E. Swatton, P. Davenport, B. Price, H. Mikkelsen, H. Stickland, K. Nishikawa, N. Gardiol, D. R. Spring, M. Welch, *Sci. Prog.* **2006**, *89*, 167.

[169] A. W. Decho, R. L. Frey, J. L. Ferry, *Chem. Rev.* **2011**, *111*, 86.

[170] S. R. Chhabra, B. Philipp, L. Eberl, M. Givskov, P. Williams, M. Cámara, in *Top. Curr. Chem.*, Springer-Verlag Berlin Heidelberg, **2005**, pp. 279–315.

[171] M. E. Shirtliff, J. T. Mader, A. K. Camper, *Chem. Biol.* **2002**, *9*, 859.

[172] T. Schwartz, S. Walter, S.-M. Marten, F. Kirschhöfer, M. Nusser, U. Obst, *Anal. Bioanal. Chem.* **2007**, *387*, 513.

[173] C. Fuqua, S. C. Winans, E. P. Greenberg, *Annu. Rev. Microbiol.* **1996**, *50*, 727.

[174] B. L. Bassler, M. Wright, M. R. Silverman, *Mol. Microbiol.* **1994**, *12*, 403.

[175] M. Thoendel, J. S. Kavanaugh, C. E. Flack, A. R. Horswill, *Chem. Rev.* **2011**, *111*, 117.

[176] J. Nakayama, Y. Cao, T. Horii, S. Sakuda, A. D. L. Akkermans, W. M. De Vos, H. Nagasawa, *Mol. Microbiol.* **2001**, *41*, 145.

[177] L. S. Håvarstein, G. Coomaraswamy, D. A. Morrison, *Proc. Natl. Acad. Sci. U. S. A.* **1995**, *92*,

11140.

[178] J. Rocha-Estrada, A. E. Aceves-Diez, G. Guarneros, M. De La Torre, *Appl. Microbiol. Biotechnol.* **2010**, *87*, 913.

[179] S. Schauder, K. Shokat, M. G. Surette, B. L. Bassler, *Mol. Microbiol.* **2001**, *41*, 463.

[180] X. Chen, S. Schauder, N. Potier, A. Van Dorsselaer, I. Pelczer, B. L. Bassler, F. M. Hughson, *Nature* **2002**, *415*, 545.

[181] M. B. Neiditch, M. J. Federle, A. J. Pompeani, R. C. Kelly, D. L. Swem, P. D. Jeffrey, B. L. Bassler, F. M. Hughson, *Cell* **2006**, *126*, 1095.

[182] M. E. Taga, S. T. Miller, B. L. Bassler, *Mol. Microbiol.* **2003**, *50*, 1411.

[183] S. Dobretsov, R. M. M. Abed, M. Teplitski, *Biofouling* **2013**, *29*, 423.

[184] S. A. Borchardt, E. J. Allain, J. J. Michels, G. W. Stearns, R. F. Kelly, W. F. McCoy, *Appl. Environ. Microbiol.* **2001**, *67*, 3174.

[185] M. Manefield, R. de Nys, N. Kumar, R. Read, M. Givskov, P. Steinberg, S. Kjelleberg, *Microbiology* **1999**, *145*, 283.

[186] D. Ren, L. A. Bedzyk, R. W. Ye, S. M. Thomas, T. K. Wood, *Biotechnol. Bioeng.* **2004**, *88*, 630.

[187] T. Zang, B. W. K. Lee, L. M. Cannon, K. A. Ritter, S. Dai, D. Ren, T. K. Wood, Z. S. Zhou, *Bioorg. Med. Chem. Lett.* **2009**, *19*, 6200.

[188] J. J. Michels, E. J. Allain, S. A. Borchardt, P. Hu, W. F. McCoy, *J. Chromatogr. A* **2000**, *898*, 153.

[189] J. C. Slaughter, *Biol. Rev.* **1999**, *74*, 259.

[190] D. Martinelli, G. Grossmann, U. Séquin, H. Brandl, R. Bachofen, *BMC Microbiol.* **2004**, *4*, 25.

[191] K. B. Xavier, B. L. Bassler, *Curr. Opin. Microbiol.* **2003**, *6*, 191.

[192] M. Manefield, T. B. Rasmussen, M. Henzter, J. B. Andersen, P. Steinberg, S. Kjelleberg, M. Givskov, *Microbiology* **2002**, *148*, 1119.

[193] F. Pantanella, F. Berlutti, C. Passariello, S. Sarli, C. Morea, S. Schippa, *J. Appl. Microbiol.* **2007**, *102*, 992.

[194] K. H. McClean, M. K. Winson, L. Fish, A. Taylor, S. R. Chhabra, M. Camara, M. Daykin, J. H. Lamb, S. Swift, B. W. Bycroft, G. S. A. B. Stewart, P. Williams, *Microbiology* **1997**, *143*, 3703.

[195] S. A. Burt, V. T. A. Ojo-Fakunle, J. Woertman, E. J. A. Veldhuizen, *PLoS One* **2014**, *9*, e93414.

[196] H. P. Steenackers, J. Levin, J. C. Janssens, A. De Weerdt, J. Balzarini, J. Vanderleyden, D. E. De Vos, S. C. De Keersmaecker, *Bioorganic Med. Chem.* **2010**, *18*, 5224.

[197] M. Syrpas, E. Ruysbergh, L. Blommaert, B. Vanelslander, K. Sabbe, W. Vyverman, N. De Kimpe, S. Mangelinckx, *Mar. Drugs* **2014**, *12*, 352.

[198] V. C. Kalia, *Quorum Sensing vs Quorum Quenching: A Battle with No End in Sight*, Springer India, New Delhi, **2015**.

[199] N. Fusetani, A. S. Clare, *Antifouling Compounds*, Springer Berlin Heidelberg, Berlin, Heidelberg, **2006**.

[200] K.-H. van Pée, in *Methods Enzymol.*, **2012**, pp. 237–257.

[201] S. Dobretsov, H.-U. Dahms, P.-Y. Qian, *Biofouling* **2006**, *22*, 43.

[202] S. Dobretsov, M. Teplitski, M. Bayer, S. Gunasekera, P. Proksch, V. J. Paul, *Biofouling* **2011**, *27*, 893.

[203] S. Dobretsov, H.-U. Dahms, H. YiLi, M. Wahl, P.-Y. Qian, *FEMS Microbiol. Ecol.* **2007**, *60*, 177.

[204] A. Camilli, B. L. Bassler, *Science* **2006**, *311*, 1113.

[205] T. B. Rasmussen, M. Givskov, *Int. J. Med. Microbiol.* **2006**, *296*, 149.

[206] R. J. Worthington, J. J. Richards, C. Melander, *Org. Biomol. Chem.* **2012**, *10*, 7457.

[207] A. Pal, M. C. Kamthania, A. Kumar, *Open Access Libr. J.* **2014**, *1*, 1.

[208] V. C. Kalia, *Biotechnol. Adv.* **2013**, *31*, 224.

[209] E. Cartagena, O. Á. Colom, A. Neske, J. C. Valdez, A. Bardón, *Chem. Pharm. Bull.* **2007**, *55*, 22.

[210] A. G. Palmer, A. C. Senechal, A. Mukherjee, J.-M. Ané, H. E. Blackwell, *ACS Chem. Biol.* **2014**, *9*, 1834.

[211] D. T. Hughes, V. Sperandio, *Nat. Rev. Microbiol.* **2008**, *6*, 111.

[212] S. Uroz, J. Heinonsalo, *FEMS Microbiol. Ecol.* **2008**, *65*, 271.

[213] E. Verhaeghe, D. Buisson, E. Zekri, C. Leblanc, P. Potin, Y. Ambroise, *Anal. Biochem.* **2008**, *379*, 60.

[214] A. Jerlich, S. Tschabuschnig, J. S. Fabjan, R. J. Schaur, *Int. J. Clin. Lab. Res.* **2000**, *30*, 33.

[215] A. R. J. Bakkenist, J. E. G. De Boer, H. Plat, R. Wever, *Biochim. Biophys. Acta* **1980**, *613*, 337.

[216] C. Wagner, I. M. Molitor, G. M. König, *Phytochemistry* **2008**, *69*, 323.

[217] P. J. Hansen, J. H. Espenson, *Inorg. Chem.* **1995**, *34*, 5839.

[218] B. W. Griffin, P. L. Ashley, *Arch. Biochem. Biophys.* **1984**, *233*, 188.

[219] B. W. Griffin, *Biochem. Biophys. Res. Commun.* **1983**, *116*, 873.

[220] J. M. Dypbukt, C. Bishop, W. M. Brooks, B. Thong, H. Eriksson, A. J. Kettle, *Free Radic. Biol. Med.* **2005**, *39*, 1468.

[221] "http://www.sigmaaldrich.com/catalog/product/fluka/32661?lang=de&region=DE," **2016**.

[222] "http://www.sigmaaldrich.com/catalog/product/sial/114545?lang=de&region=DE," **2016**.

[223] "http://www.sigmaaldrich.com/catalog/product/sial/114391?lang=de&region=DE," **2016**.

[224] "http://www.sigmaaldrich.com/catalog/product/sial/114413?lang=de&region=DE," **2016**.

[225] M. C. Terrón, F. J. M. Verhagen, M. C. R. Franssen, J. A. Field, *Chemosphere* **1998**, *36*, 1445.

[226] A. V. S. Rao, H. N. Ravishankar, T. Ramasarma, *Arch. Biochem. Biophys.* **1996**, *334*, 121.

[227] K. Herget, P. Hubach, S. Pusch, P. Deglmann, H. Götz, T. E. Gorelik, I. A. Gural'skiy, F. Pfitzner, T. Link, S. Schenk, M. Panthöfer, V. Ksenofontov, U. Kolb, T. Opatz, R. André, W. Tremel, *Adv. Mater.* **2017**, *29*, 1603823.

[228] K. Debowska, D. Debski, M. Hardy, M. Jakubowska, B. Kalyanaraman, A. Marcinek, R. Michalski, B. Michalowski, O. Ouari, A. Sikora, R. Smulik, J. Zielonka, *Pharmacol. Reports* **2015**, *67*, 756.

[229] P. Wardman, *Free Radic. Biol. Med.* **2007**, *43*, 995.

[230] C. C. Winterbourn, *Biochim. Biophys. Acta* **2014**, *1840*, 730.

[231] J. Flemmig, J. Zschaler, J. Remmler, J. Arnhold, *J. Biol. Chem.* **2012**, *287*, 27913.

[232] V. M. Martínez, G. De Cremer, M. B. J. Roeffaers, M. Sliwa, M. Baruah, D. E. De Vos, J. Hofkens, B. F. Sels, *J. Am. Chem. Soc.* **2008**, *130*, 13192.

[233] X. Jin, L. Hao, Y. Hu, M. She, Y. Shi, M. Obst, J. Li, Z. Shi, *Sensors Actuators B Chem.* **2013**, *186*, 56.

[234] X. Chen, K.-A. Lee, E.-M. Ha, K. M. Lee, Y. Y. Seo, H. K. Choi, H. N. Kim, M. J. Kim, C.-S. Cho, S. Y. Lee, W.-J. Lee, J. Yoon, *Chem. Commun.* **2011**, *47*, 4373.

[235] K.-A. Lee, S.-H. Kim, E.-K. Kim, E.-M. Ha, H. You, B. Kim, M.-J. Kim, Y. Kwon, J.-H. Ryu, W.-J. Lee, *Cell* **2013**, *153*, 797.

[236] W. Lin, L. Long, B. Chen, W. Tan, *Chem. Eur. J.* **2009**, *15*, 2305.

[237] R. C. Allen, *Haloperoxidase Acid Optimum Chemiluminescence Assay System, WO 1991005063 A1*, **1991**.

[238] M.-H. Zheng, X. Hu, X.-W. Wang, X.-L. Liu, J.-Y. Jin, *J. Fluoresc.* **2016**, *26*, 593.

[239] B. Kalyanaraman, V. Darley-Usmar, K. J. A. Davies, P. A. Dennery, H. J. Forman, M. B. Grisham, G. E. Mann, K. Moore, L. J. Roberts, H. Ischiropoulos, *Free Radic. Biol. Med.* **2012**, *52*, 1.

[240] J. Flemmig, J. Arnhold, *J. Inorg. Biochem.* **2010**, *104*, 759.

[241] E. L. Thomas, P. M. Bozeman, M. M. Jefferson, C. C. King, *J. Biol. Chem.* **1995**, *270*, 2906.

[242] M. Koelsch, R. Mallak, G. G. Graham, T. Kajer, M. K. Milligan, L. Q. Nguyen, D. W. Newsham, J. S. Keh, A. J. Kettle, K. F. Scott, J. B. Ziegler, D. I. Pattison, S. Fu, C. L. Hawkins, M. D. Rees, M. J. Davies, *Biochem. Pharmacol.* **2010**, *79*, 1156.

[243] A. V. Peskin, C. C. Winterbourn, *Free Radic. Biol. Med.* **2001**, *30*, 572.

[244] A. J. Kettle, *FEBS Lett.* **1996**, *379*, 103.

[245] A. J. Kettle, A. M. Albrett, A. L. Chapman, N. Dickerhof, L. V. Forbes, I. Khalilova, R. Turner, *Biochim. Biophys. Acta* **2014**, *1840*, 781.

[246] A. V. Sokolov, V. A. Kostevich, S. O. Kozlov, I. S. Donskyi, I. I. Vlasova, A. O. Rudenko, E. T. Zakharova, V. B. Vasilyev, O. M. Panasenko, *Free Radic. Res.* **2015**, *49*, 777.

[247] G. J. Colpas, B. J. Hamstra, J. W. Kampf, V. L. Pecoraro, *J. Am. Chem. Soc.* **1996**, *118*, 3469.

[248] D. Wischang, O. Brücher, J. Hartung, *Coord. Chem. Rev.* **2011**, *255*, 2204.

[249] K. Yonehara, K. Kamata, K. Yamaguchi, N. Mizuno, *Chem. Commun.* **2011**, *47*, 1692.

[250] N. Kato, Y. Hayashi, *Dalt. Trans.* **2013**, *42*, 11804.

[251] G. Licini, V. Conte, A. Coletti, M. Mba, C. Zonta, *Coord. Chem. Rev.* **2011**, *255*, 2345.

[252] J. A. L. da Silva, J. J. R. F. da Silva, A. J. L. Pombeiro, *Coord. Chem. Rev.* **2011**, *255*, 2232.

[253] M. J. Clague, N. L. Keder, A. Butler, *Inorg. Chem.* **1993**, *32*, 4754.

[254] S. Rana, R. Haque, G. Santosh, D. Maiti, *Inorg. Chem.* **2013**, *52*, 2927.

[255] T. S. Smith, V. L. Pecoraro, *Inorg. Chem.* **2002**, *41*, 6754.

[256] H. B. ten Brink, H. E. Schoemaker, R. Wever, *Eur. J. Biochem.* **2001**, *268*, 132.

[257] H. B. ten Brink, A. Tuynman, H. L. Dekker, W. Hemrika, Y. Izumi, T. Oshiro, H. E. Schoemaker, R. Wever, *Inorg. Chem.* **1998**, *37*, 6780.

[258] Z. Strassberger, E. V Ramos-Fernandez, A. Boonstra, R. Jorna, S. Tanase, G. Rothenberg, *Dalt. Trans.* **2013**, *42*, 5546.

[259] H. Mimoun, L. Saussine, E. Daire, M. Postel, J. Fischer, R. Weiss, *J. Am. Chem. Soc.* **1983**, *105*, 3101.

[260] S. Velusamy, T. Punniyamurthy, *Org. Lett.* **2004**, *6*, 217.

[261] T. K. Si, M. G. B. Drew, K. K. Mukherjea, *Polyhedron* **2011**, *30*, 2286.

[262]   C. Chen, Q. Sun, D.-X. Ren, R. Zhang, F.-Y. Bai, Y.-H. Xing, Z. Shi, *CrystEngComm* **2013**, *15*, 5561.

[263]   R. Zhang, J. Liu, C. Chen, Y.-H. Xing, Q.-L. Guan, Y.-N. Hou, X. Wang, X.-X. Zhang, F.-Y. Bai, *Spectrochim. Acta Part A Mol. Biomol. Spectrosc.* **2013**, *115*, 476.

[264]   T. L. Fernández, E. T. Souza, L. C. Visentin, J. V. Santos, A. S. Mangrich, R. B. Faria, O. A. C. Antunes, M. Scarpellini, *J. Inorg. Biochem.* **2009**, *103*, 474.

[265]   Y.-Z. Cao, H.-Y. Zhao, F.-Y. Bai, Y.-H. Xing, D.-M. Wei, S.-Y. Niu, Z. Shi, *Inorganica Chim. Acta* **2011**, *368*, 223.

[266]   R. M. Tótaro, P. a. M. Williams, M. C. Apella, M. a. Blesa, E. J. Baran, *J. Chem. Soc. Dalt. Trans.* **2000**, 4403.

[267]   A. T. Khan, S. Ali, *Bull. Chem. Soc. Jpn.* **2012**, *85*, 1239.

[268]   L. Saikia, D. Talukdar, R. C. Deka, A. J. Thakur, *J. Heterocycl. Chem.* **2013**, *50*, 1031.

[269]   C. U. Dinesh, R. Kumar, B. Pandey, P. Kumar, *J. Chem. Soc. Chem. Commun.* **1995**, *20*, 611.

[270]   K. Kikushima, T. Moriuchi, T. Hirao, *Chem. Asian J.* **2009**, *4*, 1213.

[271]   K. Kikushima, T. Moriuchi, T. Hirao, *Tetrahedron* **2010**, *66*, 6906.

[272]   A. Podgoršek, M. Zupan, J. Iskra, *Angew. Chem. Int. Ed.* **2009**, *48*, 8424.

[273]   G. E. Meister, A. Butler, *Inorg. Chem.* **1994**, *33*, 3269.

[274]   N. S. Islam, J. J. Boruah, *J. Chem. Sci.* **2015**, *127*, 777.

[275]   F. L. Assem, L. S. Levy, *J. Toxicol. Environ. Heal. Part B* **2009**, *12*, 289.

[276]   ECHA, "https://Echa.Europa.Eu/Home (12/12/16)," **2016**.

[277]   B. M. Choudary, Y. Sudha, P. N. Reddy, *Synlett* **1994**, *1994*, 450.

[278]   V. Conte, B. Floris, P. Galloni, A. Silvagni, *Adv. Synth. Catal.* **2005**, *347*, 1341.

[279]   F. Romano, A. Linden, M. Mba, C. Zonta, G. Licini, *Adv. Synth. Catal.* **2010**, *352*, 2937.

[280]   S. K. Kurapati, S. Pal, *Appl. Organomet. Chem.* **2016**, *30*, 116.

[281]   S. Pasayat, S. P. Dash, S. Roy, R. Dinda, S. Dhaka, M. R. Maurya, W. Kaminsky, Y. P. Patil, M. Nethaji, *Polyhedron* **2014**, *67*, 1.

[282]   P. Beinker, J. R. Hanson, N. Meindl, I. C. R. Medina, *J. Chem. Res.* **1998**, 204.

[283]   I. C. R. Medina, J. R. Hanson, *J. Chem. Res.* **2003**, *62*, 428.

[284]   P. Hazarika, D. Kalita, S. Sarmah, R. Borah, N. S. Islam, *Polyhedron* **2006**, *25*, 3501.

[285]   N. Mizuno, K. Kamata, K. Yamaguchi, *Catal. Today* **2012**, *185*, 157.

[286]   T. Yamaura, K. Kamata, K. Yamaguchi, N. Mizuno, *Catal. Today* **2013**, *203*, 76.

[287]   S.-S. Wang, G.-Y. Yang, *Chem. Rev.* **2015**, *115*, 4893.

[288]   M. R. Maurya, L. Rana, F. Avecilla, *Inorganica Chim. Acta* **2016**, *440*, 172.

[289]   E. Badetti, F. Romano, L. Marchiò, S. Taşkesenlioğlu, A. Daştan, C. Zonta, G. Licini, *Dalt. Trans.* **2016**, *45*, 14603.

[290]   M. Jafarzadeh, K. Amani, F. Nikpour, *Can. J. Chem.* **2005**, *83*, 1808.

[291]   J. H. Espenson, Z. Zhu, T. H. Zauche, *J. Org. Chem.* **1999**, *64*, 1191.

[292]   W. Adam, C. Mock-Knoblauch, C. R. Saha-Möller, M. Herderich, *J. Am. Chem. Soc.* **2000**, *122*, 9685.

[293]   J. R. Carney, B. R. Dillon, S. P. Thomas, *European J. Org. Chem.* **2016**, *2016*, 3912.

[294]   X. D. Feng, R. Zhang, X. Y. Wang, X. X. Zhang, J. X. Wang, Y. H. Xing, L. X. Sun, *Polyhedron* **2015**, *90*, 69.

[295]   S. M. Paraskevas, M. S. Paraskevas, *Catal. Commun.* **2004**, *5*, 687.

[296]   L. Menini, E. V. Gusevskaya, *Appl. Catal. A Gen.* **2006**, *309*, 122.

[297]   L. Menini, L. A. Parreira, E. V. Gusevskaya, *Tetrahedron Lett.* **2007**, *48*, 6401.

[298]   A. M. Suess, M. Z. Ertem, C. J. Cramer, S. S. Stahl, *J. Am. Chem. Soc.* **2013**, *135*, 9797.

[299]   L. Yang, Z. Lu, S. S. Stahl, *Chem. Commun.* **2009**, 6460.

[300]   W. Hao, Y. Liu, *Beilstein J. Org. Chem.* **2015**, *11*, 2132.

[301]   A. van der Werf, N. Selander, *Org. Lett.* **2015**, *17*, 6210.

[302]   X. Zhu, S. Chiba, *Chem. Soc. Rev.* **2016**, *45*, 4504.

[303]   A.-H. Liu, L.-N. He, F. Hua, Z.-Z. Yang, C.-B. Huang, B. Yu, B. Li, *Adv. Synth. Catal.* **2011**, *353*, 3187.

[304]   A.-H. Liu, R. Ma, M. Zhang, L.-N. He, *Catal. Today* **2012**, *194*, 38.

[305]   Y. Luo, X. Pan, J. Wu, *Tetrahedron Lett.* **2010**, *51*, 6646.

[306]   F.-Q. Huang, J. Xie, J.-G. Sun, Y.-W. Wang, X. Dong, L.-W. Qi, B. Zhang, *Org. Lett.* **2016**, *18*, 684.

[307]   C. Limberg, J. H. Teles, *Adv. Synth. Catal.* **2001**, *343*, 447.

[308]   C. Bonaccorsi, M. Althaus, C. Becker, A. Togni, A. Mezzetti, *Pure Appl. Chem.* **2006**, *78*, 391.

[309]   Y. Wang, G.-X. Li, G. Yang, G. He, G. Chen, *Chem. Sci.* **2016**, *7*, 2679.

[310] R. J. Field, E. Körös, R. M. Noyes, *J. Am. Chem. Soc.* **1972**, *94*, 8649.
[311] R. M. Noyes, J.-J. Jwo, *J. Am. Chem. Soc.* **1975**, *97*, 5431.
[312] J. Asakura, M. J. Robins, *J. Org. Chem.* **1990**, *55*, 4928.
[313] V. Nair, S. B. Panicker, A. Augustine, T. G. George, S. Thomas, M. Vairamani, *Tetrahedron* **2001**, *57*, 7417.
[314] A. E. Schweizer, M. E. Jones, D. A. Hickman, *Oxidative Halogenation and Optional Dehydrogenation of C3+ Hydrocarbons, US 2004/0158110 A1*, **2004**.
[315] V. Sridharan, J. C. Menéndez, *Chem. Rev.* **2010**, *110*, 3805.
[316] R. S. Babu, *Synlett* **2002**, *11*, 1935.
[317] B. Das, M. Krishnaiah, K. Venkateswarlu, V. S. Reddy, *Tetrahedron Lett.* **2007**, *48*, 81.
[318] H. Firouzabadi, N. Iranpoor, S. Kazemi, A. Ghaderi, A. Garzan, *Adv. Synth. Catal.* **2009**, *351*, 1925.
[319] A. K. Vardhaman, C. V. Sastri, D. Kumar, S. P. de Visser, *Chem. Commun.* **2011**, *47*, 11044.
[320] D. Vione, V. Maurino, S. C. Man, S. Khanra, C. Arsene, R.-I. Olariu, C. Minero, *ChemSusChem* **2008**, *1*, 197.
[321] A. Draksharapu, D. Angelone, M. G. Quesne, S. K. Padamati, L. Gómez, R. Hage, M. Costas, W. R. Browne, S. P. de Visser, *Angew. Chem. Int. Ed.* **2015**, *54*, 4357.
[322] R. Ma, C.-B. Huang, A.-H. Liu, X.-D. Li, L.-N. He, *Catal. Sci. Technol.* **2014**, *4*, 4308.
[323] T. Miyake, M. Hanaya, *Appl. Catal. A Gen.* **1995**, *121*, L13.
[324] D. Kalyani, A. R. Dick, W. Q. Anani, M. S. Sanford, *Tetrahedron* **2006**, *62*, 11483.
[325] T. W. Lyons, M. S. Sanford, *Chem. Rev.* **2010**, *110*, 1147.
[326] B. Du, X. Jiang, P. Sun, *J. Org. Chem.* **2013**, *78*, 2786.
[327] X. Peng, X.-F. Shao, Z.-Q. Liu, *Tetrahedron Lett.* **2013**, *54*, 3079.
[328] S. Liu, J. Chen, R. Zhang, F. Zhao, G.-J. Deng, *Asian J. Org. Chem.* **2014**, *3*, 1150.
[329] H.-Y. Xiong, D. Cahard, X. Pannecoucke, T. Besset, *European J. Org. Chem.* **2016**, *2016*, 3625.
[330] L. Wang, S.-S. Wang, G. VO-Thanh, Y. Liu, *J. Mol. Catal. A Chem.* **2013**, *371*, 56.
[331] D. P. Das, K. Parida, *Catal. Commun.* **2006**, *7*, 68.
[332] A. Maniatakou, S. Parsons, A. Karaliota, *J. Photochem. Photobiol. A Chem.* **2007**, *192*, 29.
[333] U. Bora, M. K. Chaudhuri, D. Dey, S. S. Dhar, *Pure Appl. Chem.* **2001**, *73*, 93.
[334] C. Liu, H. Zhang, W. Shi, A. Lei, *Chem. Rev.* **2011**, *111*, 1780.
[335] I. P. Beletskaya, D. I. Makhon'kov, *Russ. Chem. Rev.* **1981**, *50*, 534.
[336] D. A. Petrone, J. Ye, M. Lautens, *Chem. Rev.* **2016**, *116*, 8003.
[337] J. Nath, M. K. Chaudhuri, *Green Chem. Lett. Rev.* **2008**, *1*, 223.
[338] R. Lin, Y. Ding, L. Gong, J. Li, W. Chen, L. Yan, Y. Lu, *Appl. Catal. A Gen.* **2009**, *353*, 87.
[339] S. Wan, S. R. Wang, W. Lu, *J. Org. Chem.* **2006**, *71*, 4349.
[340] M. J. Earle, S. B. Katdare, *Oxidative Halogenation of Aromatic Compound, US 7084317 B2*, **2006**.
[341] K. A. Leonard, F. Zhou, M. R. Detty, *Organometallics* **1996**, *15*, 4285.
[342] M. D. Drake, M. A. Bateman, M. R. Detty, *Organometallics* **2003**, *22*, 4158.
[343] S. R. Mellegaard-Waetzig, C. Wang, J. A. Tunge, *Tetrahedron* **2006**, *62*, 7191.
[344] S. J. Balkrishna, C. D. Prasad, P. Panini, M. R. Detty, D. Chopra, S. Kumar, *J. Org. Chem.* **2012**, *77*, 9541.
[345] M. R. Detty, F. Zhou, A. E. Friedman, *J. Am. Chem. Soc.* **1996**, *118*, 313.
[346] M. R. Detty, D. E. Higgs, M. I. Nelen, *Org. Lett.* **2001**, *3*, 349.
[347] M. Abe, Y. You, M. R. Detty, *Organometallics* **2002**, *21*, 4546.
[348] E. E. Alberto, L. M. Muller, M. R. Detty, *Organometallics* **2014**, *33*, 5571.
[349] G. Shul'pin, *Catalysts* **2016**, *6*, 50.
[350] J. F. Hartwig, M. A. Larsen, *ACS Cent. Sci.* **2016**, *2*, 281.
[351] A. M. R. Smith, K. K. (Mimi) Hii, *Chem. Rev.* **2011**, *111*, 1637.
[352] J. Hagen, *Industrial Catalysis: A Practical Approach, Third Edition*, Wiley-VCH Verlag GmbH & Co. KGaA, Weinheim, Germany, **2015**.
[353] J. M. Woodley, *Trends Biotechnol.* **2008**, *26*, 321.
[354] R. N. Patel, *Coord. Chem. Rev.* **2008**, *252*, 659.
[355] S. A. Ansari, Q. Husain, *Biotechnol. Adv.* **2012**, *30*, 512.
[356] C.-H. Lee, T.-S. Lin, C.-Y. Mou, *Nano Today* **2009**, *4*, 165.
[357] L. Betancor, H. R. Luckarift, *Trends Biotechnol.* **2008**, *26*, 566.
[358] R. Andre, M. N. Tahir, F. Natalio, W. Tremel, *FEBS J.* **2012**, *279*, 1737.
[359] K. Drauz, H. Gröger, O. May, *Enzyme Catalysis in Organic Synthesis, Third Edition*, Wiley-VCH Verlag GmbH & Co. KGaA, Weinheim, Germany, **2012**.
[360] O. Kirk, T. V. Borchert, C. C. Fuglsang, *Curr. Opin. Biotechnol.* **2002**, *13*, 345.
[361] J. P. Rasor, E. Voss, *Appl. Catal. A Gen.* **2001**, *221*, 145.

[362]   J. L. Adrio, A. L. Demain, *Biomolecules* **2014**, *4*, 117.

[363]   D. R. Smith, S. Grüschow, R. J. Goss, *Curr. Opin. Chem. Biol.* **2013**, *17*, 276.

[364]   S. Brown, S. E. O'Connor, *ChemBioChem* **2015**, *16*, 2129.

[365]   A. Schmid, J. S. Dordick, B. Hauer, A. Kiener, M. Wubbolts, B. Witholt, *Nature* **2001**, *409*, 258.

[366]   C. Mateo, J. M. Palomo, G. Fernandez-Lorente, J. M. Guisan, R. Fernandez-Lafuente, *Enzyme Microb. Technol.* **2007**, *40*, 1451.

[367]   P. V. Iyer, L. Ananthanarayan, *Process Biochem.* **2008**, *43*, 1019.

[368]   L. Que, W. B. Tolman, *Nature* **2008**, *455*, 333.

[369]   Y. Lu, N. Yeung, N. Sieracki, N. M. Marshall, *Nature* **2009**, *460*, 855.

[370]   A. J. Kirby, F. Hollfelder, *From Enzyme Models to Model Enzymes*, Royal Society Of Chemistry, Cambridge, **2009**.

[371]   C. G. Bezzu, M. Helliwell, J. E. Warren, D. R. Allan, N. B. McKeown, *Science* **2010**, *327*, 1627.

[372]   B. A. Grzybowski, W. T. S. Huck, *Nat. Nanotechnol.* **2016**, *11*, 585.

[373]   G. Rothenberg, in *Catal. Concepts Green Appl.*, Wiley-VCH Verlag GmbH & Co. KGaA, Weinheim, Germany, **2008**, pp. 1–38.

[374]   R. André, F. Natálio, W. Tremel, in *New Futur. Dev. Catal. Catal. by Nanoparticles*, Elsevier, **2013**, pp. 149–173.

[375]   O. Deutschmann, H. Knözinger, K. Kochloefl, T. Turek, in *Ullmann's Encycl. Ind. Chem.*, Wiley-VCH Verlag GmbH & Co. KGaA, Weinheim, Germany, **2009**, p. 110.

[376]   Z. Wang, K. Ding, Y. Uozumi, in *Handb. Asymmetric Heterog. Catal.*, Wiley-VCH Verlag GmbH & Co. KGaA, Weinheim, Germany, **2008**, pp. 1–24.

[377]   R. Callender, R. B. Dyer, *Acc. Chem. Res.* **2015**, *48*, 407.

[378]   E. Roduner, *Chem. Soc. Rev.* **2014**, *43*, 8226.

[379]   P. del Pino, B. Pelaz, Q. Zhang, P. Maffre, G. U. Nienhaus, W. J. Parak, *Mater. Horiz.* **2014**, *1*, 301.

[380]   R. André, F. Natálio, M. Humanes, J. Leppin, K. Heinze, R. Wever, H. C. Schröder, W. E. G. Müller, W. Tremel, *Adv. Funct. Mater.* **2011**, *21*, 501.

[381]   M. N. Tahir, R. André, J. K. Sahoo, F. D. Jochum, P. Theato, F. Natalio, R. Berger, R. Branscheid, U. Kolb, W. Tremel, *Nanoscale* **2011**, *3*, 3907.

[382]   M. Kluenker, M. Nawaz Tahir, R. Ragg, K. Korschelt, P. Simon, T. E. Gorelik, B. Barton, S. I. Shylin, M. Panthöfer, J. Herzberger, H. Frey, V. Ksenofontov, A. Möller, U. Kolb, J. Grin, W. Tremel, *Chem. Mater.* **2017**, *29*, 1134.

[383]   H. Y. Shin, T. J. Park, M. Il Kim, *J. Nanomater.* **2015**, *2015*, 1.

[384]   P. Jittam, P. Boonsiri, C. Promptmas, N. Sriwattanarothai, N. Archavarungson, P. Ruenwongsa, B. Panijpan, *Biochem. Mol. Biol. Educ.* **2009**, *37*, 99.

[385]   Y. Lee, U. von Gunten, *Water Res.* **2010**, *44*, 555.

[386]   H. Gallard, F. Pellizzari, J. P. Croué, B. Legube, *Water Res.* **2003**, *37*, 2883.

[387]   M. Gazda, D. W. Margerum, *Inorg. Chem.* **1994**, *33*, 118.

[388]   J. L. Acero, P. Piriou, U. von Gunten, *Water Res.* **2005**, *39*, 2979.

[389]   U. von Gunten, U. Pinkernell, *Water Sci. Technol.* **2000**, *41*, 53.

[390]   U. von Gunten, *Water Res.* **2003**, *37*, 1469.

[391]   M. Deborde, U. von Gunten, *Water Res.* **2008**, *42*, 13.

[392]   J. G. J. Goodwin, S. Kim, W. D. Rhodes, in *Catalysis*, **2007**, pp. 320–347.

[393]   K. Korschelt, R. Ragg, C. S. Metzger, M. Kluenker, M. Oster, B. Barton, M. Panthöfer, D. Strand, U. Kolb, M. Mondeshki, S. Strand, J. Brieger, M. Nawaz Tahir, W. Tremel, *Nanoscale* **2017**, *9*, 3952.

[394]   E. de Boer, H. Plat, M. G. M. Tromp, R. Wever, M. C. R. Franssen, H. C. van der Plas, E. M. Meijer, H. E. Schoemaker, *Biotechnol. Bioeng.* **1987**, *30*, 607.

[395]   N. Narender, K. Mohan, R. Vinod Reddy, P. Srinivasu, S. J. Kulkarni, K. V. Raghavan, *J. Mol. Catal. A Chem.* **2003**, *192*, 73.

[396]   M. R. Maurya, H. Saklani, S. Agarwal, *Catal. Commun.* **2004**, *5*, 563.

[397]   B. Sels, D. De Vos, M. Buntinx, F. Pierard, A. Kirsch-De Mesmaeker, P. Jacobs, *Nature* **1999**, *400*, 855.

[398]   B. F. Sels, D. E. De Vos, M. Buntinx, P. A. Jacobs, *J. Catal.* **2003**, *216*, 288.

[399]   A.-J. Chen, S.-T. Wong, C.-C. Hwang, C.-Y. Mou, *ACS Catal.* **2011**, *1*, 786.

[400]   S. Mallik, K. M. Parida, S. S. Dash, *J. Mol. Catal. A Chem.* **2007**, *261*, 172.

[401]   M. R. Maurya, A. Kumar, P. Manikandan, S. Chand, *Appl. Catal. A Gen.* **2004**, *277*, 45.

[402]   M. R. Maurya, U. Kumar, P. Manikandan, *Dalt. Trans.* **2006**, 3561.

[403]   M. R. Maurya, N. Chaudhary, F. Avecilla, *Polyhedron* **2014**, *67*, 436.

[404] M. R. Maurya, M. Kumar, A. Arya, *Catal. Commun.* **2008**, *10*, 187.

[405] S. Bhunia, D. Saha, S. Koner, *Langmuir* **2011**, *27*, 15322.

[406] J. J. Boruah, S. P. Das, R. Borah, S. R. Gogoi, N. S. Islam, *Polyhedron* **2013**, *52*, 246.

[407] B. Sels, P. Levecque, R. Brosius, D. De Vos, P. Jacobs, D. W. Gammon, H. H. Kinfe, *Adv. Synth. Catal.* **2005**, *347*, 93.

[408] K. M. Parida, S. Parija, J. Das, P. S. Mukherjee, *Catal. Commun.* **2006**, *7*, 913.

[409] S. T. Wong, C. C. Hwang, C. Y. Mou, *Appl. Catal. B Environ.* **2006**, *63*, 1.

[410] S. Mallick, K. M. Parida, *Catal. Commun.* **2007**, *8*, 889.

[411] R. Rajagopal, S. A. Siddiqui, T. Daniel, R. J. Lahoti, K. V. Srinivasan, *J. Mol. Catal. A Chem.* **2004**, *210*, 165.

[412] D. P. Das, K. M. Parida, *J. Mol. Catal. A Chem.* **2006**, *253*, 70.

[413] M. R. Maurya, N. Kumar, F. Avecilla, *J. Mol. Catal. A Chem.* **2014**, *392*, 50.

[414] B. M. Choudary, T. Someshwar, M. L. Kantam, C. V. Reddy, *Catal. Commun.* **2004**, *5*, 215.

[415] J. V. Walker, M. Morey, H. Carlsson, A. Davidson, G. D. Stucky, A. Butler, *J. Am. Chem. Soc.* **1997**, *119*, 6921.

[416] A.-J. Chen, X.-R. Chen, C.-Y. Mou, *J. Chinese Chem. Soc.* **2010**, *57*, 820.

[417] S. M. Islam, K. Ghosh, A. S. Roy, N. Salam, T. Chatterjee, *J. Inorg. Organomet. Polym. Mater.* **2014**, *24*, 457.

[418] S. M. Islam, A. S. Roy, P. Mondal, N. Salam, S. Paul, *Catal. Letters* **2013**, *143*, 225.

[419] R. K. Sharma, C. Sharma, *Tetrahedron Lett.* **2010**, *51*, 4415.

[420] C. Gatley, L. Muller, M. Lang, E. Alberto, M. Detty, *Molecules* **2015**, *20*, 9616.

[421] B. Das, K. Venkateswarlu, G. Mahender, I. Mahender, *Tetrahedron Lett.* **2005**, *46*, 3041.

[422] B. Das, K. Venkateswarlu, M. Krishnaiah, H. Holla, *Tetrahedron Lett.* **2006**, *47*, 8693.

[423] U. Bora, G. Bose, M. K. Chaudhuri, S. S. Dhar, R. Gopinath, A. T. Khan, B. K. Patel, *Org. Lett.* **2000**, *2*, 247.

[424] F. Natalio, R. André, A. F. Hartog, B. Stoll, K. P. Jochum, R. Wever, W. Tremel, *Nat. Nanotechnol.* **2012**, *7*, 530.

[425] F. Natalio, R. André, S. A. Pihan, M. Humanes, R. Wever, W. Tremel, *J. Mater. Chem.* **2011**, *21*, 11923.

[426] P. Zhang, D. Sun, M. Wen, J. Yang, K. Zhou, Z. Wang, *Adv. Synth. Catal.* **2012**, *354*, 720.

[427] A. Leyva-Pérez, D. Cómbita-Merchán, J. R. Cabrero-Antonino, S. I. Al-Resayes, A. Corma, *ACS Catal.* **2013**, *3*, 250.

[428] R. D. Shannon, *Acta Crystallogr. Sect. A* **1976**, *32*, 751.

[429] R. G. Pearson, **1997**, 198.

[430] J. Livage, *Chem. Mater.* **1991**, *3*, 578.

[431] H. Choi, Y.-Y. Chang, Y.-U. Kwon, O. H. Han, *Chem. Mater.* **2003**, *15*, 3261.

[432] M. R. Maurya, N. Chaudhary, A. Kumar, F. Avecilla, J. Costa Pessoa, *Inorganica Chim. Acta* **2014**, *420*, 24.

[433] B. F. Sels, D. E. De Vos, P. A. Jacobs, *3rd World Congr. Oxid. Catal.* **1997**, *110*, 1051.

[434] A. Molinari, G. Varani, E. Polo, S. Vaccari, A. Maldotti, *J. Mol. Catal. A Chem.* **2007**, *262*, 156.

[435] P. Doggali, S. Waghmare, S. Rayalu, Y. Teraoka, N. Labhsetwar, *J. Mol. Catal. A Chem.* **2011**, *347*, 52.

[436] J. M. Thomas, R. Raja, *J. Organomet. Chem.* **2004**, *689*, 4110.

[437] H. Firouzabadi, N. Iranpoor, K. Amani, *J. Mol. Catal. A Chem.* **2003**, *195*, 289.

[438] L. Peng, Y. Liu, N. Kim, J. E. Readman, C. P. Grey, *Nat. Mater.* **2005**, *4*, 216.

[439] D. P. Riley, *Chem. Rev.* **1999**, *99*, 2573.

[440] G. B. Jameson, J. A. Ibers, in *Bioinorg. Chem.* (Eds.: I. Bertini, H.B. Gray, S.J. Lippard, J.S. Valentine), University Science Books, Mill Valley, CA, **1994**, pp. 167–252.

[441] R. Raja, P. Ratnasamy, *J. Catal.* **1997**, *170*, 244.

[442] D. M. McMaster, S. M. Bennett, Y. Tang, J. a Finlay, G. L. Kowalke, B. Nedved, F. V Bright, M. E. Callow, J. a Callow, D. E. Wendt, M. G. Hadfield, M. R. Detty, *Biofouling* **2009**, *25*, 21.

[443] V. Paul, A. Sudalai, T. Daniel, K. V. Srinivasan, *Tetrahedron Lett.* **1994**, *35*, 7055.

[444] G. Rothenberg, J. H. Clark, *Green Chem.* **2000**, *2*, 248.

[445] R. J. D. Tilley, *Defects in Solids*, John Wiley And Sons, **2008**.

[446] D. M. Smith, *The Defect Chemistry of Metal Oxides*, Oxford University Press, **2000**.

[447] A. Mehonic, A. J. Kenyon, *Defects at Oxide Surfaces*, Springer International Publishing, Cham, **2015**.

[448] D. R. Lide, *CRC Handbook of Chemistry and Physics, 84th Edition*, Taylor & Francis, **2003**.

[449] W. Huang, Y. Gao, *Catal. Sci. Technol.* **2014**, *4*, 3772.

[450]   J. N. Rodríguez-López, D. J. Lowe, J. Hernández-Ruiz, a N. Hiner, F. García-Cánovas, R. N. Thorneley, *J. Am. Chem. Soc.* **2001**, *123*, 11838.

[451]   S. S. Kahandal, S. R. Kale, M. B. Gawande, R. Zboril, R. S. Varma, R. V. Jayaram, *RSC Adv.* **2014**, *4*, 6267.

[452]   R. Wever, in *Peroxidases Catalases Biochem. Biophys. Biotechnol. Physiol.*, **2010**, p. 459.

[453]   R. Wever, in *Proc. Colloq. "Mechanismsm Biohalogenation Dehalogenation", Amsterdam R. Netherl. Acad. Arts Sci*, **1997**, pp. 89–100.

[454]   W. Chung, C. D. Vanderwal, *Angew. Chem. Int. Ed.* **2016**, *55*, 4396.

[455]   J. J. Li, G. Gribble, *Palladium in Heterocyclic Chemistry: A Guide for the Synthetic Chemist, 2nd Edition*, Elsevier, Oxford, UK, **2007**.

[456]   L. Kürti, B. Czakó, *Strategic Applications of Named Reactions in Organic Synthesis, 1st Edition*, Elsevier, **2005**.

[457]   J. Hassan, M. Sévignon, C. Gozzi, E. Schulz, M. Lemaire, *Chem. Rev.* **2002**, *102*, 1359.

[458]   J. Littlechild, *Curr. Opin. Chem. Biol.* **1999**, *3*, 28.

[459]   F. Hollmann, I. W. C. E. Arends, K. Buehler, A. Schallmey, B. Bühler, *Green Chem.* **2011**, *13*, 226.

[460]   M. C. R. Franssen, P. Steunenberg, E. L. Scott, H. Zuilhof, J. P. M. Sanders, *Chem. Soc. Rev.* **2013**, *42*, 6491.

[461]   M. Ayala, J. Verdin, R. Vazquez-Duhalt, *Biocatal. Biotransformation* **2007**, *25*, 114.

[462]   A. Sassolas, L. J. Blum, B. D. Leca-Bouvier, *Biotechnol. Adv.* **2012**, *30*, 489.

[463]   K. Uraisin, D. Nacapricha, S. Lapanantnoppakhun, K. Grudpan, S. Motomizu, *Talanta* **2005**, *68*, 274.

[464]   K. Uraisin, T. Takayanagi, M. Oshima, D. Nacapricha, S. Motomizu, *Talanta* **2006**, *68*, 951.

[465]   E. P. Borges, A. F. Lavorante, B. F. dos Reis, *Anal. Chim. Acta* **2005**, *528*, 115.

[466]   L. Shi, X. Liu, W. Niu, H. Li, S. Han, J. Chen, G. Xu, *Biosens. Bioelectron.* **2009**, *24*, 1159.

[467]   H. Yin, S. Ai, W. Shi, L. Zhu, *Sensors Actuators B Chem.* **2009**, *137*, 747.

[468]   É. a. C. Guedes, T. G. da Silva, J. S. Aguiar, L. D. de Barros, L. M. Pinotti, A. E. G. Sant'Ana, *Rev. Bras. Farmacogn.* **2013**, *23*, 668.

[469]   R. a Clark, S. J. Klebanoff, a B. Einstein, A. Fefer, *Blood* **1975**, *45*, 161.

[470]   K. A. Mohammed, C. F. Hossain, L. Zhang, R. K. Bruick, Y.-D. Zhou, D. G. Nagle, *J. Nat. Prod.* **2004**, *67*, 2002.

[471]   A. J. Smit, *J. Appl. Phycol.* **2004**, *16*, 245.

[472]   S. S. A. llah Al-Saif, N. Abdel-Raouf, H. A. El-Wazanani, I. A. Aref, *Saudi J. Biol. Sci.* **2014**, *21*, 57.

[473]   K.-B. Oh, J. H. Lee, S.-C. Chung, J. Shin, H. J. Shin, H.-K. Kim, H.-S. Lee, *Bioorg. Med. Chem. Lett.* **2008**, *18*, 104.

[474]   C. S. Vairappan, *Biomol. Eng.* **2003**, *20*, 255.

[475]   G. M. Cragg, D. J. Newman, *Biochim. Biophys. Acta* **2013**, *1830*, 3670.

[476]   P. Manivasagan, J. Venkatesan, K. Sivakumar, S.-K. Kim, *Microbiol. Res.* **2014**, *169*, 262.

[477]   M. T. Cabrita, C. Vale, A. P. Rauter, *Mar. Drugs* **2010**, *8*, 2301.

[478]   T. Wanke, A. C. Philippus, G. A. Zatelli, L. F. O. Vieira, C. Lhullier, M. Falkenberg, *Rev. Bras. Farmacogn.* **2015**, *25*, 569.

[479]   R. S. Rosenbaum, J. Kessler, *Bactericidal Compositions and Methods, US 4.473.550*, **1984**.

[480]   F. A. E. Torres, T. G. Passalacqua, A. M. A. Velásquez, R. A. de Souza, P. Colepicolo, M. A. S. Graminha, *Rev. Bras. Farmacogn.* **2014**, *24*, 265.

[481]   B.-G. Wang, J. B. Gloer, N.-Y. Ji, J.-C. Zhao, *Chem. Rev.* **2013**, *113*, 3632.

[482]   C. S. Vairappan, M. Suzuki, T. Ishii, T. Okino, T. Abe, M. Masuda, *Phytochemistry* **2008**, *69*, 2490.

[483]   R. Renirie, A. Dewilde, C. Pierlot, R. Wever, D. Hober, J. M. Aubry, *J. Appl. Microbiol.* **2008**, *105*, 264.

[484]   A. L. Lane, B. S. Moore, *Nat. Prod. Rep.* **2011**, *28*, 411.

[485]   P. V. R. Snelgrove, *Planta Med.* **2016**, *82*, 790.

[486]   F. J. Benitez, J. L. Acero, F. J. Real, G. Roldan, F. Casas, *Chemosphere* **2011**, *85*, 1430.

[487]   J. Rubiolo, E. Alonso, E. Cagide, in *Seaf. Freshw. Toxins*, CRC Press, **2014**, pp. 1141–1178.

[488]   M. Benaglia, *Recoverable and Recyclable Catalysts*, John Wiley & Sons, Ltd, Chichester, UK, **2009**.

[489]   E. H. Hansen, L. Albertsen, T. Schafer, C. Johansen, J. C. Frisvad, S. Molin, L. Gram, T. Schäfer, J. C. Frisvad, S. Molin, L. Gram, T. Scha, C. Johansen, *Appl. Environ. Microbiol.* **2003**, *69*, 4611.

[490]   J. Johansson, B. E. Christensen, A. Marie, S. Danielsen, M. Gjermansen, *A Method of Obtaining High Level Disinfection in a Washer Disinfector, and a Washer Disinfector, WO 2010/046142 A2*,

2010.

[491] G. Rothenberg, J. H. Clark, *Org. Process Res. Dev.* **2000**, *4*, 270.

[492] J. N. Talbert, J. M. Goddard, *Colloids Surfaces B Biointerfaces* **2012**, *93*, 8.

[493] A. I. Railkin, *Marine Biofouling: Colonization Processes and Defenses*, CRC Press, **2005**.

[494] A. I. Railkin, *Marine Biofouling: Colonization Processes and Defenses*, CRC Press, **2003**.

[495] A. G. Nurioglu, A. C. C. Esteves, G. de With, *J. Mater. Chem. B* **2015**, *3*, 6547.

[496] J. S. Mohammed, *Prog. Oceanogr.* **2015**, *134*, 451.

[497] M. Lejars, A. Margaillan, C. Bressy, *Chem. Rev.* **2012**, *112*, 4347.

[498] I. Banerjee, R. C. Pangule, R. S. Kane, *Adv. Mater.* **2011**, *23*, 690.

[499] S. Dürr, J. C. Thomason, *Biofouling*, Wiley-Blackwell, **2009**.

[500] H.-C. Flemming, P. S. Murthy, R. Venkatesan, K. E. Cooksey, *Marine and Industrial Biofouling*, Springer Berlin Heidelberg, **2009**.

[501] K. A. Dafforn, J. A. Lewis, E. L. Johnston, *Mar. Pollut. Bull.* **2011**, *62*, 453.

[502] D. M. Yebra, S. Kiil, K. Dam-Johansen, *Prog. Org. Coatings* **2004**, *50*, 75.

[503] J. B. Kristensen, R. L. Meyer, B. S. Laursen, S. Shipovskov, F. Besenbacher, C. H. Poulsen, *Biotechnol. Adv.* **2008**, *26*, 471.

[504] J. Bellas, *Chim. Oggi/Chemistry Today* **2016**, *24*, 26.

[505] I. K. Konstantinou, T. A. Albanis, *Environ. Int.* **2004**, *30*, 235.

[506] Umwelt Bundesamt, "http://www.Umweltbundesamt.De/Themen/Chemikalien/Chemikalienforschung-Im-Uba/Fliess-Stillgewaesser-Simulationsanlage/Projekte/Fate-Studie-Irgarol (14/12/16)," **2016**.

[507] Die Europäische Kommission, *Durchführungsbeschluss (EU) 2016/107 Der Kommission Vom 27. Januar 2016 Zur Nichtgenehmigung von Cybutryn Als Altem Wirkstoff Zur Verwendung in Biozidprodukten Der Produktart 21*, **2016**.

[508] S. Mohr, R. Berghahn, W. Mailahn, R. Schmiediche, M. Feibicke, R. Schmidt, *Environ. Sci. Technol.* **2009**, *43*, 6838.

[509] J. L. Zhou, *Sci. Total Environ.* **2008**, *406*, 239.

[510] European Commission (DG, Environment), *Technical Support for the Impact Assessment of the Review of Priority Substances under Directive 2000/60/EC. Substance Assessment: Cybutryne*, **2011**.

[511] A. J. Scardino, R. de Nys, *Biofouling* **2011**, *27*, 73.

[512] J. A. Callow, M. E. Callow, *Nat. Commun.* **2011**, *2*, 244.

[513] L. D. Chambers, K. R. Stokes, F. C. Walsh, R. J. K. Wood, *Surf. Coatings Technol.* **2006**, *201*, 3642.

[514] E. Almeida, T. C. Diamantino, O. de Sousa, *Prog. Org. Coatings* **2007**, *59*, 2.

[515] S. Kiil, K. Dam-Johansen, C. E. Weinell, M. S. Pedersen, *Prog. Org. Coatings* **2002**, *45*, 423.

[516] C. M. Grozea, G. C. Walker, *Soft Matter* **2009**, *5*, 4088.

[517] J. Genzer, K. Efimenko, *Biofouling* **2006**, *22*, 339.

[518] R. E. Pérez-Roa, M. A. Anderson, D. Rittschof, C. G. Hunt, D. R. Noguera, R. E. Perez-Roa, M. A. Anderson, D. Rittschof, C. G. Hunt, D. R. Noguera, R. E. Pérez-Roa, M. A. Anderson, D. Rittschof, C. G. Hunt, D. R. Noguera, *Biofouling* **2009**, *25*, 563.

[519] D. Rittschof, *Biofouling* **2000**, *15*, 119.

[520] T. V. Raveendran, V. P. L. Mol, *Curr. Sci.* **2009**, *97*, 508.

[521] M. R. Detty, R. Ciriminna, F. V. Bright, M. Pagliaro, *ChemNanoMat* **2015**, *1*, 148.

[522] B. Sykes, J. Neild, *Preventing Fouling on Marine Structures, WO 000554 A1*, **1980**.

[523] K. D. Sakrowski, *Verwendung von Basaltfasern Oder Basaltfilamenten Als Textiles Flächengebilde Zur Biozidfreien Antifouling-Beschichtung Für Umströmte Unterwasserflächen, DE 10353185 B4*, **2005**.

[524] K. D. Sakrowski, *Biocide-Free Antifouling Coating Consisting of a Fabric Based on Basalt Fibres, WO 2005047403 A1*, **2005**.

[525] E. Pinori, M. Berglin, L. M. Brive, M. Hulander, M. Dahlström, H. Elwing, *Biofouling* **2011**, *27*, 941.

[526] J. F. Destino, C. M. Gatley, A. K. Craft, M. R. Detty, F. V. Bright, *Langmuir* **2015**, *31*, 3510.

[527] C. A. Damon, C. M. Gatley, J. J. Beres, J. A. Finlay, S. C. Franco, A. S. Clare, M. R. Detty, *Biofouling* **2016**, *32*, 883.

[528] P. P. Singh, T. Thatikonda, K. A. A. Kumar, S. D. Sawant, B. Singh, A. K. Sharma, P. R. Sharma, D. Singh, R. A. Vishwakarma, *J. Org. Chem.* **2012**, *77*, 5823.

[529] A. P. Amrute, C. Mondelli, M. A. G. Hevia, J. Pérez-Ramírez, *J. Phys. Chem. C* **2011**, *115*, 1056.

[530] G. Münster, D. Wolf, M. Kremer, in *NIC Symp.*, **2008**, pp. 1–380.

[531] J. P. Guggenbichler, N. Eberhardt, H.-P. Martinz, H. Wildner, *Antimicrobial Agent, WO 2008058707 A3*, **2008**.

[532] C. Zollfrank, K. Gutbrod, P. Wechsler, J. P. Guggenbichler, *Mater. Sci. Eng. C* **2012**, *32*, 47.

[533] S. Shafaei, D. Van Opdenbosch, T. Fey, M. Koch, T. Kraus, J. P. Guggenbichler, C. Zollfrank, *Mater. Sci. Eng. C* **2016**, *58*, 1064.

[534] J. Gao, Y. Zheng, J.-M. Jehng, Y. Tang, I. E. Wachs, S. G. Podkolzin, *Science* **2015**, *348*, 686.

[535] A. B. Tesler, P. Kim, S. Kolle, C. Howell, O. Ahanotu, J. Aizenberg, *Nat. Commun.* **2015**, *6*, 8649.

[536] B. Alonso, J. Livage, *J. Solid State Chem.* **1999**, *148*, 16.

[537] O. W. Howarth, *Progess NMR Spectrosc.* **1990**, *22*, 453.

[538] H. T. Evans, *Inorg. Chem.* **1966**, *5*, 967.

[539] O. Pelletier, P. Davidson, C. Bourgaux, C. Coulon, S. Regnault, J. Livage, *Synthesis* **2000**, 5295.

[540] M. A. H. Habayeb, "^{51}V, ^{13}C and ^{1}H FT-NMR Studies on Vanadium (V) Species in Aqueous Solutions", Thesis, **1981**.

[541] W. Jeung, S. Park, K. Kim, M. Lee, *J. Korean Magn. Reson. Soc.* **1998**, 113.

[542] S. Han, S. Park, M. Lee, H. Park, *Bull. Korean Chem. Soc.* **2004**, *25*, 106.

[543] J. Masere, J. A. Pojman, *J Chem Soc Faraday Trans* **1998**, *94*, 919.

[544] B. F. Sels, D. E. De Vos, P. A. Jacobs, *J. Am. Chem. Soc.* **2001**, *123*, 8350.

[545] A. Paul, J. M. Rusin, *J. Am. Ceram. Soc.* **1969**, *52*, 657.

[546] "http://www.bloch.at/web/physikalische_testgeraete.html (06/05/17)," **2017**.

[547] BASF, "'Paint Defects Advice - BASF Refinish', http://www.refinish.basf.us/uploaded/files/Paint_Defects.pdf (18/06/17)," **2017**.

[548] International, "Toplac, Safty Data Sheet, http://www.yachtpaint.com/gbr/diy/products/MSDS.aspx?LanguageCode=eng&RegulatoryBody =gbr&Market=YA&Product=Toplac (07/05/17)," **2017**.

[549] R. André, N. F. Fischer, P. Hubach, C. Walsdorff, C. Schwidetzky, *Use of Gamma iron(II) Oxide Containing Particles for the Prevention of Biofouling And/or Growth of Microorganisms, WO 2015/193134 A1*, **2015**.

[550] M. V. Ganduglia-Pirovano, *Catal. Today* **2015**, *253*, 20.

[551] M.-H. Sun, S.-Z. Huang, L.-H. Chen, Y. Li, X.-Y. Yang, Z.-Y. Yuan, B.-L. Su, *Chem. Soc. Rev.* **2016**, *45*, 3479.

[552] N. Muhd Julkapli, S. Bagheri, S. Bee Abd Hamid, *Sci. World J.* **2014**, *2014*, 1.

[553] P. D. Steinberg, R. De Nys, S. Kjelleberg, in *Mar. Chem. Ecol. CRC Mar. Sci. Ser.* (Eds.: J.B. McClintock, B.J. Baker), CRC Press, Boca Raton, **2001**, pp. 355–387.

[554] S. A. Borchardt, E. J. Allain, J. J. Michels, G. W. Stearns, F. R. Kelly, W. F. McCoy, *Appl. Environ. Microbiol.* **2001**, *67*, 3174.

[555] P. Barnett, D. Hondmann, L. H. Simons, P. F. Ter Steeg, R. Wever, *Recombinant Vanadium Haloperoxidases and Their Uses, WO/1995/027009*, **1995**.

[556] A. Rosenhahn, S. Schilp, H. J. Kreuzer, M. Grunze, *Phys. Chem. Chem. Phys.* **2010**, *12*, 4275.

[557] S. Krishnan, C. J. Weinman, C. K. Ober, *J. Mater. Chem.* **2008**, *18*, 3405.

[558] V. Conte, A. Coletti, B. Floris, G. Licini, C. Zonta, *Coord. Chem. Rev.* **2011**, *255*, 2165.

[559] C. T. Campbell, C. H. F. Peden, *Science* **2005**, *309*, 713.

[560] J. Chen, S. Patil, S. Seal, J. F. McGinnis, *Nat. Nanotechnol.* **2006**, *1*, 142.

[561] C. Korsvik, S. Patil, S. Seal, W. T. Self, *Chem. Commun.* **2007**, 1056.

[562] Z. Ji, X. Wang, H. Zhang, S. Lin, H. Meng, B. Sun, S. George, T. Xia, A. E. Nel, J. I. Zink, *ACS Nano* **2012**, *6*, 5366.

[563] R. W. Cheary, A. Coelho, *J. Appl. Cryst.* **1992**, *25*, 109.

[564] P. Burroughs, A. Hamnett, A. F. Orchard, G. Thornton, *J. Chem. Soc. Dalt. Trans.* **1976**, *17*, 1686.

[565] T. Skála, F. Šutara, K. C. Prince, V. Matolín, *J. Electron Spectros. Relat. Phenomena* **2009**, *169*, 20.

[566] A. Butler, M. J. Clague, G. E. Meister, *Chem. Rev.* **1994**, *94*, 625.

[567] E. H. Hansen, L. Albertsen, T. Schafer, C. Johansen, J. C. Frisvad, S. Molin, L. Gram, *Appl. Environ. Microbiol.* **2003**, *69*, 4611.

[568] G. Cornelis, B. Ryan, M. J. McLaughlin, J. K. Kirby, D. Beak, D. Chittleborough, *Environ. Sci. Technol.* **2011**, *45*, 2777.

[569] D. R. Mullins, *Surf. Sci. Rep.* **2015**, *70*, 42.

[570] S. S. Lee, W. Song, M. Cho, H. L. Puppala, P. Nguyen, H. Zhu, L. Segatori, V. L. Colvin, *ACS Nano* **2013**, *7*, 9693.

[571] R. Weller, O. Schrems, *Geophys. Res. Lett.* **1993**, *20*, 125.

[572] RIWA, "Water Quality of Maas (Annual Report of Heel, Chemistry). 1–23 (2014).

http://www.riwa-maas.org/nc/de/gewassergute-maas.html," **2016**.

[573] J. Kašpar, P. Fornasiero, M. Graziani, *Catal. Today* **1999**, *50*, 285.

[574] E. P. Murray, T. Tsai, S. A. Barnett, *Nature* **1999**, *400*, 649.

[575] W. C. Chueh, Y. Hao, W. Jung, S. M. Haile, *Nat. Mater.* **2011**, *11*, 155.

[576] C. Xu, X. Qu, *NPG Asia Mater.* **2014**, *6*, e90.

[577] I. Celardo, J. Z. Pedersen, E. Traversa, L. Ghibelli, *Nanoscale* **2011**, *3*, 1411.

[578] C. Walkey, S. Das, S. Seal, J. Erlichman, K. Heckman, L. Ghibelli, E. Traversa, J. F. McGinnis, W. T. Self, *Environ. Sci. Nano* **2015**, *2*, 33.

[579] X. Ge, Z. Li, Q. Yuan, *J. Mater. Sci. Technol.* **2015**, *31*, 645.

[580] M. Nolan, S. Grigoleit, D. C. Sayle, S. C. Parker, G. W. Watson, *Surf. Sci.* **2005**, *576*, 217.

[581] M. Nolan, S. C. Parker, G. W. Watson, *Surf. Sci.* **2005**, *595*, 223.

[582] M. Nolan, J. E. Fearon, G. W. Watson, *Solid State Ionics* **2006**, *177*, 3069.

[583] F. Esch, *Science* **2005**, *309*, 752.

[584] S. Cao, F. (Feng) Tao, Y. Tang, Y. Li, J. Yu, *Chem. Soc. Rev.* **2016**, *45*, 4747.

[585] Y. Liu, C. Wen, Y. Guo, G. Lu, Y. Wang, *J. Mol. Catal. A Chem.* **2009**, *316*, 59.

[586] G. Carraro, C. Maccato, E. Bontempi, A. Gasparotto, O. I. Lebedev, S. Turner, L. E. Depero, G. Van Tendeloo, D. Barreca, *Eur. J. Inorg. Chem.* **2013**, *2013*, 5454.

[587] S. Agarwal, X. Zhu, E. J. M. Hensen, B. L. Mojet, L. Lefferts, *J. Phys. Chem. C* **2015**, *119*, 12423.

[588] M. Kovacevic, S. Agarwal, B. L. Mojet, J. G. Van Ommen, L. Lefferts, *Appl. Catal. A Gen.* **2015**, *505*, 354.

[589] Z. Wu, M. Li, J. Howe, H. M. Meyer, S. H. Overbury, *Langmuir* **2010**, *26*, 16595.

[590] Z. A. Qiao, Z. Wu, S. Dai, *ChemSusChem* **2013**, *6*, 1821.

[591] Y. Lin, Z. Wu, J. Wen, K. R. Poeppelmeier, L. D. Marks, *Nano Lett.* **2014**, *14*, 191.

[592] H. X. Mai, L. D. Sun, Y. W. Zhang, R. Si, W. Feng, H. P. Zhang, H. C. Liu, C. H. Yan, *J. Phys. Chem. B* **2005**, *109*, 24380.

[593] Tana, M. Zhang, J. Li, H. Li, Y. Li, W. Shen, *Catal. Today* **2010**, *148*, 179.

[594] T. X. T. Sayle, S. C. Parker, C. R. A. Catlow, *Surf. Sci.* **1994**, *316*, 329.

[595] Z. Wu, M. Li, S. H. Overbury, *J. Catal.* **2012**, *285*, 61.

[596] M. Kovacevic, B. L. Mojet, J. G. van Ommen, L. Lefferts, *Catal. Letters* **2016**, *146*, 770.

[597] S. Agarwal, L. Lefferts, B. L. Mojet, D. A. J. M. Ligthart, E. J. M. Hensen, D. R. G. Mitchell, W. J. Erasmus, B. G. Anderson, E. J. Olivier, J. H. Neethling, A. K. Datye, *ChemSusChem* **2013**, *6*, 1898.

[598] D. Jiang, W. Wang, L. Zhang, Y. Zheng, Z. Wang, *ACS Catal.* **2015**, *5*, 4851.

[599] T. Naganuma, E. Traversa, *Nanoscale* **2012**, *4*, 4950.

[600] E. G. Heckert, A. S. Karakoti, S. Seal, W. T. Self, *Biomaterials* **2008**, *29*, 2705.

[601] Z. Wang, X. Feng, *J. Phys. Chem. B* **2003**, *107*, 13563.

[602] G. Shen, Q. Wang, Z. Wang, Y. Chen, *Mater. Lett.* **2011**, *65*, 1211.

[603] L. Yan, R. Yu, J. Chen, X. Xing, *Cryst. Growth Des.* **2008**, *8*, 1474.

[604] A. Fujimori, *Phys. Rev. B* **1983**, *28*, 2281.

[605] E. Paparazzo, *Mater. Res. Bull.* **2011**, *46*, 323.

[606] L. Truffault, M. T. Ta, T. Devers, K. Konstantinov, V. Harel, C. Simmonard, C. Andreazza, I. P. Nevirkovets, A. Pineau, O. Veron, J. P. Blondeau, *Mater. Res. Bull.* **2012**, *47*, 3941.

[607] D. R. Mullins, S. H. Overbury, D. R. Huntley, *Surf. Sci.* **1998**, *409*, 307.

[608] E. Bêche, P. Charvin, D. Perarnau, S. Abanades, G. Flamant, *Surf. Interface Anal.* **2008**, *40*, 264.

[609] N. Wang, W. Qian, W. Chu, F. Wei, *Catal. Sci. Technol.* **2016**, *6*, 3594.

[610] S. Agarwal, X. Zhu, E. J. M. Hensen, L. Lefferts, B. L. Mojet, *J. Phys. Chem. C* **2014**, *118*, 4131.

[611] Y. Chen, T. Liu, C. Chen, W. Guo, R. Sun, S. Lv, M. Saito, S. Tsukimoto, Z. Wang, *Ceram. Int.* **2013**, *39*, 6607.

[612] J. Li, Z. Zhang, Z. Tian, X. Zhou, Z. Zheng, Y. Ma, Y. Qu, *J. Mater. Chem. A* **2014**, *2*, 16459.

[613] J. Hartmann, Bachelor Thesis: "Metalloxide Als Enzymanaloga," **2015**.

[614] B. C. Mohanty, J. W. Lee, D.-H. H. Yeon, Y.-H. H. Jo, J. H. Kim, Y. S. Cho, *Mater. Res. Bull.* **2011**, *46*, 875.

[615] S. Chen, L. Li, W. Hu, X. Huang, Q. Li, Y. Xu, Y. Zuo, G. Li, *ACS Appl. Mater. Interfaces* **2015**, *7*, 22999.

[616] D. Channei, B. Inceesungvorn, N. Wetchakun, S. Ukritnukun, A. Nattestad, J. Chen, S. Phanichphant, *Sci. Rep.* **2015**, *4*, 5757.

[617] B. Choudhury, P. Chetri, A. Choudhury, *RSC Adv.* **2014**, *4*, 4663.

[618] BAUA, "https://www.baua.de/DE/Angebote/Rechtstexte-und-Technische-Regeln/Regelwerk/TRGS/TRGS.html," **2017**.

[619] Helpdesk REACH-CLP-Biozid, "http://www.reach-clp-biozid-helpdesk.de/de/CLP/CLP.html," **2017**.

[620] S. Lin, X. Wang, Z. Ji, C. H. Chang, Y. Dong, H. Meng, Y. P. Liao, M. Wang, T. Bin Song, S. Kohan, T. Xia, J. I. Zink, S. Lin, A. E. Nel, *ACS Nano* **2014**, *8*, 4450.

[621] F. Schwabe, R. Schulin, L. K. Limbach, W. Stark, D. Bürge, B. Nowack, *Chemosphere* **2013**, *91*, 512.

[622] F. Schwabe, S. Tanner, R. Schulin, A. Rotzetter, W. Stark, A. Von Quadt, B. Nowack, *Metallomics* **2015**, *7*, 466.

[623] A. Kumar, S. Das, P. Munusamy, W. Self, D. R. Baer, D. C. Sayle, S. Seal, *Environ. Sci. Nano* **2014**, *1*, 516.

[624] T. Xia, M. Kovochich, M. Liong, L. Mädler, B. Gilbert, H. Shi, J. I. Yeh, J. I. Zink, A. E. Nel, *ACS Nano* **2008**, *2*, 2121.

[625] IBWF, "http://www.ibwf.de/index.php/about-us/patents-papers," **2017**.

[626] R. A. Dean, N. J. Talbot, D. J. Ebbole, M. L. Farman, T. K. Mitchell, M. J. Orbach, M. Thon, R. Kulkarni, J.-R. Xu, H. Pan, N. D. Read, Y.-H. Lee, I. Carbone, D. Brown, Y. Y. Oh, N. Donofrio, J. S. Jeong, D. M. Soanes, S. Djonovic, E. Kolomiets, C. Rehmeyer, W. Li, M. Harding, S. Kim, M.-H. Lebrun, H. Bohnert, S. Coughlan, J. Butler, S. Calvo, L.-J. Ma, R. Nicol, S. Purcell, C. Nusbaum, J. E. Galagan, B. W. Birren, *Nature* **2005**, *434*, 980.

[627] H. Koga, O. Nakayachi, *J. Gen. Plant Pathol.* **2004**, *70*, 11.

[628] B. Williamson, B. Tudzynski, P. Tudzynski, J. A. L. Van Kan, *Mol. Plant Pathol.* **2007**, *8*, 561.

[629] H. S. Judelson, F. A. Blanco, *Nat. Rev. Microbiol.* **2005**, *3*, 47.

[630] R. H. Y. Jiang, R. V. Stahelin, S. Bhattacharjee, K. Haldar, *Trends Microbiol.* **2013**, *21*, 145.

[631] G. Robson, P. West, G. Gadd, (Eds.), *Exploitation of Fungi*, Cambridge University Press, Cambridge, **2007**.

[632] S. Jacob, A. Yemelin, S. Bohnert, K. Andresen, E. Thines, *J. Plant Dis. Prot.* **2017**, *124*, 399.

[633] G. Unden, E. Thines, A. Schüffler, P. M. Selzer, *Host - Pathogen Interaction: Microbial Metabolism, Pathogenicity and Antiinfectives*, **2016**.

[634] E. Thines, J. Aguirre, A. J. Foster, H. B. Deising, in *Prog. Bot.*, Springer-Verlag, Berlin/Heidelberg, **2006**, pp. 134–161.

[635] H. T. Tribe, E. Thines, R. W. S. Weber, *Mycologist* **2006**, *20*, 171.

[636] G. Agrios, *Plant Pathology, 5th Edition*, Elsevier, Oxford, UK, **2004**.

[637] J. Ren, J. Gao, W. Yang, *Comput. Vis. Sci.* **2009**, *12*, 227.

[638] T. Montini, M. Melchionna, M. Monai, P. Fornasiero, *Chem. Rev.* **2016**, *116*, 5987.

[639] I. Celardo, E. Traversa, L. Ghibelli, *J. Exp. Ther. Oncol.* **2011**, *9*, 47.

[640] S. Singh, T. Dosani, A. S. Karakoti, A. Kumar, S. Seal, W. T. Self, *Biomaterials* **2011**, *32*, 6745.

[641] R. W. Tarnuzzer, J. Colon, S. Patil, S. Seal, *Nano Lett.* **2005**, *5*, 2573.

[642] J. E. Slemmer, J. J. Shacka, M. I. Sweeney, J. T. Weber, *Curr. Med. Chem.* **2008**, *15*, 404.

[643] L. G. A. Van De Water, S. Bulcock, A. F. Masters, T. Maschmeyer, *Ind. Eng. Chem. Res.* **2007**, *46*, 4221.

[644] T. W. P. Smith, J. P. Jalkanen, B. A. Anderson, J. J. Corbett, J. Faber, S. Hanayama, E. O'Keeffe, S. Parker, L. Johansson, L. Aldous, C. Raucci, M. Traut, S. Ettinger, D. Nelissen, D. S. Lee, S. Ng, A. Agrawal, J. J. Winebrake, M. Hoen, S. Chesworth, A. Pandey, *Reduction of GHG Emissions From Ships, Third IMO GHG Study 2014 - Final Report*, **2014**.

[645] J. A. Fernandes, L. Santos, T. Vance, T. Fileman, D. Smith, J. D. D. Bishop, F. Viard, A. M. Queirós, G. Merino, E. Buisman, M. C. Austen, *Mar. Policy* **2016**, *64*, 148.

[646] D. H. Baldwin, C. P. Tatara, N. L. Scholz, *Aquat. Toxicol.* **2011**, *101*, 295.

[647] "Shelter Island Yacht Basin Dissolved Copper Total Maximum Daily Load 2011 Monitoring and Progress Final Report, March 2015, https://www.portofsandiego.org/environment/copper-reduction-program/monitoring-and-data-assessment/shelter-island-yacht-basin-tmdl-," **2017**.

[648] California Department of Pesticide Regulation, *Copper-Based Antifouling Paint and Coating Products (DPR 16-005)*, United States of America, **2017**.

[649] Ranker, Shin, Litzow, Swecker, Tom, Harper, Nelson, Hobbs, Fraser, Rockefeller, White, Kilmer, Conway, Kline, *Prohibiting Copper in Antifouling Paints Used on Recreational Water Vessels (SB 5436 - 2011 - 12)*, 62, State of Washington, **2011**.

[650] D. Lai, D. Liu, Z. Deng, L. Van Ofwegen, P. Proksch, W. Lin, *J. Nat. Prod.* **2012**, *75*, 1595.

[651] R. Trepos, G. Cervin, C. Hellio, H. Pavia, W. Stensen, K. Stensvåg, J.-S. Svendsen, T. Haug, J. Svenson, *J. Nat. Prod.* **2014**, *77*, 2105.

[652] P.-Y. Qian, Z. Li, Y. Xu, Y. Li, N. Fusetani, *Biofouling* **2015**, *31*, 101.

[653] I. Fitridge, T. Dempster, J. Guenther, R. de Nys, *Biofouling* **2012**, *28*, 649.

[654] T. Nguyen, F. Roddick, L. Fan, *Membranes* **2012**, *2*, 804.

[655] C. Cha, P. Gao, Y. C. Chen, P. D. Shaw, S. K. Farrand, *Mol. Plant. Microbe. Interact.* **1998**, *11*, 1119.

[656] E. F. Dixon, R. A. Hall, *Cell. Microbiol.* **2015**, *17*, 1431.

[657] S. P. Das, J. J. Boruah, N. Sharma, N. S. Islam, *J. Mol. Catal. A Chem.* **2012**, *356*, 36.

[658] S. Miyata, *Clays Clay Miner.* **1975**, *23*, 369.

[659] J. Fikáček, J. Prokleška, J. Prchal, J. Custers, V. Sechovský, *J. Phys. Condens. Matter* **2013**, *25*, 416006.

[660] A. Kowalczyk, T. Toliński, M. Reiffers, M. Zapotoková, M. Falkowski, E. Gažo, *Acta Phys. Pol. A* **2009**, *115*, 123.

[661] G. A. Bain, J. F. Berry, *J. Chem. Educ.* **2008**, *85*, 532.

[662] W. T. Self, S. Seal, *Nanoparticles of Cerium Oxide Having Superoxidase Dismutase Activity, US 7504356 B1*, **2009**.

[663] S. Yang, W. Zhu, Z. Jiang, Z. Chen, J. Wang, *Appl. Surf. Sci.* **2006**, *252*, 8499.

[664] T. Skála, N. Tsud, K. C. Prince, V. Matolín, *J. Phys. Condens. Matter* **2011**, *23*, 215001.

[665] M. Romeo, K. Bak, J. El Fallah, F. Le Normand, L. Hilaire, *Surf. Interface Anal.* **1993**, *20*, 508.

[666] T. Jo, A. Kotani, *J. Magn. Magn. Mater.* **1985**, *52*, 396.

[667] A. Kotani, T. Jo, J. C. Parlebas, *Adv. Phys.* **1988**, *37*, 37.

[668] R. Srivastava, *J. Colloid Interface Sci.* **2010**, *348*, 600.

[669] M. H. Bani-Hashemian, S. Brück, M. Luisier, J. VandeVondele, *J. Chem. Phys.* **2016**, *144*, 44113.

[670] K. R. Hahn, M. Iannuzzi, A. P. Seitsonen, J. Hutter, *J. Phys. Chem. C* **2013**, *117*, 1701.

[671] P. Deglmann, I. Müller, F. Becker, A. Schäfer, K.-D. Hungenberg, H. Weiß, *Macromol. React. Eng.* **2009**, *3*, 496.

[672] R. Ahlrichs, M. Bär, M. Häser, H. Horn, C. Kölmel, *Chem. Phys. Lett.* **1989**, *162*, 165.

[673] R. F. Beers, I. W. Sizer, *J. Biol. Chem.* **1952**, *195*, 133.

[674] B. R. E. Childs, W. G. Bardsley, *Biochem. J.* **1975**, *145*, 93.

[675] S. Scott, W. Chen, A. Bakac, J. H. Espenson, *J. Phys. Chem.* **1993**, *97*, 6710.

[676] K. S. Shin, C. J. Kim, *Biotechnol. Lett.* **1998**, *20*, 569.

[677] A. Asthana, K. H. Lee, S. J. Shin, J. Perumal, L. Butler, S. H. Lee, D. P. Kim, *Biomicrofluidics* **2011**, *5*, 24117.

[678] "http://www.bdsoft.de/demo/index.htm?/demo/chemie/chemikalien/p/phenolrot.htm," **2013**.